JOURNAL OF SCIENCE

PART A: ENGINEERING AND INNOVATION

Year | 2023 **Volume** | 10 **Issue** | 4

e-ISSN 2147-9542

Gazi University
Journal of Science
PART A: ENGINEERING AND INNOVATION

e-ISSN 2147-9542 YEAR 2023 VOLUME 10 ISSUE 4

| Owner |

on behalf of Gazi University
Rector
Prof. Dr.
Musa YILDIZ

| Publishing Manager |

Assoc. Prof. Dr.
Uğur GÖKMEN
Gazi University

| Chief Editor |

Prof. Dr.
Sema Bilge OCAK
Gazi University

| Managing Editor |

Prof. Dr.
Mustafa Gürhan YALÇIN
Akdeniz University

Gazi University
Journal of Science
PART A: ENGINEERING AND INNOVATION

e-ISSN 2147-9542 YEAR 2023 VOLUME 10 ISSUE 4

| Editorial Board |

Prof. Dr. **Adem TATAROĞLU** — Gazi University, Physics

Prof. Dr. **Adnan SÖZEN** — Gazi University, Energy Systems Engineering

Prof. Dr. **Ali KESKİN** — Çukurova University, Automotive Engineering

Prof. Dr. **Ali Osman SOLAK** — Ankara University, Chemistry

Prof. Dr. **Alper BÜYÜKKARAGÖZ** — Gazi University, Civil Engineering

Prof. Dr. **Atilla BIYIKOĞLU** — Gazi University, Mechanical Engineering

Prof. Dr. **Aynur KAZAZ** — Akdeniz University, Civil Engineering

Prof. Dr. **Cevriye GENCER** — Gazi University, Industrial Engineering

Prof. Dr. **Çağlayan AÇIKGÖZ** — Bilecik Şeyh Edebali University, Chemical Engineering

Prof. Dr. **Çetin ÇAKANYILDIRIM** — Hitit University, Chemical Engineering

Prof. Dr. **Demet CANSARAN DUMAN** — Ankara University, The Institute of Biotechnology

Prof. Dr. **Elif ORHAN** — Gazi University, Physics

Prof. Dr. **Erdal IRMAK** — Gazi University, Electrical-Electronic Engineering

Prof. Dr. **Fatih ÖZ** — Atatürk University, Food Engineering

Prof. Dr. **Feyza DİNÇER** — Nevşehir Hacı Bektaş Veli University, Geological Engineering

Gazi University
Journal of Science
PART A: ENGINEERING AND INNOVATION

e-ISSN 2147-9542 YEAR 2023 VOLUME 10 ISSUE 4

| Editorial Board |

Prof. Dr. **Gürhan İÇÖZ** — Gazi University, Mathematics

Prof. Dr. **Hacer KARACAN** — Gazi University, Computer Engineering

Prof. Dr. **Hakan ATEŞ** — Gazi University, Metallurgical and Materials Engineering

Prof. Dr. **Hüseyin Serdar YÜCESU** — Gazi University, Automotive Engineering

Prof. Dr. **Meltem DOĞAN** — Gazi University, Chemical Engineering

Prof. Dr. **Metin GÜRÜ** — Gazi University, Chemical Engineering

Prof. Dr. **Mine TÜRKTAŞ** — Gazi University, Biology

Prof. Dr. **Murat KAYA** — Aksaray University, Biotechnology and Nanotechnology

Prof. Dr. **Nalan KABAY** — Ege University, Chemical Engineering

Prof. Dr. **Nazife ASLAN** — Ankara Hacı Bayram Veli University, Chemistry

Prof. Dr. **Niyazi Uğur KOÇKAL** — Akdeniz University, Civil Engineering

Prof. Dr. **Nuran AY** — Eskişehir Technical University, Materials Science and Engineering

Prof. Dr. **Nurdane İLBEYLİ** — Akdeniz University, Geological Engineering

Prof. Dr. **Nursel AKÇAM** — Gazi University, Electrical-Electronic Engineering

Prof. Dr. **Ömer ŞAHİN** — İstanbul Tecnhical University, Chemical Engineering

Gazi University
Journal of Science
PART A: ENGINEERING AND INNOVATION

e-ISSN 2147-9542 YEAR 2023 VOLUME 10 ISSUE 4

| Editorial Board |

Prof. Dr. **Selim ACAR** — Gazi University, Physics

Prof. Dr. **Şükrü DURSUN** — Konya Technical University, Environmental Engineering

Prof. Dr. **Veli ÇELİK** — Ankara Yıldırım Beyazıt University, Mechanical Engineering

Prof. Dr. **Yılmaz ŞİMŞEK** — Akdeniz University, Mathematics

Prof. Dr. **Yusuf URAS** — Kahramanmaraş Sütçü İmam University, Geological Engineering

Prof. Dr. **Yücel ERCAN** — TOBB University of Economics and Technology, Mechanical Engineering

Prof. Dr. **Zafer EVİS** — Middle East Technical University, Engineering Sciences

Assoc. Prof. Dr. **Defne AKAY** — Ankara University, Physics

Assoc. Prof. Dr. **Yasemin LEVENTELİ** — Akdeniz University, Geological Engineering

Assist. Prof. Dr. **Emine Şükran OKUDAN** — Akdeniz University, Basic Sciences Fisheries

Assist. Prof. Dr. **Füsun YALÇIN** — Akdeniz University, Mathematics

Assist. Prof. Dr. **Senai YALÇINKAYA** — Marmara University, Mechanical Engineering

Dr. **Murat AKIN** — Gazi University, Computer Technologies

Dr. **Silver GÜNEŞ** — Gazi University, Chemical Engineering

Gazi University
Journal of Science
PART A: ENGINEERING AND INNOVATION

e-ISSN 2147-9542 YEAR 2023 VOLUME 10 ISSUE 4

| Foreign Editorial Advisory Board |

Prof. Dr. **Abdelmejid BAYAD** Université d'Évry Val d'Essonne **FRANCE**

Prof. Dr. **Ali Behcet ALPAT** Istituto Nazionale di Fisica Nucleare (INFN) **ITALY**

Prof. Dr. **Azra SPAGO** Dzemal Bijedic University of Mostar **BOSNIA AND HERZEGOVINA**

Prof. Dr. **Bektay YERKIN** Satbayev University **KAZAKHSTAN**

Prof. Dr. **Burçin BAYRAM** Miami University **USA**

Prof. Dr. **Daeyeoul KIM** Jeonbuk National University **SOUTH KOREA**

Prof. Dr. **Elvan AKIN** Missouri University of Science and Technology **USA**

Prof. Dr. **Filiz DİK** Rockford University **USA**

Prof. Dr. **Homer RAHNEJAT** Loughborough University **UNITED KINGDOM**

Prof. Dr. **Lokesha VEERABHADRIAH** Vijayanagara Sri Krishnadevaraya University **INDIA**

Prof. Dr. **Mehmet DİK** Rockford University **USA**

Prof. Dr. **Nedim SULJIĆ** University of Tuzla **BOSNIA AND HERZEGOVINA**

Prof. Dr. **Rob DWYER-JOYCE** The University of Sheffield **UNITED KINGDOM**

Prof. Dr. **Snezana KOMATINA** University Novi Sad **SERBIA**

Prof. Dr. **Toni NIKOLIC** University Džemal Bijedić Mostar **BOSNIA AND HERZEGOVINA**

Prof. Dr. **Turysbekova Gaukhar SEYTKHANOVNA** Satbayev University **KAZAKHSTAN**

Assoc. Prof. Dr. **Burcin ŞİMŞEK** Associate Director Biostatistics (Oncology) at Bristol Myers Squibb **USA**

Assist. Prof. Dr. **Alisa BABAJIC** University of Tuzla **BOSNIA AND HERZEGOVINA**

Dr. **Daniel Ganyi NYAMSARI** Mining Company Researcher **CAMEROON**

Gazi University
Journal of Science
PART A: ENGINEERING AND INNOVATION

e-ISSN 2147-9542 YEAR 2023 VOLUME 10 ISSUE 4

| English Language Editors |

Lecturer
Gizem AÇELYA AYKAN
Gazi University
School of Foreign Languages

Lecturer
Tuğçe BÜYÜKBAYRAM
Gazi University
School of Foreign Languages

| Technical Editors |

Dr.
Fatih UÇAR
Akdeniz University

Research Assistant
Özge ÖZER ATAKOĞLU
Akdeniz University

Gazi University
Journal of Science
PART A: ENGINEERING AND INNOVATION

e-ISSN 2147-9542 YEAR 2023 VOLUME 10 ISSUE 4

| Correspondence Address |

Gazi University Graduate School of Natural and Applied Sciences
Emniyet Neighborhood, Bandırma Avenue, No:6/20B, 06560, Yenimahalle - ANKARA
B Block, Auxiliary Building

| e-mail |

gujsa06@gmail.com

| web page |

https://dergipark.org.tr/tr/pub/gujsa

Gazi University Journal of Science Part A: Engineering and Innovation
is a peer-reviewed journal.

Gazi University
Journal of Science
PART A: ENGINEERING AND INNOVATION

e-ISSN 2147-9542 YEAR 2023 VOLUME 10 ISSUE 4

| INDEXING |

| ACCESSIBILITY |

This work are licensed under a Creative Commons Attribution-ShareAlike 4.0 International License.

Gazi University
Journal of Science
PART A: ENGINEERING AND INNOVATION

e-ISSN 2147-9542 YEAR 2023 VOLUME 10 ISSUE 4

CONTENTS

Gazi University
Journal of Science
PART A: ENGINEERING AND INNOVATION

e-ISSN 2147-9542 YEAR 2023 VOLUME 10 ISSUE 4

CONTENTS

Research Article GU J Sci, Part A, 10(4): 378-391 (2023) 10.54287/gujsa.1328619

Gazi University
Journal of Science
PART A: ENGINEERING AND INNOVATION
http://dergipark.org.tr/gujsa

Consequence Analysis of An Industrial Accident at a Fuel Station

Saliha ÇETİNYOKUŞ[1*] Ece PAMUK[1]

[1] Department of Chemical Engineering, Faculty of Engineering, Gazi University, Ankara, Türkiye

Keywords

Consequence Modelling
Model Validation
Hazard Identification
Risk Analysis
Fuel Station

Abstract

Major industrial accident is a type of technological disaster that may require extraordinary intervention in areas outside the facility, in addition to those affected within the facility. It causes damage to the environment and loss of life at the time it occurs or afterward. Studies to be carried out to prevent these accidents Zor to reduce their effects are important. In this study, a case study for the consequences of an industrial accident that may occur in a fuel station was analyzed. Firstly, possible accident scenarios were created by obtaining chemical, atmospheric and source data. The LPG (Liquefied Petroleum Gas) storage tank (40m3) was considered in modeling a fuel station in the Korfez district of Kocaeli province, where the industry is dense in Turkey. The average atmospheric data of the province for the months of August and January were used to represent summer and winter conditions, respectively. Threat zones were produced with ALOHA (Areal Locations of Hazardous Atmospheres) software based on a release to atmosphere without burning, a jet fire as a result of a leak in the LPG tank and BLEVE scenarios. The two most dangerous scenarios were determined as a possible jet fire in August and a possible BLEVE (Boiling Liquid Expanding Vapor Explosion) in January. Overpressure effects were also obtained using the BST (Baker-Strehlow-Tang) method, thus ensuring the validation. With the software, the vapor cloud explosion distance as a result of the leak in August was obtained as 456m and 268m for the yellow (6.89kPa) and orange (24.13kPa) threat zones, respectively. Overpressure in an area of 500 meters was calculated as 5.06kPa with BST method. This calculated overpressure has the potential for damage that can lead to glass and window breakage in parallel with the ALOHA output. It has been determined that indirect injuries may occur to living beings.

Cite

Çetinyokuş, S., & Pamuk, E. (2023). Consequence Analysis of An Industrial Accident at a Fuel Station. *GU J Sci, Part A, 10*(4), 378-391. doi:10.54287/gujsa.1328619

Author ID (ORCID Number)

0000-0001-9955-6428 Saliha ÇETİNYOKUŞ
0009-0006-8268-3512 Ece PAMUK

Article Process

Submission Date 17.07.2023
Revision Date 13.09.2023
Accepted Date 25.09.2023
Published Date 30.10.2023

1. INTRODUCTION

In parallel with the development of science and technology, chemicals and chemical processes, the use of which increases as the number of industrial facilities increases, not only facilitates production processes and life, but also poses risks for both humans and the environment. Due to the use of hazardous chemicals, many major industrial accidents have occurred, and enormous material and moral losses have also occurred that cannot be recovered or compensated. In particular, as a result of major industrial have started.

Hazardous chemicals have the potential to affect not only the people or organizations that use these substances directly, but also the population, the environment and natural life in case of possible industrial accidents. In the literature, it has seen that consequence analyzes are made through various software and methods in industrial establishments containing various hazardous chemicals. Consequence analyzes provide important inputs for effective risk assessment. In the study by Yu et al. (2023), the risk assessment of the hydrogen-gasoline hybrid refueling station was conducted with the Accident Risk Assessment Method (ARAMIS) and an improved probabilistic failure model was used. Accident consequences were simulated using CFD methods. The risk levels on the road near the station building and the refueling area were within the acceptable range.

*Corresponding Author, e-mail: salihakilicarslan@gazi.edu.tr

A fire accident caused by the leakage of alcohol-based fuel vapor was analyzed by Wang et al. (2023). Multiple physical space loads were determined by on-site examination and CFD. A hazardous gas distribution after a leak accident was simulated through CFD by Wu et al. (2023). The effects of source location and ventilation path on the distribution characteristics were analyzed. Additionally, the relationship between individual mortality risk and source density by using H_2S as a toxic substance source was measured. Critical risks and effective safety measures for pipelines were qualitatively analyzed by Nakayama et al. (2022). 183 accident scenarios were identified through the hazard identification and preventive and mitigating safety measures were presented. Hydrogen dispersion simulations were revealed that low-pressure hydrogen dispersion leaking through small holes and cracked pipes in public spaces can lead to alarming risks depending on the size, direction, location of the leak, obstructions and ignition source. An integrated risk assessment procedure based on accident consequences and local people's sensitivity was presented by Guan et al. (2022) and then applied to a small town in China. A hazard map was obtained from the footprint of regional hazards. Population susceptibility was determined from resident exposure, sensitivity, and adaptability. On the other hand, population exposure indicators were determined from population density and residential environment. The effects and consequences of toluene release were modeled by Barjoee et al. (2022) through the ALOHA and PHAST programs. Maximum threat zone distances associated with the high toxicity, flammability and thermal radiation hazards of toluene were obtained, with the highest probability of death being 92% determined at a distance of 1 m during cold seasons. With the PHAST program, higher values than those determined in ALOHA were detected. In the study by Sun et al. (2021), the safety distances of petrochemical equipment in both underground and underground vaults were investigated. Accident consequence analyzes were performed for typical substances in the tank, such as liquid oxygen, hydrogen, LPG, LNG (Liquefied Natural Gas), and gasoline. The PLL (Potential loss of life index) was calculated to consider the average risk of district personnel. It was observed that the PLL value decreased by 36.7% when the gasoline storage tank alone was underground, and by 6.33% when only the LPG tank was underground. In the study by Ahn et al. (2020), accidents involving flammable materials such as benzene, toluene, xylene, methyl ethyl ketone and ethyl acetate were modeled with free ALOHA software and KORA software. ALOHA software applies the BST method as a VCE (Vapor Cloud Explosion) modeling technique. KORA supports TNO multi-energy method for pool fire and VCE models. Modeling results under similar conditions produced similar damage radius. It has been emphasized that chemical accidents are highly correlated with the physicochemical properties of the chemicals, and the similarity of the physicochemical properties of the investigated chemicals. In the study by Ma and Huang (2019), a quantitative risk analysis was performed to assess human safety of explosion accidents at gas stations. A case study was conducted for explosion accidents that occurred during refueling from a fuel tanker to a gas station. PHAST was used to simulate explosions. Wind directions and wind speeds were not considered. The BST model was chosen while performing the explosion analysis. For the leak scenarios, 18 cases that occurred in Western Australia between 1996 and 2008 were considered. When an area with an overpressure greater than 0.689 bar reached the nearest distributor (approximately 10 m) and storage area (20 m), the severity was determined as medium and large, respectively. In the study by Sierra et al. (2019), the problem of assessing the safety of chemical plants was examined by considering the physical layout as well as equipment types and materials processed. Focusing on the safety issues posed by VCEs, a methodology based on probabilistic modeling was proposed to evaluate the consequences of domino effects. A case study was conducted with five gas tanks and five different settlement scenarios. The probability of a tank being exposed to VCE was obtained higher than the threshold given by the value of the cumulative distribution function governing the occurrence of VCE in each tank. In the study by Lee et al. (2019), the safety distance regulations in Korea for BTX items were compared with other countries, and it was evaluated whether there was a possibility of domino explosion with the current safety distances in Korea. TNT, TNO and BST methods were used to model the explosions. The amount of flammable material stored in the tanks (L=4 m, D=2 m) was accepted as 50 000 kg. It was found that the probability of a domino explosion was low when the safety distance was longer than the distance that the 24 kPa overpressure can reach. There was no significant difference between the distances reached by the overpressure determined by each method. In the study by Witlox et al. (2018), modeling studies were carried out for the accidental release of flammable or toxic chemicals into the atmosphere. Validation was done with PHAST. Many different chemicals (including water, LNG, propane, butane, ethylene, ammonia, CO_2, hydrogen, chlorine, HF, etc.) were considered. In the by Huang and Ma (2018), a grid-based risk mapping method was used to enable effective and detailed risk screening in an area where explosion and fire accidents occurred at a hydrogen refueling station. PHAST was chosen to simulate explosions. Distributions of all leaks and wind directions were considered in the analysis. Since the storage volume inside the station was quite

small, it was determined that the spread would not exceed the hydrogen station and therefore it was assumed that the congestion would remain the same. No explosion was observed when the leakage volume was less than 3 kg.

Industrial accidents result in fire, explosion or toxic emission. Explosion events stand out with both serious losses of life and property damage. It has seen in the literature that explosion models continue to be developed in both model and experimental studies. Rocourt et al. (2023) compared the values of overpressure and flame speed in small-scale flash experiments with the values predicted from the TNO-ME method and BST method. Experiments were carried out in hydrogen-air mixtures in cylindrical compact volumes ranging from 1.77 L to 7.07 L. Reactivity was controlled by the hydrogen-air equivalence ratio. The estimated flame speed values obtained from the BST method were found to be in agreement with almost half of the experimental results, and the method exhibited consistency in most of the tested configurations. The use of the TNO ME method was validated in a small-scale experiment to predict maximum overpressures resulting from flaring of medium- and large-scale H_2/air clouds. A hybrid deep learning probabilistic model was proposed by Shi et al. (2023) to predict the spatial explosion overpressure of the offshore platform in real time using the observed overpressures. Data from both the experimental natural gas explosion and the offshore platform were used to create the comparative data set. The results showed that the model exhibited good real-time capability. In the study by Shi et al. (2021), a quantitative evaluation correlation (QEC) of flame velocity was established based on the numerical models of the three geometric scales and the CSC correlation verified by the FLACS software, in the method that can only subjectively select the detonation curve. Based on a petrochemical plant, positive phase peak pressure and impulse at different distances were estimated with the BST flame velocity table and the TNT EM, TNO MEM, FLACS and BST curve suggested. The overpressure estimated from the BST curve was shown to be closer to that obtained from FLACS. In the study by Bai et al. (2021), a triangular pyramid explosion risk model based on explosion overpressure (p), duration (t) and frequency (f) was created for petrochemical buildings. A case study was conducted for a petrochemical building and the hydro cracking unit next to it. Based on the overpressure-cumulative frequency curve and the explosion risk curve, BRDLs were determined quantitatively. Computational Fluid Dynamics (CFD) method was used in the calculation process. The main factors affecting the explosion load were the characteristics of the hazardous environment, process operating conditions, degree of obstruction, leak hole size and explosion source distance. In the study by Liu et al. (2020), the primary explosion gas cloud and the secondary explosion of the gas cloud were analyzed using pressure and flow field monitoring. Methane was preferred for experimental safety. Polyvinyl chloride was used to create a spherical gas cloud, then used to produce the impulse effect of multiple gas cloud explosions to evaluate the detonation process. Double gas cloud and multiple gas cloud explosion experiments were performed under different conditions and the consequences were compared. It was shown that the larger the size of the primary explosion gas cloud, the smaller the distance between the primary explosion gas cloud and the secondary explosion gas cloud, and the greater the explosion density of the two gas clouds were determined. A detailed comparison of the TNO multi-energy, BST and CAM models was made by Fitzgerald (2001). BST model estimations were reported to be highly reliable and the easiest to implement of the three methods.

In this study, a case study based on the consequence modeling of a possible industrial accident at a fuel station in Turkey was carried out for the first time. It was assumed that a LOC (Loss of Containment) occurred in the LPG storage tank, which is the most critical equipment in the fuel station. The possible physical effects of the LPG tank leakage were modeled over different accident scenarios for different leak hole diameters and atmospheric conditions with ALOHA software. In accident scenarios, jet fire, BLEVE and release to atmosphere without burning were considered. Overpressure effects, in which the largest and serious effects were determined, were also analyzed with the BST method, and the software results were supported.

2. MATERIAL AND METHOD

2.1. Data Supply

Hazardous Properties

In Turkey, typical LPG mixture contains 30% propane and 70% butane. Due to the limitation of modeling this mixture of the ALOHA software, modeling studies were carried out based on the highest content of butane.

Butane is used as a fuel, refrigerant, aerosol propellant and intermediate in the chemical industry. Its chemical formula is C_4H_{10}. Its CAS number is 106-97-8. Its flammability and health effects scores are 4 and 1, respectively (Figure 1). These properties make the chemical extremely dangerous (BP Group, 2021). The important physical and chemical properties of butane are shown in Table 1.

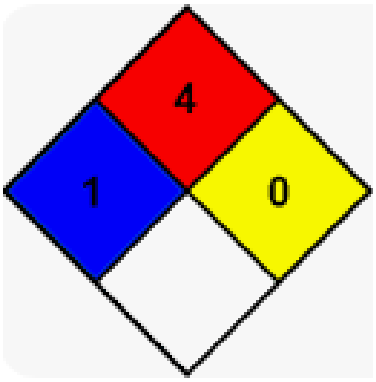

Figure 1. *Hazard diamond of butane*

Table 1. *Physical and chemical properties of butane*

Physical state	Liquefied gas
Molecular weight	58.12 g/mol
Color	Colorless
Smell	Sulphurous
Melting point	-138°C (-216.4°F)
Boiling point	<-2°C (<28.4°F)
Critical temperature	-60 °C
Flash point	In closed container:<-50°C (<-58°F)
Auto ignition temperature	365°C (689°F)
Relative gas density	1.9 - 2.1 [Air = 1]
Explosive limits	1.9 -9%

The explosive lower limit of the chemical is quite low. This highlights the danger of flammability.

Characteristics of Fuel Stations

According to the Workplace Hazard Classes Communiqué on Occupational Health and Safety, fuel stations are in the very dangerous class. As a condition of establishment of fuel stations, they must meet the Turkish Standard (TS) 12820 Fuel Stations Safety Requirements Standard. Most of the precautions taken against explosions at fuel stations are also valid in cases where LPG will be sold, and additional precautions are specified in the TS 11939 LPG Supply Stations Safety Requirements Standard and other standards required by this standard. In accordance with the relevant legislation and standards, a fuel station should not be established and operated without making a dealership agreement with the company holding the distribution license granted by EMRA (Energy Market Supervision Agency). Fuel is stored in tanks at the stations. It is manufactured as single or double walled, single compartment or multi compartment. The inner tank (main tank) of double-walled tanks is surrounded by an outer tank, the tank walls are physically separate and at a certain distance from each other, and in case of a leak in the inner tank, it is aimed to protect this leak in the space between both tanks. A maximum of 300 000 L of fuel can be stored at the fuel station, provided that it does not exceed 50 000 L per tank. For this reason, filling is done every day or every two days at large stations (Tuncay, 2014). Fuel stations containing highly dangerous chemicals pose a risk to humans and the environment. For this reason, safety distances are defined. (Table 2)

Table 2. *Minimum safety distances for underground tanks (Demircan, 2010)*

Tank volume (L)	Distance of underground tanks to neighboring plot boundary, main traffic roads or railways (m)*	The distance of the tanks to each other (m)*
≤500	0	0
500-3000	3	1
3001-10 000	5	1
10 001-50 000	7.5	1
50 001-120 000	10	1.5
120 001-250 000	15	1/4 of the sum of the diameters of the tanks adjacent to each other
250 001-600 000	15	
600 001-1 200 000	15	
1 200 001-5 000 000	15	
≥5 000 001	15	

* Distances are the shortest distance measured from the outer wall of the tank

While the distance between the tanks within the station is 1.5 m at most, the distances to the neighboring borders and access roads can reach 15 m. Safety distance is an important measure for risks, but it is not enough. Depending on the physiochemical properties of the hazardous chemical, the effects of fire, explosion or toxic emission of possible accidents can reach kilometers distance. Consequence analyzes need to be considered for emergency plans and fuel station locations (Ahn et al., 2020).

The schematic representation of the tank size for LPG storage tanks in the relevant standard is given in Figure 2, and the tank size data is given in Table 3 (GBS, 2019).

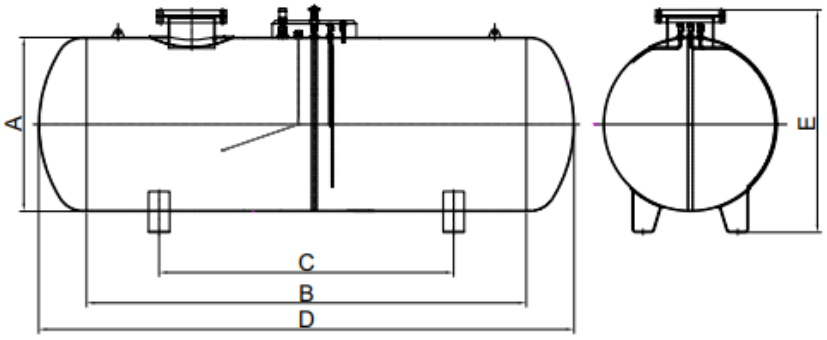

Figure 2. *Tank size schematic ılustration*

Table 3. *Data on tank size (GBS, 2019)*

Volume (L)	A (mm)	B (mm)	C (mm)	D (mm)	E_{max} (mm)
10 000	1 600	4 500	3 300	5 392	2 160
10 000	1 900	2 850	1 850	3 974	2 420
22 000	2 350	4 500	3 300	5 745	2 850
40 000	2 400	8 000	4 000	9 350	2 900
50 000	2 400	10 500	5 250	11 850	2 900

The volume per tank at fuel stations is allowed to be 45-50 m^3. LPG storage tank volumes can be preferred in smaller sizes upon request.

2.2. Determination of the Accident Scenario and Related Assumptions

It was assumed that there was a LOC in the LPG storage tank located at a fuel station in Kocaeli. The reason for choosing Kocaeli as the location is that it is an industrial area, the fuel stations are close to the settlements and the probability of a domino effect is high. Modeling studies were carried out in two different atmospheric conditions, summer and winter, with the foresight that atmospheric conditions may change the LPG release. Meteorological data of January for the winter condition and August for the summer condition were used.

The chemical source was accepted as the tank. Fuel stations sold on LPG must comply with the TS 11939 LPG Supply Stations Safety Requirements Standard, together with the TS 12820 (2006) Fuel Stations Safety Requirements Standard. It is stated that at a fuel station conforming to this standard, a maximum of 300 000 L of fuel can be stored, provided that it does not exceed 50 000 L per tank (TS 12820, 2006). Therefore, when the tank standards are examined, it is seen that 40 000 liter tanks are suitable for the accident scenario. The volume of the tank is 40 000 L (40 m^3), the width of the tank is 2 400 mm and the height of tank is 2 900 mm. Since it is necessary to automatically prevent the tanks at the LPG refueling station from being filled above 85% of the nominal water volume, the tank filling rate was taken as 80% (Tuncay, 2014).

2.3. Modeling with ALOHA Software

The main purpose of ALOHA software is to provide emergency response by estimating of the effect distances of chemical releases (Jones et al., 2013). The software has its own library of chemicals, but is used for modeling pure substances and few mixtures (Cetinyokus, 2017). ALOHA software links direct, tank, puddle or gas piplene source models to a dispersion model to predict the effect distances of toxic clouds, flammable vapors and explosive vapor clouds.

With the ALOHA software, at first location and chemical selection was made. Then, atmospheric conditions of the selected region were considered and accident scenarios were created and modeled according to the source selection.

Location and Chemical Selection

ALOHA software is limited in modeling many mixtures. For this reason, modeling was done on high content butane considering the mixture of LPG consisting of 30% propane and 70% butane. Kocaeli province was selected as the location in the software.

Atmospheric Options

Meteorological data of January for winter conditions and August for summer conditions were used (Directorate General of Spatial Planning, 2018). Atmospheric data of Kocaeli province are given in Table 4.

Table 4. *Atmospheric data*

	January	August
Air temperature	6.2°C	23.9°C
Wind speed	1.5 m/s	1.4m/s
Wind direction	West North West	South East
Cloud cover	Partly Cloudy	Partly Cloudy
Humidity	75.8%	70%
Ground roughness	Open country	Open country
Atmospheric stability	F	E
Altitude	1 m	1 m

In the software, the ground roughness was chosen as the open country where there were no congested structures around, and the selection was made for the impact distances to be at the human level. The software

automatically set the atmospheric stability class as F for January and E for August. Selections were made with no inversion and humidity of 75.8% and 70% for January and August, respectively.

Chemical Source and Scenario Selection

Modeling studies were performed over three basic scenarios, considering different leak hole diameters and atmospheric conditions. Values such as tank size and tank filling rate were taken the same for each scenario. Modeling was done by assuming the hole that caused the leak as a circular form, both while using the ALOHA software and applying the BST method (Table 5).

Table 5. *Accident scenarios*

Scenario (1): In August/January, leaking tank, chemical is not burning as it escapes into the atmosphere.
Leak hole diameter= 4 cm
Leak hole diameter= 10 cm
Scenario (2): In August/January, leaking tank, chemical is burning as a jet fire
Leak hole diameter= 4 cm
Leak hole diameter= 10 cm
Scenario (3): In August/January, BLEVE, tank explodes and chemicals burn in a fireball

2.4. Modeling with the BST Method

The BST method was used to determine overpressure and impulse estimates from vapor cloud explosions. The method is based on only the congested or partially congested portions of a flammable vapor cloud contribute to the overpressure. It estimates the detonation energy (E) based on the average stoichiometric fuel-air mixture. It also uses a family of curves to determine ΔPs as a function of the combustion energy scaled distance and a numerically determined continuous pressure and pulse curves that take the flame Mach number as a parameter. The strength of the blast wave is proportional to the maximum flame speed in the cloud. The appropriate Mach number, M_f, for each special case modeled can be taken from Table 6 (Casal, 2018).

Table 6. *Mach numbers (M_f) to be used in the BST method (Casal, 2018)*

		Congestion		
Flame expansion	Reactivity	Low	Medium	High
2D	High	0.59	DDT	DDT
	Medium	0.47	0.66	1.6
	Low	0.079	0.47	0.66
2.5D	High	0.47	DDT	DDT
	Medium	0.29	0.55	1.0
	Low	0.053	0.35	0.50
3D	High	0.36	DDT	DDT
	Medium	0.11	0.44	0.50
	Low	0.026	0.23	0.34

DDT: transition from deflagration to detonation

In Table 6, no plane limiting flame expansion is considered 3D. Presence of a single bounding plane means 2D flame expansion. The 2.5D restraint category corresponds to situations where the restraint is made from a frangible panel or nearly rigid restraint. If the congestion is below 10%, it is considered low, between 10% and 40% medium, and above 40% high. Three different categories for the reactivity of fuels were recommended as highly reactivity fuels (hydrogen, acetylene, etc.), low reactivity fuels (methane and carbon monoxide) and medium reactivity fuels (all other gases and vapors) (Casal, 2018).

Scaled distance,

$$d_n = \frac{d}{M^{1/3}} \quad (1)$$

where

d_n : scaled distance (m $kg^{-1/3}$)

d : actual distance from the center of the explosion to the point at which the overpressure should be estimated(m)

M : charge mass (kg)

When two explosives with similar geometry of the same explosive but different dimensions are detonated in the same atmosphere, similar peak overpressures are produced at the same scaled distance. This is the simplest and most common form of burst scaling. Another approach suggested by Sachs to use below. The blast wave can be expressed as a function of the scaled overpressure and is calculated by (Eq. 2)(Casal, 2018).

$$\Delta P_s = \frac{Ps}{P0} \quad (2)$$

Combustion energy -scaled distance is calculated with (Eq.3).

$$R = \frac{d}{(\frac{E}{P_0})^{1/3}} \quad (3)$$

It is calculated with the Sachs scale impulse coefficient (Eq.4).

$$i_s = \frac{iu_s}{{P_0}^{2/3}E^{1/3}} \quad (4)$$

where

i : incident impulse (Pa s)

E : energy involved in the explosion (J)

P_0 : atmospheric pressure (Pa)

ΔP_s : side-on peak overpressure (Pa)

P_s : peak pressure (Pa)

u_s : speed of sound in air (m/s) (Casal, 2018).

The chemical mass determined in the ALOHA software was taken as the vapor volume. The explosion energy (E) was calculated by multiplying the volume by 3.5 x 10^6 J m^{-3}. The scaled distance (R) was then calculated. The appropriate Mach number was selected from the values listed in the method, and finally the peak pressure was determined. The vulnerability caused by the peak pressure was interpreted.

3. RESULTS AND DISCUSSION

3.1. Evaluation of ALOHA Software Modeling Results

Horizontal and cylindrical tank (L=9.35m, D=2.4m, V=42.3m^3) was selected based on the LPG storage tanks specifications in the fuel stations. LPG is gaseous under normal conditions, but is liquefied under pressure during filling into storage tanks. For this reason, it was chosen that the tank contained liquid and was stored according to the ambient temperature. The filling rate of the tank was taken as 80%. The leak shape was circular and the leak type was taken as a hole. Since the weakest points in a storage tank are the filling and

discharge openings, it was assumed that a potential leak would occur from the filling and discharge points. The diameters of the filling and discharge openings in LPG storage tanks are approximately 5 cm for each 50 m^3 tank volume (Acikgoz, 2012). Considering this ratio, the leak hole diameter was determined as 4 cm. Model studies were also carried out by choosing a larger leak hole diameter of 10 cm. The effect distances obtained as a result of the modeling studies carried out for the months of August and January at different leak hole diameters are given in Table 7 and Table 8, respectively.

Table 7. *All effect distances obtained as a result of modeling studies carried out for August*

Leaking tank, chemical is not burning as it escapes into the atmosphere (Scenario 1)						
	4cm leak hole diameter			10cm leak hole diameter		
	Red Threat Zone	*Orange Threat Zone*	*Yellow Threat Zone*	*Red Threat Zone*	*Orange Threat Zone*	*Yellow Threat Zone*
Vapor Cloud Toxic Effects	75m	118m	194m	208 m	329 m	506 m
Vapor Cloud Flammable Effects	151m	-	348m	410 m	-	821 m
Vapor Cloud Explosion Effects	-	105m	185m	-	268 m	456 m
Leaking tank, chemical is burning as a jet fire (Scenario 2)						
	4cm leak hole diameter			10cm leak hole diameter		
Thermal Radiation Effects	23m	35m	57m	53 m	83 m	135 m
BLEVE, tank explodes and chemicals burn in a fireball (Scenario 3)						
	Red Threat Zone		*Orange Threat Zone*		*Yellow Threat Zone*	
Thermal Radiation Effects	346 m		488 m		761 m	

Table 8. *All effect distances obtained as a result of the modeling studies carried out for January*

Leaking tank, chemical is not burning as it escapes into the atmosphere (Scenario 1)						
	4cm leak hole diameter			10cm leak hole diameter		
	Red Threat Zone	*Orange Threat Zone*	*Yellow Threat Zone*	*Red Threat Zone*	*Orange Threat Zone*	*Yellow Threat Zone*
Vapor Cloud Toxic Effects	55m	83m	137m	155 m	240 m	385 m
Vapor Cloud Flammable Effects	106m	-	250m	303 m	-	674 m
Vapor Cloud Explosion Effects	-	75m	134m	-	208 m	348 m
Leaking tank, chemical is burning as a jet fire (Scenario 2)						
	4cm leak hole diameter			10cm leak hole diameter		
Thermal Radiation Effects	15m	24m	39m	36 m	57 m	94 m
BLEVE, tank explodes and chemicals burn in a fireball (Scenario 3)						
	Red Threat Zone		*Orange Threat Zone*		*Yellow Threat Zone*	
Thermal Radiation Effects	367 m		519 m		810 m	

LOCs for toxic domains are specific to chemicals. For LPG, the red zone: >53000ppm(AEGL-3[60min]), the orange zone:>17000ppm(AEGL-3[60min]) and the yellow zone: :>5500ppm(AEGL-3[60min]) represent threshold values. In AEGL-3, the general population suffers from serious life- or death-threatening problems from toxic spread. In AEGL-2, the general population suffers irreversible and severe effects; in AEGL-1, the general population suffers from serious non-harmful and reversible effects. For the flammable effects, the red zone and yellow zone represent >9600 ppm (60% LEL), >1600 ppm (10% LEL), respectively. LEL (Lower Explosion Limit) refers to the minimum vapor rate of flammable substances that should be in the air. Overpressure effects in three phases in the software are evaluated as red zone: 55.16kPa (building collapse), orange zone: 24.13kPa (serious injuries), and yellow zone: 6.89kPa (breaking glass). Threshold values for thermal radiation correspond to red zone: >10.0 kW/m^2, orange zone: >5.0 kW/m^2 and yellow zone: >2.0 kW/m^2. From the tables, as the leak hole diameter increased, the effect distances increased due to the increase in the amount of hazardous chemicals released into the environment. The effect distances determined for Scenario (1) and Scenario (2) in August were found to be higher than the effect distances determined in January. However, in the case of Scenario (3), the effect distances in August was less than in January. Since the gas diffusion around the cold environment was reduced, more dense gas in the limited area had led to this consequence. The most dangerous scenario was identified as the BLEVE in January. In the above tables, each effect distance was found to be significantly higher than the related safety distances (Table 2). Determining the effect distances, considering the relevant physicochemical properties and accident scenarios, is extremely important in preventing loss of life and property (Lee at al., 2019; Sierra et al., 2019).

It was observed that the thermal radiation area that will be formed by the explosion of the tank in Kocaeli can be of a dangerous size. The Google Earth images of the BLEVE threat zones determined for August and January are presented in Figure 3.

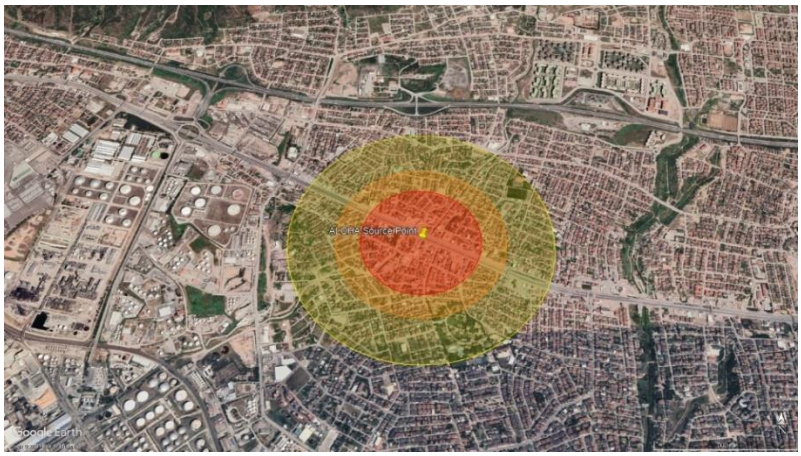

(a)

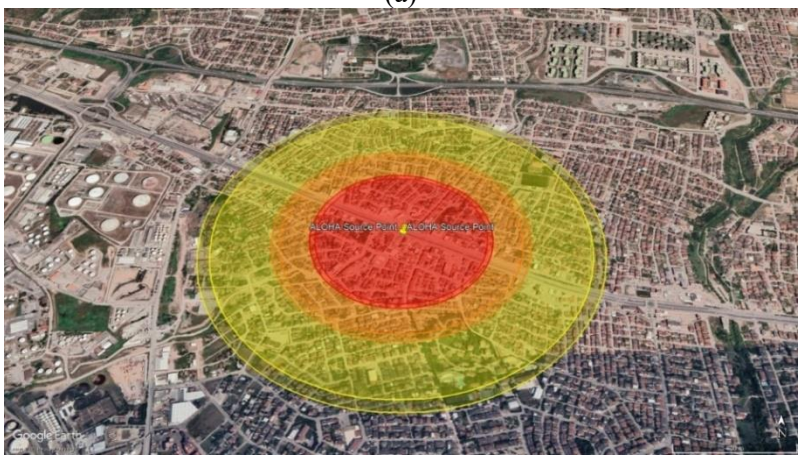

(b)

Figure 3*. Google Earth images of BLEVE threat zones determined for* ***a)*** *August and* ***b)*** *January (Scenario 3)*

The explosion of the LPG tank was modeled at a fuel station in Guney neighbourhood, located in Korfez district of Kocaeli province. The reason for choosing this region is its proximity to the Körfez refinery area. In addition, there are approximately 40 LPG storage, tube-tanker filling, fuel storage and filling, ammonia production and storage facilities and ports belonging to these facilities located around the refinery. In parallel with the increasing influence with the development of industry in the Korfez, a rapid urbanization dynamic has occurred, which has led to the rapid growth of the city and the random increase in residential areas. The explosion at the fuel station located close to this place both affected the population and showed the possibility of internal and external domino effects. From the Google Earth images, it was seen that the affected neighborhoods were Kuzey, Esentepe, Barbaros, Guney and Yeniyalı. According to data of Turkish Statistical Institute, the number of households is 2 063 in Kuzey, 2 900 in Esentepe, 1 349 in Barbaros, 5 513 in Guney, and 3 476 in Yeniyalı. Many residences, workplaces and buildings were in threat zones. When the average number of people living in the household was taken as 3 and the most affected area according to the map was the Guney neighborhood, the affected population was determined as 16 539 people. From -Figure 3, it was seen that the effect distances in January were higher than in August. ALOHA software calculated the liquid LPG in the tank as 20 161 kg in January. In August, this was 19 492 kg. It was observed that the increase in the effect distance depended on the amount of LPG.

3.2. Evaluation of BST Method Modeling Results

Calculations were made at different limiting planes (2D, 2.5D, 3D) and at different target distances (d=300m, 500m and 650m) for comparison with ALOHA software outputs (vapor cloud explosion areas). Medium reactivity and medium congestion were considered. The temperature was included in the calculations in parallel with the ALOHA software, considering the months of January and August. Consequences of overpressure based on damage to buildings and structure and also people can be found in related referance tables (Casal, 2018).

BST Modeling results for four different target distances for August and January are presented in Table 9 comparatively.

Table 9. *Comparison of BST Modeling results on peak pressures(kPa) at different target distances for August and January*

	2D			*2.5D*			*3D*		
	300 m	500 m	650 m	300 m	500 m	650 m	300 m	500 m	650 m
August (T=23.9°C)	10.13	8.11	6.08	9.12	7.09	4.05	8.11	5.06	3.04
January (T=6.2°C)	8.11	7.09	4.56	8.11	7.09	3.04	8.11	3.04	2.03

In Table 9, it was observed that the overpressures decreased as the confining plane increased. It was obtained that the overpressure values in August were higher than in January. It was determined that the overpressure effects in summer will be greater than in winter. The results obtained with the BST method showed parallelism with the results of the ALOHA software (vapor cloud explosion areas). This is a natural consequence of the software being based on the BST method (Bai et al., 2021). However, the software also allows different selections (wind speed, wind direction, etc.) and simultaneously provides thermal radiation effects as well as overpressure effects. In ALOHA software, the vapor cloud explosion distance was 456m (6.89kPa) and 268m (24.13kPa) as a result of the leak in August. In Table 9, an overpressure of 5.06kPa occurred in an area of 500 meters for 3D. From the reference table (Casal, 2018), it was seen that this overpressure caused glass and window breakages in parallel with the ALOHA software result. It is important to ensure reasonable safety that people stay away from windows so that they are not affected by these glass and window breakages, and that they can lie on the ground if inside or outside a reinforced structure.

Hazards should be identified at stations and risk assessments should be carried out on a regular basis. Employees at the stations should be informed about workplace environmental factors, working conditions, hazards and risks, precautions to be taken, and training should be provided. The people of the region close to

the fuel stations should be informed and their awareness should be increased within the scope of accident effects and emergency plans for possible accidents. The participation of the surrounding population in emergency plans should be ensured. LPG pipes installed above and underground, the placement of pipes, valves, sealing elements and other elements used in the installation must have ATEX properties in accordance with the relevant standards. The railway line passing between the flammable and explosive material storage facilities and the refinery makes it difficult to control the region and increases the risk of sabotage. Damage to these facilities may cause a domino effect and may cause explosions at nearby fuel stations.

4. CONCLUSION

Consequences analyzes were carried out at a fuel station in Turkey, which is located in a dense population and industry area. The LPG tank was taken as a critical equipment, and models were made with ALOHA software in different leak hole diameters and atmospheric conditions. Physical effects were determined by modeling a LPG leak in the tank based on not burning chemical release into atmosphere, jet fire and BLEVE scenarios. The two most dangerous scenarios were determined as the release of LPG without burning in August and BLEVE in January. It was observed that with the increase in the diameter of the leak, all the effect distances increased due to the release of more hazardous chemicals into the environment. BLEVE threat zones, where the largest effect distances for August and January, were transferred to Google Earth and affected areas were analyzed. It was shown that there may be serious exposures and domino effects may occur inside and outside the establishment in Guney neighborhood, which is located in Korfez district of Kocaeli province. Overpressure values were calculated with the BST method and the effects on the loss of property and life were investigated. In August, the vapor cloud explosion distance was determined as 456 m for 6.89kPa overpressure. With the BST method, an overpressure of 5.06 kPa was obtained in an area of 500 m with medium reactivity and congestion (3D). It has been determined that this overpressure may cause glass and window breaks and may cause injuries to living beings exposed to broken glass. In order to prevent these effects, it is important for living beings to stay away from windows and lie on the ground inside a reinforced structure or outside if they are outside to ensure safety. It was shown by this case study that the software and correlation results were compatible with each other. It was determined that the relevant safety distances at the stations were insufficient in risk assessment studies. It has been shown that the physicochemical properties of the chemical that may be involved in the accident, equipment specifications, atmospheric conditions and scenario selection, as well as the relevant facility environmental factors should be taken into account especially in risk assessment studies.

CONFLICT OF INTEREST

The authors declare no conflict of interest.

ABBREVIATIONS

ALOHA : Areal Locations of Hazardous Atmospheres
ATEX : Atmosphere Explosible
BLEVE : Boiling Liquid Expanding Vapor Explosion
BST : Baker-Strehlow-Tang
CFD : Computational Fluid Dynamics
D : Diameter(m)
DDT : Transition from Deflagration to Detonation
E : Explosion Energy(J)
EMRA : Energy Market Supervision Agency
L : Length (m)
LEL : Lower Explosion Limit
LNG : Liquefied Natural Gas
LOC : Loss of Containment
LPG : Liquefied Petroleum Gas
M_f : Mach Number
PLL : Potential Loss of Life Index
R : Combustion Energy Scaled Distance (m)
TS : Turkish Standard
VCE : Vapor Cloud Explosion

REFERENCES

Acikgoz, V. (2012). *Modeling of Fire and Explosion Conditions in LPG Storage Tanks*. MSc Thesis, Yildiz Technical University Institute of Science and Technology, İstanbul.

Ahn, M. S., Lee, H. E., Cheon, K. S., Joo, H. G., Ochang Chemical Safety Community, & Son, B.-S. (2020). Feasibility Evaluation of Designated Quantities for Chemicals Requiring Preparation for Accidents in the Korean Chemical Accident Prevention System. *International Journal of Environmental Research and Public Healty*, *17*(6), 1927. https://www.doi.org/10.3390/ijerph17061927

Bai, Y., Xin, B., Yu, J., Dang, W., Yan, X., & Yu, A. (2021). Risk-based quantitative method for determining blast-resistant and defense loads of petrochemical buildings. *Journal of Loss Prevention in the Process Industries*, *70*, 104407. https://www.doi.org/10.1016/j.jlp.2021.104407

Barjoee, S. S., Elmi, M. R., Varaoon, V. T., Keykhosravi, S. S., & Karimi, F. (2022). Hazards of toluene storage tanks in a petrochemical plant: modeling effects, consequence analysis, and comparison of two modeling programs. *Environmental Science and Pollution Research*, *29*(3), 4587-4615. https://www.doi.org/10.1007/s11356-021-15864-5

BP Group (2021). Safety Data Sheet, BP Butane, BP Australia. (Accessed:18/09/2023) PDF

Casal, J. (2018). *Evaluation of the effects and consequences of major accidents in industrial plants* (Second Edition). Elsevier. https://www.doi.org/10.1016/C2016-0-00740-4

Cetinyokus, S. (2017). Determination of explosion, fire and toxic emission physical effect areas. *Pamukkale University Journal of Engineering Sciences*, *23*(7), 845-853. https://www.doi.org/10.5505/pajes.2016.90093

Demircan, Y. (2010). *Determination of Risks in Storage of Flammable, Explosive and Toxic Substances in Industrial Facilities*. MSc Thesis, Sakarya University, Institute of Science and Technology, Sakarya.

Fitzgerald, G. A. (2001, October 30-31). *A comparison of simple vapor cloud explosion prediction methodologies*. In: 2nd Annual Symposium Beyond Regulatory Compliance: Making Safety Second Nature (pp. 1-46). Texas.

GBS (2019). Horizontal LPG Storage Tank Technical Specifications. GBS Pressure Vessels Inc. (Accessed:18/09/2023) URL

Directorate General of Spatial Planning (2018). Basiskele district, 1/5000 Master and 1/1000 scale Implementation Plans for Harbor Area. Republic of Türkiye, Minister of Environment, Urbanisation and Climate Change.

Guan, W., Liu, Q., & Dong, C. (2022). Risk assessment method for industrial accident consequences and human vulnerability in urban areas. *Journal of Loss Prevention in the Process Industries*, *76*, 104745. https://www.doi.org/10.1016/j.jlp.2022.104745

Huang, Y., & Ma, G. (2018). A grid-based risk screening method for fire and explosion events of hydrogen refuelling stations. *International Journal of Hydrogen Energy*, *43*(1), 442-454. https://www.doi.org/10.1016/j.ijhydene.2017.10.153

Jones, R., Lehr, W., Simecek-Beatty, D., & Reynolds, M. (2013). ALOHA® (Areal Locations of Hazardous Atmospheres) 5.4. 4. NOAA Technical Memorandum NOS OR&R 43. Technical Documentation. (Accessed:18/09/2023) PDF

Lee, H., Yoon, S., Sohn, J.-R., Huh, D.-A., Lee, B., & Moon, K. (2019). Flammable Substances in Korea Considering the Domino Effect: Assessment of Safety Distance. *International Journal of Environmental Research and Public Health*, *16*(6), 969. https://www.doi.org/10.3390/ijerph16060969

Liu, C., Wang, Z., Ma, C., & Wang, X. (2020). Influencing factors of the chain effect of spherical gas cloud explosion. *Process Safety and Environmental Protection*, *142*, 359-369. https://www.doi.org/10.1016/j.psep.2020.06.007

Ma, G., & Huang, Y. (2019). Safety assessment of explosions during gas stations refilling process. *Journal of Loss Prevention in the Process Industries*, *60*, 133-144. https://www.doi.org/10.1016/j.jlp.2019.04.012

Nakayama, J., Suzuki, T., Owada, S., Shiota, K., Izato, Y., Noguchi, K., & Miyake, A. (2022). Qualitative risk analysis of the overhead hydrogen piping at the conceptual process design stage. *International Journal of Hydrogen Energy*, *47*, 11725-11738. https://www.doi.org/10.1016/j.ijhydene.2022.01.199

Rocourt, X., Sochet, I., & Pellegrinelli, B. (2023). Application of the TNO multi-energy and Baker-Strehlow-Tang methods to predict hydrogen explosion effects from small-scale experiments. *Journal of Loss Prevention in the Process Industries*, *81*, 104976. https://www.doi.org/10.1016/j.jlp.2023.104976

Shi, Y., Xie, C., Li, Z., & Ding, Y. (2021). A quantitative correlation of evaluating the flame speed for the BST method in vapor cloud explosions. *Journal of Loss Prevention in the Process Industries*, *73*, 104622. https://www.doi.org/10.1016/j.jlp.2021.104622

Shi, J., Zhang, H., Li, J., Xie, W., Zhao, W., Usmani, A. S., & Chen, G. (2023). Real-time natural gas explosion modeling of offshore platforms by using deep learning probability approach. *Ocean Engineering*, *276*, 114244. https://www.doi.org/10.1016/j.oceaneng.2023.114244

Sierra, D., Montecchi, L., & Mura, I. (2019). Stochastic modeling and analysis of vapor cloud explosions domino effects in chemical plants. *Journal of the Brazilian Computer Society*, *25*(1), 11. https://www.doi.org/10.1186/s13173-019-0092-8

Sun, J., Sun, D., Asif, M., Fang, B., Bai, Y., Qin, W., Pan, T., Jiang, J., Zhang, M., & Wang, Z. (2021). Insight into the safety distance of ground and underground installations in typical petrochemical plant. *Journal of Loss Prevention in the Process Industries*, *69*, 104355. https://www.doi.org/10.1016/j.jlp.2020.104355

TS 12820 (2006). Fuel Stations Safety Requirements Standard, TSE. (Accessed:18/09/2023) URL

Tuncay, H. S. (2014). *Investigation of Explosive Environments Specific to Fuel Stations and Preparation of Occupational Health and Safety Guide in Explosive Environments*. Occupational Health and Safety Specialization Thesis, Ministry of Labor and Social Security Directorate General of Occupational Health and Safety, Ankara.

Wang, X., Shen, X., Qian, X., Hu, Q., Yuan, M., Li, M., & Jiang, J. (2023). Case study of fire and explosion accident based on damage consequence and numerical results: Explosion medium traceability. *Case Studies in Thermal Engineering*, *49*, 103171. https://www.doi.org/10.1016/j.csite.2023.103171

Witlox, H. W. M., Fernandez, M., Harper, M., Oke, A., Stene, J., & Xu, Y. (2018). Verification and validation of PHAST consequence models for accidental releases of toxic or flammable chemicals to the atmosphere. *Journal of Loss Prevention in the Process Industries*, 55, 457-470. https://www.doi.org/10.1016/j.jlp.2018.07.014

Wu, M., Zhang, G.-W., An, Z.-Y., & Liu, X.-P. (2023). Modelling of hazardous chemical gas building ingress and consequence analysis during a leak accident, *Indoor and Built Environment*, *32*(4), 783-796. https://www.doi.org/10.1177/1420326X221137244

Yu, X., Kong, D., He, X., & Ping, P. (2023). Risk Analysis of Fire and Explosion of Hydrogen-Gasoline Hybrid Refueling Station Based on Accident Risk Assessment Method for Industrial System. *Fire*, *6*(5), 181. https://www.doi.org/10.3390/fire6050181

Research Article GU J Sci, Part A, 10(4): 392-401 (2023) 10.54287/gujsa.1339151

Gazi University
Journal of Science
PART A: ENGINEERING AND INNOVATION
http://dergipark.org.tr/gujsa

An Example of Kriging Method based on Environmental Temperature for Altitude Mapping Using ArcGIS Software

Mitra SALEHI[1*] Hasan Volkan ORAL[1]

[1] Department of Civil Engineering, İstanbul Aydin University, Istanbul, Türkiye

Keywords

GIS
Kriging
Environmental Analysis
Interpolation
Geostatistical Analyst
Civil Engineering

Abstract

The purpose of this study is to demonstrate how Geographic Information System (GIS) software can be used for geographical interpolation, geostatistical analysis, and the creation of maps using relatively sparse data and highlighting the significance of this software in engineering and decision making. The method used in this study is applying ordinary kriging analysis on a gathered database to develop a variation map with interpolation analysis. The selected Z-values are the altitude and Environmental temperature of the selected zone which can contain a vast range. GIS can recognize and analyze the spatial relationships that exist within digitally stored spatial data. This method can bring ease for collecting data from a location that may have difficulties in visiting and gathering data by hand. By the use of semivariogram which is a graphical representation, and the covariance between every pair of points are used to calculate the spatial relationships between interpolating points. As a result, the final output of ArcGIS is a developed map showing altitude variation in the central area of Istanbul. This option can be used in making complex maps in every desired area by predicting Z-values for all the wanted zone based on the given database. Hence, the utility of GIS can bring a great improvement and ease in decision making and planning in civil engineering branches such as transportation, infrastructure, soil mechanics, and construction.

Cite

Salehi, M., & Oral, H. V. (2023). Altitude Mapping Using ArcGIS Software. *GU J Sci, Part A, 10*(4), 392-401. doi:10.54287/gujsa.1339151

Author ID (ORCID Number)

0000-0001-5578-4699 Mitra SALEHI
0000-0002-5743-1931 Hasan Volkan ORAL

Article Process

Submission Date 07.08.2023
Revision Date 21.08.2023
Accepted Date 05.10.2023
Published Date 30.10.2023

1. INTRODUCTION

GIS are analysis and modelling tools that integrate the relation between features of the Earth's surface and their environmental effects. It is also employed in basic spatial analysis and operations (Dewata & Putra, 2021). For many disciplines that investigate spatial events, GIS provides extremely powerful analysis capabilities. Since spatial phenomena are the foundation of geostatistics, many researchers have used geostatistical analysis associated with GIS technologies (Uyan & Dursun, 2021).

Spatial interpolation is an important GIS function that is used for spatial query, spatial data visualization, and spatial decision-making processes in GIS and environmental science (Meng et al., 2013). Inverse Distance Weighting (IDW), kriging, spline interpolation, and interpolating polynomials are some popular approaches for spatial interpolation. Ordinary Kriging (OK) and IDW are the most widely used, compared, and recommended interpolation techniques (Bhattacharjee et al., 2013).

Kriging is an interpolation technique used to estimate a variable at an unknown location based on observed values at nearby locations (Shad et al., 2009). In terms of accuracy and precision, the use of kriging techniques in mining studies and reserve estimates has resulted in positive outcomes. The incorporation of GIS into these studies has elevated the mapping and visualization dimensions to new heights (Uyan & Dursun, 2021). (IDW)

*Corresponding Author, e-mail: mitrasalehi@stu.aydin.edu.tr

is one of the interpolation techniques that is seen as being user-friendly. In this case, the locations used either have computed values or other, unnamed places have values. Using this technique, it is possible to predict unknown values for any geographic location data. For instance, levels of pollution, height, depth, chemical parameter concentrations, and precipitation (Paramasivam & Venkatramanan, 2019). Kriging weights are deduced from a semivariogram generated by examining the spatial structure of the data. Predictions are generated for locations in the research area based on the semivariogram and the spatial arrangement of measured values that are close by in order to create a continuous surface or map of the phenomena (Shad et al., 2009). The method of kriging interpolation that is most commonly applied is ordinary kriging. By utilizing estimated location data in the area, this aids in calculating a value at a point in a region known to be a semivariogram. The mean in a moving zone with local second-order stationarity is implicitly tested by ordinary kriging (Ali & Mustafa, 2020).

In the fields of GIS and Remote Sensing (RS), predicting spatial properties is a difficult issue. To develop derived spatial features, RS satellite imagery is handled further through a number of intermediary stages (Bhattacharjee et al., 2013). It is currently possible to detect changes and design plans based on these changes thanks to recent advancements in remote sensing and GIS. Urban planners now have access to more robust and adaptable geostatistical techniques based on GIS. GIS is able to map and evaluate the population's geographic distribution in order to improve planning for future decisions and the development of the economy, education, and healthcare as well as other properties in a specific zone that are noticeable in planning (Ali & Mustafa, 2020). The GIS mainly holds these derived attributes as vector data in the form of thematic layers (Bhattacharjee et al., 2013).

Kriging techniques use statistical models that take into account the autocorrelation among a collection of measured points to produce prediction surfaces (Johnston et al., 2001). The correlation or similarity of values, usually values close to one another in a dataset. When values recorded near together in time are more comparable than values measured far apart in time, spatial information is said to display serial autocorrelation. When values measured close together in space are more comparable than values measured farther apart, geographic data is said to display spatial autocorrelation. A statistical technique called regression is used to examine the relationship between a single dependent variable and one or more independent variables that are believed to have an impact on the dependent variable. It is used to forecast the value of the dependent variable or to establish whether and how much an independent variable does, in fact, affect the dependent variable. Another statistical metric for the linear relationship between two variables is covariance. It gauges how closely two variables move in tandem with respect to their respective mean returns. (ESRI, 2023)

When these data include errors and missing values, prediction is essential (Bhattacharjee et al., 2013).

In order to weigh the spatial configuration of observed sampling points, weights are applied to measurement points based on the distance at which spatial autocorrelation is determined (Johnston et al., 2001). Environmental geochemistry data are common spatial data that may be stored in a GIS and include geographic coordinates (such as longitude and latitude) and geochemical properties (such as element concentrations) (Xu & Zhang, 2022).

A strategy for incorporating the spatial and temporal coordinates of observations into data processing is called geostatistics (Ali & Mustafa, 2020). Spatial position, distribution, and linkage are calculated via a GIS database. In its most basic form, spatial analysis is a set of techniques that yields precise outcomes with spatial correlation. Geometric and thematic data show a spatial relationship and qualities in the data components are reported (Paramasivam & Venkatramanan, 2019).

Hence, both geographic locations and qualities must also be taken into consideration while conducting data analysis in environmental geochemistry. A rising variety of spatial analysis and statistical methodologies have been combined into GIS as a result of advancements in computer hardware and software, and this has greatly aided in the monitoring and evaluation of the environment (Xu & Zhang, 2022). GIS data represents real-world phenomena including highways, land use, elevation, trees, waterways, and states. Two conceptualizations can be used to categorize the most prevalent forms of phenomena that are represented in data: discrete objects, such as a home or a road, and continuous fields such as rainfall amount or population density (Longley et al.,

2015). Latitudes are horizontal lines that indicate how far away from the equator a location is. Longitudes are vertical lines that represent the east and west directions relative to Greenwich, England's meridian. Cartographers, geographers, and others can pinpoint points or locations on the globe by combining latitude and longitude. Nowadays, positions are related to other aspects and information, both geographic and non-spatial, by modules intended to manage spatial data (Paramasivam & Venkatramanan, 2019).

Numerous tasks in civil engineering are performed in an unfriendly and complicated environment, which makes it challenging for the employees to perform their duties effectively. However, the process is done more easily with the aid of GIS (Simmons, 1996). Topography, hydrology, geology, soils, utility infrastructure, and transportation are just a few of the many topics covered by GIS in civil engineering (Parker, 1996). Thematic mapping and graphic output data can be superimposed on a map image in the map display, which is the most aesthetically distinctive aspect of GIS software. The primary feature that sets GIS apart from other data systems is how geographic data are stored and accessible (Luna et al., 2008). Due to their difficulty in accessing and evaluating, formerly deemed distinct geographic information themes have been brought together by GIS. Such themes have been overlooked when carrying out activities. This creates the possibility for greater task planning, task design, and task execution decisions (Parker, 1996).

The purpose of this study is to illustrate how GIS software can be used to perform geographical interpolation, geostatistical analysis, and the development of maps depends on environmental temperature data from briefly compact data. The altitude of 20 different locations from sea surface and the temperature in Istanbul have been chosen for this study in order to make a map that shows the difference in altitude and temperature in Istanbul's center region and to highlight the usefulness of this software in civil engineering.

2. METHODOLOGY

This study has been performed in the central part of Istanbul, Turkey, with the use of GPS waypoints points have been collected in this area. With the help of ArcGIS (version 10.8.2), Kriging analysis has been performed to develop a map for altitude difference.

2.1. Study Area

The study area is Istanbul, Turkey. The following maps (Figure 1) show Turkey on world map and Istanbul's location in this country (Figure 2).

Figure 1. *Turkey (modified from Google Earth, 2023)*

Figure 2. *Istanbul, Turkey (modified from Google Earth, 2023)*

2.2 Collection of Waypoints from the Study Area

The waypoints were collected from the study area by using Google Earth (2023) and GPS Waypoint Android Applications. Smartphone GPS units often use aided GPS (A-GPS) technology, which allows the GPS sensor to obtain ephemeris and an archive through a mobile data network (Liao, 2022).

2.3 Kriging Application on ARCGIS

In this study, the Arctoolbox in the ArcMap 10.8.2 Software was employed in this analysis. Our attribute table and data can be subjected to numerous analyses using this option. In this case, the spatial analyst's interpolation tool, Kriging was employed.

Based on the supplied data, this approach provides us with a prediction for the entire map.

Although kriging methods vary in terms of formats, they are all founded on the idea of a simple linear regression approach (Shad et al., 2009). It is possible to describe the prediction at location u in mathematical explanation as:

$$Z(u) = \sum_{\alpha=1}^{n} \lambda_\alpha(u) Z(u_\alpha) \quad (1)$$

The random variable model at location u_α is indicated by $Z(u_\alpha)$ is. The n data locations are presented by u_α, the ordinary kriging weights are shown as λ_α (u), and Z(u) is the predicted value. Here the weights λ_α (u) are subject to the process (Shad et al., 2009). However, with the kriging method, the weights are based not only on the distance between the measured points and the prediction location but also on the overall spatial arrangement of the measured points. To use the spatial arrangement in the weights, the spatial autocorrelation must be quantified. Thus, in ordinary kriging, the weight, λ_α (u), depends on a fitted model to the measured points, the distance to the prediction location, and the spatial relationships among the measured values around the prediction location (ESRI, 2023)

The predictability relation between data points located a certain distance apart is described numerically (or graphically) by a geostatistical function. Because of this predictability, the degree of confidence in a value's estimation is constrained, and as a result, risk estimation is established (Shad et al., 2009).

A semivariogram is a visual representation that shows the spatial connection of data (Ali & Mustafa, 2020). The covariance between every pair of points is used to calculate the spatial relations between interpolating points. The semivariogram model is generated using known data points, and covariance is determined using that model (Bhattacharjee et al., 2013). Kriging produces the most accurate predictions by using covariance and semi-variogram (Ali & Mustafa, 2020). The nearby local features of the sample points are not regarded by the covariance or the semivariogram. They are independent of the nearby affecting spatial characteristics and functions of distance (Euclidean distance in 2-D space) (Bhattacharjee et al., 2013). The covariance and autocorrelation matrices of the 20 data points are provided in the results section.

The semivariogram's basic properties are the semivariance value at which the variogram hits saturation is named the sill. In the semivariogram, Sill denotes the amplitude of a specific element. Range is the location where the semivariogram intersects with the lag distance. The range autocorrelation is zero after that. A semivariogram should potentially have zero at its origin. The nugget is the value of the semivariogram if it is not zero (Bostan, 2017).

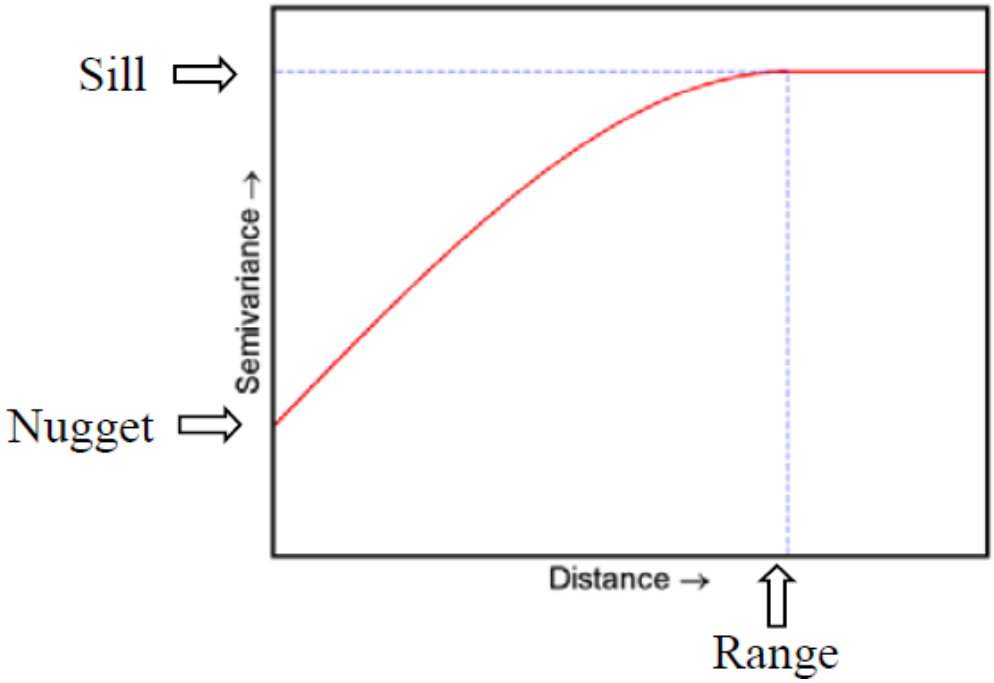

***Figure 3**. Semivariogram models (Bostan, 2017)*

This software includes a geostatistical wizard that is used to produce the geostatistical outcomes as well. By applying Ordinary Kriging interpolation, the samples dataset is utilized to estimate the spatial distribution of population size with respect to the local area.

3. RESULTS AND DISCUSSION

This section provides information about the gathered database about altitude differences in Istanbul. Moreover, it gives the final results for this analysis using the GIS software to estimate a map for the whole area with ordinary kriging.

The database for this study is shown in the attribute table (Table 1), which includes 20 waypoints in Istanbul, Turkey's central region. This data was acquired using RS Google Earth (2023) and recorded on 13th of December 2022. Latitude and longitude are the two distinctive essential characteristics of each point measured in decimal degrees (DD). Therefore, it is impossible for two places to share the same latitude and longitude at the same moment. The study's variable Z value serves as the table's altitude attribute. The accuracy of this dataset is defined by GPS.

***Table 1**. The provided attribute table in this study*

Point	Latitude (DD)	Longitude (DD)	Altitude (m)	Temperature (°C)
1	40.99201	28.79558	63.0366	8
2	41.00944	28.65986	141.5022	7
3	41.02828	28.69562	68.6096	6
4	40.98781	28.72255	86.24174	7
5	40.98661	28.78823	53.21566	7
6	40.9943	28.79487	62.66478	7
7	41.01913	28.70347	101.151	6
8	40.98538	28.78006	45.18151	7
9	40.98656	28.77104	6.255881	7
10	40.98838	28.77263	4.910122	7
11	40.95709	28.8225	2.490139	8
12	40.96272	28.82487	14.94113	8
13	41.06398	28.80444	67.73499	6
14	41.03689	28.98507	77.44993	7
15	41.02005	28.68759	130.399	7
16	41.00905	28.98022	36.99921	7
17	41.01158	28.97479	39.01994	7
18	41.01605	28.97675	1.999988	7
19	41.10793	29.0058	79.33485	6
20	41.00341	28.68726	53.39499	8

By means of data analysis tool in Microsoft Excel, the covariance and autocorrelation of the data can be displayed as Table 2 and Table 3.

***Table 2**. The provided covariance matrix*

	Latitude	Longitude	Altitude	Temperature
Latitude	0.001102056			
Longitude	0.001269322	0.012133545		
Altitude	0.550961771	-1.728845581	1525.566595	
Temperature	-0.015204706	-0.003956919	-9.148377445	0.4

A positive covariance indicates that both variables frequently exhibit high or low values together. While two variables have a negative covariance, they are often low while one is high.

***Table 3.** The provided autocorrelation matrix*

	Latitude	Longitude	Altitude	Temperature
Latitude	1			
Longitude	0.347117057	1		
Altitude	0.424916853	-0.401834079	1	
Temperature	-0.724179301	-0.056798028	-0.370338185	1

The coordinate system utilized here is GCS WGS 1984. The following map (Figure 4) is produced by choosing Kriging in the spatial analyst tool in Arctoolbox's interpolation option using both altitude and temperature.

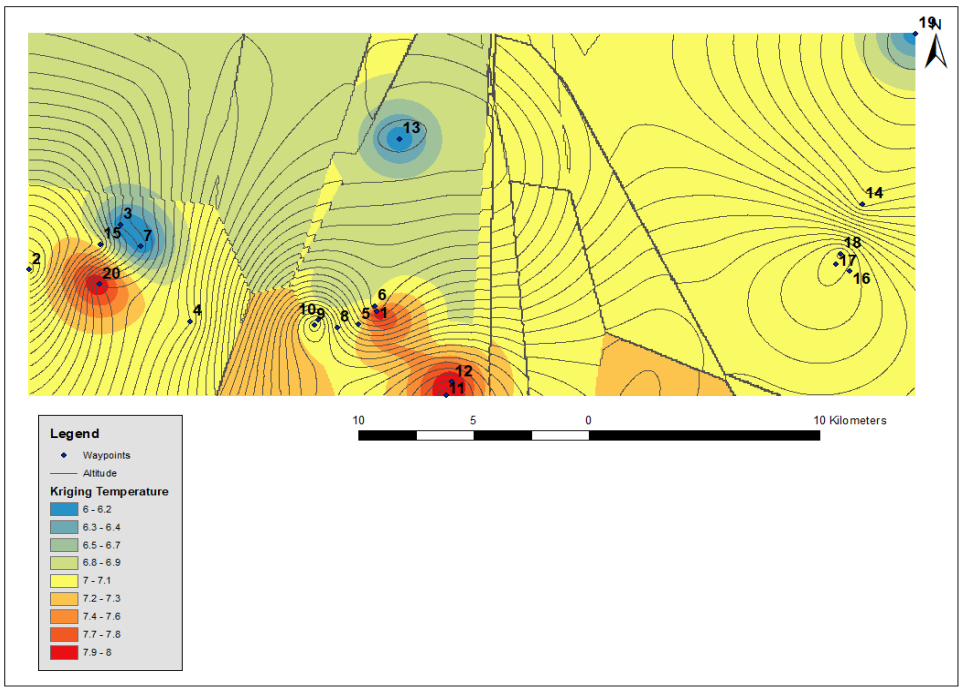

Figure 4. *The environmental temperature map of kriging interpolation*

The resulting semivariogram (Figure 5) is then displayed using the geostatistical wizard function in ArcMap. Before applying kriging to the graph, a semivariogram associated with the attribute table is necessary. The necessary factors for creating a semivariogram include Lag number, Lag distance, Angle, and Frequency, among others**.**

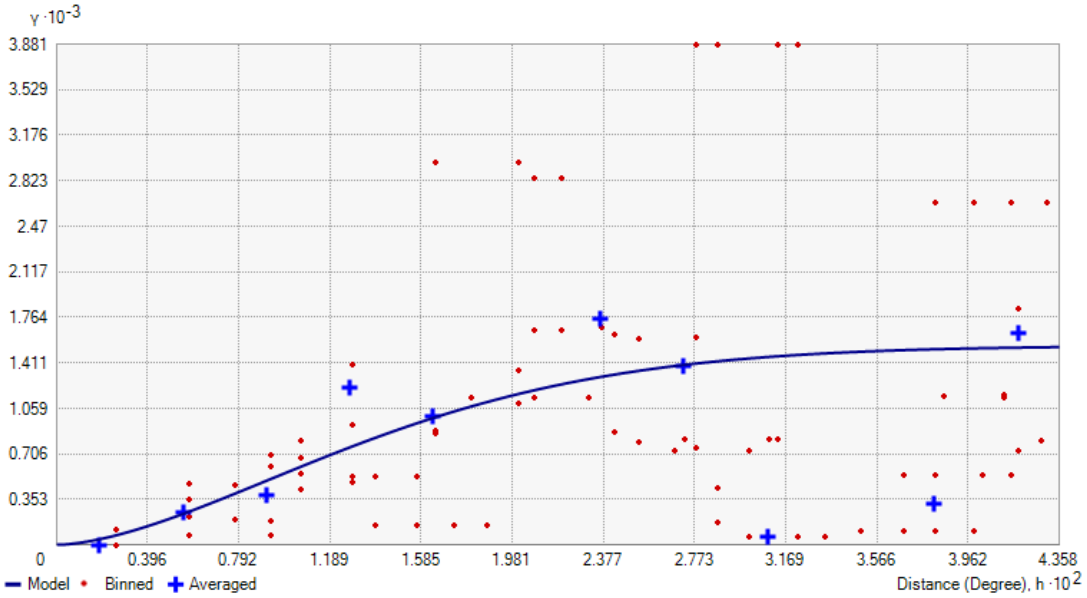

Figure 5: *Altitude variation in Istanbul semivariogram*

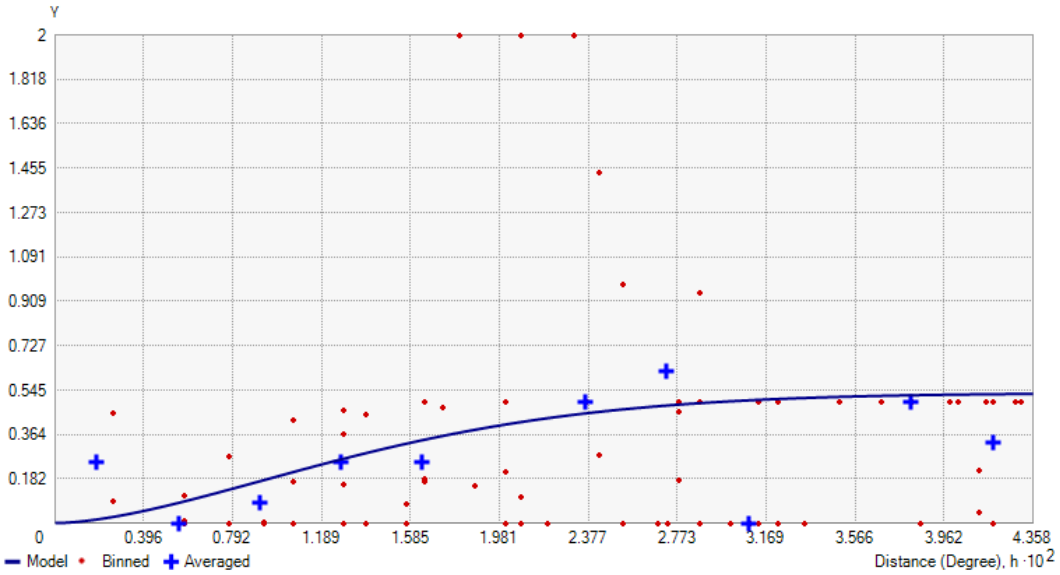

Figure 6: *Temperature variation in Istanbul semivariogram*

Semivariogram can be completed, and then ordinary kriging can be used. Therefore, the maps would be colored differently depending on the sample values. The maps after kriging are displayed below:

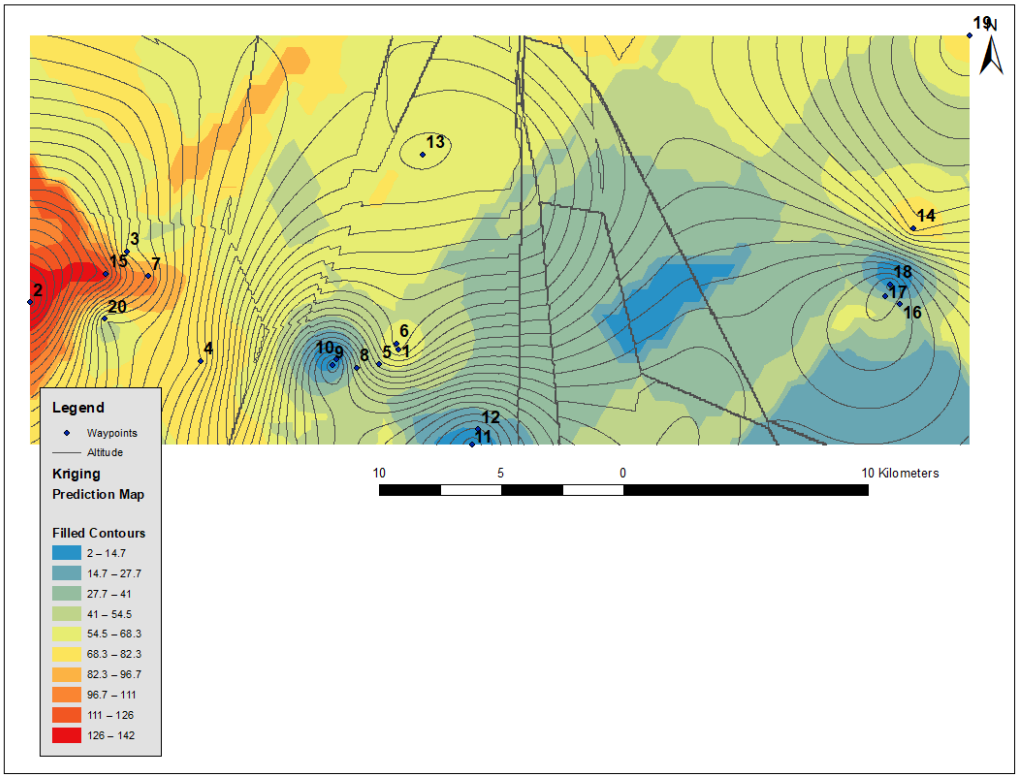

Figure 6. *Altitude variation in Istanbul (Ordinary Kriging)*

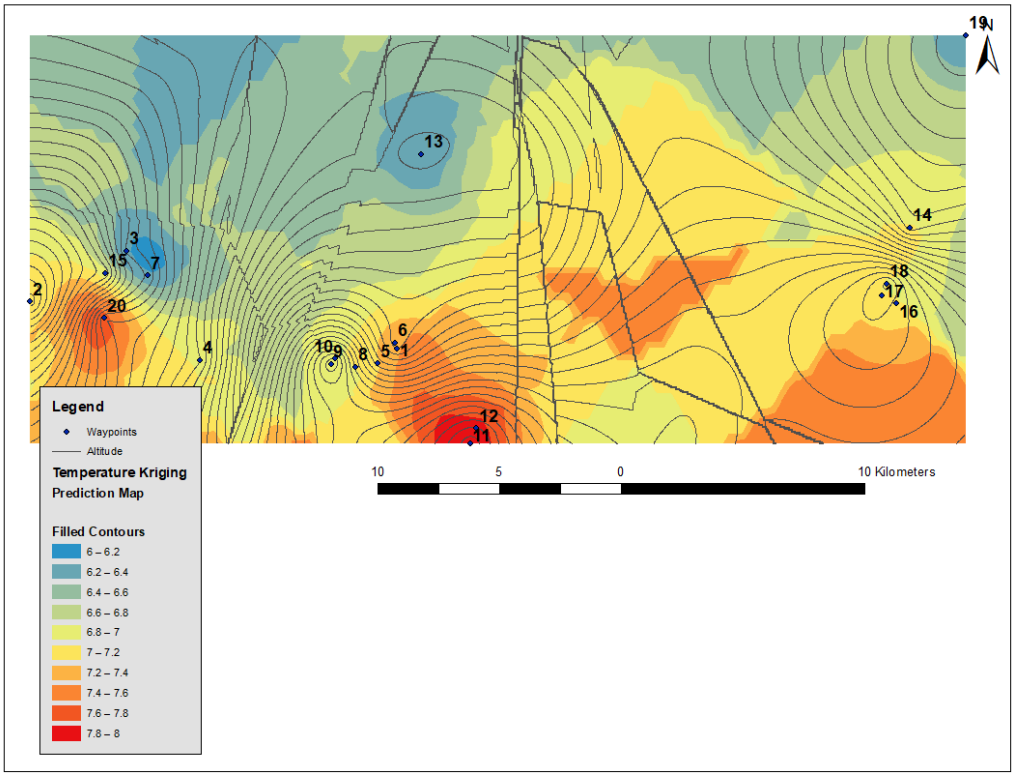

Figure 7. *Temperature variation in Istanbul (Ordinary Kriging)*

In Figure 6, the red area denotes high-altitude lands, meanwhile, the blue area indicates a low-altitude region that is simply close to the water and approximately near sea level.

With these results, as Dewata and Putra (2021) revealed, this method is useful to investigate the earth's surface to develop maps and analysis for decision makings in engineering and environmental topics. This software is one of the greatest solutions to reach this goal. As it is shown, by means of ordinary kriging GIS can make a prediction for all over the selected land based on the given database. The necessary and sufficient condition for this approach is possible by having the semivariogram of the project.

The visualized surface demonstrates X, Y, and Z positions along with topographic 3D projections. The spatial approach using different methods can provide a smooth map of the variogram and spatial query even though these techniques are relatively undeveloped (Paramasivam & Venkatramanan, 2019).

A highly accurate interpolation technique is kriging. The best estimator, which is linear and free of systematic variations, is the kriging approach. Nowadays, investigations involving geographical analysis typically use the kriging interpolation approach (Uyan & Dursun, 2021). Regression kriging is a very effective method for spatial interpolation, and findings from related investigations confirm this claim. (Meng et al., 2013).

4. CONCLUSION

As a matter of conclusion, this study has shown that GIS could be a quite helpful tool for many scientific purposes in engineering, decision making, planning, and many other engineering and management branches. Moreover, in the discuccion section, this study has covered ordinary kriging which is a highly accurate interpolation technique by means of gathered data and predicting the Z-value for a set range of locations and performing it with the use of provided semivariogram by the geostatistical wizard and having a map showing the latitude range as the result of this analysis.

GIS methodology provides considerable skills in the study of engineering and developing maps in locations that humans cannot easily have access to. This software is a powerful technique for transforming spatial changes into an understandable form that can be used for other connected objectives.

CONFLICT OF INTEREST

The authors declare no conflict of interest.

REFERENCES

Ali, S. H., & Mustafa, F. A. (2020). Evaluation of the population distribution using GIS-based geostatistical analysis in Mosul City. *Korean Journal of Remote Sensing*, *36*(1), 83-92. https://www.doi.org/10.7780/kjrs.2020.36.1.7

Bhattacharjee, S., Mitra, P., & Ghosh, S. K. (2013). Spatial interpolation to predict missing attributes in GIS using semantic kriging. *IEEE Transactions on Geoscience and Remote Sensing*, *52*(8), 4771-4780. https://www.doi.org/10.1109/TGRS.2013.2284489

Bostan, P. (2017). Basic Kriging Methods in Geostatistics. *Yuzuncu Yıl University Journal of Agricultural Sciences*, *27*(1), 10-20. https://www.doi.org/10.29133/yyutbd.305093

Dewata, I., & Putra, A. (2021). Kriging-GIS model for the spatial distribution of seawater heavy metals. *Periodicals of Engineering and Natural Sciences*, *9*(2), 629-637. https://www.doi.org/10.21533/pen.v9i2.1851

ESRI (2023). ESRI Community, ArcGIS. (Accessed:13/02/2023) URL

Google Earth (2023). (Accessed:21/02/2023) URL

Johnston, K., Ver Hoef, J. M., Krivoruchko, K., & Lucas, N. (2001). *Using ArcGIS Geostatistical Analyst*. Redlands. (Accessed:21/02/2023) PDF

Liao, G. H. (2022). *Configuring Waypoints and Patterns for Autonomous Arduino Robot with GPS and Bluetooth Using an Android App*. In: K. Arai (Eds.), Proceedings of the 2021 Intelligent Systems Conference (IntelliSys) Volume 3 (pp. 304-312). Springer International Publishing. https://www.doi.org/10.1007/978-3-030-82199-9_18

Longley, P. A., Goodchild, M. F., Maguire, D. J., & Rhind, D. W. (2015). *Geographic Information Science and Systems* (4th ed). John Wiley & Sons.

Luna, R., Hall, R., Hilgers, M., Bham, G., Elgin, R., Morris, C., & Morrison, G. (2008, June 22-25). *Introduction of GIS into civil engineering curricula*. In: 2008 Annual Conference & Exposition (pp. 13-808), Pittsburgh, Pennsylvania. https://www.doi.org/10.18260/1-2--4433

Meng, Q., Liu, Z., & Borders, B. E. (2013). Assessment of regression kriging for spatial interpolation–comparisons of seven GIS interpolation methods. *Cartography and Geographic Information Science*, *40*(1), 28-39. https://www.doi.org/10.1080/15230406.2013.762138

Paramasivam, C. R., & Venkatramanan, S. (2019). An introduction to various spatial analysis techniques. In: *GIS and Geostatistical Techniques for Groundwater Science*, (pp. 23-30). Elsevier. https://www.doi.org/10.1016/B978-0-12-815413-7.00003-1

Parker, D. (1996). An introduction to GIS and the impact on civil engineering. *Proceedings of the Institution of Civil Engineers-Civil Engineering*, *114*(6), 3-11. https://www.doi.org/10.1680/icien.1996.28911

Shad, R., Mesgari, M. S., abkar, A., & Shad, A. (2009). Predicting air pollution using fuzzy genetic linear membership kriging in GIS. *Computers, Environment and Urban Systems*, *33*(6), 472-481. https://www.doi.org/10.1016/j.compenvurbsys.2009.10.004

Simmons, G. (1996). Practical applications of GPS for GIS and civil engineering. *Proceedings of the Institution of Civil Engineers-Civil Engineering*, *114*(6), 30-34. https://www.doi.org/10.1680/icien.1996.28913

Uyan, M., & Dursun, A. E. (2021). Determination and modeling of lignite reserve using geostatistical analysis and GIS. *Arabian Journal of Geosciences*, *14*(4), 312. https://www.doi.org/10.1007/s12517-021-06633-2

Xu, H., & Zhang, C. (2022). Development and applications of GIS-based spatial analysis in environmental geochemistry in the big data era. *Environmental Geochemistry and Health*, *45*(4), 1079-10901. https://www.doi.org/10.1007/s10653-021-01183-8

Research Article GU J Sci, Part A, 10(4): 402-416 (2023) 10.54287/gujsa.1333067

Gazi University
Journal of Science
PART A: ENGINEERING AND INNOVATION
http://dergipark.org.tr/gujsa

An Improvement in Estimating the Population Mean Based on Family of Estimators with Different Application Areas

Ceren UNAL[1*] Cem KADILAR[1]

[1] Department of Statistics, Faculty of Science, Hacettepe University, Ankara, Türkiye

Keywords

Population Mean
Family of Estimators
Auxiliary Information
Non-Response
Efficiency

Abstract

In a sampling study, the complete information for the necessary variables may not always be available in practice. Therefore, the non-response situation has been considered for estimating the unknown population parameters with different types of estimators. The families of estimators are proposed for the population mean in the case of non-response under two different cases with the approach of an exponential function. Their properties are derived in detail. We compare these estimators with the main estimators in the literature to present the efficiencies, theoretically. Moreover, the three different empirical studies are illustrated and, in that way, we found that the theoretical conclusion is supported by the obtained results numerically for each data set.

Cite

Unal, C., & Kadilar, C. (2023). An Improvement in Estimating the Population Mean Based on Family of Estimators with Different Application Areas. *GU J Sci, Part A, 10*(4), 402-416. doi:10.54287/gujsa.1333067

Author ID (ORCID Number)

0000-0002-9357-1771 Ceren UNAL
0000-0003-4950-9660 Cem KADILAR

Article Process

Submission Date 26.07.2023
Revision Date 13.09.2023
Accepted Date 28.11.2023
Published Date 11.12.2023

1. INTRODUCTION

In sampling theory, the sample describes as a sub-group of the population and is utilized to avoid the difficulty of money, time, labor, etc. which originated from the population. Under these circumstances, the choice of sample and sampling method becomes evident. The process of the estimation for any unknown population parameters begins after determining the sample. The estimator, which is a mathematical equation, utilize for estimating these parameters. In general, the most efficient estimator is preferred compared to others. Here, one of the most appropriate methods is the utilize of information of auxiliary variable (x) for increasing efficiency. Many researchers propose different types of estimators to estimate the mean of the population utilizing auxiliary variable information. At this point, Yadav and Zaman (2021) proposed ratio type estimators using non-conventional and conventional parameters. Tailor and Lone (2014); Mehta and Tailor (2020); Singh and Nigam (2020) and Yadav et al. (2021) suggested various ratio type estimators for estimation of population mean using different sampling methods. Oncel Cekim & Kadilar (2018); Javed et al. (2019); Shabbir and Onyango (2022) and Oncel Cekim (2022) introduced unbiased estimators under various sampling methods.

When complete information is obtained on both the variable of study (y) and the variable of auxiliary (x), some of the important estimators for estimating the population mean ($\bar{Y}$) in literature are as follows:

Cochran (1940, 1977) is introduced both classical ratio and classical regression estimators for $\bar{Y}$, respectively

$$t_R = \frac{\bar{y}}{\bar{x}}\bar{X}, \tag{1}$$

$$t_{reg} = \bar{y} + b(\bar{X} - \bar{x}), \tag{2}$$

*Corresponding Author, e-mail: cerenunal@hacettepe.edu.tr

where $\bar{x}$ and $\bar{y}$ are the sample mean due to *x* and *y*, respectively. $\bar{X}$ is the population mean for *x*. b represents the regression coefficient of Y on X.

The MSE equations of (1) and (2) are given by

$$\mathrm{MSE}(t_R) = \lambda \bar{Y}^2 \left(C_y^2 + C_x^2 - 2C_{yx}\right), \tag{3}$$

$$\mathrm{MSE}\left(t_{reg}\right) = \lambda \bar{Y}^2 C_y^2 \left(1 - \rho_{xy}^2\right), \tag{4}$$

respectively, where $f = \frac{n}{N}, \lambda = \frac{1-f}{n}, C_x^2 = \frac{S_x^2}{\bar{X}^2}, C_y^2 = \frac{S_y^2}{\bar{Y}^2}, C_{xy} = \rho_{xy} C_x C_y$. Here, coefficient of f means sampling rate. The coefficient of population correlation is denoted as ρ_{xy} .

A family of estimators has been defined by Khoshnevisan et al. (2007). This family of estimators and their minimum MSE are given as follows:

$$t_K = \bar{y}\left(\frac{a\bar{X}+b}{\alpha(a\bar{x}+b)+(1-\alpha)a\bar{X}+b}\right)^g, \tag{5}$$

and

$$\mathrm{MSE}_{\min}(t_K) = \lambda \bar{Y}^2 C_y^2 \left(1 - \rho_{xy}^2\right). \tag{6}$$

Later, studies have concentrated on creating modified modified estimators. Numerous researchers introduce various kinds of estimators. Among these type of estimators, Bahl and Tuteja (1991) were the first to provide estimators using exponential function strategy as

$$t_{BT} = \bar{y}\exp\left(\frac{\bar{X}-\bar{x}}{\bar{X}+\bar{x}}\right), \tag{7}$$

and MSE of Eq. (7) is given as

$$\mathrm{MSE}(t_{BT}) = \lambda \bar{Y}^2 \left(C_y^2 + \frac{C_x^2}{4} - C_{yx}\right). \tag{8}$$

After this estimator in Eq. (7), Shabbir et al. (2014); Özel Kadilar (2016); Zaman and Kadilar (2019, 2021a, 2021b); Ahmad et al. (2021) provided exponential type of estimators under various sampling methods.

All of the mentioned estimators are defined in a case that the variables have only response units. This situation can be considered in theory but may not be obtained in practice. Therefore, the estimation in the presence of non-response units has become prominent in recent years. In literature, Hansen and Hurwitz (1946) presented a new method to deal with this situation.

In the Hansen and Hurwitz (1946) procedure, a sample size of n units is drawn from the population of N units with SRSWOR, which is denoted as $= \{S_1, S_2, \ldots, S_N\}$. For y and x respectively, the individual elements for the i^{th} unit in the population are represented as (y_i, x_i). This method divides the size of the population N into two parts: the number of respondent units (N_1) and the number of non-respondent units (N_2). Similar to this situation, the sample size, n, is also split into two parts, which are referred to as n_1 and n_2. In addition, a sub-sample size of r (where $r = {}^{n_2}/_{p}$) is drawn from the n_2 units by means of extra effort. Some studies refer to this aspect of the method as the subsampling technique. It is important to note that p (where p > 1) represents the inverse of the sampling rate in the sample of size n in the second phase. This means that this technique can be used to estimate using the total number of units $(n_1 + r)$, which replaces n. Using this procedure, the unbiased estimator with total $(n_1 + r)$ units for the nonresponse population was introduced by Hansen and Hurwitz (1946) as

$$t_{HH} = w_1\bar{y}_1 + w_2\bar{y}_{2(r)}, \quad (9)$$

where $w_2 = {n_2}/{n}$ and $w_1 = {n_1}/{n}$. For clarity, w_1 is the proportion of respondent units while w_2 is the proportion of non-respondent units for the sample. For the study variable, the $\bar{y}_{2(r)}$ and $\bar{y}_1$ refer the sample means due to the *r* and n_1 units, respectively.

The variance of $t_{HH}$is given by

$$V(t_{HH}) = \bar{Y}^2\left(\lambda C_y^2 + \frac{W_2(p-1)}{n}C_{y(2)}^2\right). \quad (10)$$

Here, $C_{y(2)}^2 = {S_{y(2)}^2}/{\bar{Y}^2}$.

There are two main forms of these non-response problems. Firstly, Case I is defined as units that do not respond on the *y* only. Secondly, Case II is defined by units that do not respond at both the *y* and *x*. The $(\bar{X})$ is known for both of these cases. In theoretical terms, $\bar{x}^*$ and $\bar{y}^*$ refer to the mean of the sample for x and y in the presence of nonresponse. Following the pioneering work of Hansen and Hurwitz (1946), the researchers propose the estimators for the $(\bar{Y})$ by taking into account the two different non-response cases.

For the Case I, Rao (1986) defines the following classical ratio and classical regression estimators, respectively, as follows:

$$t_R^* = \frac{\bar{y}^*}{\bar{x}}\bar{X}, \quad (11)$$

$$t_{reg}^* = \bar{y}^* + b(\bar{X} - \bar{x}), \quad (12)$$

where $b^* = {S_{xy}^*}/{S_{x^*}^2}$. To obtain the MSE of the estimators in Eq. (11) – Eq. (12), we have $\bar{y}^* = \bar{Y}(1 + e_0^*)$ and $\bar{x} = \bar{X}(1 + e_1)$.

Then, $E(e_0^*) = E(e_1) = 0, E(e_1^2) = \lambda C_x^2, E(e_0^{*^2}) = \lambda C_y^2 + \frac{W_2(p-1)}{n}C_{y(2)}^2$, and , $E(e_0^* e_1) = \lambda\rho_{xy}C_yC_x$.

By utilizing the provided these definitions, the MSE of the t_R^* and t_{reg}^* are given as

$$MSE(t_R^*) = \bar{Y}^2\left(\lambda\left(C_y^2 + C_x^2 - 2C_{yx}\right) + \frac{W_2(p-1)}{n}C_{y(2)}^2\right), \quad (13)$$

$$MSE\left(t_{reg}^*\right) = \bar{Y}^2\left(\lambda C_y^2\left(1 - \rho_{xy}^2\right) + \frac{W_2(p-1)}{n}C_{y(2)}^2\right). \quad (14)$$

Singh et al. (2010) presented the first exponential estimators, utilizing Eq. (7) for Case I, in accordance with Bahl and Tuteja (1991) as

$$t_{BT}^* = \bar{y}^*\exp\left(\frac{\bar{X}-\bar{x}}{\bar{X}+\bar{x}}\right), \quad (15)$$

whose MSE is given by

$$MSE(t_{BT}^*) = \bar{Y}^2\left(\lambda\left(C_y^2 + \frac{C_x^2}{4} - C_{yx}\right) + \frac{W_2(p-1)}{n}C_{y(2)}^2\right). \quad (16)$$

For the Case 2, Cochran (1977) suggested the following classical ratio and classical regression estimators as

$$t_R^{**} = \frac{\bar{y}^*}{\bar{x}^*}\bar{X}, \quad (17)$$

$$t_{reg}^{**} = \bar{y}^* + b(\bar{X} - \bar{x}^*), \quad (18)$$

respectively.

Singh et al. (2010) also proposed the estimator using the exp. function for the Case II as

$$t_{BT}^{**} = \bar{y}^* \exp\left(\frac{\bar{X}-\bar{x}^*}{\bar{X}+\bar{x}^*}\right). \quad (19)$$

To obtain the MSE of the estimators in Eq. (17) – Eq. (19), we have $\bar{x}^* = \bar{X}(1 + e_1^*)$.

Then, $E(e_1^*) = 0$, $E(e_1^{*^2}) = \lambda C_x^2 + \frac{W_2(p-1)}{n} C_{x(2)}^2$, $E(e_0^* e_1^*) = \lambda \rho_{xy} C_y C_x + \frac{W_2(p-1)}{n} \rho_{xy(2)} C_{y(2)} C_{x(2)}$, and using these equations, the MSE of the mentioned estimators are, respectively, obtained by

$$MSE(t_R^{**}) = \bar{Y}^2 \left(\lambda\left(C_y^2 - 2C_{yx} + C_x^2\right) + \frac{W_2(p-1)}{n}\left(C_{y(2)}^2 + C_{x(2)}^2 - 2C_{yx(2)}\right)\right), \quad (20)$$

$$MSE\left(t_{reg}^{**}\right) = \bar{Y}^2 \left(\lambda C_y^2\left(1 - \rho_{xy}^2\right) + \frac{W_2(p-1)}{n}\left(C_{y(2)}^2 + \rho_{xy}^2 \frac{C_y^2}{C_x^2} C_{x(2)}^2 - 2\rho_{xy} \frac{C_y}{C_x} C_{yx(2)}\right)\right), \quad (21)$$

$$MSE(t_{BT}^{**}) = \bar{Y}^2 \left(\lambda\left(C_y^2 - C_{yx} + \frac{C_x^2}{4}\right) + \frac{W_2(p-1)}{n}\left(C_{y(2)}^2 + \frac{C_{x(2)}^2}{4} - C_{yx(2)}\right)\right), \quad (22)$$

and $\rho_{xy(2)} = \frac{C_{yx(2)}}{C_{y(2)} C_{x(2)}}$ is the coefficient of population correlation for the non-response group.

On the line of these estimators, Sanaullah et al. (2019), Anieting et al. (2020); Ahmad et al. (2022); Ahmadini et al. (2022); Fatima et al. (2022); Rehman and Shabbir (2022) and Sharma et al. (2022) recently proposed various type of estimators for the estimation of $\bar{Y}$ under both cases in the literature. Especially, there are also many proposed estimators using exponential function strategy in the literature under non-response scheme. Under the non-response condition, Khan et al. (2023) suggested a new exp-ratio type estimator using double sampling for estimating the $\bar{Y}$. Zahid et al. (2022) proposed a generalized dual to exp-ratio type estimator. Kumar and Bhougal (2011) modified ratio-product type exp. estimator following Singh et al. (2008) study. Kumar (2013); Yunusa and Kumar (2014) and Unal and Kadilar (2021, 2022a, 2022b) proposed estimators using exp. function for the estimating $\bar{Y}$. Kumar and Kumar (2017) and Pal and Singh (2017, 2018) proposed various estimators taking the advantage of the exp. function. Dansawad (2019) introduced a class of exp. type estimators. Singh and Usman (2019a, 2019b) proposed a general family of exp. type and the ratio-product type difference-cum-exp. type estimators, respectively in their studies.

The estimator that is proposed by Khoshnevisan et al. (2007) and given in Eq. (5) is important in the literature and has formed the basis for many studies. In this present study, this estimator was specifically used and proposed again by adding an exponential function in the case of non-response in Section 2. Results of the efficiency comparisons are made theoretically and numerically, as well, which are obtained in Sections 3 and 4, respectively. In final part, Section 5 introduces the results of the study.

2. THE ADAPTED ESTIMATORS

Following Khoshnevisan et al. (2007), we suggest the new estimator with adapt the family of estimators in Eq. (5) under two different cases as first case and second case.

2.1. The adapted estimators for the first case:

The first proposed family of estimators is given by

$$t_{C1} = \bar{y}^* \exp\left(\frac{a\bar{X}+b}{\alpha_1(a\bar{x}+b)+(1-\alpha_1)(a\bar{X}+b)} - 1\right), \quad (23)$$

where α_1 is a chosen constant which using for the MSE minimum. In Eq. (23), the values of α and b can be correlation coefficient, coefficient of variation, skewness, kurtosis etc.

In terms of e_0^* and e_1, we have

$$t_{C1} = \bar{Y}\left(1 + e_0^* - \alpha_1\theta e_1 + \frac{3\alpha_1^2\theta^2 e_1^2}{2} - \alpha_1\theta e_0^* e_1\right) \quad (24)$$

where $\theta = \frac{a\bar{X}}{a\bar{X}+b}$.

If $\bar{Y}$ is subtracted and get the expected value from both sides in Eq. (24):

$$E(t_{C1} - \bar{Y}) = B(t_{C1}) = \bar{Y}\lambda C_x^2\alpha_1\theta\left(\frac{3\alpha_1\theta}{2} - \rho_{yx}\frac{C_y}{C_x}\right). \quad (25)$$

When taking square of Eq. (25), we get MSE of the t_{C1} estimator as

$$MSE(t_{C1}) = \bar{Y}^2\left(\lambda\left(C_y^2 + \alpha_1^2\theta^2 C_x^2 - 2\alpha_1\theta C_{yx}\right) + \frac{W_2(p-1)}{n}C_{y(2)}^2\right). \quad (26)$$

By the minimization of (26), the MSE of the t_{C1} is min. for the optimal value of

$$\alpha_1^* = \left(\frac{1}{\theta}\rho_{xy}\frac{C_y}{C_x}\right). \quad (27)$$

We get the min MSE of the t_{C1}, using the value of α_1^* in Eq. (26), as follows:

$$MSE_{min}(t_{C1}) = \bar{Y}^2\left(\lambda C_y^2\left(1 - \rho_{xy}^2\right) + \frac{W_2(p-1)}{n}C_{y(2)}^2\right). \quad (28)$$

It is important to note that the $MSE_{min}(t_{C1})$ equals the $MSE(t_{reg}^*)$ in Eq. (14) under the first case.

We see that there are 10 different θ as $(\theta_1, \theta_2, \ldots, \theta_{10})$ in Table 1.

Table 1. *θ Values*

$\theta_i, i = 1,2,\ldots,10$	α	b
1	1	1
2	1	$\beta_2(x)$
3	1	C_x
4	1	ρ
5	$\beta_2(x)$	C_x
6	C_x	$\beta_2(x)$
7	C_x	ρ
8	ρ	C_x
9	$\beta_2(x)$	ρ
10	ρ	$\beta_2(x)$

2.2. The adapted estimators for the second case:

The second proposed family of estimators is given by

$$t_{C2} = \bar{y}^*\exp\left(\frac{a\bar{X}+b}{\alpha_2(a\bar{x}^*+b)+(1-\alpha_2)(a\bar{X}+b)} - 1\right), \quad (29)$$

where α_2 is a chosen constant that determines the MSE of the proposed estimator minimum. We can also generate some members for the t_{C2} estimator under the second case as in Table 1 by replacing $\bar{x}$ with$\bar{x}^*$.

In terms ofe_i^* $(i = y, x)$, we can write

$$t_{C2} = \bar{Y}\left(1 + e_0^* - \alpha_2\theta e_1^* + \frac{3\alpha_2^2\theta^2 {e_1^*}^2}{2} - \alpha_2\theta e_0^* e_1^*\right). \tag{30}$$

Using the t_{C1} estimator's similar procedure, we arrive at the bias and MSE of the t_{C2}, respectively, as follows:

$$B(t_{C2}) = \bar{Y}\left(\lambda\left(\frac{3\alpha_2^2\theta^2}{2}C_x^2 - \alpha_2\theta C_{yx}\right) + \frac{W_2(p-1)}{n}\left(\frac{3\alpha_2^2\theta^2}{2}C_{x(2)}^2 - \alpha_2\theta C_{yx(2)}\right)\right), \tag{31}$$

$$MSE(t_{C2}) = \bar{Y}\left(\lambda\left(C_y^2 + \alpha_2^2\theta^2 C_x^2 - 2\alpha_2\theta C_{yx}\right) + \frac{W_2(p-1)}{n}\left(C_{y(2)}^2 + \alpha_2^2\theta^2 C_{x(2)}^2 - 2\alpha_2\theta C_{yx(2)}\right)\right), \tag{32}$$

We obtain the optimal value of α_2 by the minimization of the MSE equation in Eq. (32) as

$$\alpha_2^* = \frac{\lambda C_{yx} + \frac{W_2(p-1)}{n}C_{yx(2)}}{\theta\left(\lambda C_x^2 + \frac{W_2(p-1)}{n}C_{x(2)}^2\right)}. \tag{33}$$

Using the value ofα_2^*, the $MSE_{min}(t_{C2})$ equation is determined as follows:

$$MSE_{min}(t_{C2}) = \bar{Y}^2\left[\lambda C_y^2 + \frac{W_2(p-1)}{n}C_{y(2)}^2 - \frac{\left(\lambda C_{yx} + \frac{W_2(p-1)}{n}C_{yx(2)}\right)^2}{\lambda C_x^2 + \frac{W_2(p-1)}{n}C_{x(2)}^2}\right]. \tag{34}$$

3. EFFICIENCY COMPARISONS

To prove the efficiency, comparison of the t_{C1} and t_{C2} estimators has been made with the mentioned classical estimators under both cases, respectively. The efficiency conditions have also been stated. Firstly, we utilize Eq. (10), (13), (16), and Eq. (29) to compare the efficiencies of the t_{C1} with the t_{HH}, t_R^*, and t_{BT}^* for the Case I. Here, comparison between the t_{C1}estimator and the regression estimator t_{reg}^* is not included because the minimum MSEs of the estimators are equal to each other. We obtain the following efficiency conditions of the t_{C1} estimator.

$$[MSE(t_{HH}) - MSE_{min}(t_{C1})] = \lambda\rho_{xy}^2 C_y^2 > 0, \tag{35}$$

$$[MSE(t_R^*) - MSE_{min}(t_{C1})] = \left(C_x - \rho_{xy}C_y\right)^2 > 0, \tag{36}$$

$$[MSE(t_{BT}^*) - MSE_{min}(t_{C1})] = \left(\frac{C_x}{2} - \rho_{xy}C_y\right)^2 > 0. \tag{37}$$

The t_{C1} estimator perform better at the optimal value of α_1 than t_{HH}, t_R^*, and t_{BT}^* estimators, according to the conditions between Eq. (35) – Eq. (37), as these conditions are always satisfied.

Secondly, we compare the MSEs of the t_{C2} with the $t_{HH}, t_R^{**}, t_{reg}^{**}$ and t_{BT}^{**} for the Case II. Using Eq. (10), (20), (21), (22), and Eq. (34), we respectively have

$$[MSE(t_{HH}) - MSE_{min}(t_{C2})] = \left(\lambda C_{yx} + \frac{W_2(p-1)}{n}C_{yx(2)}\right)^2 > 0, \tag{38}$$

$$[MSE(t_R^{**}) - MSE_{min}(t_{C2})] = \left(\left(\lambda C_x^2 + \frac{W_2(p-1)}{n}C_{x(2)}^2\right) - \left(\lambda C_{yx} + \frac{W_2(p-1)}{n}C_{yx(2)}\right)\right)^2 > 0, \tag{39}$$

$$[MSE(t_{BT}^{**}) - MSE_{min}(t_{C2})] = \left(\left(\lambda C_{yx} + \frac{W_2(p-1)}{n}C_{yx(2)}\right) - \frac{1}{2}\left(\lambda C_x^2 + \frac{W_2(p-1)}{n}C_{x(2)}^2\right)\right)^2 > 0, \tag{40}$$

$$iv)\ \left[\mathrm{MSE}\left(\mathrm{t}_{\mathrm{reg}}^{**}\right)-\mathrm{MSE}_{\min}(\mathrm{t}_{C2})\right]=\left(\left(\frac{\mathrm{W}_2(\mathrm{p}-1)}{\mathrm{n}}\mathrm{C}_{\mathrm{x}(2)}^2\rho_{\mathrm{yx}}\frac{\mathrm{C}_{\mathrm{y}}}{\mathrm{C}_{\mathrm{x}}}\right)-\left(\frac{\mathrm{W}_2(\mathrm{p}-1)}{\mathrm{n}}\mathrm{C}_{\mathrm{yx}(2)}\right)\right)^2>0. \quad (41)$$

The conditions Eq. (38) – Eq. (41) are always satisfied, thus we conclude that the t_{C2} estimator perform better at the optimal value of α_2 than the compared estimators.

4. EMPIRICAL STUDY

As we show that the proposed t_{C1} and t_{C2} estimators, using the optimal values of α_1 andα_2, respectively, are always the most efficient estimators among compared estimators for the first and second cases, respectively, in Section 3, we obtain the ranges of α_1 and α_2 values that make the proposed families of estimators, respectively, more efficient than other estimators, based on the different values of *p*, in this section. We also compute the MSE values and using these values obtain the percent relative efficiencies (PRE) for each proposed and compared estimators by using Eq. (43) as below:

$$PRE(t_*)=\frac{Var(t_{HH})}{MSE(t_*)}x100\,. \quad (42)$$

In this equation, t_* symbolizet$_{\mathrm{R}}^{*}$, t$_{\mathrm{BT}}^{*}$, t$_{C1}$, t$_{\mathrm{R}}^{**}$, t$_{\mathrm{BT}}^{**}$, t$_{\mathrm{reg}}^{**}$, and t_{C2} estimators, respectively. For the comparison, the reference estimator is t_{HH} estimator. We have utilized the popular data sets of three populations in Unal and Kadilar (2019), referred by many studies in literature, as well. In this way, we try to prove the performance of the t_{C1} and t_{C2} estimators for the first and second cases, respectively, in practice. In this section, we have utilized three distinct datasets from various sources.

The first dataset (Population 1) consists of seventy observations indicating the population of the village and cultivated area (Khare & Srivastava, 1993). This Population 1 represents the cultivated area as the variable of study "y" and the village population as the variable of auxiliary "x". The second dataset (Population 2) originates from Khare and Sinha (2009) and involves the variable of study being the number of agriculture labors, while the variable of auxiliary is the area of the village. Lastly, the third dataset (Population 3) is obtained from Satici and Kadilar (2011). In Population 3, the variable of study is the number of successful students, and the variable of auxiliary is the number of teachers. The underlying population parameters are briefly summarized for Populations 1-3 as follows:

Population 1. *(Khare & Srivastava, 1993)*

N=70, n=35	$\bar{X}$ =1755.53	$\rho_{yx(2)}$ =0.45	C_{yx} =0.39	$C_{yx(2)}$ =0.10
λ=0.014	$\bar{Y}$ =981.29	ρ_{yx} =0.78	C_x =0.80	$C_{x(2)}$ =0.57
f=0.50	W_2 =0.2	$\beta_2(x)$ =0.34	C_y =0.63	$C_{y(2)}$ =0.41

Population 2. *(Khare & Sinha, 2009)*

N=96, n=40	$\bar{X}$ =144.87	$\rho_{yx(2)}$ =0.72	C_{yx} =0.82	$C_{yx(2)}$ =1.41
λ=0.01458	$\bar{Y}$ =137.92	ρ_{yx} =0.77	C_x =0.81	$C_{x(2)}$ =0.94
f=0.42	W_2 =0.25	$\beta_2(x)$ =1.19	C_y =1.32	$C_{y(2)}$ =2.08

Population 3. *(Satici & Kadilar, 2011)*

N=261, n=90	$\bar{X}$ =306.44	$\rho_{yx(2)}$ =0.97	C_{yx} =3.19	$C_{yx(2)}$ =1.46
λ=0.01	$\bar{Y}$ =222.58	ρ_{yx} =0.97	C_x =1.76	$C_{x(2)}$ =1.23
f=0.35	W_2 =0.25	$\beta_2(x)$ =21.36	C_y =1.87	$C_{y(2)}$ =1.22

In Table 2, we observe the values of θ_i that are utilized to find the MSE values of the t_{C1} and t_{C2} by Eq. (26) and Eq. (32), respectively, considering the data of Populations 1-3.

Table 2. *The values of θ_i for Populations 1-3*

	Populations		
$\theta_i, i = 1,2,\dots,10$	*I*	*II*	*III*
1	0.9994307	0.9931446	0.9967473
2	0.9998066	0.9917850	0.9348373
3	0.9995440	0.9944399	0.9942909
4	0.9995570	0.9947130	0.9968429
5	0.9986581	0.9953621	0.9997313
6	0.9997586	0.9898775	0.9618934
7	0.9994470	0.9934809	0.9982033
8	0.9994139	0.9927910	0.9941184
9	0.9986965	0.9955902	0.9998518
10	0.9997515	0.9893572	0.9329893

As discussed in Section 2, the min. MSE equation in Eq. (28) for the t_{C1} estimator is equivalent to the MSE equation of the t^*_{reg} estimator in Eq. (14) for Case I. Therefore, when determining the ranges of α_1 values that make the t_{C1} estimator performs better than other estimators, the regression estimator is not taken into consideration. For the first case, we obtain the ranges of α_1 values that make the proposed t_{C1}estimator more efficient than other compared estimators, based on the different values of *p*, in Tables 3-5. In other words, the ranges of α_1 values, as presented in Tables 3-5 for Populations 1-3, respectively, demonstrate that the t_{C1} estimator exhibits the min.

Table 3. *The α_1 values range for the family of t_{C1} estimators for Population 1*

	p				
$\theta_i, i = 1,2,\dots,10$	*2*	*3*	*4*	*5*	*6*
1	(0,501; 0,715)	(0,501; 0,715)	(0,501; 0,715)	(0,501; 0,715)	(0,501; 0,715)
2	(0,501; 0,715)	(0,501; 0,715)	(0,501; 0,715)	(0,501; 0,715)	(0,501; 0,715)
3	(0,501; 0,715)	(0,501; 0,715)	(0,501; 0,715)	(0,501; 0,715)	(0,501; 0,715)
4	(0,501; 0,715)	(0,501; 0,715)	(0,501; 0,715)	(0,501; 0,715)	(0,501; 0,715)
5	(0,501; 0,716)	(0,501; 0,716)	(0,501; 0,716)	(0,501; 0,716)	(0,501; 0,716)
6	(0,501; 0,715)	(0,501; 0,715)	(0,501; 0,715)	(0,501; 0,715)	(0,501; 0,715)
7	(0,501; 0,715)	(0,501; 0,715)	(0,501; 0,715)	(0,501; 0,715)	(0,501; 0,715)
8	(0,501; 0,715)	(0,501; 0,715)	(0,501; 0,715)	(0,501; 0,715)	(0,501; 0,715)
9	(0,501; 0,716)	(0,501; 0,716)	(0,501; 0,716)	(0,501; 0,716)	(0,501; 0,716)
10	(0,501; 0,715)	(0,501; 0,715)	(0,501; 0,715)	(0,501; 0,715)	(0,501; 0,715)

Table 4. *The α_1 values range for the family of t_{C1} estimators for Population 2*

	p				
$\theta_i, i = 1,2,\dots,10$	*2*	*3*	*4*	*5*	*6*
1	(1,007; 1,520)	(1,007; 1,520)	(1,007; 1,520)	(1,007; 1,520)	(1,007; 1,520)
2	(1,009; 1,522)	(1,009; 1,522)	(1,009; 1,522)	(1,009; 1,522)	(1,009; 1,522)
3	(1,006; 1,518)	(1,006; 1,518)	(1,006; 1,518)	(1,006; 1,518)	(1,006; 1,518)
4	(1,006; 1,517)	(1,006; 1,517)	(1,006; 1,517)	(1,006; 1,517)	(1,006; 1,517)
5	(1,005; 1,516)	(1,005; 1,516)	(1,005; 1,516)	(1,005; 1,516)	(1,005; 1,516)
6	(1,011; 1,525)	(1,011; 1,525)	(1,011; 1,525)	(1,011; 1,525)	(1,011; 1,525)
7	(1,007; 1,519)	(1,007; 1,519)	(1,007; 1,519)	(1,007; 1,519)	(1,007; 1,519)
8	(1,008; 1,520)	(1,008; 1,520)	(1,008; 1,520)	(1,008; 1,520)	(1,008; 1,520)
9	(1,010; 1,516)	(1,010; 1,516)	(1,010; 1,516)	(1,010; 1,516)	(1,010; 1,516)
10	(1,011; 1,525)	(1,011; 1,525)	(1,011; 1,525)	(1,011; 1,525)	(1,011; 1,525)

Table 5. *The α_1 values range for the family of t_{C1} estimators for Population 3*

	p				
$\theta_i, i = 1,2,\dots,10$	*2*	*3*	*4*	*5*	*6*
1	(1,004; 1,061)	(1,004; 1,061)	(1,004; 1,061)	(1,004; 1,061)	(1,004; 1,061)
2	(1,07; 1,131)	(1,07; 1,131)	(1,07; 1,131)	(1,07; 1,131)	(1,07; 1,131)
3	(1,006; 1,063)	(1,006; 1,063)	(1,006; 1,063)	(1,006; 1,063)	(1,006; 1,063)
4	(1,004; 1,061)	(1,004; 1,061)	(1,004; 1,061)	(1,004; 1,061)	(1,004; 1,061)
5	(1,001; 1,058)	(1,001; 1,058)	(1,001; 1,058)	(1,001; 1,058)	(1,001; 1,058)
6	(1,040; 1,099)	(1,040; 1,099)	(1,040; 1,099)	(1,040; 1,099)	(1,040; 1,099)
7	(1,002; 1,059)	(1,002; 1,059)	(1,002; 1,059)	(1,002; 1,059)	(1,002; 1,059)
8	(1,006; 1,064)	(1,006; 1,064)	(1,006; 1,064)	(1,006; 1,064)	(1,006; 1,064)
9	(1,001; 1,057)	(1,001; 1,057)	(1,001; 1,057)	(1,001; 1,057)	(1,001; 1,057)
10	(1,072; 1,133)	(1,072; 1,133)	(1,072; 1,133)	(1,072; 1,133)	(1,072; 1,133)

When we examine Tables 3 and 4, we see that the ranges of α_1 values are nearly the same for all θ_i, because all θ_i values are nearly 1 for the Populations 1 and 2, as given in Table 2. However, in Table 5, we see that the ranges of α_1 values are different with each other, according to the parameter θ_i, because θ_i values differ with each other for the Population 3, as given in Table 2. In addition, it is surprising that the values of *p* do not affect the ranges of α_1 values for all the populations in the Case 1.

For the second case, we obtain the ranges of α_2 values that make the proposed t_{C2}estimator more efficient than other compared estimators, based on the different values of *p*, in Tables 6-8. For this case, the ranges of α_2 values for the efficiency of the second proposed t_{C2} estimator, relative to others, are provided in Tables 6-8 for Populations 1-3, respectively. These ranges are based on different values of p and obtained for allθ_i ($i = 1,2,\dots,10$).

Table 6. *The α_2 values range for the family of t_{C2} estimators for Population 1*

	p				
$\theta_i, i = 1,2,\dots,10$	*2*	*3*	*4*	*5*	*6*
1	(0,509; 0,607)	(0,501; 0,546)	(0,494; 0,500)	(0,454; 0,500)	(0,421; 0,500)
2	(0,509; 0,607)	(0,501; 0,545)	(0,494; 0,500)	(0,453; 0,500)	(0,421; 0,500)
3	(0,509; 0,607)	(0,501; 0,546)	(0,494; 0,500)	(0,454; 0,500)	(0,421; 0,500)
4	(0,509; 0,607)	(0,501; 0,546)	(0,494; 0,500)	(0,454; 0,500)	(0,421; 0,500)
5	(0,510; 0,608)	(0,501; 0,546)	(0,495; 0,500)	(0,454; 0,500)	(0,422; 0,500)
6	(0,509; 0,607)	(0,501; 0,545)	(0,494; 0,500)	(0,454; 0,500)	(0,421; 0,500)
7	(0,509; 0,607)	(0,501; 0,546)	(0,494; 0,500)	(0,454; 0,500)	(0,421; 0,500)
8	(0,509; 0,607)	(0,501; 0,546)	(0,494; 0,500)	(0,454; 0,500)	(0,421; 0,500)
9	(0,510; 0,608)	(0,501; 0,546)	(0,495; 0,500)	(0,454; 0,500)	(0,422; 0,500)
10	(0,509; 0,607)	(0,501; 0,545)	(0,494; 0,500)	(0,454; 0,500)	(0,421; 0,500)

Table 7. *The α_2 values range for the family of t_{C2} estimators for Population 2*

	p				
$\theta_i, i = 1,2,\dots,10$	*2*	*3*	*4*	*5*	*6*
1	(1,264; 1,512)	(1,264; 1,628)	(1,264; 1,695)	(1,264; 1,738)	(1,264; 1,769)
2	(1,266; 1,514)	(1,266; 1,630)	(1,266; 1,697)	(1,266; 1,741)	(1,266; 1,771)
3	(1,262; 1,510)	(1,262; 1,626)	(1,262; 1,693)	(1,262; 1,736)	(1,262; 1,767)
4	(1,262; 1,510)	(1,262; 1,626)	(1,262; 1,692)	(1,262; 1,736)	(1,262; 1,766)
5	(1,261; 1,509)	(1,261; 1,624)	(1,261; 1,691)	(1,261; 1,735)	(1,261; 1,765)
6	(1,268; 1,517)	(1,268; 1,633)	(1,268; 1,701)	(1,268; 1,744)	(1,268; 1,775)
7	(1,266; 1,512)	(1,264; 1,628)	(1,264; 1,694)	(1,264; 1,738)	(1,264; 1,768)
8	(1,264; 1,513)	(1,264; 1,629)	(1,264; 1,696)	(1,264; 1,739)	(1,264; 1,770)
9	(1,261; 1,509)	(1,261; 1,624)	(1,261; 1,691)	(1,261; 1,734)	(1,261; 1,765)
10	(1,269; 1,518)	(1,269; 1,634)	(1,269; 1,701)	(1,269; 1,745)	(1,269; 1,776)

When we examine the ranges in Tables 6 and 7 in detail for the Case II, again we can simply say that there is no important difference for the range values of α_2 in Populations 1 and 2; on the other hand, when we examine the ranges in Table 8, there is a clear difference for the range values according to θ_i $(i = 1,2,\dots,10)$ for Population 3, because of the same reason as in Case I. It is also surprising that there is no effect of the values of p on the ranges of α_2 values for all of the populations in Case II, as well.

The PRE results of t_{C1} and t_{C2} estimators with respect to the competing estimators are presented in Tables 9–10 for the Population 1, 2, and 3, respectively, under both cases.

Table 8. *The α_2 values range for the family of t_{C2} estimators for Population 3*

	p				
$\theta_i, i = 1,2,\ldots,10$	*2*	*3*	*4*	*5*	*6*
1	(1,013; 1,032)	(1,004; 1,027)	(1,004; 1,016)	(1,004; 1,007)	(1,001; 1,003)
2	(1,080; 1,100)	(1,070; 1,095)	(1,070; 1,083)	(1,070; 1,074)	(1,067; 1,069)
3	(1,015; 1,034)	(1,006; 1,029)	(1,006; 1,018)	(1,006; 1,010)	(1,004; 1,005)
4	(1,013; 1,032)	(1,004; 1,027)	(1,004; 1,016)	(1,004; 1,007)	(1,001; 1,003)
5	(1,010; 1,029)	(1,001; 1,024)	(1,001; 1,013)	(1,001; 1,004)	(0,998; 1,000)
6	(1,050; 1,069)	(1,040; 1,064)	(1,040; 1,053)	(1,040; 1,044)	(1,037; 1,039)
7	(1,011; 1,030)	(1,002; 1,025)	(1,002; 1,014)	(1,002; 1,006)	(1,000; 1,001)
8	(1,016; 1,035)	(1,006; 1,029)	(1,006; 1,018)	(1,006; 1,010)	(1,004; 1,005)
9	(1,010; 1,029)	(1,001; 1,024)	(1,001; 1,013)	(1,001; 1,004)	(0,998; 1,000)
10	(1,082; 1,102)	(1,072; 1,097)	(1,072; 1,085)	(1,072; 1,076)	(1,070; 1,071)

Table 9. *The PRE results for all data sets under the Case I with respect to t_{HH}*

	Pop. 1					*Pop. 2*					*Pop. 3*				
	p					*p*					*p*				
	2	*3*	*4*	*5*	*6*	*2*	*3*	*4*	*5*	*6*	*2*	*3*	*4*	*5*	*6*
t_{HH}	100.0	100.0	100.0	100.0	100.0	100.0	100.0	100.0	100.0	100.0	100.0	100.0	100.0	100.0	100.0
t_R^*	143.1	135.7	130.4	126.5	123.5	138.0	122.2	115.7	112.1	109.9	524.0	344.4	271.7	232.3	207.6
t_{BT}^*	200.3	177.6	163.3	153.4	146.2	122.4	113.8	109.9	107.8	106.4	247.4	209.4	187.0	172.2	161.7
t_{C1}	***207.0***	***182.2***	***166.7***	***156.1***	***148.5***	***140.3***	***123.4***	***116.5***	***112.7***	***110.4***	***525.7***	***345.1***	***272.1***	***232.6***	***207.8***

Table 10. *The PRE results for all data sets under the Case II with respect to t_{HH}*

	Pop. 1					*Pop. 2*					*Pop. 3*				
	p					*p*					*p*				
	2	*3*	*4*	*5*	*6*	*2*	*3*	*4*	*5*	*6*	*2*	*3*	*4*	*5*	*6*
t_{HH}	100.0	100.0	100.0	100.0	100.0	100.0	100.0	100.0	100.0	100.0	100.0	100.0	100.0	100.0	100.0
t_R^{**}	124.4	108.6	98.9	92.3	87.5	202.3	194.4	190.7	188.6	187.2	1719.3	1735.3	1748.0	1758.3	1766.9
t_{BT}^{**}	208.3	188.9	176.2	167.2	160.5	148.1	144.4	142.7	141.7	141.0	330.8	334.8	337.9	340.5	342.6
t_{reg}^{**}	209.0	184.9	169.7	159.3	151.7	218.5	211.1	207.6	205.6	204.3	1726.5	1731.2	1734.9	1737.9	1740.4
t_{C2}	***210.8***	***189.2***	***176.2***	***167.5***	***161.2***	***220.7***	***215.0***	***212.6***	***211.3***	***210.6***	***1729.2***	***1739.3***	***1749.2***	***1758.4***	***1766.9***

Boldfaced values indicate the “best” performances.

From Tables 9–10, it is shown that the t_{C1} and t_{C2} estimators perform better than all other compared estimators for all data sets under both cases. Accordingly, it can be inferred that among competing estimators, t_{C1} and t_{C2} are the most effective ones in general. For the t_{C1} estimator, it is observed that the PRE value decreased as the value of p increased in all populations. For the t_{C2} estimator, a similar situation is observed only in Populations 1 and 2. In Population 3, it is concluded that PRE values increase as p increases. At this point, Figures 1 and 2 represents the PRE results of the proposed t_{C1} and t_{C2} estimators for the Population 1, 2, and 3, respectively. In both cases, the highest PRE values obtained in Population 3 are noteworthy.

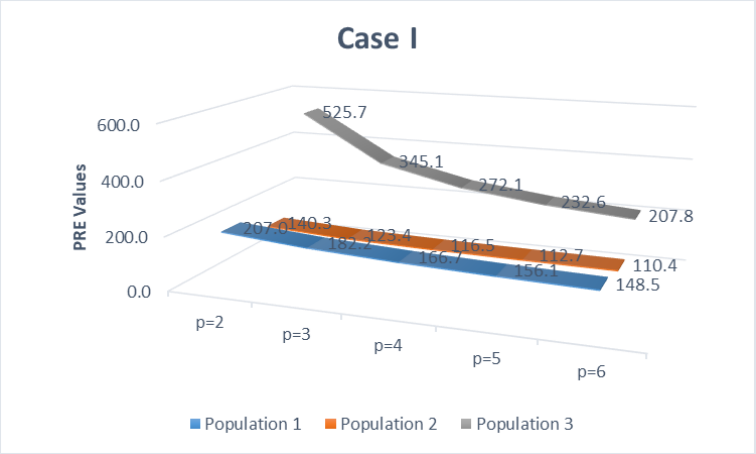

Figure 1. *The PRE results of t_{C1} estimator for all populations*

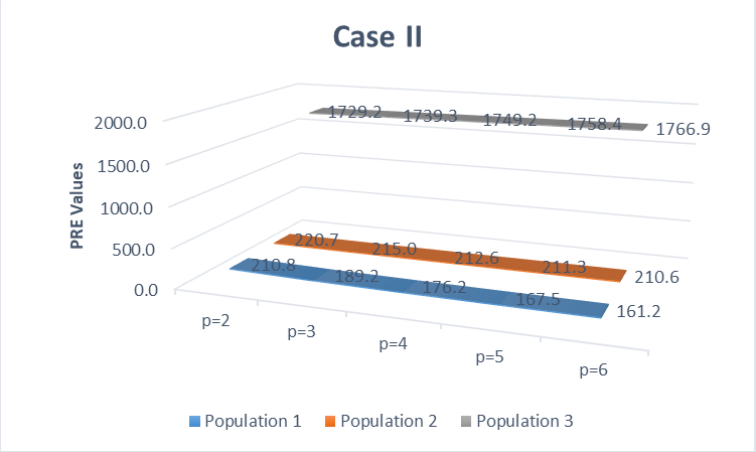

Figure 2. *The PRE results of t_{C2} estimator for all populations*

5. CONCLUSION

We consider the estimation of the $\bar{Y}$ when non-response occurs in two different cases and propose two families of estimators, t_{C1} and t_{C2}, using the exponential function under these cases. The bias and minimum MSE of the t_{C1} and t_{C2}estimators are obtained. We compare the proposed estimators with the mentioned estimators in theory and in application using three different data sets. We demonstrate that the t_{C1} and t_{C2} estimators are always recommended based on theory in Section 3 and obtain the efficiency intervals of α_1 and α_2 for the first and the second proposed families of estimators in practice using three different population data in Section 4. Additionally, PRE values are included in the application. When we look at the compared and proposed estimators, it is seen that the values of the suggested estimators are the highest for both cases and these values increase even more, especially for Population 3.

CONFLICT OF INTEREST

The authors declare no conflict of interest.

REFERENCES

Ahmad, S., Arslan, M., Khan, A., & Shabbir, J. (2021). A generalized exponential-type estimator for population mean using auxiliary attributes. *Plos One*, *16*(5), e0246947. https://www.doi.org/10.1371/journal.pone.0246947

Ahmad, S., Hussain, S., Aamir, M., Khan, F., Alshahrani, M. N., & Alqawba, M. (2022). Estimation of finite population mean using dual auxiliary variable for non-response using simple random sampling. *Aims Mathematics*, *793*, 4592-4613. https://www.doi.org/10.3934/math.2022256

Ahmadini, A. A. H., Yadav, T., Yadav, S. K., & Al Luhayb, A. S. M. (2022). Restructured searls family of estimators of population mean in the presence of nonresponse. *Frontiers in Applied Mathematics and Statistics*, *8*, 969068. https://www.doi.org/10.3389/fams.2022.969068

Anieting, A. E., Enang, E. I., & Onwukwe, C. E. (2020). Efficient estimator for Population mean in stratified double sampling in the presence of nonresponse using one auxiliary variable. *Statistics*, *4*(2), 40-50. https://www.doi.org/10.52589/AJMSS-YF4V11QV

Bahl, S., & Tuteja, R. K. (1991). Ratio and product type exponential estimators. *Journal of Information and Optimization Sciences*, *12*(1), 159-164. https://www.doi.org/10.1080/02522667.1991.10699058

Cochran, W. G. (1940). The estimation of the yields of the cereal experiments by sampling for the ratio of grain to total produce. *The Journal of Agricultural Science*, *30*(2), 262-275. https://www.doi.org/10.1017/S0021859600048012

Cochran, W. G. (1977) *Sampling Techniques*. John Wiley and Sons, New-York

Dansawad, N. (2019). A class of exponential estimator to estimate the population mean in the presence of non-response. *Naresuan University Journal: Science and Technology*, *27*(4), 20-26. https://www.doi.org/10.14456/nujst.2019.33

Fatima, M., Shahbaz, S. H., Hanif, M., & Shahbaz, M. Q. (2022). A modified regression-cum-ratio estimator for finite population mean in presence of nonresponse using ranked set sampling. *AIMS Mathematics*, *7*(4), 6478-6488. https://www.doi.org/10.3934/math.2022361

Hansen, M. H., & Hurwitz, W. N. (1946). The problem of non-response in sample surveys. *Journal of the American Statistical Association*, *41*(236), 517-529. https://www.doi.org/10.1080/01621459.1946.10501894

Javed, M., Irfan, M., & Pang, T. (2019). Hartley-Ross type unbiased estimators of population mean using two auxiliary variables. *Scientia Iranica*, *26*(6), 3835-3845. https://www.doi.org/10.24200/sci.2018.5648.1397

Khare, B. B., & Sinha, R. R. (2009). On class of estimators for population mean using multi-auxiliary characters in the presence of non-response. *Statistics in Transition*, *10*(1), 3-14.

Khare, B. B., & Srivastava, S. (1993). Estimation of population mean using auxiliary character in presence of non-response. *National Academy Science Letters*, *16*, 111-114.

Khan, A., Ali, A., Ijaz, M., Azeem, M., & El-Morshedy, M. (2023). An exponential ratio type estimator of the population mean in the presence of non-response using double sampling. *Journal of Statistics Applications and Probability*, *12*(1), 191-205. https://www.doi.org/10.18576/jsap/120118

Khoshnevisan, M., Singh, R., Chauhan, P., Sawan, N., & Smarandache, F. (2007). A general family of estimators for estimating population mean using known value of some population parameter(s). *Far East Journal of Theoretical Statistics*, *22*, 181-191.

Kumar, S. (2013). Improved exponential estimator for estimating the population mean in the presence of non-response. *Communications for Statistical Applications and Methods*, *20*(5), 357-366. https://www.doi.org/10.5351/CSAM.2013.20.5.357

Kumar, S, & Bhougal, S. (2011). Estimation of the population mean in presence of non-response. *Communications for Statistical Applications and Methods*, *18*(4), 537-548. https://www.doi.org/10.5351/CKSS.2011.18.4.537

Kumar, K., & Kumar, M. (2017). Improved exponential ratio and product type estimators for population mean in the presence of nonresponse. *Bulletin of Mathematics and Statistics Research*, *5*(2), 68-76.

Mehta, P., & Tailor, R. (2020). Chain ratio type estimators using known parameters of auxiliary variates in double sampling. *Journal of Reliability and Statistical Studies*, *13*(2-4), 243-252. https://www.doi.org/10.13052/jrss0974-8024.13242

Oncel Cekim, H., & Kadilar, C. (2018). New families of unbiased estimators in stratified random sampling. *Journal of Statistics and Management Systems*, *21*(8), 1481-1499. https://www.doi.org/10.1080/09720510.2018.1530176

Oncel Cekim, H. (2022). Modified unbiased estimators for population variance: An application for COVID-19 deaths in Russia. *Concurrency and Computation: Practice and Experience*, *34*(22), e7169. https://www.doi.org/10.1002/cpe.7169

Özel Kadilar, G. (2016). A new exponential type estimator for the population mean in simple random sampling. *Journal of Modern Applied Statistical Methods*, *15*(2), 207-214. http://www.doi.org/10.22237/jmasm/1478002380

Pal, S. K., & Singh, H. P. (2017). A class of ratio-cum-ratio-type exponential estimators for population mean with sub sampling the nonrespondents. *Jordan Journal of Mathematics and Statistics*, *10*(1), 73-94.

Pal, S. K., & Singh, H. P. (2018). Estimation of finite population mean using auxiliary information in presence of non-response. *Communications in Statistics-Simulation and Computation*, *47*(1), 143-165. https://www.doi.org/10.1080/03610918.2017.1280161

Rao, P. S. R. S. (1986). Ratio estimation with sub sampling the non-respondents. *Survey Methodology*, *12*(2), 217-230.

Rehman, S. A., & Shabbir, J. (2022). An efficient class of estimators for finite population mean in the presence of non-response under ranked set sampling (RSS). *Plos One*, *17*(12), e0277232. https://www.doi.org/10.1371/journal.pone.0277232

Sanaullah, A., Ehsan, I., & Noor-Ul-Amin, M. (2019). Estimation of mean for a finite population using sub-sampling of non-respondents. *Journal of Statistics and Management Systems*, *22*(6), 1015-1035. https://www.doi.org/10.1080/09720510.2019.1572981

Satici, E., & Kadilar, C. (2011). Ratio estimator for the population mean at the current occasion in the presence of non-response in successive sampling. *Hacettepe Journal of Mathematics and Statistics*, *40*(1), 115-124.

Shabbir, J., Haq, A., & Gupta, S. (2014). A new difference-cum-exponential type estimator of finite population mean in simple random sampling. *Revista Colombiana de Estadística*, *37*(1), 199-211. https://www.doi.org/10.15446/rce.v37n1.44366

Shabbir, J., & Onyango, R. (2022). Use of an efficient unbiased estimator for finite population mean. *Plos One*, *17*(7), e0270277. https://www.doi.org/10.1371/journal.pone.0270277

Sharma, P., Pal, S. K., & Singh, H. P. (2022). Improved estimators of population mean under nonresponse in successive sampling. *Mathematical Problems in Engineering*, *2022*(1), 1-8. https://www.doi.org/10.1155/2022/1349689

Singh, R., Chauhan, P., & Sawan, N. (2008). On linear combination of ratio and product type exponential estimator for estimating the finite population mean. *Statistics in Transition - New Series*, *9*, 105-115.

Singh, R., Kumar, M., Chaudhary, M. K., & Smarandache, F. (2010). Estimation of mean in presence of non-response using exponential estimator. *Multispace & Multistructure Neutrosophic Transdisciplinarity (100 Collected Papers of Sciences)*, (vol IV, pp. 758-768). https://doi.org/10.48550/arXiv.0906.2462

Singh, H. P., & Nigam, P. (2020). Ratio-Ratio-Type exponential estimator of finite population mean in double sampling for stratification. *International Journal of Agricultural and Statistical Science*, *16*(1), 251-257.

Singh, G. N., & Usman, M. (2019a). Ratio-to-product exponential-type estimators under non-response. *Jordan Journal of Mathematics and Statistics*, 12(4), 593-616.

Singh, G. N., & Usman, M. (2019b). Efficient combination of various estimators in the presence of non-response. *Communications in Statistics Simulation and Computation*, *50*(8), 2432-2466. https://www.doi.org/10.1080/03610918.2019.1614618

Tailor, R., & Lone, H. A. (2014). Separate ratio-type estimators of population mean in stratified random sampling. *Journal of Modern Applied Statistical Methods*, *13*(1), 223-233. https://www.doi.org/10.22237/jmasm/1398917580

Unal, C., & Kadilar, C. (2019). Exponential type estimator for the population mean in the presence of non-response. *Journal of Statistics and Management Systems*, *23*(3), 603-615. https://www.doi.org/10.1080/09720510.2019.1668158

Unal, C., & Kadilar, C. (2021). Improved family of estimators using exponential function for the population mean in the presence of nonresponse. *Communications in Statistics - Theory and Methods*, *50*(1), 237-248. https://www.doi.org/10.1080/03610926.2019.1634818

Unal, C., & Kadilar, C. (2022a). A new population mean estimator under non-response cases. *Journal of Taibah University for Science*, *16*(1), 111-119. https://www.doi.org/10.1080/16583655.2022.2034343

Unal, C., & Kadilar, C. (2022b). Exponential type estimators using sub-sampling method with applications in agriculture. *Journal of Agricultural Sciences (Tarim Bilimleri Dergisi)*, *28*(3), 457-472. https://www.doi.org/10.15832/ankutbd.915999

Yadav, S. K., Sharma, D. K., & Mishra, S. S. (2021). New modified ratio type estimator of the population mean using the known median of the study variable. *International Journal of Operational Research*, *41*(2), 151-167. https://www.doi.org/10.1504/IJOR.2021.115625

Yadav, S. K., & Zaman, T. (2021). Use of some conventional and non-conventional parameters for improving the efficiency of ratio-type estimators. *Journal of Statistics and Management Systems*, *24*(5), 1077-1100. https://www.doi.org/10.1080/09720510.2020.1864939

Yunusa, O., & Kumar, S. (2014). Ratio-cum-product estimator using exponential estimator in the presence of non-response. *Journal of Advanced Computing*, *3*(1), 1-11. https://www.doi.org/10.7726/jac.2014.1001

Zahid, S., Kamal, A., & Makhdum, M. (2022). Generalized Dual to Exponential Ratio Type Estimator for the Finite Population Mean in the Presence of Nonresponse. In: O. O. Awe, K. Love, & E. A. Vance (Eds.), *Promoting Statistical Practice and Collaboration in Developing Countries* (2nd ed., pp. 249-263). Chapman and Hall/CRC. https://www.doi.org/10.1201/9781003261148

Zaman, T., & Kadilar, C. (2019). Novel family of exponential estimators using information of auxiliary attribute. *Journal of Statistics and Management Systems*, *22*(8), 1499-1509. https://www.doi.org/10.1080/09720510.2019.1621488

Zaman, T., & Kadilar, C. (2021a). Exponential ratio and product type estimators of the mean in stratified two-phase sampling. *AIMS Mathematics*, *6*(5), 4265-4279. https://www.doi.org/10.3934/math.2021252

Zaman, T., & Kadilar, C. (2021b). New class of exponential estimators for finite population mean in two-phase sampling. *Communications in Statistics-Theory and Methods*, *50*(4), 874-889. https://www.doi.org/10.1080/03610926.2019.1643480

Research Article GU J Sci, Part A, 10(4): 417-441 (2023) 10.54287/gujsa.1357216

Gazi University
Journal of Science
PART A: ENGINEERING AND INNOVATION
http://dergipark.org.tr/gujsa

FOPID Controller Design for a Buck Converter System Using a Novel Hybrid Cooperation Search Algorithm with Pattern Search for Parameter Tuning

Cihan ERSALI [1*] Baran HEKİMOĞLU [1]

[1] Department of Electrical and Electronics Engineering, Batman University, Batman, Türkiye

Keywords

FOPID Controller
Buck Converter
Cooperation Search Algorithm
Pattern Search
Opposition-Based Learning

Abstract

This research introduces a novel metaheuristic algorithm, OCSAPS, representing an upgraded cooperation search algorithm (CSA) version. OCSAPS incorporates opposition-based learning (OBL) and pattern search (PS) algorithms. The proposed algorithm's application aims to develop a fractional order proportional-integral-derivative (FOPID) controller tailored for a buck converter system. The efficacy of the proposed algorithm is assessed by statistical boxplot and convergence response analyses. Furthermore, the performance of the OCSAPS-based FOPID-controlled buck converter system is benchmarked against CSA, Harris hawk optimization (HHO), and genetic algorithm (GA). This comparative analysis encompasses transient and frequency responses, performance indices, and robustness analysis. The outcomes of this comparison highlight the distinctive advantages of the proposed approach-based system. Moreover, the proposed approach's performance was compared with six other approaches used to control buck converter systems similarly regarding both time and frequency domain responses. Overall, the findings underscore the efficacy of the OCSAPS algorithm as a robust solution for designing FOPID controllers in buck converter systems.

Cite

Ersali, C., & Hekimoglu, B. (2023). FOPID Controller Design for a Buck Converter System Using a Novel Hybrid Cooperation Search Algorithm with Pattern Search for Parameter Tuning. *GU J Sci, Part A, 10*(4), 417-441. doi:10.54287/gujsa.1357216

Author ID (ORCID Number)

0000-0001-8368-1195 Cihan ERSALI
0000-0002-1839-025X Baran HEKİMOĞLU

Article Process

Submission Date 08.09.2023
Revision Date 10.10.2023
Accepted Date 25.10.2023
Published Date 11.12.2023

1. INTRODUCTION

Over the past decade, there has been a surge in the popularity of battery-powered iterations of corded electronic devices like household appliances and consumer electronics. The convenience and portability drive this trend that these battery-powered versions offer. These devices rely on power electronics converters to ensure optimal DC-DC voltage and power utilization within their circuits. The buck converter has emerged as a favored choice for regulating and fine-tuning output voltage in these devices (Zhang & Qiu, 2014). Its widespread adoption is attributed to its simplicity, low cost, uncomplicated structure, and exceptional dynamic performance, making it versatile for various applications, including power conversion and motor drives (Lee et al., 1997). Designing a standout controller for the DC-DC buck converter is critical for establishing stable, efficient, and reliable systems. However, the inherent nonlinear characteristics of buck converters pose challenges in controller design (Wang et al., 2017). Researchers have responded to these challenges by exploring diverse controller types to achieve the desired system qualities (Al-Majidi et al., 2019).

There have been extensive studies utilizing different types of optimization approaches for DC-DC buck converters. In Izci et al. (2002a) and Izci and Ekinci (2022), state-of-the-art metaheuristic algorithms have been used to optimize FOPID controllers for DC-DC buck converters, which are some of the best-performing systems in the field. In Izci et al. (2002a) a hybrid version of the Levy flight distribution (LFD) algorithm is utilized to optimize a FOPID controller for the buck converter. The algorithm they proposed resulted in a

*Corresponding Author, e-mail: cihan.ersali@batman.edu.tr

12.9% better transient response and 14.8% better frequency response compared to the original LFD. Izci and Ekinci (2022) proposed an improved version of the hunger games search (HGS) algorithm to optimally control a FOPID controller for a DC-DC buck converter. They obtained a 21.8% faster rise time and 27.9% more bandwidth than the original HGS algorithm.

Similarly, in Sangeetha et al. (2023), a FOPID controller has been optimized for a DC-DC buck converter using a hybrid of Golden Jackal Optimization (GJO) and Capuchin Search Algorithm (CapSA), which they proposed in their study. They managed to improve the efficiency by 12.9% compared to the second-best method in their study, which is the genetic algorithm (GA). They also reduced the cost by 18.9% compared to particle swarm optimization (PSO).

In Warrier & Shah (2021), a cohort intelligence (CI) optimization has been used to optimize a FOPID controller for a DC-DC buck converter. They achieved 61.6% less overshoot and 24.7% less computation time compared to second best approaches reported in their study.

Effective controllers are expected to exhibit stability, robustness, swift transient response, accurate tracking, and precise frequency response. PID controllers are the most popular due to their straightforward structure, adaptability, and wide-scale industrial application (Hsieh & Chou, 2007). Despite the advantages of PID controllers, their parameter-tuning process is often laborious, relying on trial and error. Moreover, scenarios involving nonlinear effects, load fluctuations, disturbances, and parameter changes challenge the efficacy of PID controllers. This has spurred the need for more advanced control strategies (Monje et al., 2008).

In recent decades, fractional calculus and its application, particularly fractional control, have captivated the interest of researchers (Shah & Agashe, 2016; Ortiz-Quisbert et al., 2018; Chevalier et al., 2019; Micev et al., 2020; Dolai et al., 2022). FOPID controllers offer increased flexibility by incorporating fractional integral (λ) and derivative (μ) terms, making them adept at handling uncertainties and parameter variations. They effectively govern fractional and integer-order systems (Maâmar & Rachid, 2014), making them suitable for managing nonlinear systems like DC-DC converters (Cech & Schlegel, 2013). Given their attributes, this study embraces a FOPID controller for a DC-DC buck converter system. With its five parameters, the FOPID controller provides ample room for tuning, potentially resulting in highly stable DC-DC converter systems. Precise tuning of these parameters is paramount to meet design specifications such as robustness against parameter changes, improved overshoot, and settling time (Dastjerdi et al., 2019).

Literature reveals extensive exploration into parameter tuning for controllers using metaheuristic algorithms such as (HHO) (Izci et al., 2023), particle swarm optimization (PSO) (Demir & Demirok, 2023), hybrid whale optimization (HWO) algorithm (Hekimoğlu & Ekinci, 2020), Lévy flight distribution (LFD) (Izci et al., 2022b), artificial ecosystem-based optimization (AEO) (Izci et al., 2022c), and genetic algorithm (GA) (Ortatepe, 2023). While HHO offers high accuracy in parameter optimization, it can stagnate in local search spaces. PSO is straightforward and resource-efficient. It suffers from premature convergence and local trapping. HWO excels in providing effective solutions but demands substantial computational power. LFD efficiently handles constrained search spaces but can get stuck in local solutions. AEO is powerful yet tends to be trapped in local minima.

The positive outcomes demonstrated by metaheuristic algorithms in fine-tuning controller parameters for regulating the buck converter system, as evidenced in the studies mentioned above, fostered the adoption of a newly introduced optimization technique known as the CSA (Feng et al., 2021). This study introduces an enhanced version incorporating OBL to improve exploration and leverage PS technique for better local optimization within CSA. This algorithm streamlines the design of a FOPID controller for a buck converter system, delivering improved efficiency, robustness, and stability.

Contributions

• An innovative hybrid metaheuristic algorithm has been developed by enhancing the CSA algorithm with OBL and PS. This enhancement effectively elevates the original CSA's exploration and exploitation capabilities.

• The supremacy of the newly proposed algorithm over CSA, HHO, and GA has been established via statistical boxplot and convergence response analyses.

• The OCSAPS algorithm was skillfully applied to fine-tune the parameters of a FOPID controller in a DC-DC buck converter system. An array of tests were conducted to showcase the superior performance of the OCSAPS-driven FOPID-controlled buck converter system. These tests encompassed evaluations of transient and frequency responses, a comparison of diverse performance metrics, and a robustness analysis.

• Moreover, a comparison was executed between the proposed approach and six other methodologies documented in existing literature. These methodologies were utilized for controlling DC-DC buck converter systems with FOPID controllers, focusing on both transient and frequency responses. This examination yet again underscored the preeminence of the OCSAPS algorithm.

2. MATERIAL AND METHOD

2.1. Cooperation Search Algorithm

The CSA is rooted in a company's core operational principle of keeping pace with a changing world, enhancing efficiency, and striving for excellence (Feng et al., 2021). To achieve these objectives, continuous enhancement of knowledge, experience, and productivity is required from all tiers of the organization. This involves sharing wisdom among each other and replacing underperforming staff with more capable individuals. The pivotal factor in attaining the mentioned objectives is effective collaboration between teams. Notably, even the highest-ranking executives can be substituted with talented and motivated newcomers if it serves the company's betterment.

The algorithm embodies problem optimization through staff members and teams. It compares problem fitness to staff performance, with executive managers and the board of directors symbolizing different solution levels. The algorithm employs three operators within the company for solution enhancement.The steps outlining the operational mechanism of the CSA algorithm are as follows:

***Team building phase*:** Here, all team members are chosen randomly using Eq. (1). After evaluating the accomplishments of all solutions, a set of M∈[1, *I*] promising solutions is picked from the initial batch to form the higher-ranking set.

$$x_{i,j}^{k} = \emptyset\left(\underline{x}_j, \bar{x}_j\right), i \in [1, I], j \in [1, J], k = 1 \tag{1}$$

where $x_{i,j}^{k}$ represents the j^{th} value of the i^{th} solution during the k^{th} cycle. *I* denotes the solutions count within the present batch, while *J* signifies the number of variables that align with the optimization problem's dimension. Additionally, $\emptyset(L, U)$ refers to the function that generates a uniformly distributed random number within the range of $[L, U]$, where *L* and *U* denote the lower and upper constraints of the optimization variables, respectively.

Team communication operator: Each staff member can acquire fresh insights by exchanging knowledge with higher-ups, the board of directors, and supervisors. As indicated in Eq. (2), the communication process is divided into three segments: *A* stands for the chairperson's intellectual capacity, *B* denotes the cumulative knowledge retained by the board of directors, and *C* represents the combined intelligence held by the board of supervisors. The chairperson's selection is made arbitrarily from among the board of directors to replicate the rotational mechanism. Simultaneously, the values of *B* and *C* are calculated using identical positional information granted to all members of the board of directors and supervisors.

$$u_{i,j}^{k+1} = x_{i,j}^{k} + A_{i,j}^{k} + B_{i,j}^{k} + C_{i,j}^{k}, i \in [1, I], j \in [1, J], k \in [1, K] \tag{2}$$

$$A_{i,j}^{k} = \log\left(1/\emptyset(0,1)\right).\left(gbest_{m,j}^{k} - x_{i,j}^{k}\right) \tag{3}$$

$$B_{i,j}^{k} = \alpha.\emptyset(0,1).\left[\frac{1}{M}\sum_{m=1}^{M} gbest_{m,j}^{k} - x_{i,j}^{k}\right] \quad (4)$$

$$C_{i,j}^{k} = \beta.\emptyset(0,1).\left[\frac{1}{I}\sum_{i=1}^{I} pbest_{i,j}^{k} - x_{i,j}^{k}\right] \quad (5)$$

where $u_{i,j}^{k+1}$ signifies the j^{th} value within the i^{th} group solution during the $(k+1)^{th}$ cycle. The j^{th} value of the i^{th} personal best-known solution at the k^{th} cycle is represented by $pbest_{i,j}^{k}$. Similarly, $gbest_{m,j}^{k}$ stands for the j^{th} value within the global best-known solution of the m^{th} instance, from the beginning until the k^{th} cycle. The value of m is randomly selected from the set $\{1,2,\dots,M\}$. Knowledge acquired from the chairman is indicated as $A_{i,j}^{k}$. The learning factors α and β are used to fine-tune the influence of $B_{i,j}^{k}$ and $C_{i,j}^{k}$, respectively. $B_{i,j}^{k}$ corresponds to the average knowledge derived from the M best-known solutions achieved thus far over a wide range, while $C_{i,j}^{k}$ pertains to the personal best-known solutions of I instances.

The computational coefficients (α, β, and M) are assigned the values 0.1, 0.15, and 3, respectively, in alignment with the original paper introducing the CSA algorithm (Feng et al., 2021).

Reflective learning operator: In addition to gaining insights from the top-performing candidate solutions, the staff also has the opportunity to access novel information by consolidating its expertise in the opposite direction, as detailed in the equations below.

$$v_{i,j}^{k+1} = \begin{cases} r_{i,j}^{k+1} & if\left(u_{i,j}^{k+1} \geq c_j\right) \\ p_{i,j}^{k+1} & if\left(u_{i,j}^{k+1} < c_j\right) \end{cases}, i \in [1,I], j \in [1,J], k \in [1,K] \quad (6)$$

$$r_{i,j}^{k+1} = \begin{cases} \emptyset\left(\bar{x}_j + \underline{x}_j - u_{i,j}^{k+1}, c_j\right) & if\left(\left|u_{i,j}^{k+1} - c_j\right| < \emptyset(0,1).\left|\bar{x}_j - \underline{x}_j\right|\right) \\ \emptyset\left(\underline{x}_j, \bar{x}_j + \underline{x}_j - u_{i,j}^{k+1}\right) & \text{otherwise} \end{cases} \quad (7)$$

$$p_{i,j}^{k+1} = \begin{cases} \emptyset\left(c_j, \bar{x}_j + \underline{x}_j - u_{i,j}^{k+1}\right) & if\left(\left|u_{i,j}^{k+1} - c_j\right| < \emptyset(0,1).\left|\bar{x}_j - \underline{x}_j\right|\right) \\ \emptyset\left(\bar{x}_j + \underline{x}_j - u_{i,j}^{k+1}, \bar{x}_j\right) & \text{otherwise} \end{cases} \quad (8)$$

$$c_j = \left(\bar{x}_j + \underline{x}_j\right).0.5 \quad (9)$$

where $v_{i,j}^{k+1}$ is the j^{th} value of the i^{th} reflective solution at the $(k+1)^{th}$ cycle.

Internal competition operator: The team consistently retains staff members exhibiting superior performance, thereby facilitating a gradual improvement in their competitive edge within the market. This preservation is ensured through the following expression.

$$x_{i,j}^{k+1} = \begin{cases} u_{i,j}^{k+1} & if\left(F\left(\boldsymbol{u}_i^{k+1}\right) \leq F\left(\boldsymbol{v}_i^{k+1}\right)\right) \\ v_{i,j}^{k+1} & if\left(F\left(\boldsymbol{u}_i^{k+1}\right) > F\left(\boldsymbol{v}_i^{k+1}\right)\right) \end{cases}, i \in [1,I], j \in [1,J], k \in [1,K] \quad (10)$$

where $F(\boldsymbol{x})$ represents the fitness value of the solution $\boldsymbol{x}$.

Pseudo code of the CSA can be observed in Algorithm 1. Here, the algorithm initiates by establishing the population size, defining the applicable boundaries, and initializing the iteration count. Subsequently, the designated objective function, outlined in section 4, is specified. The initial candidates are generated randomly, from which the initial solutions are derived. Key positions, including the personal best position, are determined

by utilizing CSA's operators. It is at this juncture that the essential boundary verification procedure is implemented. Ultimately, the updated versions of global best and personal best solutions are ascertained by employing reflective learning and internal competition operators. The algorithm exports the global best-known solution upon reaching the maximum iteration count.

Algorithm 1. *Pseudo Code of the CSA.*

Initialize

Define initial parameters and objective function.

Generate random population in the practicable space.

Calculate the fitness of the initial randomly generated solutions.

Set t = 0

Set max iteration

while t < max iteration **do**

for each solution in the population **do**

Apply team communication operator using Eqs. (3-5)

Calculate group solution $u_{i,j}$

Update the $u_{i,j}^{k+1}$ position.

Apply reflective learning operator.

if $\frac{\left|u_{i,j}^{k+1}-c_j\right|}{\left|\bar{x}_j-\underline{x}_j\right|} < \emptyset(0,1)$ **then**

Determine $r_{i,j}^{k+1}$ and $p_{i,j}^{k+1}$ according to Eq. (7) and (8).

end if

if $u_{i,j}^{k+1} \geq c_j$ **then**

Determine $v_{i,j}^{k+1}$ according to Eq. (6).

end if

Perform boundary check.

Apply internal competition operator.

if $F(\boldsymbol{u}_i^{k+1}) \leq F\left(\boldsymbol{v}_i^{k+1}\right)$ **then**

Determine $x_{i,j}^{k+1}$ according to Eq. (10).

end if

end for

Update the personal best-known solutions from the initial population.

Update the global best-known solutions.

Increment *t* by 1.

if t >= max_iteration **then**

Export the global best-known solution.

end if

end while

2.2. Opposition-Based Learning

OBL is a widely recognized methodology that bolsters the exploration capacities of metaheuristic algorithms, as detailed by Tizhoosh (2005). A set of potential positions is generated randomly to identify the optimal solution. However, when there's no prior information regarding the proximity of the initially chosen position *x* to the optimal solution, the journey towards reaching the desired best solution could be notably protracted. In cases where the initially selected solution appears to be distant from the optimal solution or is situated unfavorably, it becomes prudent to simultaneously explore all directions, or more effectively, the direction opposite to the current position – a notion that aligns logically. The fundamental premise of OBL revolves around approaching the optimal solution by concurrently considering both the original value of the current position *x* and its opposite position $\overline{x}$.

Consider *x* as a real number confined within the interval of $[L, U]$. In a one-dimensional spatial context, the term 'opposite' denoted as $\overline{x}$ is defined as follows:

$$\overline{x} = U + L - x \tag{11}$$

For *n*-dimensional space, consider $x_i \in [L_i, U_i]$, and $i = 1,2, \dots, n$. In this case, $\overline{x}$ is defined as follows,

$$\bar{x}_i = U_i + L_i - x_i \tag{12}$$

Upon the random generation or recent update of all *x* positions, the corresponding opposing positions $\overline{x}$ are concurrently computed. Subsequently, the fitness evaluation is performed for both groups of positions (*x* and $\overline{x}$), identifying the most optimal positions. This iterative process progressively narrows the proximity to the optimal solution with each iteration.

2.3. Pattern Search Algorithm

Pattern Search (PS) techniques involve identifying successful search point patterns from recent history and leveraging this knowledge to forecast potentially fruitful search points in forthcoming iterations. These methods fall within the purview of direct search techniques, encompassing algorithms like the Simplex algorithm (Torczon, 1997). In this context, the Multidirectional Search (MDS) algorithm, a variant of the pattern search approach, was introduced by Torczon (1989) to tackle unconstrained minimization problems. The MDS algorithm excels at pinpointing optimal solutions by maintaining the most promising prior vertex and simultaneously conducting line searches in various directions, thereby accumulating valuable exploratory data. The flowchart illustrating the PS algorithm is depicted in Figure 1.

In this algorithm, the procedure begins with selecting the initial simplex, denoted as S_0, alongside expansion and contraction factors μ and θ. In each iteration, a search is executed from the current best vertex v_0^k, along each of the 'n' directions established by the edges connected to v_0^k. The primary objective of this search is to identify a fresh vertex boasting a function value lower than that of v_0^k. The algorithm proceeds with the reflection step if such a vertex is located. If not, it proceeds with the contraction step. During contraction, the algorithm continues until the condition $f(c_i^k) < f(v_0^k)$ is met. At this juncture, the current vertex is swapped with c_i^k, which exhibits a lower function value.

Conversely, in the expansion step, the algorithm computes $f(e_i^k)$ and compares it with $f(c_i^k)$. Depending on the outcome of this comparison, the algorithm decides to replace v_i^k with either the expansion vertex e_i^k or the reflection vertex r_i^k. The parameters θ, ρ, and μ, governing the lengths of the steps relative to the original simplex edges, play a pivotal role in these steps. For this implementation, θ, ρ, and μ, values are assigned as 0.5, 1, and 2, respectively, as in (Hekimoğlu, 2023). Additionally, a tolerance value crucial for algorithm termination and an initial step size required for generating the first simplex and are set to 10^{-5} and 0.05, respectively (Hekimoğlu, 2023).

Termination of the PS algorithm transpires either when the iteration count equals the stipulated maximum iteration count (set at 50 in this scenario) or when the difference between the worst and best solutions, referred to as the "distance," becomes smaller than the tolerance value.

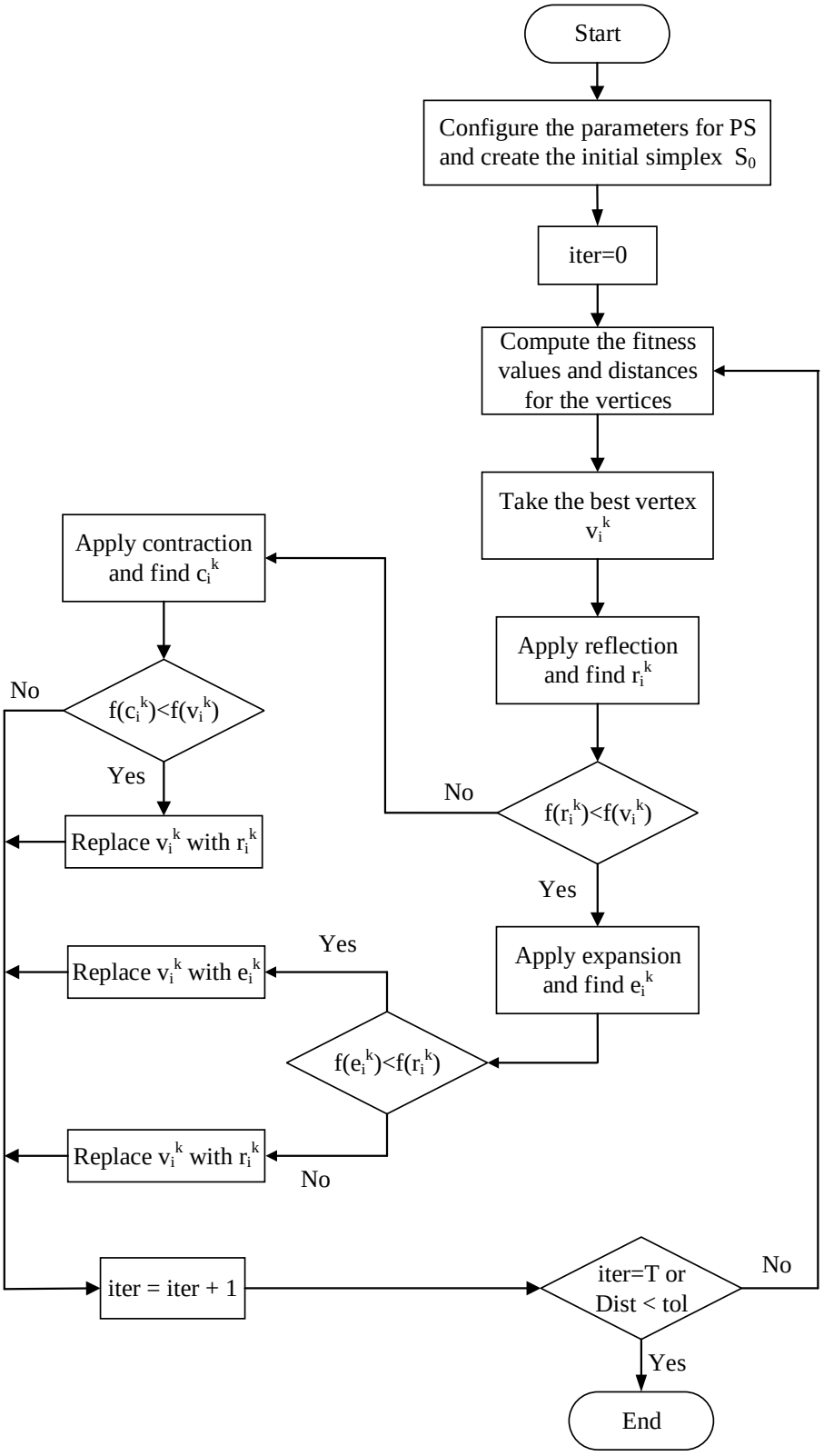

Figure 1. *Flowchart of PS algorithm.*

2.4. Proposed OCSAPS Algorithm

While CSA exhibits superior overall performance compared to various traditional evolutionary algorithms (Feng et al., 2021), it's important to note that certain limitations are highlighted in (Feng et al., 2022). These limitations signify potential areas for enhancement. In the CSA approach, the reduction in staff variation gradually occurs over iterations, which might lead to premature convergence issues during the global search phase (Feng et al., 2022). To address this concern, an effective strategy involves integrating the OBL mechanism into CSA.

In the proposed hybrid algorithm named OCSAPS, this OBL mechanism introduces the capability to explore opposite directions within the global search space. This enhancement subsequently heightens the likelihood of discovering improved local search regions. Additionally, the proposed approach incorporates the PS algorithm to enhance its exploitation capabilities further. A visual representation of the OCSAPS algorithm's process can be found in Figure 2.

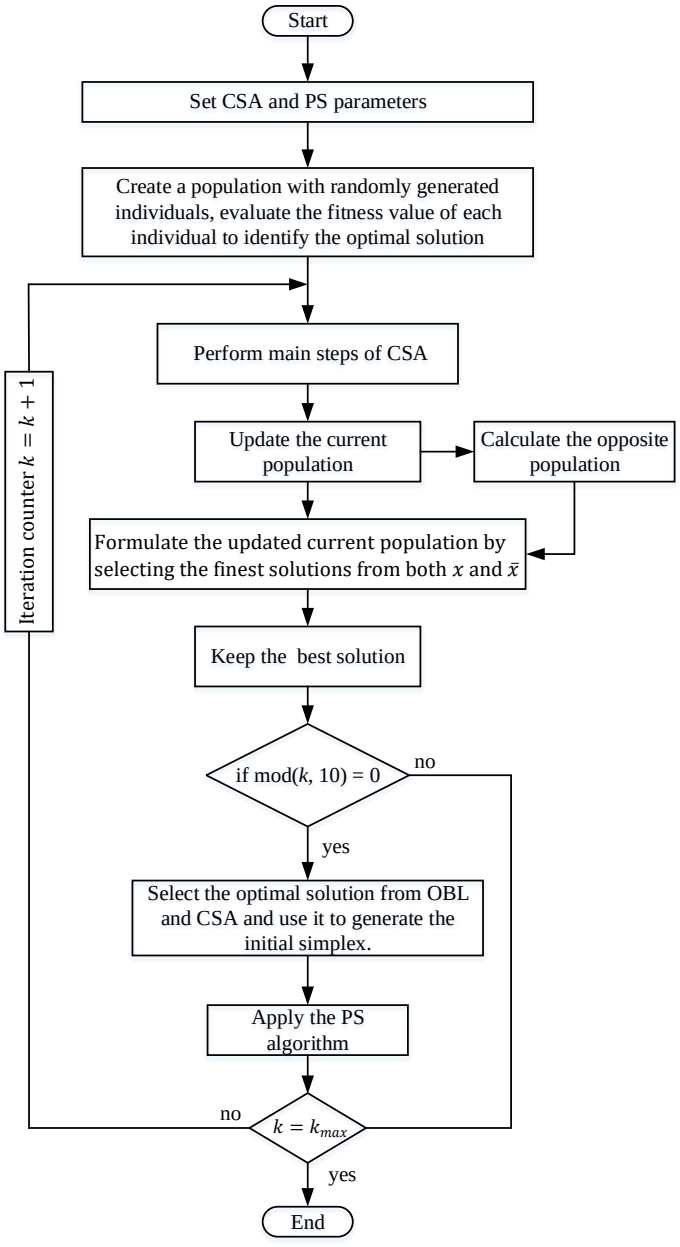

Figure 2. *Flowchart of the proposed OCSAPS algorithm.*

3. BUCK CONVERTER SYSTEM WITH FOPID CONTROLLER

3.1. Mathematical Model of the Buck Converter

The DC-DC buck converter functions as a time-variant nonlinear switching circuit. Given its inherent nonlinearity, deriving a linearized model becomes imperative when designing a linear controller. Circuit or state-space averaging techniques are typically employed to achieve this linearized model (Erickson & Maksimović, 2000). The circuit diagram for the DC-DC buck converter is depicted in Figure 3.

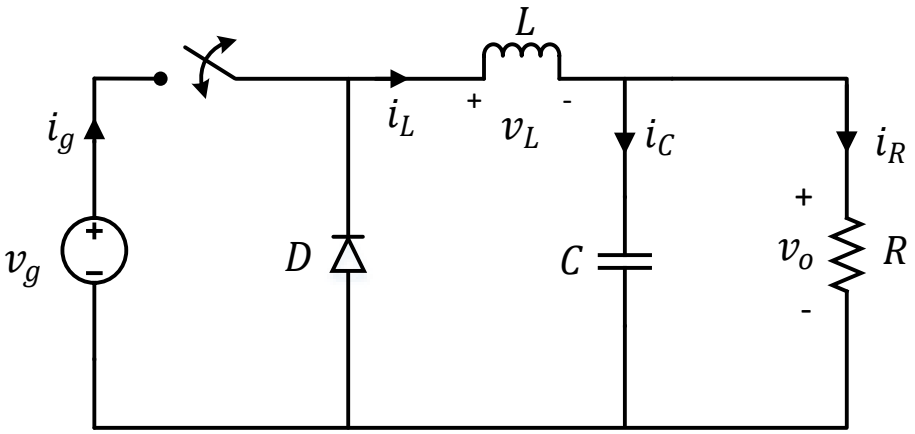

Figure 3*. DC-DC buck converter.*

In the pursuit of linearization, a method called the switching signal-flow graph (SSFG) (Smedley & Cuk, 1994), based on state-space averaging, is utilized. This approach facilitates the computation of small-signal transfer functions required for controller design. The SSFG method employs visual representation to simplify deriving small-signal models for switching converters. The SSFG for the DC-DC buck converter is presented in Figure 4.

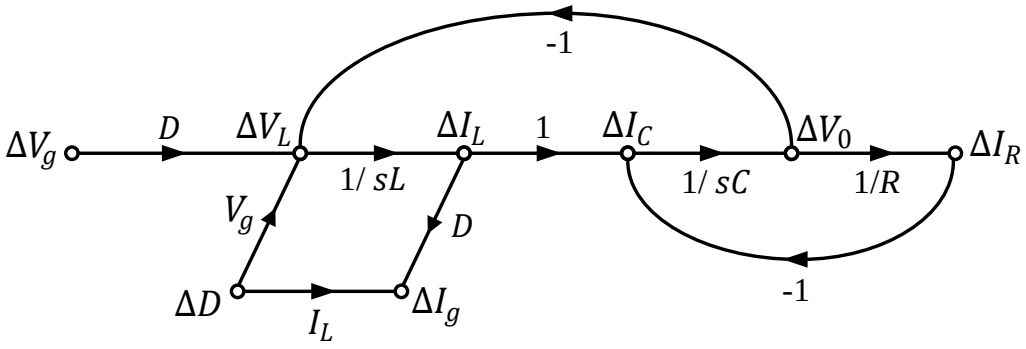

Figure 4. *Small-signal model of DC-DC buck converter with SSFG method.*

Eq. (15) gives the transfer function from control to output, which stems from the small-signal model of the buck converter illustrated in Figure 4.

$$G_{vd}(s) = \frac{\Delta V_o(s)}{\Delta D(s)} = \frac{V_g/LC}{s^2 + s/RC + 1/LC} \tag{15}$$

where V_g stands for the input voltage, D denotes the duty cycle, L signifies the inductance, C represents the capacitance, and R denotes the load resistance. The step response of the open-loop buck converter, employing the parameters detailed in Table 1, is illustrated in Figure 5.

Table 1. *Buck converter parameters.*

Parameters	Values
V_g	36 V
D	1/3
V_{ref}	12 V
L	1 mH
C	100 µF
R	6 Ω
f	40 kHz

A brief examination of Figure 5 immediately reveals that the step response of the buck converter, lacking a controller, falls short of the desired ideal behavior. It displays significant overshoot, an extended settling period, and a prolonged duration to attain a stable state. Integrating a controller into the buck converter system becomes imperative to rectify these unfavorable traits within the converter's transient response. In this instance, a fractional order proportional integral derivative (FOPID) controller will be implemented to enhance the aforementioned transient response attributes.

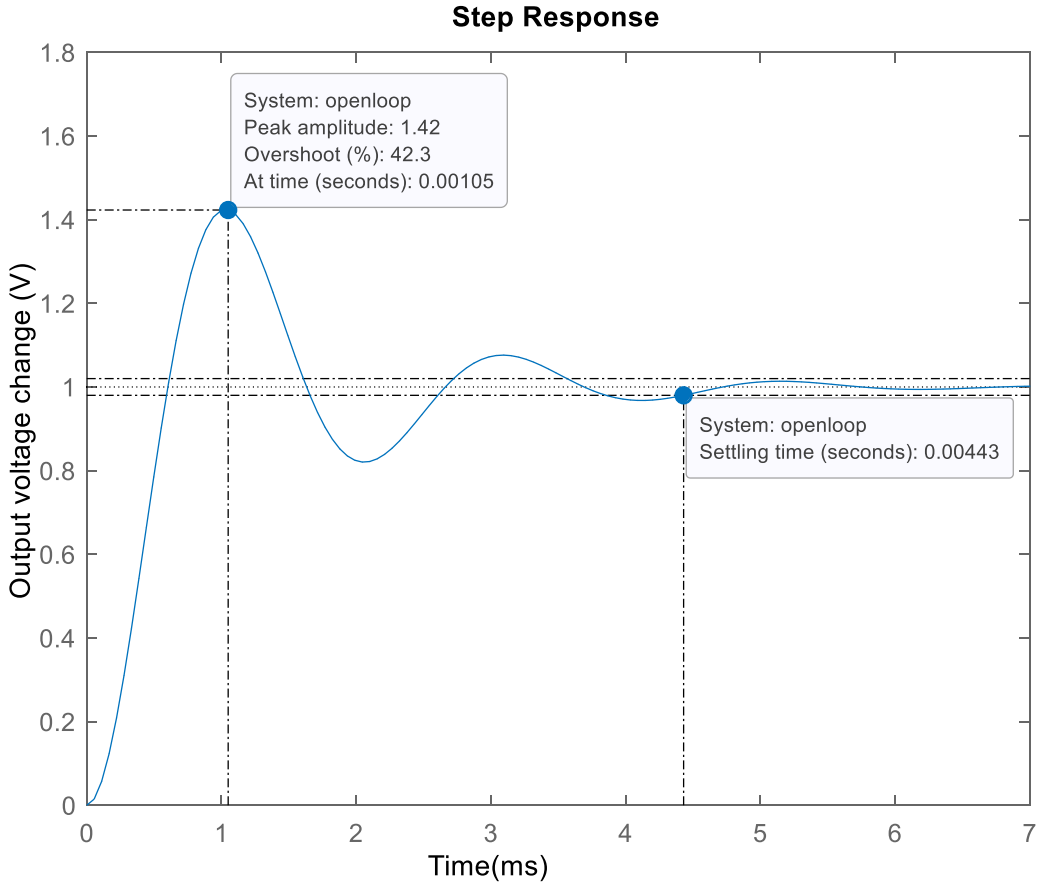

Figure 5. *Open-loop response of the buck converter system.*

3.2. Fractional Order PID (FOPID) Controller

The FOPID controller represents a broader version of the conventional PID controller, specifically designed to accommodate fractional orders. It was initially introduced by Podlubny (1999). This controller incorporates two auxiliary parameters, namely λ and μ, which correspond to the fractional orders associated with the integral and derivative terms, respectively. These parameters introduce increased versatility and enhanced robustness. Fractional-order controllers, including fractional PID controllers, are acknowledged for delivering superior control performance in nonlinear systems featuring intricate dynamics, surpassing the capabilities of conventional integer-order controllers, as demonstrated in (Martinez-Patiño et al., 2023). They additionally provide enhanced adaptability when fine-tuning the controller's response to diverse system types attributed to the fractional derivative and proportional parameters at their disposal (Mohd Tumari et al., 2023). The transfer function of the FOPID controller is given in Eq. (16).

$$K_p + \frac{K_i}{s^{\lambda}} + K_d s^{\mu} \tag{16}$$

where K_p, K_i, and K_d represent the proportional, integral, and derivative gains, respectively. Compared to a PID controller, FOPID incorporates two supplementary parameters, offering enhanced precision in fine-tuning the controller's behavior and thereby bolstering the system's overall stability. Nonetheless, including these additional parameters demands a more intricate parameter adjustment process than a conventional PID controller. Moreover, implementing FOPID controllers presents specific challenges, such as memory requirements. As non-integer integrators and differentiators necessitate an infinite memory capacity, conventional methods are inadequate for executing non-integer order controllers (Li & Zhao, 2015). Consequently, the efficient realization of FOPID controllers hinges on employing appropriate approximations. In the present scenario, the chosen approach is Oustaloup's approximation method (Oustaloup et al., 2000), which addresses the need for effective FOPID controller design.

Denote the frequency range as (ω_b, ω_h) where N represents the degree and $2N+1$ stands for the order of the approximation. The methodology proposed by Oustaloup for s^{α}, where $0 < \alpha < 1$, is derived and detailed in Equations (16) and (17).

$$G_f(s) = K \prod_{k=-N}^{N} \frac{s + \omega_k'}{s + \omega_k} \tag{16}$$

$$\omega_k' = \omega_b \left(\frac{\omega_h}{\omega_b}\right)^{\frac{k+N+\frac{1}{2}(1-\alpha)}{2N+1}}, \omega_k = \omega_b \left(\frac{\omega_h}{\omega_b}\right)^{\frac{k+N+\frac{1}{2}(1+\alpha)}{2N+1}}, K = \omega_h^{\alpha} \tag{17}$$

where K denotes the DC gain of the filter, ω_k' and ω_k represent the frequencies associated with the zeros and poles, respectively. For this study, an 11th order Oustaloup's approximation was adopted with N set at 5. This approximation was applied within the frequency range of $(10^{-3}, 10^{3})$ rad/s. As such, the lower and upper boundaries of this approximation, designated as ω_b and ω_h, respectively, were established as 10^{-3} rad/s and 10^{3} rad/s.

3.3. FOPID-Controlled Buck Converter System

Figure 6 illustrates the block diagram incorporating the FOPID controller to the buck converter. Additionally, the closed-loop transfer function for the buck converter system, enhanced by the FOPID controller, is defined by Eq. (18).

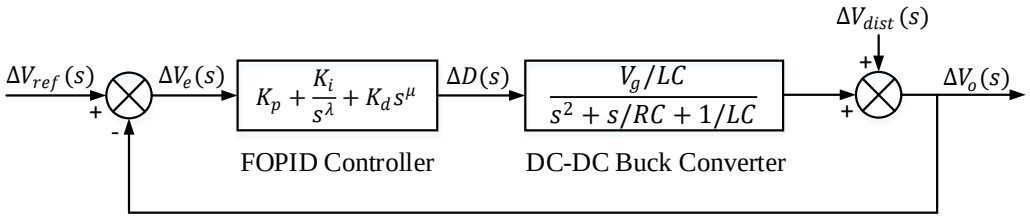

Figure 6. *FOPID-controlled buck converter system*

$$\frac{\Delta V_o(s)}{\Delta V_{ref}(s)} = \frac{G_{FOPID}(s)G_{Buck}(s)}{1 + G_{FOPID}(s)G_{Buck}(s)}, \Delta V_{dist}(s) = 0 \tag{18}$$

where $\Delta V_o(s)$, $\Delta V_{ref}(s)$, and $\Delta V_{dist}(s)$ denote changes in the output voltage, reference voltage, and disturbance voltage, respectively. The closed-loop transfer function for the FOPID-controlled buck converter is given in Eq. (19).

$$\frac{\Delta V_o(s)}{\Delta V_{ref}(s)} = \frac{\left(K_p s^\lambda + K_i + K_d s^{\lambda+\mu}\right)V_g/LC}{s^\lambda(s^2 + s/RC + 1/LC) + \left(K_p s^\lambda + K_i + K_d s^{\lambda+\mu}\right)V_g/LC} \tag{19}$$

The ranges within which the FOPID parameters are employed for this study are specified in Equation (20).

$$\begin{gathered} 1 \le K_p \le 50 \\ 0.01 \le K_i \le 10 \\ 0.001 \le K_d \le 0.02 \\ 0 \le \lambda, \mu \le 2 \end{gathered} \tag{20}$$

4. PERFORMANCE INDEX AND OBJECTIVE FUNCTION

The paramount objective in designing a control system is minimizing the error between the output and the reference value. This pursuit significantly contributes to the system's robustness and overall stability. Consequently, integral performance metrics are widely adopted to evaluate the performance of a controller (Boudjehem & Boudjehem, 2016). Various integral performance metrics have recently been applied to craft fractional-order control systems (Das et al., 2012; Pan & Liu, 2016; Eshaghi & Tavazoei, 2023; Ranjan & Mehta, 2023). From this assortment of performance metrics, the integral absolute error (IAE) will be utilized in this study to minimize the error mentioned above and subsequently enhance the output voltage of the buck converter.

The choice to utilize the IAE objective function arises from the observation that implementing this approach during the algorithmic process for determining the necessary parameters of the FOPID controller results in the most favorable outcomes.

$$IAE = \int_0^T |e(t)|\, dt \tag{21}$$

Eq. (21) provides the integral formulation of the aforementioned performance index. In this equation, $e(t)$ signifies the error arising from subtracting the closed-loop buck converter system's output voltage from its reference voltage. The simulation duration, denoted as *T*, is $5\text{x}10^{-6}$ seconds.

5. IMPLEMENTATION OF OCSAPS TO BUCK CONVERTER SYSTEM

Figure 7 presents a block diagram that depicts the integration of OCSAPS into the buck converter system. The diagram reveals that the FOPID controller parameters derived from OCSAPS dictate the buck converter system's output voltage. Subsequently, the output voltage is compared with the reference voltage, and the

objective is to minimize the error between these values to achieve the targeted system performance. The objective function plays a crucial role in minimizing this error, aiming to bring the comparison outcome as close to zero as possible.

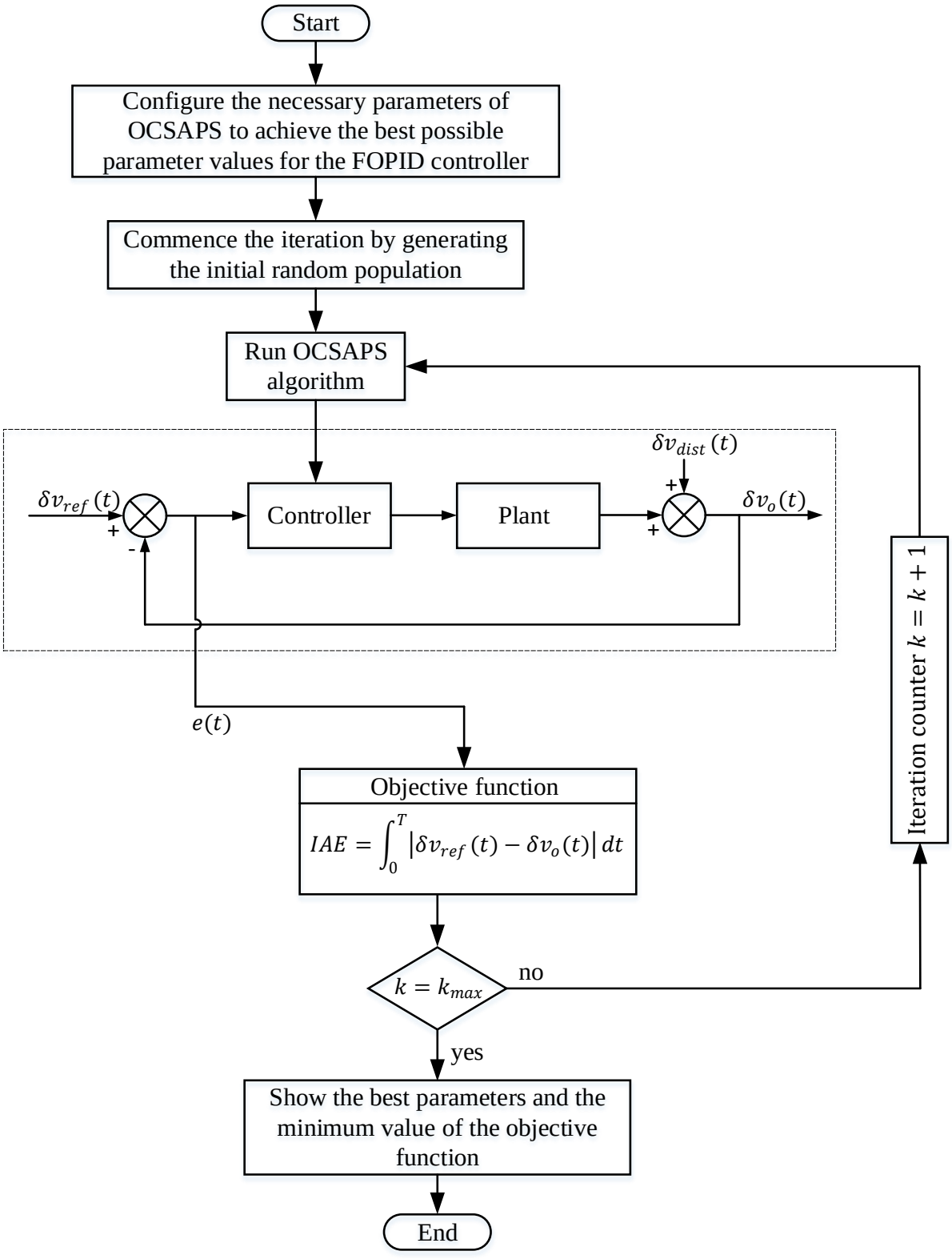

Figure 7. *Application of the OCSAPS algorithm to the FOPID-controlled buck converter system.*

6. SIMULATION RESULTS AND DISCUSSION

The proposed OCSAPS algorithm underwent a comparative analysis against several other algorithms: the original CSA (Feng et al., 2021) and two highly successful algorithms, HHO and GA, in controlling the buck converter system with the FOPID controller. The algorithms were executed with uniform settings: a maximum iteration count of 30 and 25 runs. Evaluations were conducted on a desktop computer equipped with an Intel Core i5 3.30 GHz processor and 16 GB of RAM. MATLAB software was the chosen platform for conducting the analyses.

6.1. Statistical Boxplot Analysis

A visual representation of the data distribution is presented through boxplot analysis for OCSAPS, CSA, HHO, and GA algorithms, offering readers a straightforward initial assessment. Statistical metrics encompassing best, mean, median variance, standard deviation, and worst (detailed in Table 2) underscore that the OCSAPS algorithm outperforms the original CSA and the other compared algorithms. The results depicted in Figure 8 illustrate how the OCSAPS algorithm attains notably lower values in terms of upper quartile, lower quartile, maximum score, median, and minimum score compared to the mentioned algorithms. This pattern suggests the superiority of the proposed OCSAPS approach over the other compared algorithms.

Table 2. *Statistical results of IAE objective function for the compared algorithms.*

Statistical metric	OCSAPS	CSA	HHO	GA
Best	$\mathbf{1.10979x10^{-7}}$	$1.15239x10^{-7}$	$1.14736x10^{-7}$	$1.18042x10^{-7}$
Mean	$\mathbf{1.11789x10^{-7}}$	$1.43149x10^{-7}$	$3.18071x10^{-7}$	$3.21815x10^{-7}$
Median	$\mathbf{1.11222x10^{-7}}$	$1.39617x10^{-7}$	$1.44622x10^{-7}$	$2.39439x10^{-7}$
Variance	$\mathbf{1.27131x10^{-18}}$	$2.62815x10^{-16}$	$6.28873x10^{-13}$	$5.68841x10^{-14}$
Standard deviation	$\mathbf{1.12753x10^{-9}}$	$1.62116x10^{-8}$	$7.93015x10^{-8}$	$2.38504x10^{-7}$
Worst	$\mathbf{1.14826x10^{-7}}$	$1.85696x10^{-7}$	$4.53744x10^{-6}$	$1.06497x10^{-6}$

6.2. Convergence Response

In Figure 9, the convergence extent of the objective function values achieved through the execution of the OCSAPS, CSA, HHO, and GA are displayed. It's important to note that due to the inherent stochastic nature of metaheuristic algorithms, not all runs produce identical outcomes. Accordingly, among the nearly 30 iterations of these algorithms, it becomes apparent that CSA, HHO, and GA consistently deliver less favorable outcomes than OCSAPS. This observation is substantiated by the insights derived from the statistical boxplot analysis depicted in Figure 8.

The data presented in Figure 9 underscores the significant impact of incorporating the OBL and pattern search techniques into CSA, resulting in a substantial improvement in discovering superior solutions at an accelerated pace.

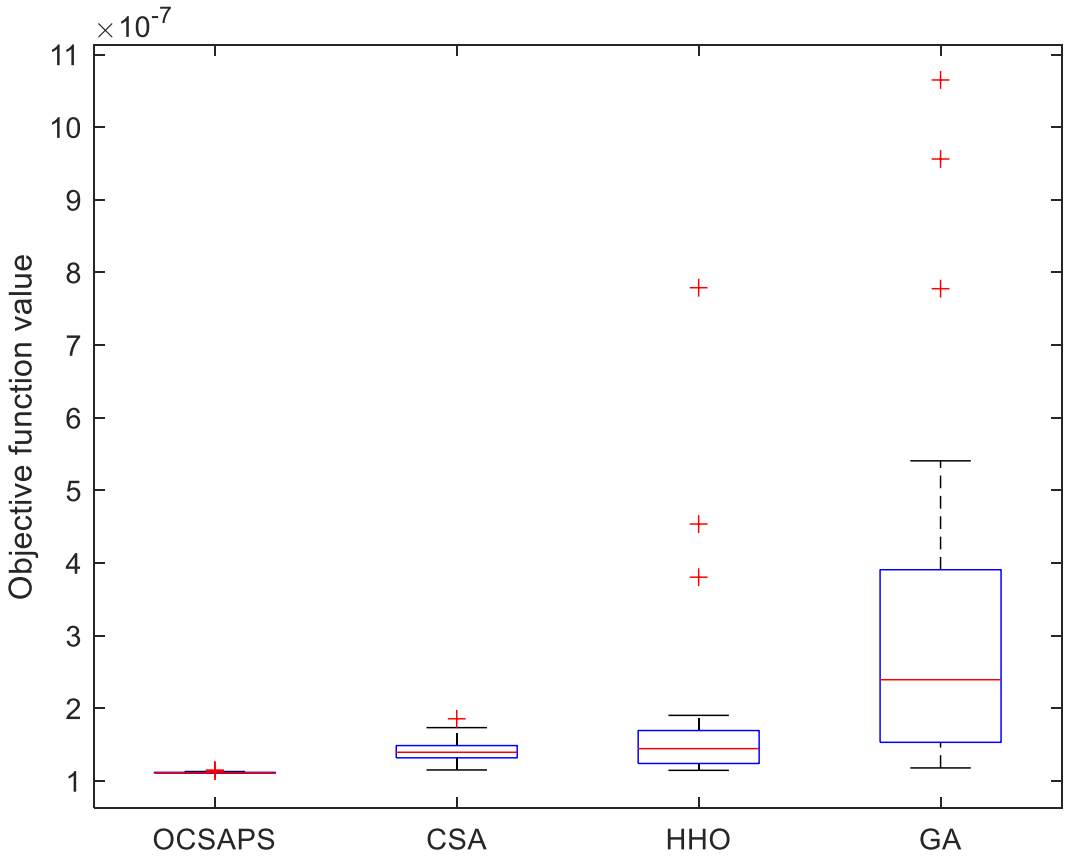

Figure 8. *Comparison of the proposed OCSAPS, CSA, HHO, and GA in terms of boxplot analysis.*

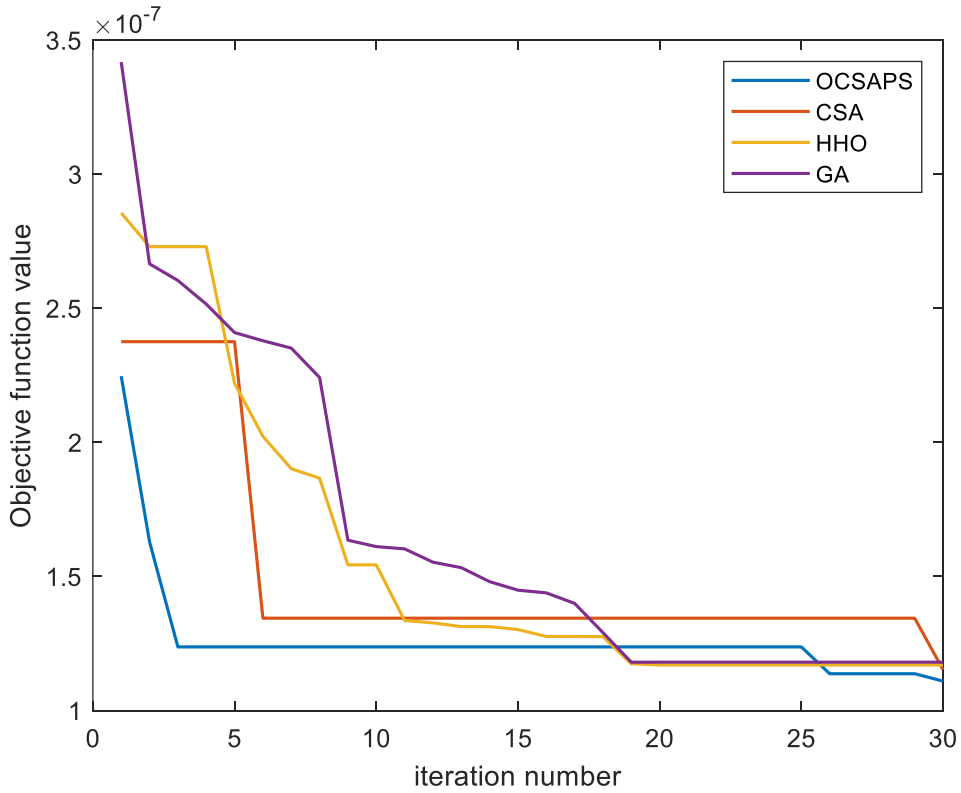

Figure 9. *Comparison of the proposed OCSAPS, CSA, HHO, and GA in terms of convergence behavior.*

Table 3 presents the optimal FOPID controller parameters achieved through the optimization process for compared algorithms that govern the buck converter system. Additionally, employing these parameters, the closed-loop transfer functions of the integrated system have been calculated, as denoted by Eqs. (22), (23), (24), and (25).

Table 3. *Optimal FOPID controller parameters of compared algorithms.*

FOPID parameter	OCSAPS	CSA	HHO	GA
K_p	28.4424	32.4591	18.0622	28.5346
K_i	9.3765	0.5960	1.6709	3.8269
K_d	0.01	0.00841	0.009924	0.0097
μ	1.0522	1.0553	0.6094	0.2620
λ	1.1231	1.1146	1.0972	1.0959

$$\mathrm{G_{OCSAPS}}(s) = \frac{0.36s^{2.1753} + 1023.9s^{1.0522} + 337.55}{10^{-7}s^{3.0522} + 0.36s^{2.1753} + 0.0001667s^{2.0522} + 1024.9s^{1.0522} + 337.55} \tag{22}$$

$$\mathrm{G_{CSA}}(s) = \frac{0.30276s^{2.1699} + 1168.5s^{1.0553} + 21.456}{10^{-7}s^{3.0553} + 0.30276s^{2.1699} + 0.0001667s^{2.0553} + 1169.5s^{1.0553} + 21.456} \tag{23}$$

$$\mathrm{G_{HHO}}(s) = \frac{0.35726s^{1.7066} + 650.24s^{0.6094} + 60.152}{10^{-7}s^{2.6094} + 0.35726s^{1.7066} + 0.0001667s^{1.6094} + 651.24s^{0.6094} + 60.152} \tag{24}$$

$$\mathrm{G_{GA}}(s) = \frac{0.3492s^{1.3579} + 1027.2s^{0.262} + 137.77}{10^{-7}s^{2.262} + 0.3492s^{1.3579} + 0.0001667s^{1.262} + 1028.2s^{0.262} + 137.77} \tag{25}$$

6.3. Transient Response Analysis

Figure 10 illustrates a comparison of the unit step responses for the buck converter system employing different algorithms with FOPID controller. The comparison is conducted using the proposed OCSAPS, CSA, HHO, and GA algorithms. Additionally, a comparison of the transient response performance of systems based on these algorithms is presented in Table 4. Both the figure and the table collectively demonstrate that the FOPID-controlled buck converter system using the proposed OCSAPS algorithm exhibits the quickest rise time, settling time, and peak time compared to the other algorithms under consideration.

This observation implies that the FOPID-controlled buck converter system, utilizing the proposed OCSAPS algorithm, achieves superior operational efficiency compared to the algorithms mentioned earlier.

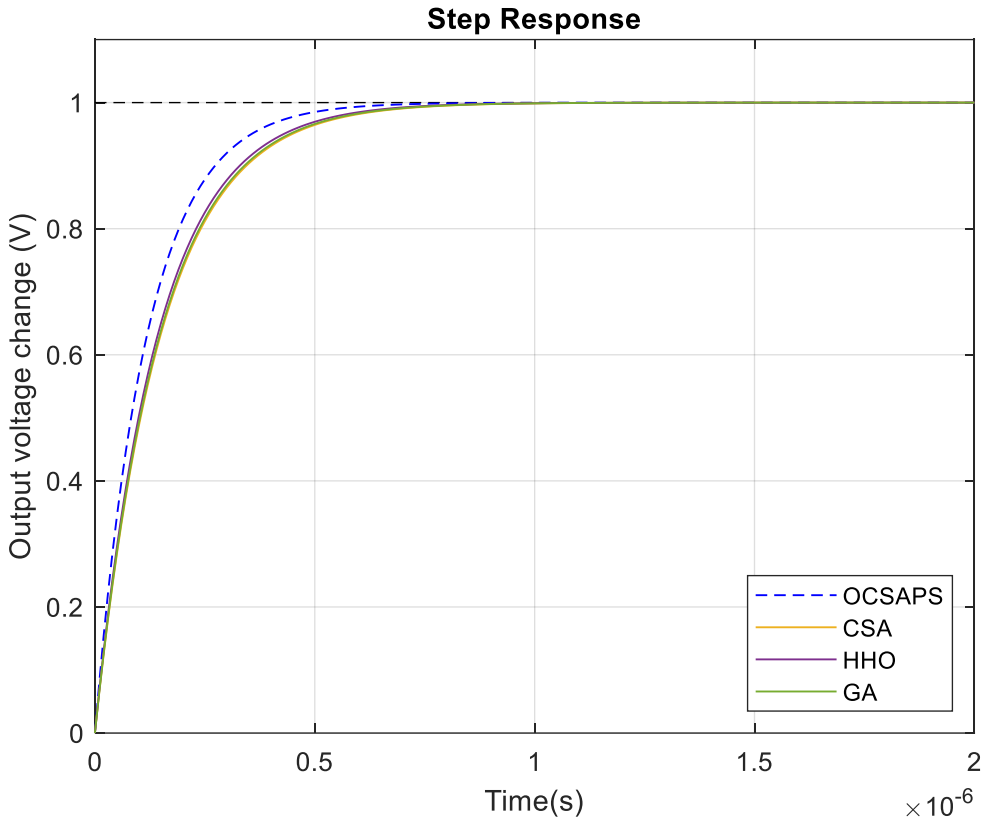

Figure 10. *Transient response comparison of FOPID controllers for different algorithms.*

Table 4. *Transient response metrics of compared algorithms.*

Controller type	Maximum overshoot (%)	Rise time (s)	Settling time (s)	Peak time (s)
OCSAPS-FOPID	0	**$2.6081\text{x}10^{-7}$**	**$4.6467\text{x}10^{-7}$**	**$6.8863\text{x}10^{-7}$**
CSA-FOPID	0	$3.2880\text{x}10^{-7}$	$5.8550\text{x}10^{-7}$	$8.6839\text{x}10^{-7}$
HHO-FOPID	0	$3.1434\text{x}10^{-7}$	$5.6030\text{x}10^{-7}$	$8.2980\text{x}10^{-7}$
GA-FOPID	0	$3.2441\text{x}10^{-7}$	$5.7781\text{x}10^{-7}$	$8.5670\text{x}10^{-7}$

6.4. Frequency Response Analysis

Figure 11 illustrates the Bode plots for the buck converter system employing the OCSAPS algorithm proposed in this study. These plots are compared with those of the original CSA, HHO, and GA-based systems. In addition, Table 5 provides performance metrics in the frequency domain, including gain margin, phase margin, and bandwidth. The findings from the presented figure and table indicate that the system utilizing the proposed algorithm boasts a considerably broader bandwidth and phase margin than other systems mentioned. Consequently, the proposed algorithm-based system exhibits improved stability when compared against the other systems under comparison.

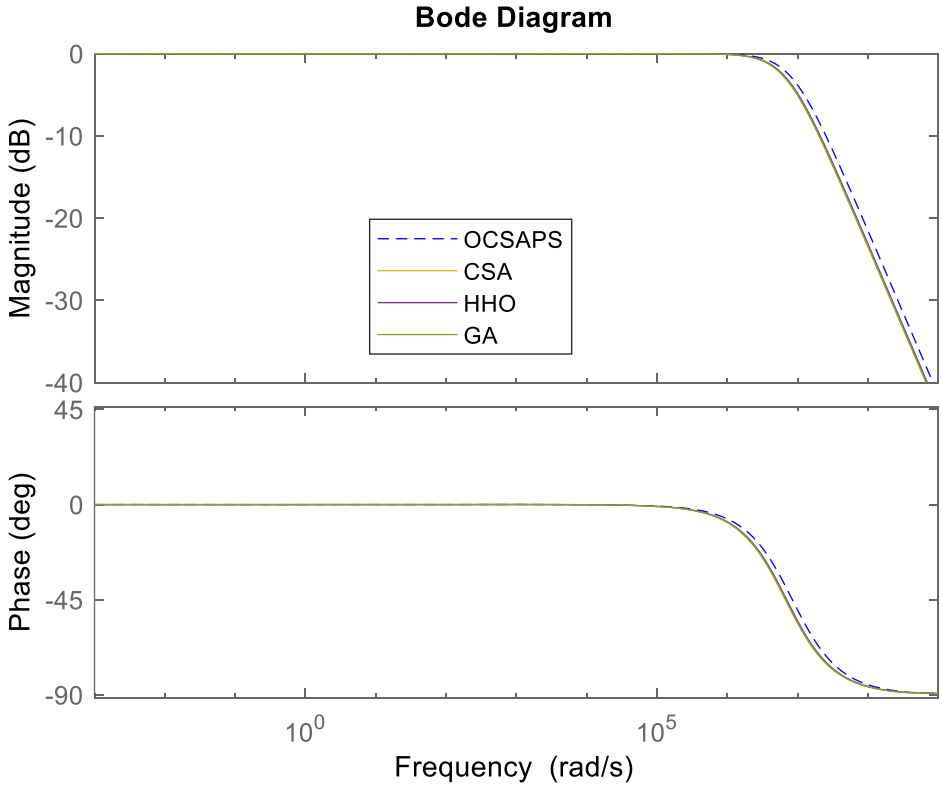

Figure 11. *Closed-loop frequency responses of FOPID-controlled systems under comparison.*

Table 5. *Comparison of frequency response metrics of different algorithms.*

Controller type	Gain margin (dB)	Phase margin (deg)	Bandwidth (Hz)
OCSAPS-FOPID	**Inf.**	**89.9970**	**8.4051×10^6**
CSA-FOPID	**Inf.**	89.9882	6.6660×10^6
HHO-FOPID	**Inf.**	1.1785	6.9774×10^6
GA-FOPID	**Inf.**	0.9419	6.7639×10^6

6.5. Comparison of Performance Indices

Other than the previously mentioned IAE presented in Eq. (21), several commonly employed performance measures exist. These include the integral of time-weighted squared error (ITSE), integral of time-weighted absolute error (ITAE), integral of squared error (ISE), and the time domain performance metric ZLG (Hekimoğlu, 2019), which was introduced by Gaing (2004). These metrics further highlight the exceptional performance of the proposed OCSAPS algorithm-based buck converter system. The formulations for these performance measures are provided in Eqs. (26), (27), (28), and (29) respectively.

$$ISE = \int_0^T \left(\delta v_{ref}(t) - \delta v_o(t)\right)^2 dt \tag{26}$$

$$ITAE = \int_0^T t\left|\delta v_{ref}(t) - \delta v_o(t)\right| dt \tag{27}$$

$$ITSE = \int_0^T t\left(\delta v_{ref}(t) - \delta v_o(t)\right)^2 dt \tag{28}$$

$$ZLG = (1 - e^{-\rho})\left(M_p + E_{ss}\right) + e^{-\rho}(T_s - T_r) \tag{29}$$

where T represents the simulation duration, set at 5 microseconds, while δv_{ref} signifies the change in reference voltage and δv_o denotes the change in output voltage, the weighting coefficient is represented as ρ, M_p stands for the maximum overshoot, E_{ss} represents the steady-state error, T_s indicates the settling time, and T_r signifies the rise time. Minimizing these performance measures translates to enhanced robustness and stability for the buck converter system. Consequently, lower values correspond to heightened system stability. As shown in Table 6, the buck converter system based on the proposed OCSAPS algorithm boasts the smallest values across all the aforementioned performance measures. Once again, this underscores the system's superiority driven by the proposed algorithm.

Table 6. *Performance indices of compared algorithms.*

Controller type	ZLG	IAE	ISE	ITAE	ITSE
OCSAPS-FOPID	$\mathbf{2.1929x10^{-7}}$	$\mathbf{1.1888x10^{-7}}$	$\mathbf{5.9487x10^{-8}}$	$\mathbf{1.4212x10^{-14}}$	$\mathbf{3.5142x10^{-15}}$
CSA-FOPID	$2.7182x10^{-7}$	$1.4972x10^{-7}$	$7.4941x10^{-8}$	$2.2399x10^{-14}$	$5.5912x10^{-15}$
HHO-FOPID	$2.6165x10^{-7}$	$1.4329x10^{-7}$	$7.1637x10^{-8}$	$2.0682x10^{-14}$	$5.1082x10^{-15}$
GA-FOPID	$2.6865x10^{-7}$	$1.4776x10^{-7}$	$7.3939x10^{-8}$	$2.1853x10^{-14}$	$5.4423x10^{-15}$

6.6. Robustness Analysis

A crucial aspect of a controller's effectiveness lies in its ability to withstand unforeseen scenarios, such as alterations in component values within the system due to environmental factors like temperature fluctuations, humidity changes, and gradual degradation over time. With this consideration in mind, variations in the inductor and capacitor values have been introduced in four distinct cases, outlined in Table 7, to assess the transient response characteristics of the system in response to the perturbations mentioned above. For comparison, the same changes in component values have been applied to the other three algorithm-based systems against which the proposed OCSAPS approach has been benchmarked so far.

Table 8 provides a comprehensive overview of the transient response metrics obtained by implementing said cases on the various algorithm-driven FOPID-controlled systems being evaluated. Across all instances, the buck converter system controlled by the proposed OCSAPS method consistently exhibits the shortest rise time, settling time, and peak time. Notice the robustness shortcomings of HHO in the case of increasing C by 20% and of GA in the case of decreasing L by 20 %. This illustrates that the proposed approach imparts greater robustness and stability to the buck converter system than other algorithm-based counterparts. These results further validate and reinforce the superiority of the proposed algorithm in this context.

Table 7. *Impacts of altering system parameters on the transient response across different algorithms.*

Case	Algorithm	Maximum overshoot (%)	Rise time (s)	Settling time (s)	Peak time (s)
Increasing *C* by %20	OCSAPS	0	**$3.1294\text{x}10^{-7}$**	**$5.5743\text{x}10^{-7}$**	**$8.4051\text{x}10^{-7}$**
	CSA	0	$3.9451\text{x}10^{-7}$	$7.0222\text{x}10^{-7}$	$10.421\text{x}10^{-7}$
	HHO	0	$1.7651\text{x}10^{-4}$	$2.1623\text{x}10^{-4}$	$2.2056\text{x}10^{-4}$
	GA	0	$3.8924\text{x}10^{-7}$	$6.9304\text{x}10^{-7}$	$10.281\text{x}10^{-7}$
Decreasing *C* by %20	OCSAPS	0	**$2.0866\text{x}10^{-7}$**	**$3.7185\text{x}10^{-7}$**	**$5.5089\text{x}10^{-7}$**
	CSA	0	$2.6308\text{x}10^{-7}$	$4.6866\text{x}10^{-7}$	$6.9468\text{x}10^{-7}$
	HHO	0	$2.5149\text{x}10^{-7}$	$4.4387\text{x}10^{-7}$	$6.6383\text{x}10^{-7}$
	GA	0	$2.5957\text{x}10^{-7}$	$4.6248\text{x}10^{-7}$	$6.8533\text{x}10^{-7}$
Increasing *L* by %20	OCSAPS	0	**$3.1298\text{x}10^{-7}$**	**$5.5769\text{x}10^{-7}$**	**$8.2634\text{x}10^{-7}$**
	CSA	0	$3.9457\text{x}10^{-7}$	$7.0261\text{x}10^{-7}$	$10.421\text{x}10^{-7}$
	HHO	0	$3.7724\text{x}10^{-7}$	$6.7255\text{x}10^{-7}$	$9.9574\text{x}10^{-7}$
	GA	0	$3.8930\text{x}10^{-7}$	$6.9342\text{x}10^{-7}$	$10.280\text{x}10^{-7}$
Decreasing *L* by %20	OCSAPS	0	**$2.0864\text{x}10^{-7}$**	**$3.7167\text{x}10^{-7}$**	**$5.5091\text{x}10^{-7}$**
	CSA	0	$2.6034\text{x}10^{-7}$	$4.6840\text{x}10^{-7}$	$6.9471\text{x}10^{-7}$
	HHO	0	$2.5146\text{x}10^{-7}$	$4.4811\text{x}10^{-7}$	$6.6386\text{x}10^{-7}$
	GA	0	$2.1954\text{x}10^{-4}$	$2.6894\text{x}10^{-4}$	$2.7433\text{x}10^{-4}$

Apart from the effects of changes in component values on the output of the system, trajectory tracking performance has also been examined. Figure 12 provides performance comparison of different algorithms against output voltage change. At 2 ms and 4 ms, the output voltage has been changed by -25% and +25%, respectively, to see the trajectory tracking performance of the compared algorithms. Similar to Figure 10, the proposed approach-based controller performs better than the other algorithm-based controllers, which also validates its superior capability in terms of robustness.

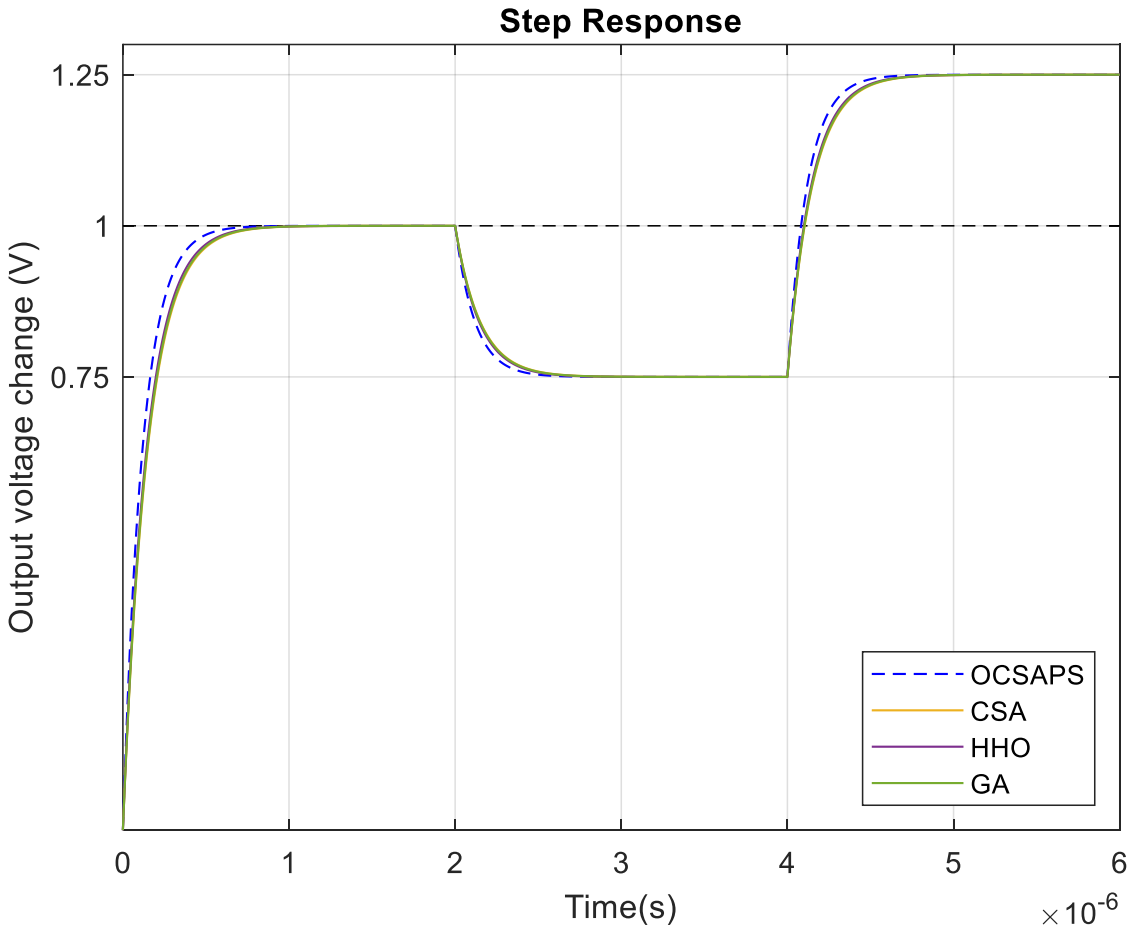

Figure 12. Trajectory tracking comparison for different algorithms against output voltage change.

6.7. Comparison with the Published Works

Numerous algorithms based on metaheuristic techniques can be found in existing literature. These algorithms aim to manage a buck converter system effectively, ensuring favorable stability and robustness outcomes. Many of these methodologies have demonstrated commendable achievements in this endeavor. In this context, the suggested approach involving the OCSAPS algorithm for FOPID-controlled buck converter systems was evaluated alongside other algorithms listed in Table 8.

Table 8 comprehensively compares the proposed algorithm and other methods previously presented in the relevant domain. This evaluation encompasses diverse metrics associated with transient response, encompassing overshoot, rise time, settling time, and peak time, along with frequency response parameters like gain margin, phase margin, and bandwidth. The analysis underscores that, except in phase margin, the proposed algorithm outperforms these previously published approaches across both transient and frequency response criteria. As such, the data presented in Table 8 distinctly substantiates the proposed algorithm's superior performance compared to its counterparts.

Table 8. *Comparison of transient and frequency response measures of some of the most effective algorithms for FOPID controllers documented in the literature.*

Controller type	Maximum overshoot (%)	Rise time (s)	Settling time (s)	Peak time (s)	Gain margin (dB)	Phase margin (deg)	Bandwidth (Hz)
OCSAPS-FOPID	**0**	**$2.6081x10^{-7}$**	**$4.6467x10^{-7}$**	**$6.8863x10^{-7}$**	**Inf.**	89.9970	**$8.4051x10^{6}$**
CSA-FOPID	**0**	$3.2880x10^{-7}$	$5.8550x10^{-7}$	$8.6839x10^{-7}$	**inf.**	89.9882	$6.6660x10^{6}$
IHGS-FOPID (Izci & Ekinci, 2022)	**0**	$2.8510x10^{-7}$	$5.0765x10^{-7}$	$1.3686x10^{-6}$	**Inf.**	89.9995	$7,6879x10^{6}$
LFDSA-FOPID (Izci et al., 2022a)	**0**	$3.5068x10^{-7}$	$6.2519x10^{-7}$	$1.6823x10^{-6}$	**Inf.**	**90.0081**	$6.2520x10^{6}$
LFD-FOPID (Izci et al., 2022a)	**0**	$4.0260x10^{-7}$	$7.1709x10^{-7}$	$1.9322x10^{-6}$	**Inf.**	90.0020	$5.4445x10^{6}$
ABC-FOPID (Izci et al., 2022a))	**0**	$4.2808x10^{-7}$	$7.6297x10^{-7}$	$2.0539x10^{-6}$	**Inf.**	90.0063	$5.1212x10^{6}$
PSO-FOPID (Izci et al., 2022a)	**0**	$4.6066x10^{-7}$	$8.2062x10^{-7}$	$2.2108x10^{-6}$	**Inf.**	90.0029	$4.7584x10^{6}$

7. CONCLUSION

A new method, the OCSAPS algorithm, presents a novel hybrid metaheuristic approach for enhancing the efficiency of controlling a FOPID controller in a buck converter system. This novel approach integrates the OBL mechanism and the PS algorithm, enhancing the exploration and exploitation abilities of the original CSA. Statistical boxplot and convergence response analyses were conducted to establish the superiority of OCSAPS over CSA. Furthermore, the effectiveness of the proposed algorithm-based FOPID controller in the buck converter system was compared to established algorithms like HHO, GA, and CSA, using comprehensive testing such as transient and frequency response analysis and robustness assessment. Across these evaluations, the OCSAPS algorithm-based FOPID-controlled buck converter system demonstrated remarkable robustness, stability, and efficiency, outperforming its counterparts. Moreover, the proposed approach was compared with six other approaches regarding time and frequency domain responses. This comparative analysis affirmed the OCSAPS approach's exceptional performance, solidifying its preeminence in the relevant field. This innovative algorithm can also optimize various controllers in different systems, such as DC motor speed control, battery voltage management systems, and cruise control systems, which could be subject to investigation in future studies.

CONFLICT OF INTEREST

The authors declare no conflict of interest.

REFERENCES

Al-Majidi, S. D., Abbod, M. F., & Al-Raweshidy H. S. (2019). Design of an Efficient Maximum Power Point Tracker Based on ANFIS Using an Experimental Photovoltaic System Data. *Electronics*, *8*(8), 858. https://www.doi.org/10.3390/electronics8080858

Boudjehem, B., & Boudjehem, D. (2016). Fractional PID Controller Design Based on Minimizing Performance indices. *IFAC-PapersOnLine*, *49*(9), 164-168. https://www.doi.org/10.1016/j.ifacol.2016.07.522

Cech, M., & Schlegel, M. (2013, February 25-28). *Generalized robust stability regions for fractional PID controllers*. In: Proceedings of the 2013 IEEE International Conference on Industrial Technology (ICIT), (pp. 76-81). https://www.doi.org/10.1109/ICIT.2013.6505651

Chevalier, A., Francis, C., Copot, C., Ionescu, C. M., & Keyser, R. D. (2019). Fractional-order PID design: Towards transition from state-of-art to state-of-use. *ISA Transactions*, *84*, 178-186. https://www.doi.org/10.1016/j.isatra.2018.09.017

Das, S., Pan, I., Das, S., & Gupta, A. (2012). A novel fractional order fuzzy PID controller and its optimal time domain tuning based on integral performance indices. *Engineering Applications of Artificial Intelligence*, *25*(2), 430-442. https://www.doi.org/10.1016/j.engappai.2011.10.004

Dastjerdi, A. A., Vinagre, B. M., Chen, Y. Q., & HosseinNia, S. H. (2019). Linear fractional order controllers; A survey in the frequency domain. *Annual Reviews in Control*, *47*, 51-70. https://www.doi.org/10.1016/j.arcontrol.2019.03.008

Demir, M. H., & Demirok, M. (2023). Designs of Particle-Swarm-Optimization-Based Intelligent PID Controllers and DC/DC Buck Converters for PEM Fuel-Cell-Powered Four-Wheeled Automated Guided Vehicle. *Applied Sciences*, *13*(5), 2919. https://www.doi.org/10.3390/app13052919

Dolai, S. K., Mondal, A., & Sarkar, P. (2022). Discretization of Fractional Order Operator in Delta Domain. *Gazi University Journal of Science Part A: Engineering and Innovation*, *9*(4), 401-420. https://www.doi.org/10.54287/gujsa.1167156

Erickson, R. W., & Maksimović, D. (2000). *Fundamentals of Power Electronics* (Second Edition). Springer.

Eshaghi, S., & Tavazoei, M. S. (2023). Finiteness conditions for performance indices in generalized fractional-order systems defined based on the regularized Prabhakar derivative. *Communications in Nonlinear Science and Numerical Simulation*, *117*, 106979. https://www.doi.org/10.1016/j.cnsns.2022.106979

Feng, Z., Niu, W., & Liu, S. (2021). Cooperation Search Algorithm: A Novel Metaheuristic Evolutionary Intelligence Algorithm for Numerical Optimization and Engineering Optimization Problems. *Applied Soft Computing*, *98*, 106734. https://www.doi.org/10.1016/j.asoc.2020.106734

Feng, Z. K., Shi, P. F., Yang, T., Niu, W. J., Zhou, J. Z., & Cheng, C. T. (2022). Parallel cooperation search algorithm and artificial intelligence method for streamflow time series forecasting. *Journal of Hydrology*, *606*, 127434. https://www.doi.org/10.1016/j.jhydrol.2022.127434

Gaing, Z. L. (2004). A Particle Swarm Optimization Approach for Optimum Design of PID Controller in AVR System. *IEEE Transactions on Energy Conversion*, *19*(2), 384-391. https://www.doi.org/10.1109/TEC.2003.821821

Hekimoğlu, B. (2019). Optimal Tuning of Fractional Order PID Controller for DC Motor Speed Control via Chaotic Atom Search Optimization Algorithm. *IEEE Access*, *7*, 38100-38114. https://www.doi.org/10.1109/ACCESS.2019.2905961

Hekimoğlu, B. (2023). Determination of AVR System PID Controller Parameters Using Improved Variants of Reptile Search Algorithm and a Novel Objective Function. *Energy Engineering*, *120*(7), 1515-1540. https://www.doi.org/10.32604/ee.2023.029024

Hekimoğlu, B., & Ekinci, S. (2020). Optimally Designed PID Controller for A DC-DC Buck Converter via A Hybrid Whale Optimization Algorithm with Simulated Annealing. *Electrica*, *20*(1), 19-27. https://www.doi.org/10.5152/electrica.2020.19034

Hsieh, C. H., & Chou, J. H. (2007). Design of optimal PID controllers for pwm feedback systems with bilinear plants. *IEEE Transactions on Control Systems Technology*, *15*(6), 1075-1079. https://www.doi.org/10.1109/TCST.2007.908084

Izci, D., & Ekinci, S. (2022). A novel improved version of hunger games search algorithm for function optimization and efficient controller design of buck converter system. *e-Prime - Advances in Electrical Engineering, Electronics and Energy*, *2*, 100039. https://www.doi.org/10.1016/j.prime.2022.100039

Izci, D., Ekinci, S., & Hekimoğlu, B. (2022a). Fractional-Order PID Controller Design for Buck Converter System via Hybrid Lévy Flight Distribution and Simulated Annealing Algorithm. A*rabian Journal for Science and Engineering*, *47*, 13729-13747. https://www.doi.org/10.1007/s13369-021-06383-z

Izci, D., Ekinci, S., & Hekimoğlu, B. (2022b). A Novel Modified Lévy Flight Distribution Algorithm to Tune Proportional, Integral, Derivative and Acceleration Controller on Buck Converter System. *Transactions of the Institute of Measurement and Control*, *44*(2), 393-409. https://www.doi.org/10.1177/01423312211036591

Izci, D., Hekimoğlu, B., & Ekinci, S. (2022c). A New Artificial Ecosystem-Based Optimization Integrated with Nelder-Mead Method for PID Controller Design of Buck Converter. *Alexandria Engineering Journal*, *61*(3), 2030-2044. https://www.doi.org/10.1016/j.aej.2021.07.037

Izci, D., Ekinci, S., & Zeynelgil, H. L. (2023). Controlling an automatic voltage regulator using a novel Harris hawks and simulated annealing optimization technique. *Advanced Control for Applications: Engineering and Industrial Systems*, e121. https://www.doi.org/10.1002/adc2.121

Lee, Y. S., Wang, J. S., & Hui, S. Y. R. (1997). Modeling, Analysis, and Application of Buck Converters in Discontinuous-Input-Voltage Mode Operation. *IEEE Transactions on Power Electronics*, *12*(2), 350-360. https://www.doi.org/10.1109/63.558762

Li, Y., & Zhao, Y. (2015, May 23-25). *Memory identification of fractional order systems: Background and theory*. In: Proceedings of the 27th Chinese Control and Decision Conference (2015 CCDC), (pp. 1038-1043). https://www.doi.org/10.1109/CCDC.2015.7162070

Maâmar, B., & Rachid, M. (2014). IMC-PID-fractional-order-filter controllers design for integer order systems. *ISA Transactions*, *53*(5), 1620-1628. https://www.doi.org/10.1016/j.isatra.2014.05.007

Martinez-Patiño, L. M., Perez-Pinal, F. J., Soriano-Sánchez, A. G., Rico-Secades, M., Zarate-Orduño, C., & Nuñez-Perez, J. C. (2023). Fractional PID Controller for Voltage-Lift Converters. *Fractal and Fractional*, *7*(7), 542. https://www.doi.org/10.3390/fractalfract7070542

Micev, M., Ćalasan, M., & Oliva, D. (2020). Fractional Order PID Controller Design for an AVR System Using Chaotic Yellow Saddle Goatfish Algorithm. *Mathematics*, *8*(7), 1182. https://www.doi.org/10.3390/math8071182

Mohd Tumari, M. Z., Ahmad, M. A., Suid, M. H., & Hao, M. R. (2023). An Improved Marine Predators Algorithm-Tuned Fractional-Order PID Controller for Automatic Voltage Regulator System. *Fractal and Fractional*, *7*(7), 561. https://www.doi.org/10.3390/fractalfract7070561

Monje, C. A., Vinagre, B. M., Feliu, V., & Chen, Y. Q. (2008). Tuning and auto-tuning of fractional order controllers for industry applications. *Control Engineering Practice*, *16*, 798-812. https://www.doi.org/10.1016/j.conengprac.2007.08.006

Ortatepe, Z. (2023). Genetic Algorithm based PID Tuning Software Design and Implementation for a DC Motor Control System. *Gazi University Journal of Science Part A: Engineering and Innovation*, *10*(3), 286-300. https://www.doi.org/10.54287/gujsa.1342905

Ortiz-Quisbert, M. E., Duarte-Mermoud, M. A., Milla, F., Castro-Linares, R., & Lefranc, G. (2018). Optimal fractional order adaptive controllers for AVR applications. *Electrical Engineering*, *100*, 267-283. https://www.doi.org/10.1007/s00202-016-0502-2

Oustaloup, A., Levron, F., Mathieu B., & Nanot, F. M. (2000). Frequency-Band Complex Noninteger Differentiator: Characterization and Synthesis. *IEEE Transactions on Circuits and Systems I: Fundamental Theory and Applications*, *47*(1), 25-39. https://www.doi.org/10.1109/81.817385

Pan, F., & Liu, L. (2016, May 28-30). *Research on different integral performance indices applied on fractional-order systems*. In: Proceedings of the 2016 Chinese Control and Decision Conference (CCDC), (pp. 324-328). https://www.doi.org/10.1109/CCDC.2016.7531003

Podlubny, I. (1999). Fractional-Order Systems and PIλDμ-Controllers. *IEEE Transactions on Automatic Control*, *44*(1), 208-214. https://www.doi.org/10.1109/9.739144

Ranjan, A., & Mehta, U. (2023). Fractional-Order Tilt Integral Derivative Controller Design Using IMC Scheme for Unstable Time-Delay Processes. *Journal of Control, Automation and Electrical Systems*, *34*, 907-925. https://www.doi.org/10.1007/s40313-023-01020-6

Sangeetha, S., Sri Revathi, B., Balamurugan, K., & Suresh G. (2023). Performance analysis of buck converter with fractional PID controller using hybrid technique. *Robotics and Autonomous Systems*, *169*, 104515. https://www.doi.org/10.1016/j.robot.2023.104515

Shah, P., & Agashe, S. (2016). Review of fractional PID controller. *Mechatronics*, *38*, 29-41. https://www.doi.org/10.1016/j.mechatronics.2016.06.005

Smedley, K., & Cuk, S. (1994). Switching Flow-Graph Nonlinear Modeling Technique. *IEEE Transactions on Power Electronics*, *9*(4), 405-413. https://www.doi.org/10.1109/63.318899

Tizhoosh, H. R. (2005, November 28-30). *Opposition-Based Learning: A New Scheme for Machine Intelligence*. In: Proceedings of the International Conference on Computational Intelligence for Modelling, Control and Automation and International Conference on Intelligent Agents, Web Technologies and Internet Commerce (CIMCA-IAWTIC'06), (pp. 695-701). https://www.doi.org/10.1109/CIMCA.2005.1631345

Torczon, V. (1989). *Multi-Directional Search: A Direct Search Algorithm for Parallel Machines*. PhD Thesis, Rice University, Houston, Texas, USA.

Torczon, V. (1997). On the Convergence of Pattern Search Algorithms. *SIAM Journal on Optimization*, *7*(1), 1-25. https://www.doi.org/10.1137/S1052623493250780

Wang, Z., Li, S., Wang, J., & Li, Q. (2017). Robust control for disturbed buck converters based on two GPI observers. *Control Engineering Practice*, *66*, 13-22. https://www.doi.org/10.1016/j.conengprac.2017.06.001

Warrier, P., & Shah, P. (2021). Optimal Fractional PID Controller for Buck Converter Using Cohort Intelligent Algorithm. *Applied System Innovation*, *4*(3):50. https://www.doi.org/10.3390/asi4030050

Zhang, B., & Qiu, D. (2014). Sneak Circuits of DC-DC Converters. In: *Sneak Circuits of Power Electronic Converters* (pp. 59-103). IEEE. https://www.doi.org/10.1002/9781118379950.ch3

Research Article GU J Sci, Part A, 10(4): 442-451 (2023) 10.54287/gujsa.1358177

Gazi University
Journal of Science
PART A: ENGINEERING AND INNOVATION
http://dergipark.org.tr/gujsa

Systematic Investigation on the Synergistic Impact of Gallium (Ga)-Boron (B) Co-Doping on the Features of ZnO Films

Kenan OZEL[1*] Abdullah ATILGAN[2]

[1] Department of Electrical and Energy, GAMA Vocational School, Ankara University, Ankara, Türkiye
[2] Department of Energy Systems Engineering, Faculty of Engineering and Natural Sciences, Ankara Yıldırım Beyazıt University, Ankara, Türkiye

Keywords

Co-doped ZnO Thin Film
Ga Doping
B Doping
Spin Coating Method

Abstract

Herein, gallium-boron co-doped ZnO (GBZO) thin films (TFs) of varying percentages of Ga and B doping content were coated on glass slides via spin-coating technique. The impact of doping content on the features of GBZO TFs was comprehensively probed in this work. The characterization results demonstrate that the doping content has a profound impact on the features of GBZO TFs. The X-ray diffraction results verify the polycrystalline nature of GBZO TFs with varying diffraction peak intensities. AFM images disclose the smooth coating of GBZO TFs with low surface roughness. UV–Vis-NIR transmittance spectra reveal that the deposited TFs exhibit high transparency over 86 % in range of 400-800 nm wavelength with excellent optical properties. The electrical resistance measurements indicate that GBZO TFs having doping concentrations of 2.5 at. % of Ga and 0.5 at. % of B has the lower resistivity, and the resistivity of the samples are strongly affected by the doping content. The obtained knowledge from this study could be useful for the fabrication of TF based optoelectronic devices.

Cite

Ozel, K., & Atılgan, A. (2023). Systematic Investigation on the Synergistic Impact of Gallium (Ga)-Boron (B) Co-Doping on the Features of ZnO Films. *GU J Sci, Part A, 10*(4), 442-451. doi:10.54287/gujsa.1358177

Author ID (ORCID Number)

0000-0002-0250-3731 Kenan OZEL
0000-0002-5624-3664 Abdullah ATILGAN

Article Process

Submission Date 13.09.2023
Revision Date 14.11.2023
Accepted Date 04.12.2023
Published Date 12.12.2023

1. INTRODUCTION

Metal oxides are popularly utilized materials for the design of various electronic and optoelectronic devices extending from transparent transistor to photovoltaic cells (Chen & Lan, 2019; Ozel & Yildiz, 2021a, 2022). Of the metal oxides, zinc oxide (ZnO) is at the centre of intense investigations thanks to its desirable features including high transparency, wide band gap, high electron mobility, low-cost production, facile preparation procedures, high stability, nontoxicity etc. (Yildiz et al., 2012). Notwithstanding, the investigations on the undoped ZnO have disclose the fact that tuning the features of undoped ZnO makes it eligible candidate for various applications (Kara et al., 2017). One of the effective strategies is the incorporation of dopant elements, especially trivalent cations such as Al, In, B, and Ga, into the structure of undoped ZnO (Shukla et al., 2006; Zhao et al., 2022). Among the trivalent cations, boron could effectively modify the features of ZnO TFs because of its lowest ionic radius and greatest electronegativity (Tsay & Hsu, 2013). In addition, it has been reported in some studies that boron doping reduces degradation and provides stable electrical properties (Chen et al., 2007; Steinhauser et al., 2008). Moreover, gallium has been frequently preferred elements for doping of ZnO TFs owing to its higher resistance to oxidation and greater electronegativity (Tsay et al., 2012). Therefore, the synergistic effect of these dopant elements may be effective in adjusting the features of ZnO TFs.

In recent years, the increasing need for sensor-based technologies has led to diversity in sensor architectures and increased efforts to develop highly sensitive TF based sensors with a low-cost production. Specifically,

*Corresponding Author, e-mail: kozel@ankara.edu.tr

ZnO is popular conductive oxides employed in sensor fabrication. Soltabayev et al. (2021) reported Ni doped ZnO TFs can be utilized in NO gas sensing applications. Lee at al. (2021) achieved to obtain ZnO TF based piezo pressure sensor. Dash et al. (2018) reported the production and characterization of photonic crystals based on AZO that can be used in sensor production.

To date, the properties of single-doped ZnO TFs have been comprehensively ascertained, whereas the features of co-doped ZnO TFs have been poorly reported (Kara et al., 2016). Hence, it remains a challenge to fully analyze the synergistic impact of co-additive atoms on the features of ZnO TFs. To optimize GBZO TFs for device fabrication, it is of utmost importance to comprehend their morphological, structural, optical, and electrical characteristics. According to our observation, there is no reported work that has focused on the effect of varying gallium and boron content on GBZO TFs.

In the present study, we concentrated our effort on understanding the effectivity of co-additive atoms on the features of ZnO TFs. In this regard, GBZO TFs with varying percentages of Ga and B doping content were spin-coated on glass slides. The features of the GBZO TFs were systematically examined by measurements made with some characterization systems.

2. MATERIAL AND METHOD

The solutions for the deposition of GBZO TFs were prepared with different percentages of Ga and B doping content. The concentration of dopant elements in the solutions ([Ga+B]/([Ga+B]+[Zn])) was fixed to 3 at. %. First, 0.4 M/l of zinc acetate dihydrate, various at. % of gallium nitrate hydrate (i.e., 3, 2.75, 2.5, 2.25 and 2 at. %) and various at. % of trimethyl borate ($C_3H_9BO_3$; Merck) (i.e., 0, 0.25, 0.5, 0.75 and 1 at. %) were dissolved in methanol (CH_3OH; Merck) and monoethanolamine was added into the solutions. To maintain high transparency and homogeneity for the prepared solutions of co-doped ZnO, they were agitated for 2 h at 60°C utilizing a hot&plate. After aging for 48 h, the resulting solutions were coated on glass slides at a velocity of 2000 rpm for 30 s. Ten cycles of spin-coating and pre-heating at 500°C were realized to get the GBZO TFs. Finally, annealing process was fulfilled at 500°C for 1 h to attain polycrystalline TFs. Hereafter, the obtained co-doped ZnO thin films having doping concentrations of 3 at. % of Ga and 0 at. % of B, 2.75 at. % of Ga and 0.25 at. % of B, 2.5 at. % of Ga and 0.5 at. % of B, 2.25 at. % of Ga and 0.75 at. % of B, 2 at. % of Ga and 1 at. % of B content are called GBZO-1, GBZO-2, GBZO-3, GBZO-4, and GBZO-5, respectively. The dopant contents and boron/gallium doping ratios in the deposited film are given in Table 1.

Table 1. *The dopant contents and boron/gallium doping ratios in the co-doped ZnO TFs*

Sample	Ga ratio (at. %)	B ratio (at. %)	B/Ga ratio (%)	Total dopant ration (at. %)
GBZO-1	3	0	0	3
GBZO-2	2.75	0.25	9	3
GBZO-3	2.5	0.5	20	3
GBZO-4	2.25	0.75	33	3
GBZO-5	2	1	50	3

The crystal structures and structural features of GBZO TFs was unveiled by X-rays diffractometry (XRD) measurements. The topographical analyses of GBZO TFs were achieved by employing atomic force microscope (AFM). The optical features of GBZO TFs were recorded by UV/VIS spectrophotometer. The resistivities of the obtained TFs were characterized by a four-point probe.

3. RESULTS AND DISCUSSION

XRD patterns for co-doped ZnO TFs with varying percentages of Ga and B doping content are illustrated in Figure 1. The XRD results manifest that the observed diffraction peaks are matched with the hexagonal structure of ZnO. As seen, the deposited GBZO films exhibit six diffraction peaks, indicating the polycrystal nature of the films (Serin et al., 2017). The intensity of these peaks changes with doping concentrations of Ga and B elements. Note that our findings are compatible with the results of reported works (Yoshino et al., 2005; Serin et al., 2011).

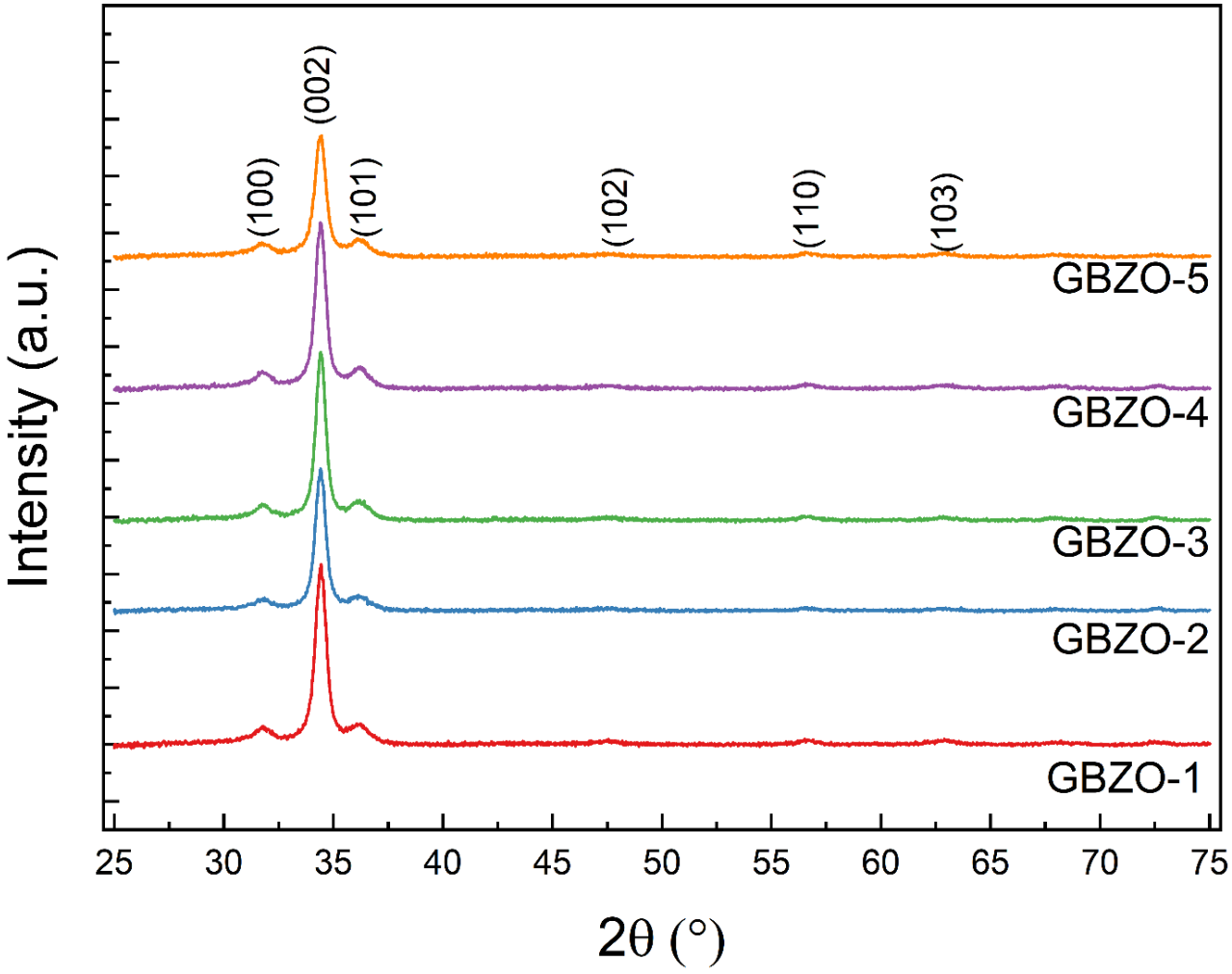

Figure 1. *X-ray diffractogram for GBZO TFs having different percentages of Ga and B content*

An evaluation of the grain size (L) of GBZO TFs by Debye Scherrer equation yields to be in the range of ~14–17 nm. The Debye Scherrer equation is depicted as the following formula (1) (Yildiz et al., 2016).

$$L = \frac{0.9\lambda}{B\cos\theta} \tag{1}$$

Here, λ, B and θ denote the X-rays wavelength (0.154 nm), FWHM, and Bragg angle. Moreover, the values lattice strain (ε) induced from the dopant elements in the GBZO TFs are calculated by using the equations given elsewhere (Liu & Zhu, 2019). All the calculated structural parameters for the deposited GBZO films are delineated in Table 2. As observed, the values of D slightly vary with the doping content and the values of ε increased to some extent with the changes of doping concentrations. As well known, the values of lattice strain strongly affected by the types and concentrations of the doping elements (Zhang et al., 2016).

Table 2. *Obtained parameters for the deposited GBZO films*

Sample	B/dopant ratio	2θ (°)	L (nm)	ε x10-3	Tav (%) (400-800nm)	T (%) @550nm	Eg (eV)
GBZO-1	0	34.42	14.9	0.8986	87.7	93.0	3.278
GBZO-2	0.08	34.41	15.6	1.2853	88.6	94.0	3.280
GBZO-3	0.17	34.42	16.6	1.0905	88.1	86.8	3.283
GBZO-4	0.25	34.40	14.8	1.5057	86.8	87.9	3.275
GBZO-5	0.33	34.41	15.9	1.1440	88.2	91.5	3.273

Figure 2 depicts the 2-dimensional and 3-dimensional AFM images. The surface topographies of the GBZO TFs are characterized with the RMS values which change with the varying doping content. As estimated from AFM images, the RMS values of GBZO TFs are found to be 2.9 nm for GBZO-1, 2.0 nm for GBZO-2, 1.8 nm for GBZO-3, 3.3 nm for GBZO-4 and 3.0 nm for GBZO-5, respectively. Table 3 summarizes the obtained structural and optical parameters for the deposited GBZO TFs. As seen, there is no obvious variation in the surface roughness values of GBZO TFs having different percentages of Ga and B doping content. The lower rougness values indicate that the deposited films possess very smooth surfaces, which ensures high transparency (Farrag & Balboul, 2017). Furthermore, the volume values of the GBZO TFs are calculated to be at around ~13-23 μm^3.

Table 3. *Structural and optical parameters for the deposited GBZO films*

Sample	B/dopant ratio	RMS (nm)	Volume (μm^3)	Thickness (nm)	Resistivity (Ω.cm)	R/T (MΩ)
GBZO-1	0	2.9	18.1	615	150.7	2.45
GBZO-2	0.08	2.0	13.3	615	196.7	3.20
GBZO-3	0.17	1.8	17.0	560	131.5	2.35
GBZO-4	0.25	3.3	22.6	662	170.5	2.58
GBZO-5	0.33	3.0	17.8	596	166.9	2.80

UV–Vis-NIR transmittance *vs.* wavelength profiles of GBZO TFs are delineated in Figure 3. From the profiles, one can observe that the transparency of GBZO TFs is above 86 % in wavelength region of 400-800 nm, which enables the investigated films suitable for optoelectronic applications (Al-Ghamdi et al., 2014). Note that the well-specified interference fringe patterns of the transmittance spectra notify the high-optical-quality of GBZO TFs (Kaur et al., 2015). The calculated average transparency between 400 nm and 800 nm and the transparency at 550 nm of GBZO TFs are given in Table 2. Based on the calculated parameters, one can infer that GBZO-2 exhibits the highest transparency of 94 %, suggesting this film highly suitable for the utilization as a window layer for the fabrication of photovoltaic cells and transparent electronics devices (Kaur et al., 2015).

Thickness of GBZO TFs can be extracted from transmittance profiles by utilizing the following equations (2-4) (Mártil & Díaz, 1992);

$$T_{min} = \frac{6n^2}{(n^4 + 3.25n^2 + 2.25)} \quad (2)$$

$$2nt = (h + 1/2)\lambda_{max} \quad (3)$$

$$2nt = h\lambda_{max} \quad (4)$$

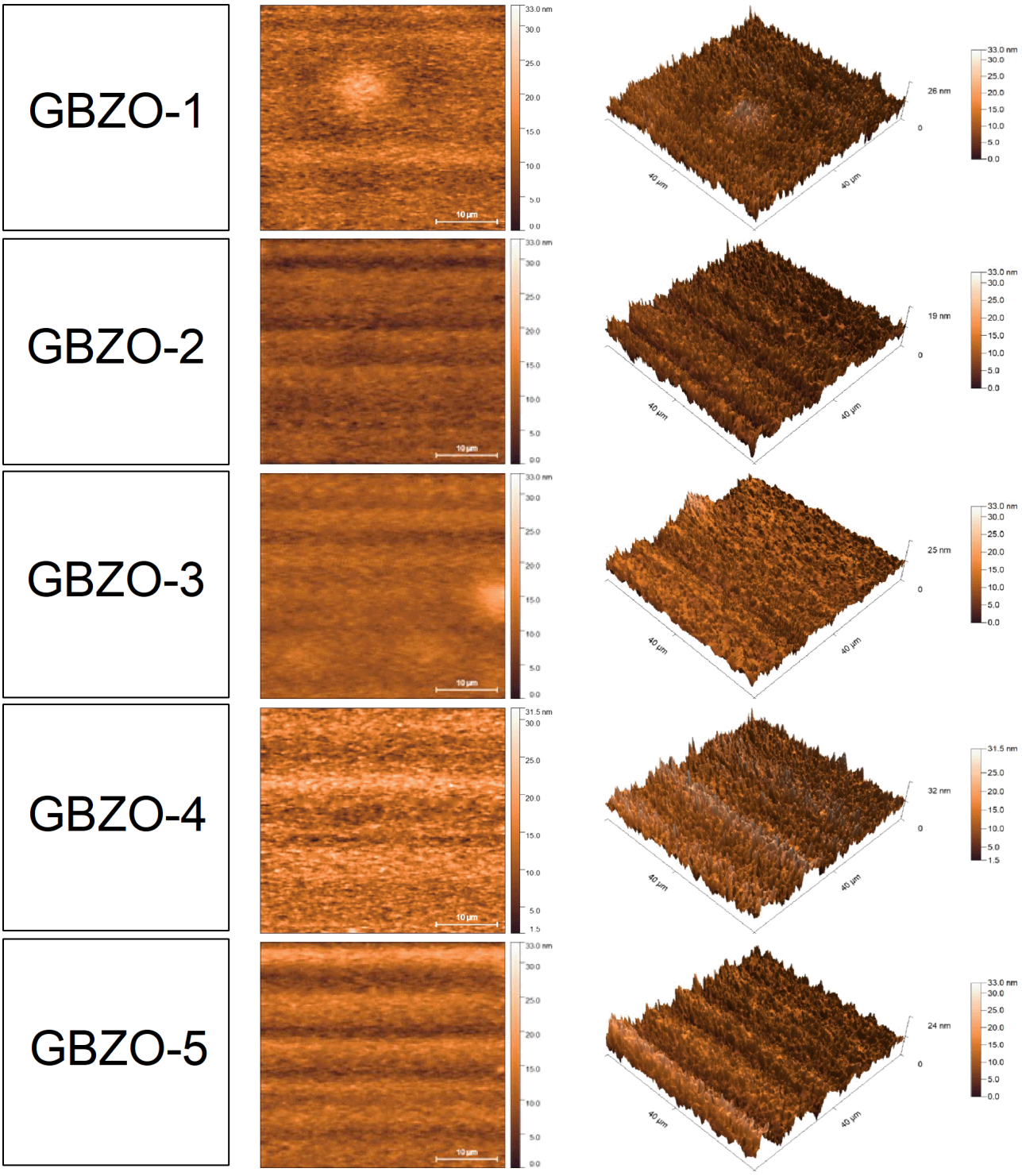

Figure 2. *AFM images of GBZO TFs with different percentages of Ga and B content*

Where T_{min}, n and h stand for the transmittance minima in the optical pattern, refractive index value of the investigated thin film, interface order, respectively. By solving the equation (1), the n values of the films can be obtained. The values of thickness (t) of the GBZO films can be obtained by substituting the n values of TFs in equations (2) and (3). The determined values of t of the investigated TFs are listed in Table 3.

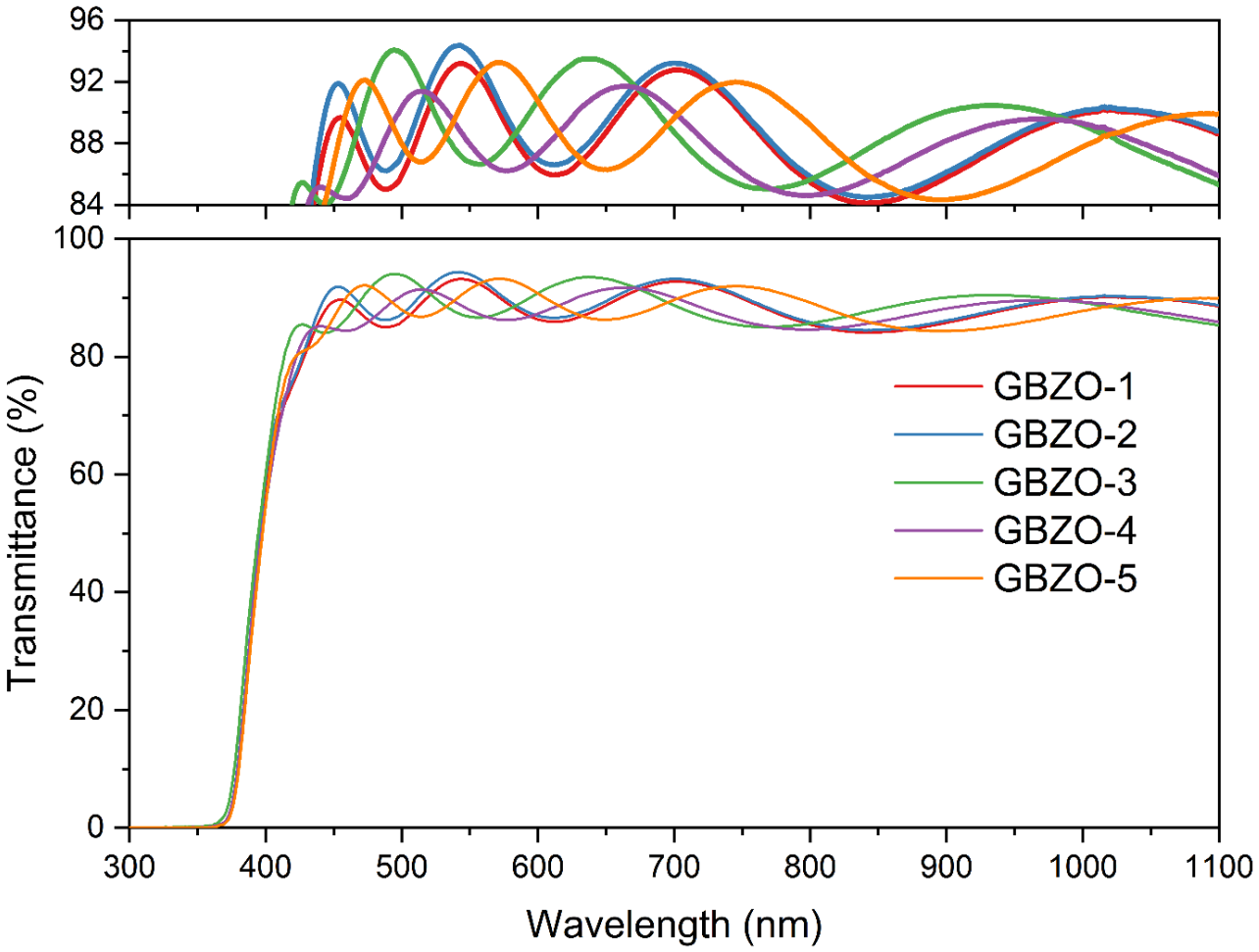

Figure 3. *UV–Vis-NIR transmittance vs. wavelength profiles of GBZO TFs*

Figure 4 illustrates the plots of $(\alpha h\upsilon)^2$as a function of $h\upsilon$ for the investigated GBZO films. Herein, the values of absorption coefficient (α) for GBZO TFs can be extracted from the transmittance data by utilizing Lambert's formula (5) (Choi et al., 2013);

$$\alpha = \frac{1}{t}\ln\left[\frac{1}{T}\right] \tag{5}$$

where T denotes the transmittance of GBZO TFs. The band gap energy (E_g) values of GBZO TFs are calculated by implementing Tauc's equation (6) (Ozel & Yildiz, 2021b);

$$\alpha h\upsilon = D(h\upsilon - E_g)^n \tag{6}$$

where $h\upsilon$ symbolizes the photon energy and D signify the band edge constant. If n=1/2, linear dependence of $(\alpha h\upsilon)^2$ versus $h\upsilon$ is observed in the band edge region, which implies the existence of the direct allowed transition. The extrapolation of linear region in the plots of $(\alpha h\upsilon)^2$ as a function of $h\upsilon$ allows us to extract the values of E_g for GBZO TFs. The extracted values of E_g for the investigated films are found to be as 3.278, 3.280, 3.283, 3.275 and 3.273 eV for GBZO-1, GBZO-2, GBZO-3, GZBO-4 and GBZO-5, respectively and

shown in Table 2. From the results, it can be said that the E_g values of GBZO TFs slightly change with varying content of Ga and B elements.

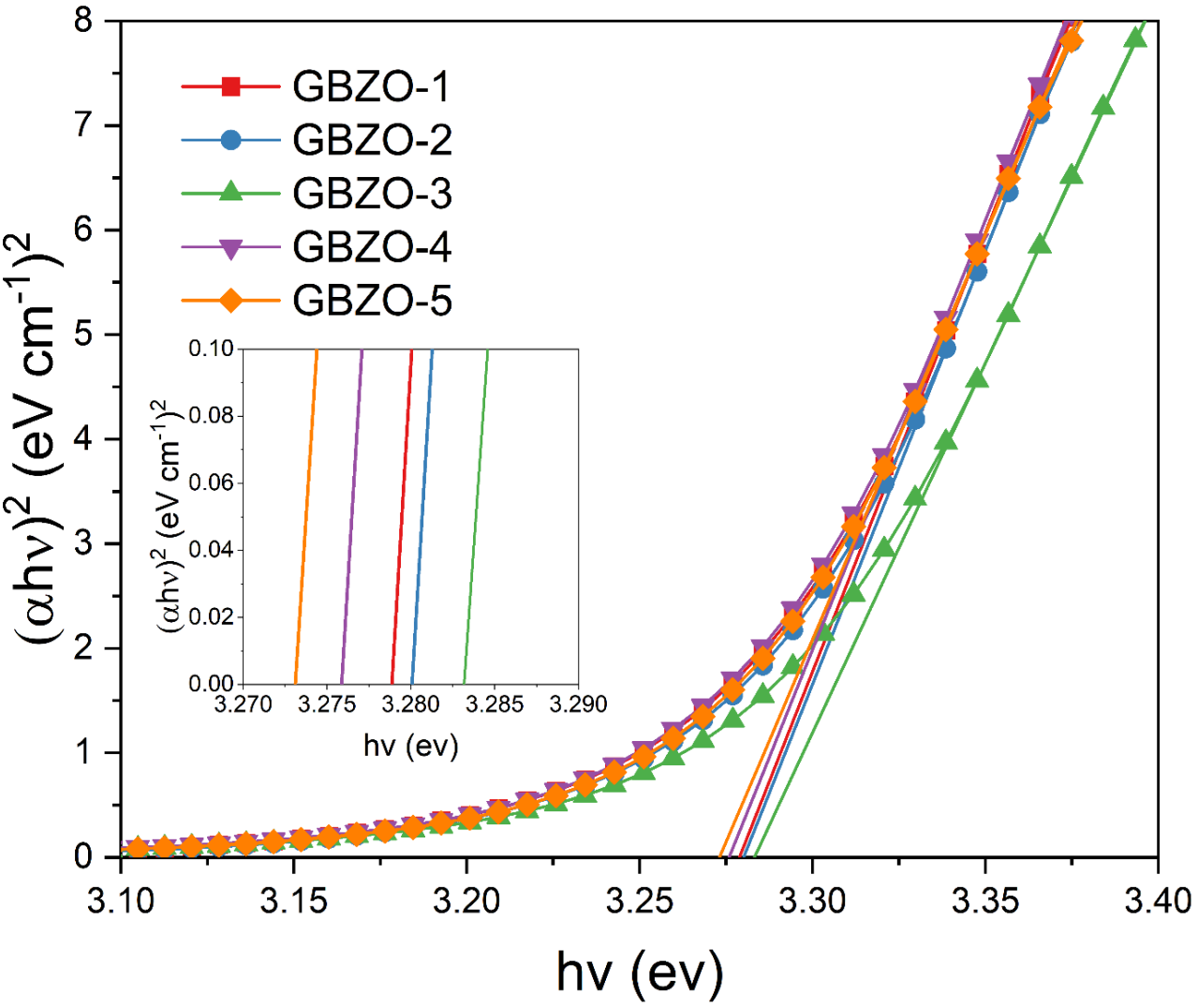

Figure 4. *The plots of* $(\alpha h\upsilon)^2$ *as a function of* $h\upsilon$ *for the investigated GBZO films*

Figure 5 manifests the variation graphs of resistivity (*R*) and sheet resistance (*R/T*) values against Ga doping content in GBZO TFs. The estimated parameters are summarized in Table 3. From the results, one can clearly observe that the GBZO TF with Ga doping content of 2.5 at. % (i.e., GBZO-3; 2.5 at. % of Ga and 0.5 at. % of B) has the lower values of resistivity (*R*) and sheet resistance (*R/T*). Moreover, one can notice that the *R* values decrease with increasing *t* values. The lower value of *R* of GBZO-3 also results from smooth surface and better crystallinity of the sample because the rough surface and low crystallinity deteriorate the flow of electrons (Kaur et al., 2015).

In summary, the features of ZnO TFs can be effectively tuned by co-doping process. Although there are many reported papers on pure and doped ZnO TFs, but a gap exists in literature considering the synergistic impact of gallium and boron co-doping on the features of ZnO TFs. Comparing the experimental findings with the reported studies, one can observe that the characteristic features including grain size, transparency, band gap size, surface roughness, electrical resistivity values of our films are in harmonies with the reported ones (Tsay et al., 2010; Chahmat et al., 2014; Mahroug et al., 2014). Moreover, it can be said that tuning doping content leads to considerable modification in the features of ZnO TFs. Hence, it can be emphasized that the obtained GBZO TFs may be well-qualified for use in different applications such as thin-film-based sensors, photovoltaic cells, and optical filters.

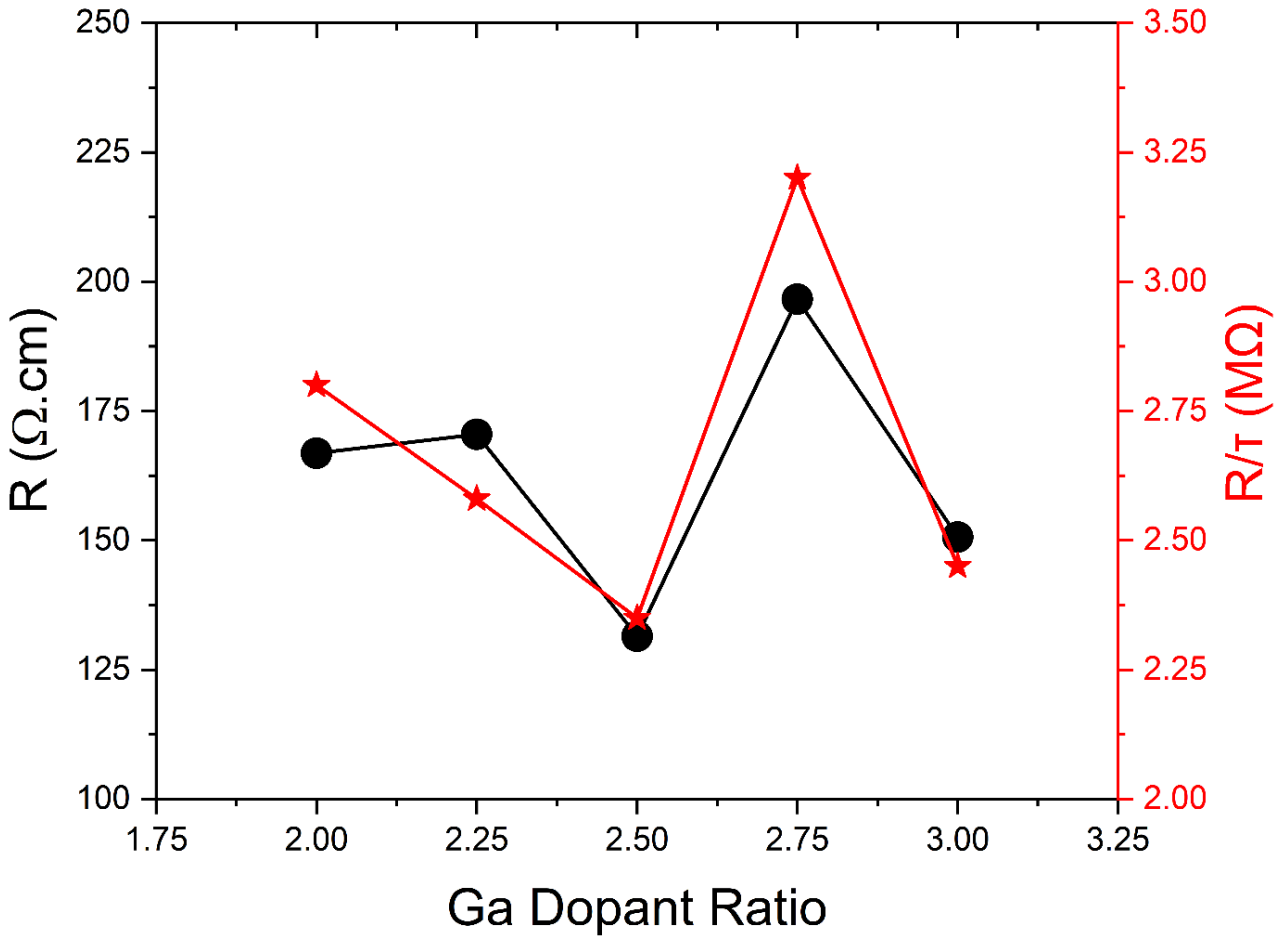

Figure 5. *The graphs of resistivity (R) and sheet resistance (R/T) values against Ga doping content in the GBZO films*

4. CONCLUSION

In summary, the features of GBZO TFs of varying percentages of Ga and B doping content obtained by a spin-coating method were analyzed by various characterization systems. The XRD diffractograms of GBZO TFs demonstrate that the deposited TFs are polycrystalline, demonstrating preferential orientation in (002) plane.

The values of L and ε change with varying doping content because of the difference in the ionic radii of Ga, B and Zn elements. Surface morphology investigations from AFM images show that the deposited films possess very smooth surfaces with small values of RMS. UV–Vis-NIR transmittance profiles of GBZO TFs indicate that the transparency of the deposited TFs is above 86 % in between 400 nm and 800 nm. The t and E_g values of the TFs is extracted from their transmittance data. The electrical resistance measurements point out that the electrical conduction features of the TFs are mightily dependent to their morphological, structural, physical properties. As a result, we can tune the features of co-doped ZnO TFs by changing the doping content and ensure their applicability to different optoelectronic applications.

ACKNOWLEDGEMENT

We would like to thank Professor Abdullah Yildiz and Professor Mohamed Sbeta for providing the necessary laboratory facilities for the realization of this investigation.

CONFLICT OF INTEREST

The authors declare no conflict of interest.

REFERENCES

Al-Ghamdi, A. A., Al-Hartomy, O. A., El Okr, M., Nawar, A. M., El-Gazzar, S., El-Tantawy, F., & Yakuphanoglu, F. (2014). Semiconducting properties of Al doped ZnO thin films. *Spectrochimica Acta Part A: Molecular and Biomolecular Spectroscopy*, *131*, 512-517. https://www.doi.org/10.1016/j.saa.2014.04.020

Chahmat, N., Souier, T., Mokri, A., Bououdina, M., Aida, M. S., & Ghers, M. (2014). Structure, microstructure and optical properties of Sn-doped ZnO thin films. Journal of alloys and compounds, *593*, 148-153. https://www.doi.org/10.1016/j.jallcom.2014.01.024

Chen, X. L., Xu, B. H., Xue, J. M., Zhao, Y., Wei, C. C., Sun, J., Wang, Y., Zhang, X. D., & Geng, X. H. (2007). Boron-doped zinc oxide thin films for large-area solar cells grown by metal organic chemical vapor deposition. Thin Solid Films, *515*(7-8), 3753-3759. https://www.doi.org/10.1016/j.tsf.2006.09.039

Chen, R., & Lan, L. (2019). Solution-processed metal-oxide thin-film transistors: A review of recent developments. *Nanotechnology*, *30*(31), 312001. https://www.doi.org/10.1088/1361-6528/ab1860

Choi, Y. J., Gong, S. C., Johnson, D. C., Golledge, S., Yeom, G. Y., & Park, H. H. (2013). Characteristics of the electromagnetic interference shielding effectiveness of Al-doped ZnO thin films deposited by atomic layer deposition. *Applied Surface Science*, *269*, 92-97. https://www.doi.org/10.1016/j.apsusc.2012.09.159

Dash, J. N., Das, R., & Jha, R. (2018). AZO coated microchannel incorporated PCF-based SPR sensor: a numerical analysis. IEEE Photonics Technology Letters, *30*(11), 1032-1035. https://www.doi.org/10.1109/LPT.2018.2829920

Farrag, A. A. G., & Balboul, M. R. (2017). Nano ZnO thin films synthesis by sol–gel spin coating method as a transparent layer for solar cell applications. *Journal of Sol-Gel Science and Technology*, *82*, 269-279. https://www.doi.org/10.1007/s10971-016-4277-8

Kara, I., Atilgan, A., Serin, T., & Yildiz, A. (2017). Effects of Co and Cu dopants on the structural, optical, and electrical properties of ZnO nanocrystals. *Journal of Materials Science: Materials in Electronics*, *28*, 6088-6092. https://www.doi.org/10.1007/s10854-016-6285-4

Kara, I., Yildiz, A., Yildiz, G., Dogan, B., Serin, N., & Serin, T. (2016). Al and X (Sn, Cu, In) co-doped ZnO nanocrystals. *Journal of Materials Science: Materials in Electronics*, *27*, 6179-6182. https://www.doi.org/10.1007/s10854-016-4546-x

Kaur, G., Mitra, A., & Yadav, K. L. (2015). Pulsed laser deposited Al-doped ZnO thin films for optical applications. *Progress in Natural Science: Materials International*, *25*(1), 12-21. https://www.doi.org/10.1016/j.pnsc.2015.01.012

Lee, P. C., Hsiao, Y. L., Dutta, J., Wang, R. C., Tseng, S. W., & Liu, C. P. (2021). Development of porous ZnO thin films for enhancing piezoelectric nanogenerators and force sensors. *Nano Energy*, *82*, 105702. https://www.doi.org/10.1016/j.nanoen.2020.105702

Liu, Y., & Zhu, S. (2019). Preparation and characterization of Mg, Al and Ga co-doped ZnO transparent conductive films deposited by magnetron sputtering. *Results in Physics*, *14*, 102514. https://www.doi.org/10.1016/j.rinp.2019.102514

Mahroug, A., Boudjadar, S., Hamrit, S., & Guerbous, L. (2014). Structural, optical and photocurrent properties of undoped and Al-doped ZnO thin films deposited by sol–gel spin coating technique. Materials Letters, *134*, 248-251. https://www.doi.org/10.1016/j.matlet.2014.07.099

Mártil, I., & Díaz, G. G. (1992). Undergraduate laboratory experiment: Measurement of the complex refractive index and the band gap of a thin film semiconductor. *American Journal of Physics*, *60*(1), 83-86. https://www.doi.org/10.1119/1.17049

Ozel, K., & Yildiz, A. (2021a). Comprehensive understanding of the role of emitter layer thickness for metal–oxide–semiconductors based solar cells. *IEEE Journal of Photovoltaics*, *12*(1), 251-258. https://www.doi.org/10.1109/jphotov.2021.3119612

Ozel, K., & Yildiz, A. (2021b). The potential barrier-dependent carrier transport mechanism in n-SnO2/p-Si heterojunctions. *Sensors and Actuators A: Physical*, *332*, 113141. https://www.doi.org/10.1016/j.sna.2021.113141

Ozel, K., & Yildiz, A. (2022). Estimation of maximum photoresponsivity of n-SnO_2/p-Si heterojunction-based UV photodetectors. *Physica Status Solidi (RRL) – Rapid Research Letters*, *16*(2), 2100490. https://www.doi.org/10.1002/pssr.202100490

Serin, T., Atilgan, A., Kara, I., & Yildiz, A. (2017). Electron transport in Al-Cu co-doped ZnO thin films. *Journal of Applied Physics*, *121*(9), 095303. https://www.doi.org/10.1063/1.4977470

Serin, T., Yildiz, A., Uzun, Ş., Çam, E., & Serin, N. (2011). Electrical conduction properties of In-doped ZnO thin films. *Physica Scripta*, *84*(6), 065703. https://www.doi.org/10.1088/0031-8949/84/06/065703

Shukla, R. K., Srivastava, A., Srivastava, A., & Dubey, K. C. (2006). Growth of transparent conducting nanocrystalline Al doped ZnO thin films by pulsed laser deposition. *Journal of crystal growth*, *294*(2), 427-431. https://www.doi.org/10.1016/j.jcrysgro.2006.06.035

Soltabayev, B., Er, İ. K., Yildirim, M. A., Ates, A., & Acar, S. (2021). The Dependence of The Nickel Concentration of ZnO Thin Films for Gas Sensors Applications. *Gazi University Journal of Science Part A: Engineering and Innovation*, *8*(1), 157-165.

Steinhauser, J., Faÿ, S., Oliveira, N., Vallat-Sauvain, E., Zimin, D., Kroll, U., & Ballif, C. (2008). Electrical transport in boron-doped polycrystalline zinc oxide thin films. *physica status solidi (a)*, *205*(8), 1983-1987. https://www.doi.org/10.1002/pssa.200778878

Tsay, C. Y., Fan, K. S., & Lei, C. M. (2012). Synthesis and characterization of sol–gel derived gallium-doped zinc oxide thin films. *Journal of Alloys and Compounds*, *512*(1), 216-222. https://www.doi.org/10.1016/j.jallcom.2011.09.066

Tsay, C. Y., & Hsu, W. T. (2013). Sol–gel derived undoped and boron-doped ZnO semiconductor thin films: preparation and characterization. *Ceramics International*, *39*(7), 7425-7432. https://www.doi.org/10.1016/j.ceramint.2013.02.086

Tsay, C. Y., Wu, C. W., Lei, C. M., Chen, F. S., & Lin, C. K. (2010). Microstructural and optical properties of Ga-doped ZnO semiconductor thin films prepared by sol–gel process. *Thin Solid Films*, *519*(5), 1516-1520. https://www.doi.org/10.1016/j.tsf.2010.08.170

Yildiz, A., Serin, T., Öztürk, E., & Serin, N. (2012). Barrier-controlled electron transport in Sn-doped ZnO polycrystalline thin films. *Thin Solid Films*, *522*, 90-94. https://www.doi.org/10.1016/j.tsf.2012.09.006

Yildiz, A., Uzun, S., Serin, N., & Serin, T. (2016). Influence of grain boundaries on the figure of merit of undoped and Al, In, Sn doped ZnO thin films for photovoltaic applications. *Scripta Materialia*, *113*, 23-26. https://www.doi.org/10.1016/j.scriptamat.2015.10.004

Yoshino, K., Fukushima, T., & Yoneta, M. (2005). Structural, optical and electrical characterization on ZnO film grown by a spray pyrolysis method. *Journal of Materials Science: Materials in Electronics*, *16*, 403-408. https://www.doi.org/10.1007/s10854-005-2305-5

Zhang, Y., Liu, C., Liu, J., Xiong, J., Liu, J., Zhang, K., Liu, Y., Peng, M., Yu, A., Zhang, A., Zhang, Y., Wang, Z., Zhai, J., & Wang, Z. L. (2016). Lattice strain induced remarkable enhancement in piezoelectric performance of ZnO-based flexible nanogenerators. *ACS Applied Materials & Interfaces*, *8*(2), 1381-1387. https://www.doi.org/10.1021/acsami.5b10345

Zhao, D., Sathasivam, S., Wang, M., & Carmalt, C. J. (2022). Transparent and conducting boron doped ZnO thin films grown by aerosol assisted chemical vapor deposition. *RSC Advances*, *12*(51), 33049-33055. https://www.doi.org/10.1039/D2RA05895B

Research Article GU J Sci, Part A, 10(4): 452-471 (2023) 10.54287/gujsa.1373305

Gazi University
Journal of Science
PART A: ENGINEERING AND INNOVATION
http://dergipark.org.tr/gujsa

Systematic Analysis of Infrastructure as Code Technologies

Erdal ÖZDOĞAN[1*] Onur CERAN[1] Mutlu Tahsin ÜSTÜNDAĞ[2]

[1] IT Department, Gazi University, Ankara, Türkiye
[2] Distance Education Application and Research Center, Gazi University, Ankara, Türkiye

Keywords

Infrastructure as Code
Network Automation
IaC Tools
Configuration Management

Abstract

"Infrastructure as Code" technologies are the network automation concept used in configuring network devices, allocating network resources, and deploying developed applications. By using machine-readable codes, various tasks that previously required time and effort can now be done dynamically with infrastructure as code tools. Although Infrastructure as Code is a technology that brings many advantages and is still at the beginning of its popularity, there are not enough resource in the literature. In this study, the key concepts of Infrastructure as Code technologies are discussed and infrastructure as code tools are systematically examined. The six most used Infrastructure as Code tools were examined in terms of management, language, data representation, code approach, stateful and stateless, architectural perspectives. Also, they were compared over these key concepts. The main purpose of this article is to define, classify, and elucidate the emerging infrastructure as code tools.

Cite

Ozdogan, E., Ceran, O., & Ustundag, M.T (2023). Systematic Analysis of Infrastructure as Code Technologies. *GU J Sci, Part A, 10*(4), 452-471. doi:10.54287/gujsa.1373305

Author ID (ORCID Number)

0000-0002-3339-0493 Erdal OZDOGAN
0000-0003-2147-0506 Onur CERAN
0000-0001-6198-2819 Mutlu Tahsin USTUNDAG

Article Process

Submission Date 09.10.2023
Revision Date 30.10.2023
Accepted Date 14.11.2023
Published Date 12.12.2023

1. INTRODUCTION

Today's Information Technologies (IT) have fundamental needs for both consumers of IT services and the software development sector that provides these services, such as speed, consistency, and security. With the support of virtualization and cloud computing technologies, IT resources have begun to be utilized more efficiently, and the needs of service providers and users have been relatively met. Increasing consumer demands and new technological trends have necessitated cloud-based resource provisioning to be much faster and error-resistant. This requirement has led to the use of automation in the sharing and provisioning of infrastructure resources such as storage, processors, memory, and networking, giving rise to the concept of Infrastructure as Code (IaC). On the other hand, the growing popularity of cloud technologies has particularly led to the development of new types of applications targeting cloud environments or efficient operation of cloud-based applications or network applications, the automation of various infrastructures and the dynamization of the software development process are required (Tankov et al., 2021). The use of Infrastructure as Code, which is a software engineering tactic that reduces the technical and organizational distance between software development and infrastructure provisioning processes, has become quite widespread in the IT sector (Artac et al., 2017).

IaC is a set of applications that uses "code" instead of manually entered commands to set up virtual machines, networks, and software packages, and to configure the environments that applications require (Patni et al., 2020). In IaC technologies, tasks such as provisioning infrastructure and installing software are managed through automation using code. In cloud service providers, meeting users' varying demands at different times using traditional methods can be time-consuming and error prone. However, thanks to IaC, efficient

*Corresponding Author, e-mail: erdal.ozdogan@gazi.edu.tr

distribution and sharing of infrastructure resources can be achieved in much shorter periods. Tasks such as resource sharing, device configuration, preparation of application development and testing environments, application deployment, and resource management, as depicted in Figure 1, can be accomplished using various tools within the IaC framework.

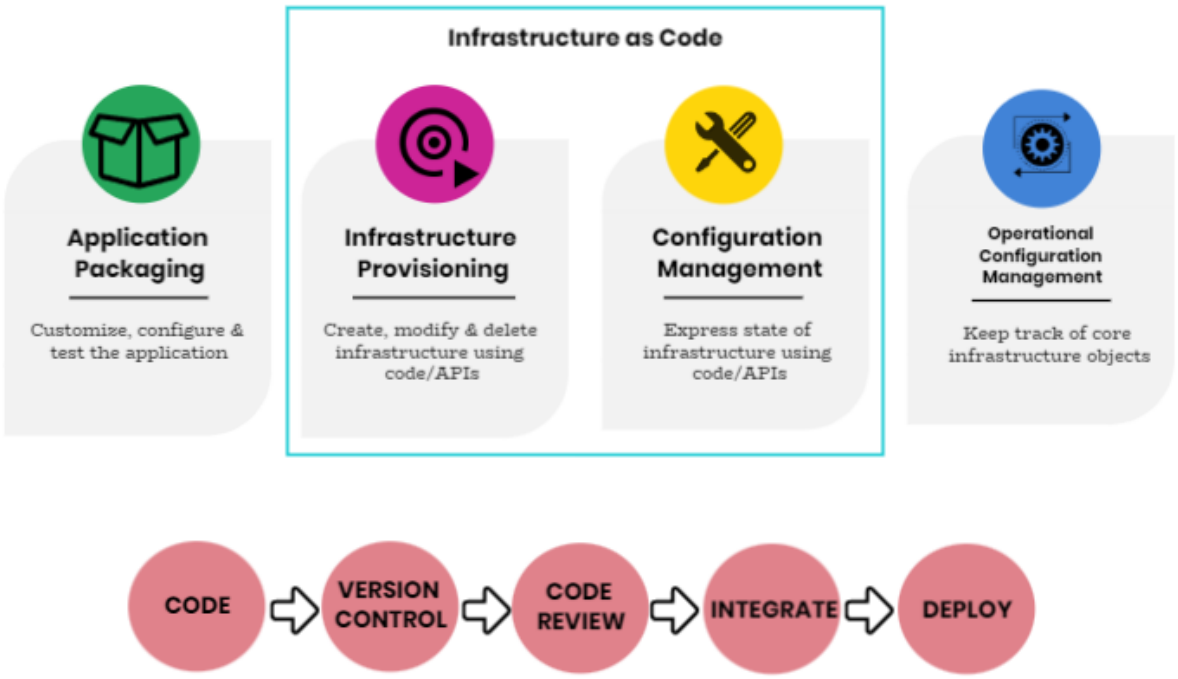

Figure 1. *Structure of Infrastructure as Code*

Infrastructure as Code, a technology that offers many advantages such as rapid resource sharing, efficient scalability, and low probability of errors, is still at the early stages of its popularity. Many organizations providing cloud-based services in the IT market are utilizing IaC technologies. However, there is still limited understanding of how the code underlying IaC applications can be maintained and developed in a measurable manner (Artac et al., 2017; Guerriero et al., 2019; Dalla Palma et al., 2020). Also there are challenges encountered in its implementation (Chen et al., 2018; Sandobalin et al., 2019). While there have been various research efforts in the literature regarding the widespread adoption of IaC technologies and tools in the industry, there still exists a shortage of resources on the subject (Kumara et al., 2021; Falazi et al., 2022; Alonso et al., 2023).

Infrastructure as Code has become a frequently employed tool by software developers with the aim of facilitating the rapid delivery of DevOps applications and services to end-users. In order to systematically assess studies related to IaC, research domains for IaC were identified in a mapping study conducted by Rahman et al. (2019).

Due to the early stage of research in the field of IaC, there is a limited amount of academic literature available on the subject. Artac et al. (2017) have discussed key elements and abstractions in the Topology and Orchestration Specification for Cloud Applications (TOSCA) standards, pertaining to IaC. The study summarizes the specialized TOSCA standard for IaC as a tactic to expedite Development and Operations (DevOps) based lifecycles, aiming to accelerate the cycle of development and operations activities. In the study by Sandobalin et al. (2017), a tool is presented that supports the management of IaC based DevOps tools. This tool enables modeling the current state of infrastructure provisioning in the cloud and facilitates the creation of scripts. In another work by the same authors, a model-based approach is proposed for infrastructure provisioning (Sandobalin et al., 2019).

Dalla Palma et al. (2020) have pointed out that software quality metrics developed for general-purpose programming languages may not be suitable for IaC. In their relevant study, they focused on a specific IaC tool and developed a new catalog comprising 46 metrics.

In the study by Opdebeeck et al. (2020) the role transition in Ansible, which is one of the Infrastructure as Code tools, was analyzed. The authors designed a structural model for Ansible roles and developed a unique algorithm to extract structural changes between two versions of a role. In a study focused on comparing Infrastructure as Code tools, an analysis was conducted regarding features that do not lead to runtime errors in the code but require improvement (known as code smells). The study compared two IaC tools based on these aspects (Schwarz et al., 2018). The authors categorized deficiencies and features that need improvement in the code as technology-dependent and technology-independent in their study. In another study related to "code smells" in Infrastructure as Code, three IaC tools were examined from a security perspective (Rahman & Williams, 2021).

In Infrastructure as Code applications, very little is still known about sustainability and usability. As a result, some literature studies have directly focused on this issue. Indeed, in a study conducted by Guerriero et al., (2019), semi-structured interviews were conducted with senior developers from various companies. This study highlighted the state of implementation and the fundamental challenges in software engineering in relation to IaC adoption, exploring the reasons behind its adoption or non-adoption. The study clearly emphasizes the need for further research in this field. Furthermore, in the same study, it is noted that the support provided by existing tools is still limited.

In the study by Shvetcova et al. (2019) a method is proposed for the unified description and deployment of infrastructures, including hardware and software requirements. In the study, the authors describe an improved Infrastructure as Code tool's (Ansible) module that deploys the necessary infrastructure in a cloud environment based on specific descriptions. In the work by Tankov et al. (2021), a novel approach is presented that significantly simplifies the development of local applications in the cloud, enabling developers to create infrastructure without needing expert-level knowledge about a specific cloud platform. In the study, a direct code-based approach was developed for provisioning infrastructure, eliminating the need to create manifest files for infrastructure allocation. In a study that can be considered an advancement in Infrastructure as Code application, the author aims to enhance the quality of IaC scripts by identifying the characteristics of the development process associated with scripts and errors that may compromise security and privacy (Rahman, 2018).

Infrastructure as Code is extensively used in modern times for critical software's code reviews, testing environments, and development processes. Consequently, the techniques employed while writing code can also be applied when defining infrastructure (Heap, 2016). The experimental study aimed to enhance the quality of Infrastructure as Code through practitioner assistance. It aimed to assist practitioners in identifying the source code characteristics of erroneous IaC scripts (Rahman et al., 2019). In another study focused on identifying code errors, Dalla Palma et al. (2020) developed an innovative method for error prediction using three different techniques. In the study by Chen et al. (2018), a machine learning-based approach is proposed to address frequently occurring errors in Infrastructure as Code.

Considering the studies conducted in the field of Infrastructure as Code, it is evident that development processes are still ongoing and there is a need for systematic analyses of IaC and IaC tool usage. In our study, we conduct a static analysis by identifying key concepts used to define Infrastructure as Code tools in both the literature and grey literature. We explain the features of these tools and compare them. Additionally, within the framework of these key concepts, we conduct a static examination of these tools, revealing which tools are used for specific purposes. This study explores the concepts of IaC technology to provide insights and facilitate future research endeavors. The tools utilized in IaC technology are discussed, and a systematic approach is employed to analyze key concepts.

The study distinguishes itself by incorporating insights from the latest articles and gray literature sources, ensuring that the findings are not only grounded in established knowledge but also reflect the most current trends and developments in the field of IaC technologies. By capturing cutting-edge practices and emerging

challenges, the research offers a forward-looking perspective, contributing to a more nuanced understanding of the evolving landscape of IaC tools. Going beyond traditional literature reviews, this study constructs a recommendation tree for the strategic usage of IaC tools. This structured framework provides practical guidance to decision-makers and practitioners, aiding them in navigating the complexities of IaC implementation. By outlining tailored strategies based on specific project requirements, organizational goals, and integration needs, the research offers actionable insights that can be directly applied in real-world scenarios.

The rest of the article is organized as follows:

In the methodology section, the IaC tools are examined through key concepts, aligning with the primary objective of this study. In the third section, an evaluation was conducted based on key concepts, and a recommendation tree for the strategic usage of IaC tools was generated. The results and discussion section presents the findings acquired and offers recommendations believed to be beneficial for prospective research in the realm of IaC technologies. In the final section, the contributions of the study have been presented, and the article concludes with future potential research directions.

2. METHODOLOGY

This section includes the fundamental concepts that will be used for evaluating Infrastructure as Code tools, along with explanations of these concepts. Understanding the meanings of these key concepts accurately is essential for comprehending the efficiency of the tools. The correct interpretation of these key concepts enables us to grasp the effectiveness of the tools.

The method we followed in the study is shown in Figure 2.

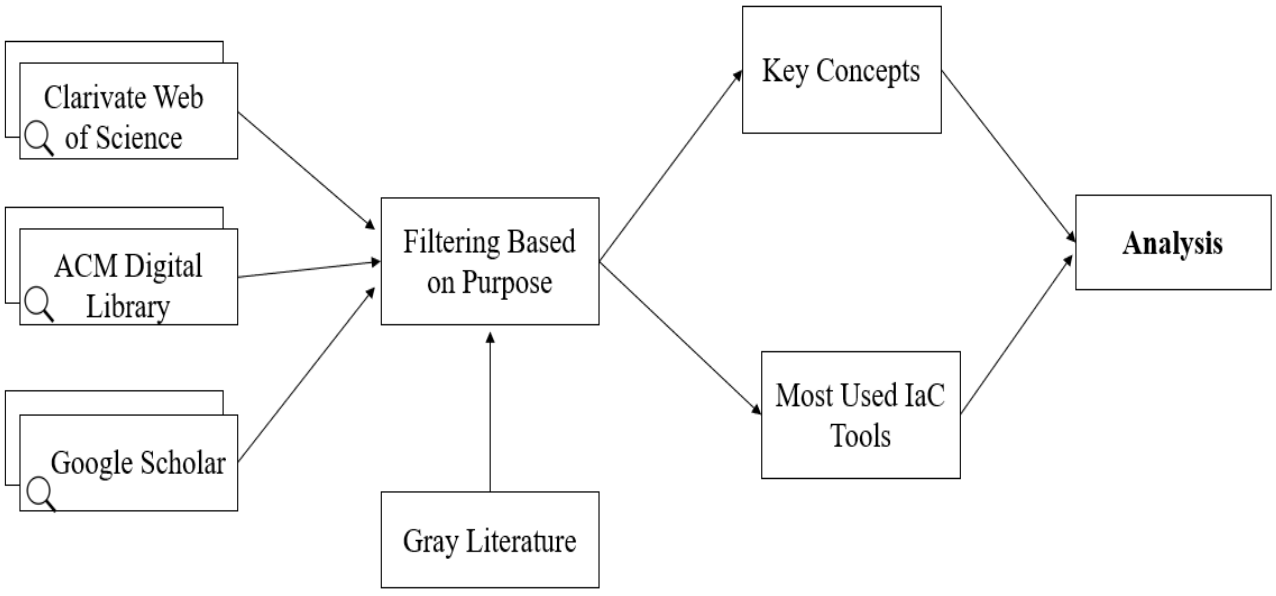

Figure 2*. The workflow we followed in this study*

Firstly, to identify the most used Infrastructure as Code tools, we conducted searches in ACM Digital Library, Clarivate Web of Science and Google Scholar for studies published in the last two years using the keywords "*Infrastructure as Code ∨ IaC ∨ IaC Management v IaC Tools*". The studies we have examined are presented in Table 1. Subsequently, we identified the IaC tools discussed in the studies and extracted the key concepts used in their definitions.

***Table 1**. Studies published within the last two years within the scope of the article*

No	The Examined Studies
1	Automated Application Deployment on Multi-Access Edge Computing: A Survey (Santos et al., 2023)
2	Static Analysis of Infrastructure as Code: a Survey (Chiari et al., 2022)
3	Practitioner Perceptions of Ansible Test Smells (Zhang et al., 2023)
4	Infrastructure as Code for Dynamic Deployments (Sokolowski, 2022)
5	Comparison of infrastructure as code frameworks from a developer perspective (Karlsson, 2023)
6	Infrastructure-as-Code Ecosystems (Opdebeeck et al., 2023a)
7	The SODALITE Model-Driven Approach (Gorroñogoitia et al., 2022)
8	DevOps and IaC to Automate the Delivery of Hands-On Software Lab Exams (Sorour & Hamdy, 2022)
9	Embracing IaC Through the DevSecOps Philosophy (Alonso et al., 2023)
10	IEM: A Unified Lifecycle Orchestrator for Multilingual IaC Deployments (Diaz-De-Arcaya et al., 2023)
11	Extensible Testing for Infrastructure as Code (Spielmann et al., 2023)
12	Control and Data Flow in Security Smell Detection for Infrastructure as Code: Is It Worth the Effort? (Opdebeeck et al., 2023b)
13	Cybercompetitions: A survey of competitions, tools, and systems to support cybersecurity education (Balon & Baggili, 2023)
14	Towards Reliable Infrastructure as Code (Sokolowski & Salvaneschi, 2023)
15	Decentralizing Infrastructure as Code (Sokolowski et al., 2023)
16	Formal Verification of Infrastructure as Code (De Pascalis, 2022)
17	A Structured Literature Review Approach to Define Serverless Computing and Function as a Service (Manner, 2023)
18	“Through the looking-glass." An Empirical Study on Blob Infrastructure Blueprints in TOSCA (Dalla Palma et al., 2023)
19	Building an IT Security Laboratory for Complex Teaching Scenarios Using ’Infrastructure as Code’ (Soll et al., 2023)
20	Provisioning Secure Cloud Environment Using Policy-as-code and Infrastructure-as-code (Tripathi, 2023)
21	DevSecOps: A Security Model for Infrastructure as Code Over the Cloud (Ibrahim et al., 2022)
22	A comparison between Terraform and Ansible on their impact upon the lifecycle and security management for modifiable cloud infrastructures in OpenStack (Gurbatov, 2022)
23	Ansible in different cloud environments (Witt & Westling, 2023)
24	Ansible: A Reliable Tool for Automation (Daffalla Elradi, 2023)
25	DevOps and Tools Used: A Systematic Review (Raj et al., 2022)
26	Adoption of Infrastructure as Code (IaC) in Real World (Murphy, 2022)

Within the scope of this study, the works that define, examine, or utilize IaC tools are listed in Table 2. The table illustrates which tools are addressed in each study and the percentage weight of their presence across all studies.

According to Table.1, the most frequently used tools are Ansible, Puppet, Chef, Terraform, CloudFormation, and SaltStack. For these tools mentioned in the literature, we determined the most widely used IaC tools for cloud configuration purposes in 2023, based on Statista (2023). Accordingly, CloudFormation has a usage rate of 51%, Terraform: 30%, Ansible: 20%, Chef: 14%, Puppet: 15%, and SaltStack: 10%. The usage statistics of IaC tools covered in this article, which have been the subject of academic studies in the last two years, are also provided in Table 2.

***Table 2**. IaC tools are addressed in each study and the percentage weight of their presence*

IaC Tool Name	References	Weight %
Ansible	[1],[2],[3],[4],[6],[7],[8],[9],[10],[12],[13],[14],[16],[18],[19],[21],[22],[23],[24],[25],[26]	81%
Chef	[1],[2],[4],[7],[9],[10],[12],[13],[14],[16],[18],[19],[21],[22],[23],[24],[25],[26]	69%
CloudFormation	[2],[4],[5],[9],[15],[16],[18],[19],[22],[26]	38%
Puppet	[1],[2],[4],[7],[10],[12],[13],[14],[21],[22],[23],[24],[26]	50%
SaltStack	[10],[13],[16],[21],[24]	19%
Terraform	[1],[2],[4],[8],[9],[10],[11],[13],[14],[15],[16],[19],[20],[21],[22],[23],[24],[26]	69%

We examined these tools statically. We identified the keywords that authors used in defining IaC, explaining IaC tools, or conducting comparisons. Additionally, we browsed the websites of the most frequently used tools and conducted a gray literature review. This allowed us to identify not only the key concepts from previous studies but also new concepts (Rahman et al., 2020). These key concepts are provided in Table 3.

***Table 3**. Key concepts used in definitions*

Key Concept	References
Approach	[1],[2],[4],[5],[13],[16],[21],[22],[23],[26]
Architecture	[1],[7],[10],[13],[21],[22],[23],[24]
Idempotency	[1],[2],[6],[8],[16],[22]
Programming Language	[4],[5],[14],[15],[23],[24]
Data Format	[1],[4],[5],[12],[14],[21],[22],[23],[24],[26]
Scalability	[1],[15],[19],[22],[24]
Infrastructure State	[6],[15],[22]
Management Purpose	[1],[2],[6],[7],[8],[9],[10],[11],[12],[14],[15],[16],[20],[22],[26]
Security & Code Smells	[2],[12],[19],[24]
Cloud Integration	[5],[21],[22]
Application Deployment & Distribution	[1],[2],[6],[7],[9],[19]
Usability	[2],[5],[7],[12],[13],[14],[19],[24],[26]

When considering the concepts expressed in the studies, it is observed that the most used terms in defining IaC tools are management purpose, data format, approach, architecture, and usability.

2.1 IaC Tools

Infrastructure as Code tools use scripts to define, update, and execute the creation of cloud infrastructure. Each IaC tool has its own scripting language to describe the infrastructure and processes to be carried out. Commonly used IaC tools (Achar, 2021).

Ansible: Ansible is an IT (Information Technology) automation engine that automates cloud applications (Singh et al., 2016). With both open source and paid versions available, Ansible is primarily utilized as a configuration management tool for managing resources (Artac et al., 2018). The Ansible management tool works on almost all Linux machines running Python 2 or 3. Management of infrastructure resources is achieved through SSH connections established via the node where this configuration management tool operates as seen in Figure 3. This enables the execution of scripts on remote hardware, the removal of executed scripts, and the installation of Python libraries. Similarly, configuration can also be performed on remote hardware through REST APIs (Ning, 2023).

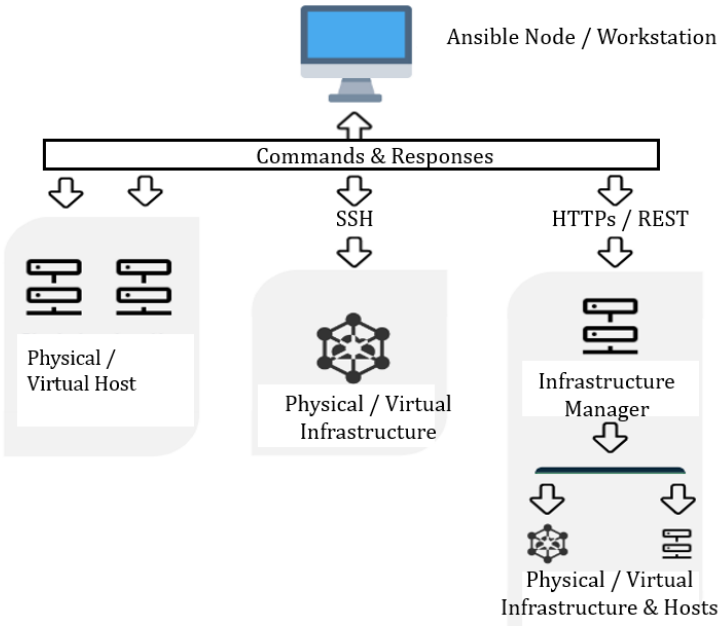

***Figure 3**. The architecture of Ansible*

Chef: Chef is an open-source IaC configuration management tool that enables developers and operations teams to automate the process of configuring and deploying infrastructure and applications (L'Esteve, 2023). It serves as a significant IaC tool for managing complex environments. With Chef, users can define infrastructure as code using a domain-specific language (DSL) called Chef DSL (Mustafa, 2023). This allows for the desired state of infrastructure components and applications to be defined, including software packages, system configurations, user accounts, and security settings.

Chef operates by breaking down the configuration process into small, reusable components called "recipes" and collections of relevant recipes known as "cookbooks" (Figure 4). Recipes are individual components of the configuration code, while cookbooks are collections of related recipes (Surianarayanan & Chelliah, 2023). Users can share and reuse cookbooks to create their own infrastructure and applications, thereby facilitating the management of larger, complex environments.

As seen in Figure 4, Chef also includes a powerful tool called "Chef Server," which serves as a centralized repository for configuration data and provides a way to manage configuration changes across multiple nodes. This server ensures that all nodes are consistently configured and aids in simplifying the management of large, complex environments.

Puppet: Puppet is an IaC configuration management tool that was founded as an open-source solution in 2005 but later evolved into a commercial platform. The Puppet Server, also known as Puppet Master, is the core

component, which includes the information gathering service called Facter, and components like PuppetDB that store events, node catalogs, current configurations, and historical data.

Puppet consists of both client and server components. The client, also known as the Agent, is securely installed, and configured on target machines. The client and server authenticate each other using self-signed certificates. The Agent collects events under the control of the Facter service and applies configuration changes as directed by the Puppet Server (Bessghaier et al., 2023). Puppet includes modules that enable connectivity for Cloud APIs and hardware that cannot run agents. User interactions are typically conducted through SSH and the command line (Figure 5).

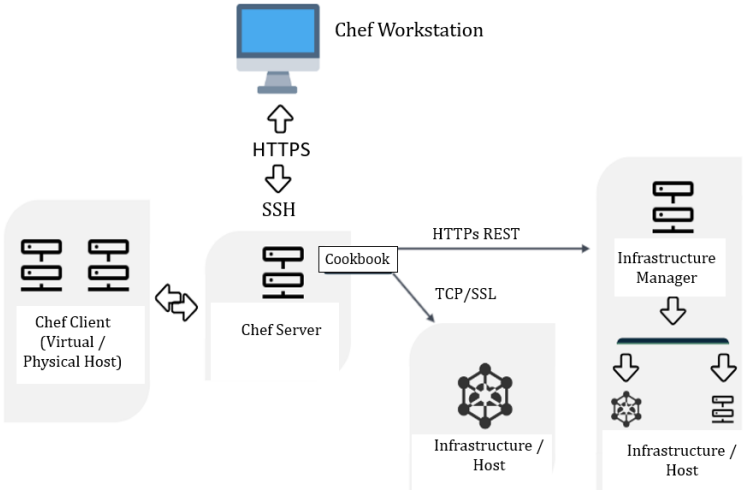

***Figure 4**. The Chef tool architecture*

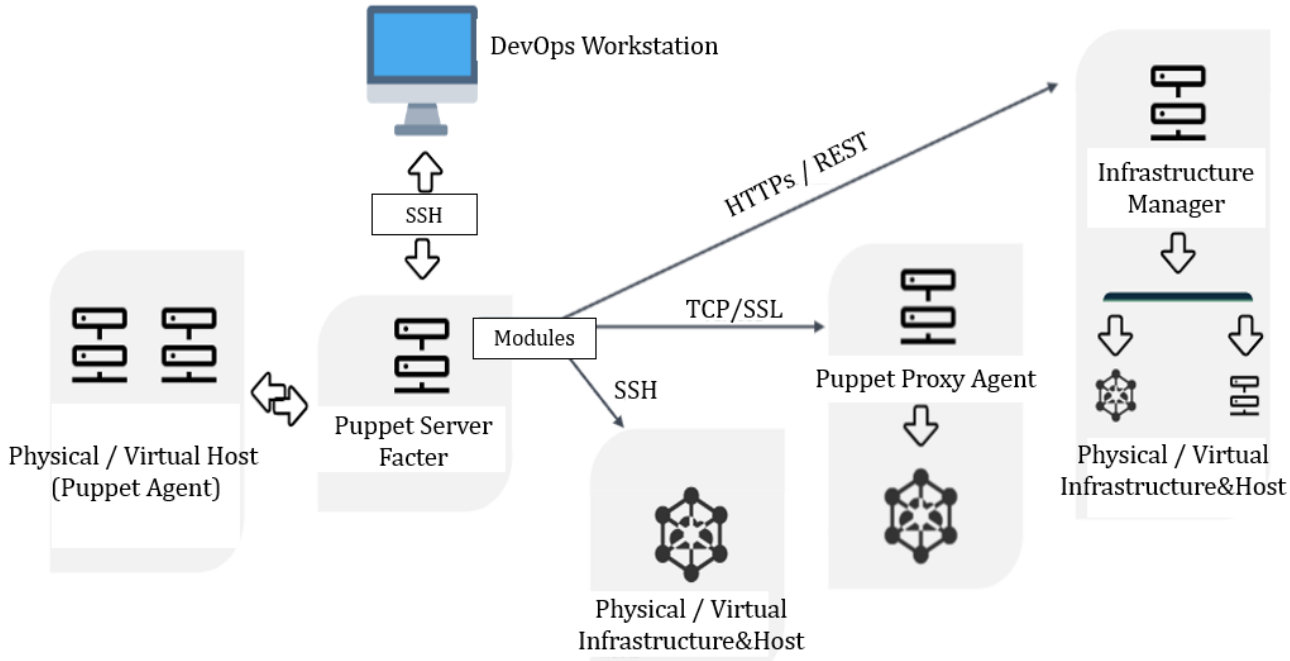

***Figure 5**. The architecture of Puppet tool*

After the Puppet server is operational, the Puppet Agent tool can be installed on the desired client to manage it. Server configuration information is stored in the puppet.conf file on the client. The server can now collect information from the client and update its status with any configuration changes. Notifications to be configured are stored in manifest files. Notification files typically have a .pp extension and are written in a declarative language resembling Ruby.

SaltStack: SaltStack is a decentralized model-based Infrastructure as Code tool that operates through a server (Zadka, 2019). As seen in Figure 6, it consists of a central server called Salt Master and clients known as Salt Minions, which act as agents on nodes. One of its notable features is the use of Python scripts and the YAML language (Ning, 2023). Configuration commands are sent to clients via the SSH protocol as events. In the SaltStack architecture, clients and configuration templates are organized in groups, allowing for easier management of the environment. Salt servers can operate redundantly. In case one server becomes unavailable, clients can seek support from another server. This means that multiple master servers can be utilized.

Terraform: Terraform is an open-source IaC orchestration tool developed by HashiCorp (Gupta et al., 2021). It is used to create, manage, and update server infrastructure, storage, networking, and various other services using written configuration files (Terraform, 2023). Terraform enables users to manage infrastructure using explicitly defined configuration files. With Terraform, users can create and configure resources on various platforms such as cloud service providers and on-premises virtual machines. Users utilize a language called HashiCorp Configuration Language (HCL) to define infrastructure in Terraform. HCL allows users to define infrastructure resources in a human-readable and writable format. In Figure 7, the Terraform architecture is depicted.

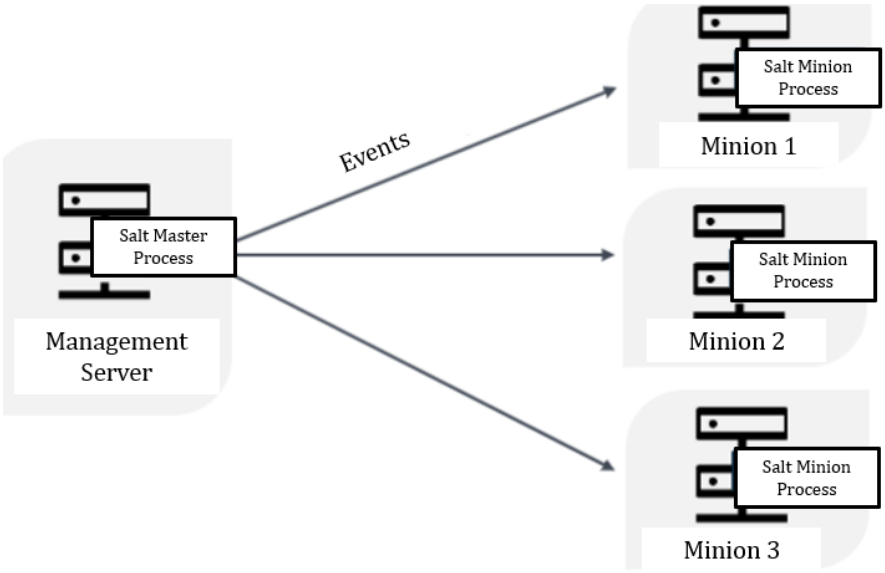

***Figure 6**. The architecture of Saltstack*

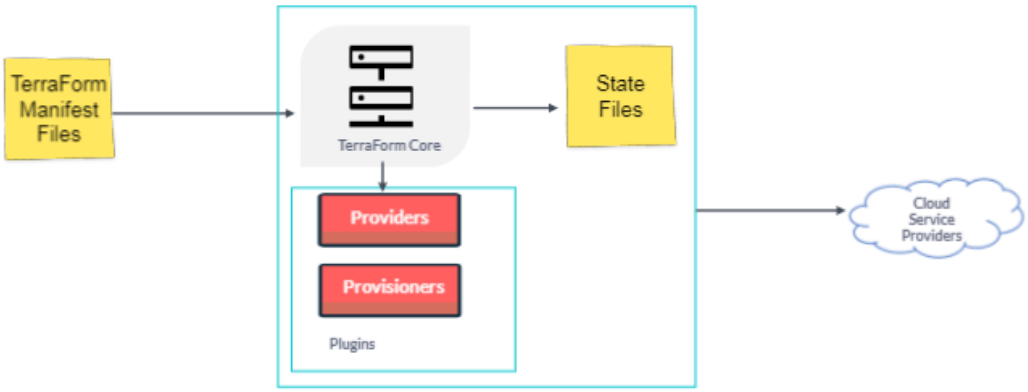

***Figure 7**. The architecture of Terraform*

Terraform projects are written in a specialized language called HCL. This language enables the definition and configuration of infrastructure and is formatted to be readable and writable by humans. The command-line interface of Terraform allows users to execute Terraform commands. These commands perform various tasks such as planning, applying, and managing infrastructure.

Terraform can manage various infrastructures, including different cloud providers or on-premises infrastructure providers. Each infrastructure provider includes a custom "provider" plugin that enables Terraform to communicate with these platforms. Terraform's operational state is stored in a 'state file.' This file is used to track the current state of the managed infrastructure and changes made by Terraform. It is crucial to securely store this state file as it represents the actual state of the infrastructure. Terraform modules are used to define reusable infrastructure components. Modules are independent blocks representing different sections of the infrastructure and can be customized with parameters. Configuration Files: Terraform projects typically include configuration files such as 'main.tf,' 'variables.tf,' and 'outputs.tf.' These files determine how the infrastructure is defined and configured. Terraform creates and updates resources as defined, ensuring a specific state, making it a tool suitable for continuous integration and continuous deployment (CI/CD) processes without manual intervention.

CloudFormation: CloudFormation is a service provided by Amazon Web Services (AWS) that allows automatic creation and management of infrastructure resources (AWS, 2023). It is a managed AWS service that enables users to define AWS infrastructure using template files in JSON or YAML format, known as templates. These template files assist users in specifying the resources, relationships, and configurations they want to create. CloudFormation enables users to deploy their infrastructure quickly and in a repeatable manner. These templates can include resources such as virtual private clouds (VPCs), servers, databases, storage solutions, and other AWS services. In Figure 8, the CloudFormation architecture is depicted.

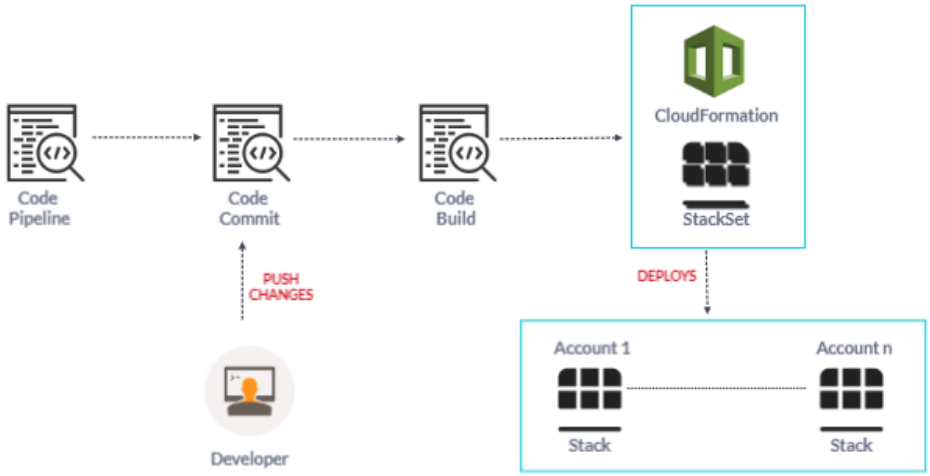

Figure 8. *The architecture of CloudFormation*

Code Pipeline is a fully managed continuous delivery service that automates the build, test, and deployment phases. Code Commit is a fully managed source control service that hosts secure and scalable Git repositories. CodeBuild is a fully managed build service that compiles source code, runs tests, and produces software packages that are ready to deploy. CloudFormation is a service that allows to define and provision AWS infrastructure as code using a template. The template is a JSON or YAML file that describes the resources needed and their configurations.

In summary, the user creates a template and pushes it to CloudFormation. CloudFormation then provides provisioning based on the specified resources. CloudFormation automates tasks such as tracking infrastructure changes, configuring security settings, and documenting the infrastructure. This allows users to manage their infrastructures and utilize their resources.

2.2. Key Concepts for Analyzing IaC Tools

Various concepts need to be considered when provisioning network infrastructure and providing a software development platform. It can be said that these concepts play a key role in the examination and evaluation of

IaC tools. In this section, these concepts that will be used in the analysis are discussed within the framework of IaC.

Idempotency: It is a concept that refers to producing the same result every time a software or script is executed (Rahman et al., 2020). Both in infrastructure provisioning and the delivery of software platforms, the presence of multiple components such as memory, bandwidth, and platforms are required within a collection structure. When scripts are executed, it is expected that these collections yield the same results consistently. The concept of idempotence is related to the situation where a script, even if it has been run before, can be executed again without causing any harm to the intended collections being created. Within this context, idempotence allows for the creation of new, consistent, and standard infrastructure while also facilitating the easy generation of collection components. Another advantage provided by idempotence is the ability to revert to a correctly functioning configuration to rectify errors stemming from incorrect configurations. When an IaC tool with idempotence feature is used, it allows for the reversal of erroneous changes and quick reconstruction within a short period. Idempotence also offers advantages in dynamic structures like cloud computing resource provisioning. It makes it easier to securely fix infrastructure-related issues, perform gradual upgrades, modify configurations, or manage scaling (Salonen, 2020). In essence, idempotence ensures that scripts, like code, reliably achieve the desired end goal on a collection of interconnected resources or components.

Approach: In both software development and infrastructure provisioning processes, the desired outcome is to create an idempotent collection of resources. IaC tools utilize two different approaches to achieve this: procedural and declarative methods (Bellendorf & Mann, 2020; Vladusic & Radolovic, 2020). The procedural approach involves preparing automation scripts by performing specific steps each time. In this approach, scaling creates more management overhead. However, existing configuration scripts are usually more understandable, making it generally an easier approach. In the declarative approach model, the desired infrastructure collection is expressed statically through declarations. In IaC tools that use this model, the existing conditions are examined to provide configurations dynamically, ensuring compatibility by calculating differences to achieve the desired infrastructure. Ansible and Puppet are declarative-based, while Chef is a procedural IaC tool (Muthoni et al., 2021).

Stateless: This concept refers to not storing session information or additional details about the used tool on the server or target systems within the IaC configuration tool. Automation yields the best results when applications are made stateless. In stateless approaches, each configuration request is treated as an independent request. This provides advantages in terms of speed and resource consumption (Salonen, 2020).

Architecture: This refers to whether IaC tools require code running as an agent on the target system to perform the configuration process on the target system (Alonso et al., 2023). Some IaC tools operate in an agent-based manner, while others work without requiring an agent. The installation of an agent onto the target system adds an extra process and burden. Therefore, it can be said that the agentless approach is more flexible (Hasbi et al., 2022). Agent-based approaches often utilize a client/server architecture.

*Infrastructure Stat*e: The process of changing production infrastructure components while all services or applications continue to run normally is known as mutable infrastructure. Such infrastructures bring together and organize components and resources to create a fully functional service or application. If any component, service, or configuration needs a change, it is updated by redeployment without any editing or modification. The old version is stopped, releasing resources for reuse, while the new version is compiled, tested, verified, and deployed. Patching and reconfiguration processes are not performed. One of the significant advantages of mutable infrastructures is the ability to quickly revert to a previous version when needed. On the other hand, immutable infrastructures can simplify configuration management by reducing the server space that needs to be managed by definition files (Johann, 2017).

Programming Language: IaC tools have been developed in various programming languages. The capabilities of these programming languages naturally determine the capabilities of the IaC tool as well (Rahman et al., 2021). Library support and module support, as language-specific capabilities, enhance the usability of an IaC tool. The modular structure provided by the development language assists in ease of maintenance, readability, and familiarity with the language. Furthermore, it allows changes to be applied incrementally and

independently (Shvetcova et al., 2019). Therefore, the language of an IaC tool being a widely-used language or closely related to a high-level programming language is an important advantage.

Data Format: Configuration commands executed by IaC tools need to be in a machine-readable format. For this purpose, XML, YAML, and JSON data types are commonly used data representation formats (Quattrocchi & Tamburri, 2023). Having configuration parameters or commands easily extractable in a readable form enhances the capabilities of an IaC tool. While XML is a self-descriptive data representation format, the process of extracting parameters for automation processes by machines can be more complex (Wąsowski & Berger, 2023). JSON is a more commonly used data representation format that expresses data in key-value pairs. Compared to XML, it is easier to read, and key-value pairs can be extracted more easily. Additionally, its similarity to the dictionary data format in the Python programming language has provided it with a broader range of applications. Another data representation format, YAML, consists of a simple structure of key-value pairs. As a result, it is commonly used for automating device configurations.

Management Purpose: IaC tools are used in the realms of provisioning, configuration, deployment, and orchestration from a managerial perspective. Provisioning refers to the acquisition of real or virtual computing, storage, and network infrastructure, enabling communication, bringing services online, and preparing them for use by operators and developers (Sandobalin et al., 2019). Configuration involves performing the necessary tasks, processes, and tests to set up fundamental applications and services, as well as preparing a low-level platform to deploy applications or a higher-level platform. Deployment typically refers to the creation, arrangement, integration, and preparation of multi-component applications or higher-level platforms across multiple nodes (Achar, 2021). Orchestration refers to the processes or workflows that connect automation tasks together to manage workload lifecycles in container environments, dynamically respond to changing conditions, and provide business advantages such as self-service. This is particularly relevant in container environments where various tasks are coordinated to achieve efficient and effective management (Artac et al., 2017).

Scalability: Scalability refers to the ability to manage infrastructure resources in a manner that aligns with the size, complexity, and requirements of an organization or project. In the context of Infrastructure as Code tools, scalability indicates the capability to effectively operate in larger and more complex systems. Scalable IaC solutions are noteworthy for their ability to adapt to factors such as increased workloads, user numbers, or data volumes. The ability of Infrastructure as Code tools to integrate with the cloud is also related to scalability. (Patni et al., 2020).

Security & Code Smells: Security in IaC refers to the built-in mechanisms and practices that help ensure the security of the deployed infrastructure. These features are essential for protecting sensitive data, preventing unauthorized access, and maintaining the overall security posture of the system. IaC tools often integrate with secrets management systems to securely store and manage sensitive information such as API keys, passwords, and certificates. These secrets are accessed programmatically by the IaC scripts without exposing them in the configuration files (Petrović et al., 2022). IaC tools can integrate with vulnerability scanning tools to identify security weaknesses in the deployed infrastructure. Automated scans help detect vulnerabilities, misconfigurations, and potential security threats, enabling timely remediation.

Cloud Integration: Cloud integration capability for IaC tools refers to the ability of these tools to seamlessly interact and integrate with various cloud service providers' APIs (Application Programming Interfaces) to provision, manage, and configure cloud resources (Diaz-De-Arcaya et al., 2023). IaC tools with cloud integration capabilities enable users to automate the deployment and management of cloud-based infrastructures using code.

3. RESULTS AND DISCUSSION

Infrastructure as Code is an application that defines complex processes, often cloud-based deployments, and configurations, through machine-readable code. It encompasses tasks such as configuration, resource allocation, application distribution, and sharing, achieved through various IaC tools. Despite its growing popularity, this study focuses on fundamental key concepts of IaC tools, as presented in Table 4. The same table also includes features that reflect the conceptual differences among IaC tools.

***Table 4**. Conceptual differences of IaC tools*

	Ansible	**Puppet**	**Chef**	**SaltStack**	**TerraForm**	**CloudFormation**
Code Approach	Procedural	Declarative	Procedural	Declarative	Declarative	Declarative
Architecture	Agentless	Client/Server	Client/Server	Client/Server	Agentless, Client-only	Agentless, Client-Server
Language	Python	Ruby	Ruby	Python	Go	AWS Lambda
Data Format	YAML	Embedded DSL	DSL / JSON	YAML	HCL	JSON, YAML
Configuration Tool	Playbook	Recipes / Cookbook	Cookbook	States	Modules, Resources	Template
Infrastructure	Mutable	Mutable	Mutable	Mutable	Mutable / Immutable	Mutable / Immutable
Management Purpose	Orchestration, Deployment, Provisioning	System Management, Code Management, Configuration Automation, Reporting	Developer Based Infrastructure Automation, Automatized workload deployment	System Management, Orchestration, Deployment	Orchestration, Provisioning, Configuration Management, Deployment	Provisioning, Configuration Management, Deployment
Model	Push	Pull	Pull	Pull	Push / Pull	Push/Pull
Ease of Use	Easy	Medium	Medium	Easy	Hard	Medium / Hard
Dependencies	Minimal	Medium	Medium	Medium	Minimal/ Medium	High
Cloud Integration	Multi Cloud	Multi Cloud	Multi Cloud	Multi Cloud	Multi Cloud	AWS Cloud

Idempotency has not been treated as a key value in the comparison and has not been shown in the table, as it is a goal for all IaC technologies. Puppet is a declarative IaC tool, whereas Ansible and Chef are procedural ones. The chef, being procedural, requires creating code step by step to specify how to reach an intended end state. Additionally, a Chef Client agent is needed on each server to be configured. Terraform and CloudFormation are declarative, allowing users to define the desired state of their infrastructure without specifying the step-by-step procedures to reach that state.

From an architectural perspective, when examined, the statelessness of IaC tools provides ease of use and flexibility. In the event of a potential server failure, Salt offers redundancy, making it highly advantageous. Puppet achieves the same effect through an alternative server, while Chef utilizes a backup server. Similarly, Ansible, operating without an agent, becomes a preferred configuration tool. Terraform follows a client-only architecture. It operates as a standalone command-line tool without the need for a central server or agent. CloudFormation operates using a centralized service architecture. CloudFormation uses a client-server model where the client (user or automation tool) sends requests to the CloudFormation service, which then takes care of coordinating the deployment and management.

The languages in which IaC tools are developed contribute to the tool's development and ensuring long-term support. Ansible is a tool written in the Python language, which is why it has found a broader range of applications. When examined in terms of data representation, YAML is more akin to natural language and is considered an easier language compared to XML, JSON, and DSLs due to its higher level of human-readability. Ansible can be considered more successful in this regard when compared to other tools. However, there is variability in syntax integrity within playbooks and other components, resulting in differences from one product to another. Terraform uses the HashiCorp Configuration Language. HCL is designed to be human-readable and easy to write. It uses a simple syntax with a focus on readability. CloudFormation templates are written in JSON or YAML. Terraform operates on a different paradigm. Instead of Cookbooks and Recipes, Terraform uses the concept of modules and resources. Modules are collections of Terraform configurations and resources represent the infrastructure components. CloudFormation uses a template-based approach in

which the entire infrastructure is defined as code in a single document.

Configuration management tools like Chef, Puppet, Ansible, and SaltStack inherently follow a mutable infrastructure paradigm. For example, when a new version of an application needs to be deployed, the software update runs on existing servers, and changes occur on the nodes. However, over time, as more updates are performed, each server accumulates a distinct and unique change history. This can lead to difficult-to-diagnose, subtle configuration errors. SaltStack uses a declarative language called Salt State Language to define how systems should be configured. The States in SaltStack are similar in concept to Cookbooks in Chef, but the terminology and approach are different. States define the desired state of a system, and the SaltStack system then applies those states to manage and configure the infrastructure. Both Terraform and CloudFormation provide flexibility in managing both mutable and immutable infrastructure.

When viewed from the perspective of server configuration, Ansible, Chef, Puppet, and SaltStack are tools specifically designed to configure servers using the infrastructure-as-code approach. They utilize configuration definition files with a Domain Specific Language designed for server configuration. The IaC tool reads definitions from these files and applies the relevant configuration to a server. Many server configuration tools use an agent installed on each server. Both Chef and Puppet are designed to work in this manner by default. The concepts of Pull and Push are related to how changes in infrastructure are applied and managed. Ansible uses push model to configure. By default, it uses SSH keys to connect to servers and execute commands. It benefits from not requiring configuration agents installed on managed servers, yet SSH usage can slow down large-scale networks. Furthermore, Ansible is more focused on orchestration rather than just configuration management. Puppet, Saltstack and Chef use pull model. Terraform is more explicitly pull-oriented, both Terraform and CloudFormation can be integrated into CI/CD workflows, allowing for automation and collaboration in a push-centric or pull-centric manner, depending on the use case and preferences.

Cloud integration is an important feature for IaC tools. While Ansible, SaltStack, Chef, Puppet, and Terraform support multi-cloud systems such as Google Cloud, AWS, and Azure, CloudFormation is specific to AWS. Ansible uses modules to interact with cloud APIs, allowing users to manage cloud resources alongside other infrastructure components. Puppet modules and tasks can be used to manage cloud resources, and there are specific modules for different cloud providers.

From a development environment perspective, Ansible and SaltStack are perceived as more advantageous management tools compared to others. These tools are more oriented towards system operators. Conversely, Puppet and Chef tools are arguably more developer focused. The user-friendliness of Ansible makes it ideal for entry-level operations. However, Puppet and Terraform, requiring knowledge of Domain Specific Language, is more developer-oriented in terms of usability when compared to other tools. CloudFormation utilizes AWS Lambda, a serverless computing service that enables users to execute code without the need to explicitly provision or manage servers.

When looking at ease of use, various factors such as the structure of tasks, the prevalence of the programming language, scalability, user knowledge, and code complexity affect usability. In this regard, although Ansible and SaltStack are perceived as more user-friendly and practical, they can still pose challenges for individuals like everyday users or professors who lack highly technical expertise. Conversely, Terraform takes it a step further by introducing its own configuration language, thereby adding another layer of complexity.

Another factor affecting ease of use is the dependencies of the tools being used. Another factor affecting ease of use is the dependencies of the tools being used. Ansible requires minimal dependencies on the managed nodes. It communicates using SSH for Unix-based systems and Windows. Therefore, it doesn't necessitate agent installation on target machines. Terraform is a standalone binary that doesn't require installation on the target systems. It communicates with APIs of cloud providers and other infrastructure services. While it has minimal dependencies, the necessary provider plugins need to be available. Chef requires the installation of a Chef client on each node that it manages. This client communicates with the Chef server. The server, in turn, stores configuration data and cookbooks. SaltStack uses a master-minion architecture. The Salt Minion needs to be installed on target nodes, and they communicate with the Salt Master. While this introduces some dependencies, SaltStack is known for its flexibility and scalability. Puppet follows a master-agent architecture

similar to SaltStack. The Puppet agent needs to be installed on managed nodes, communicating with the Puppet Master. It also requires the installation of the Puppet server. CloudFormation is specific to AWS and is primarily used within the AWS ecosystem. Users need to have AWS credentials and permissions. Dependencies are managed by AWS itself.

In light of all these key concepts, we developed a recommendation tree regarding which tool to use. This tree structure is provided in Figure 9.

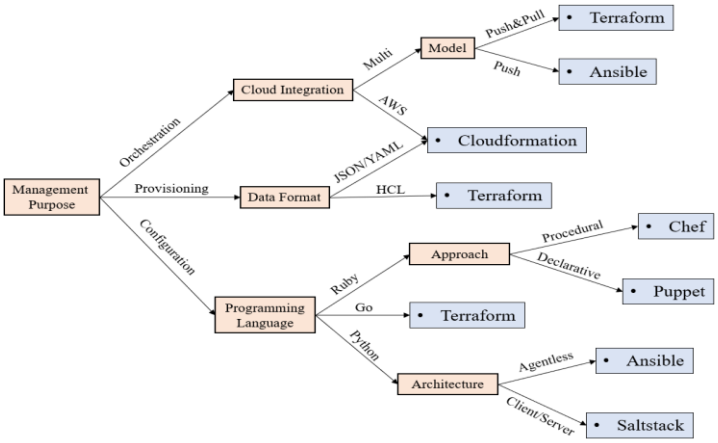

***Figure 9**. Differentiation based on the features of IaC tools*

Provisioning, orchestration, and configuration applications can be implemented using Infrastructure as Code (IaC) tools. Depending on the purpose, a network automation or cloud application can be developed by following the tree structure shown in Figure 9. For example, if the goal is to provide provisioning and one is familiar with which data format (HCL, YAML, JSON), options like CloudFormation or Terraform can be chosen. If an orchestration process needs to be performed, the choice between Ansible and Terraform depends on whether Cloud integration is multi-cloud supported or specific to AWS. To make the selection more specific, choosing between a Push model or a push&pull model can be determined, and a choice between these two IaC tools can be made. Relative concepts such as ease of use were not taken into consideration when constructing the tree structure.

This tree structure has been created to clarify the specific use of Infrastructure as Code tools. Objectives, architecture, programming language, data format, and cloud integration capability, among other distinguishing features, assist in focusing on each IaC tool's particular strengths. For instance, for the purpose of provisioning, tools like Cloudformation and Terraform are recommended, while a choice between Ansible and Terraform may be necessary for orchestration processes. Additionally, taking into account factors such as compatibility with a specific cloud infrastructure and ease of use, this tree structure guides the selection of IaC tools tailored to specific use cases. Consequently, users can make more informed and effective decisions when choosing the most suitable IaC tool for their needs.

4. CONCLUSION

In this study, a comprehensive systematic review of Infrastructure as Code tools has been presented with the aim of assessing the current state, highlighting potential future trends, and emphasizing existing challenges. This study significantly contributes to the existing literature by conducting a comprehensive and systematic review of Infrastructure as Code tools. By thoroughly examining IaC tools through key concepts and fundamental aspects such as code approach, architecture, language, data format, configuration tool, infrastructure management, model, and ease of use, this research provides valuable insights into the current state of IaC technologies. The study not only identifies the characteristics and advantages of these tools but also emphasizes the positive impact of integrating multiple IaC tools within the same environment on network automation processes.

In addition to the comprehensive analysis of Infrastructure as Code tools, this study stands out by focusing on the latest updates from articles and gray literature sources. By extracting key concepts from these recent publications, the research ensures that the findings are not only grounded in established knowledge but also reflect the most current trends and developments in the field of IaC technologies. This approach provides a forward-looking perspective, allowing for a nuanced understanding of the evolving landscape of IaC tools. By incorporating insights from the latest articles and gray literature, the study captures cutting-edge practices and emerging challenges, enriching the overall analysis, and contributing to a more holistic view of the subject matter. This approach not only strengthens the validity of the research findings but also positions the study as a valuable resource for both scholars and practitioners seeking up-to-date and relevant information on IaC tools. This study goes a step further by constructing a recommendation tree for the strategic usage of IaC tools. By creating this structured framework, the research provides practical guidance to decision-makers and practitioners in navigating the complexities of IaC implementation. The recommendation tree outlines tailored strategies based on the specific requirements and goals of different projects and organizations.

This structured approach not only helps in the selection of appropriate IaC tools but also guides users on their optimal utilization, ensuring alignment with organizational objectives, scalability, security, and efficiency. The recommendation tree serves as a valuable roadmap, aiding in the decision-making process and enhancing the strategic deployment of IaC tools within diverse contexts. By integrating this strategic perspective, the study not only enriches the scholarly discourse but also offers actionable insights that can be directly applied in real-world scenarios, making it a valuable resource for both academic research and practical implementations in the field.

This study contributes to our understanding of the overall performance and utilization of IaC tools, potentially helping shape future developments more effectively. In addition, aspects such as security, resource utilization, and user-friendliness were not considered within the scope of this study. Conducting research that evaluates IaC tools based on these features would lead to more effective benefits from IaC technologies. Similarly, when considering scenarios involving the simultaneous use of multiple IaC tools in the same environment, conducting analysis and studies on the integration and interoperability of these tools would provide positive contributions to network automation processes.

While aspects like security, resource utilization, and user-friendliness were not within the scope of this study, the research highlights the need for future investigations in these areas. By evaluating IaC tools based on these features and conducting analysis on the integration and interoperability of multiple tools in the same environment, future studies can further enhance the effectiveness and benefits of IaC technologies, contributing significantly to the advancement of network automation processes.

CONFLICT OF INTEREST

The authors declare no conflict of interest.

REFERENCES

Achar, S. (2021). Enterprise SaaS Workloads on New-Generation Infrastructure-as-Code (IaC) on Multi-Cloud Platforms. *Global Disclosure of Economics and Business*, *10*(2), 55-74. https://www.doi.org/10.18034/gdeb.v10i2.652

Alonso, J., Piliszek, R., & Cankar, M. (2023). Embracing IaC Through the DevSecOps Philosophy: Concepts, Challenges, and a Reference Framework. *IEEE Software*, *40*(1), 56-62. https://www.doi.org/10.1109/MS.2022.3212194

Artac, M., Borovssak, T., Di Nitto, E., Guerriero, M., & Tamburri, D. A. (2017, May 20-28). *DevOps: Introducing infrastructure-as-code*. In: Proceedings of the IEEE/ACM 39th International Conference on Software Engineering Companion (ICSE-C 2017), (pp. 497-498). https://www.doi.org/10.1109/ICSE-C.2017.162

Artac, M., Borovsak, T., Di Nitto, E., Guerriero, M., Perez-Palacin, D., & Tamburri, D. A. (2018, April 30 - May 4). *Infrastructure-as-Code for Data-Intensive Architectures: A Model-Driven Development Approach*.

In: Proceedings of the IEEE 15th International Conference on Software Architecture (ICSA 2018), (pp. 156-165). https://www.doi.org/10.1109/ICSA.2018.00025

AWS Architecture Blog. (2023). AWS Cloudformation (Accesed:13/11/2023) URL

Balon, T., & Baggili, I. (Abe). (2023). Cybercompetitions: A survey of competitions, tools, and systems to support cybersecurity education. *Education and Information Technologies*, *28(9)*, 11759-11791. https://www.doi.org/10.1007/s10639-022-11451-4

Bellendorf, J., & Mann, Z. Á. (2020). Specification of cloud topologies and orchestration using TOSCA: a survey. *Computing*, *102*(8), 1793-1815. https://www.doi.org/10.1007/s00607-019-00750-3

Bessghaier, N., Sayagh, M., Ouni, A., & Mkaouer, M. W. (2023). What Constitutes the Deployment and Run-Time Configuration System? An Empirical Study on OpenStack Projects. *ACM Transactions on Software Engineering and Methodology*, *33*(1), 1-37. https://www.doi.org/10.1145/3607186

Chen, W., Wu, G., & Wei, J. (2018, October 15-18). *An Approach to Identifying Error Patterns for Infrastructure as Code*. In: Proceedings of the 29th IEEE International Symposium on Software Reliability Engineering Workshops (ISSREW 2018), (pp. 124-129). https://www.doi.org/10.1109/ISSREW.2018.00-19

Chiari, M., De Pascalis, M., & Pradella, M. (2022, March 12-15). *Static Analysis of Infrastructure as Code: a Survey*. In: Proceedings of the IEEE 19th International Conference on Software Architecture Companion (ICSA-C), (pp. 218-225). https://www.doi.org/10.1109/ICSA-C54293.2022.00049

Daffalla Elradi, M. (2023). Ansible: A Reliable Tool for Automation. *Electrical and Computer Engineering Studies*, *2*(1), 1-10. https://www.doi.org/10.58396/eces020104

Dalla Palma, S., van Asseldonk, C., Catolino, G., Di Nucci, D., Palomba, F., & Tamburri, D. A. (2023). "Through the looking-glass …" An empirical study on blob infrastructure blueprints in the Topology and Orchestration Specification for Cloud Applications. *Journal of Software: Evolution and Process*, 1-22. https://www.doi.org/10.1002/smr.2533

Dalla Palma, S., Di Nucci, D., Palomba, F., & Tamburri, D. A. (2020). Toward a catalog of software quality metrics for infrastructure code. *Journal of Systems and Software*, *170*, 110726. https://www.doi.org/10.1016/j.jss.2020.110726

De Pascalis, M. (2022). *Formal verification of infrastructure as code*. MSc Thesis, Polytechnic University of Milan.

Diaz-De-Arcaya, J., Osaba, E., Benguria, G., Etxaniz, I., Lobo, J. L., Alonso, J., Torre-Bastida, A. I., & Almeida, A. (2023, April 15-19). *IEM: A Unified Lifecycle Orchestrator for Multilingual IaC Deployments*. In: Proceedings of the Companion of the 2023 ACM/SPEC International Conference on Performance Engineering (ICPE 2023), (pp. 195-199). https://www.doi.org/10.1145/3578245.3584938

Falazi, G., Breitenbucher, U., Leymann, F., Stotzner, M., Ntentos, E., Zdun, U., Becker, M., & Heldwein, E. (2022, March 12-15). *On Unifying the Compliance Management of Applications Based on IaC Automation*. In: Proceedings of the IEEE 19th International Conference on Software Architecture Companion (ICSA-C 2022), (pp. 226-229). https://www.doi.org/10.1109/ICSA-C54293.2022.00050

Gorroñogoitia, J., Radolović, D., Vasileiou, Z., Meditskos, G., Karakostas, A., Vrochidis, S., & Bachras, M. (2022). The SODALITE Model-Driven Approach. In: E. Di Nitto, J. Gorroñogoitia Cruz, I. Kumara, D. Radolović, K. Tokmakov, & Z. Vasileiou (Eds.), *Deployment and Operation of Complex Software in Heterogeneous Execution Environments* (pp. 23-52). SpringerBriefs in Applied Sciences and Technology, Springer, Cham. https://www.doi.org/10.1007/978-3-031-04961-3_3

Guerriero, M., Garriga, M., Tamburri, D. A., & Palomba, F. (2019, September 29 - October 4). *Adoption, Support, and Challenges of Infrastructure-as-Code: Insights from Industry*. In: Proceedings of the IEEE International Conference on Software Maintenance and Evolution (ICSME 2019), (pp. 580-589). https://www.doi.org/10.1109/ICSME.2019.00092

Gupta, M., Chowdary, M. N., Bussa, S., & Chowdary, C. K. (2021, October 22-23). *Deploying Hadoop Architecture Using Ansible and Terraform*. In: Proceedings of the 5th International Conference on Information

Systems and Computer Networks (ISCON), (pp. 1-6). https://www.doi.org/10.1109/ISCON52037.2021.9702299

Gurbatov, G. (2022). *A comparison between Terraform and Ansible on their impact upon the lifecycle and security management for modifiable cloud infrastructures in OpenStack*. MSc Thesis, Blekinge Institute of Technology.

Hasbi, M., Reza Aristiadi Nurwa, A., Febriyan Priambodo, D., Riski Aulia Putra, W., Sinar Nusantara, S., & Siber dan Sandi Negara, P. (2022). Infrastructure as Code for Security Automation and Network Infrastructure Monitoring. *Teknik Informatika Dan Rekayasa Komputer*, *22*(1), 203-217. https://www.doi.org/10.30812/matrik.v22i1.2471

Heap, M. (2016). *Ansible: from beginner to pro*. Apress. https://www.doi.org/10.1007/978-1-4842-1659-0

Ibrahim, A., Yousef, A. H., & Medhat, W. (2022, May 8-9). *DevSecOps: A Security Model for Infrastructure as Code over the Cloud*. In: Proceedings of the 2nd International Mobile, Intelligent, and Ubiquitous Computing Conference (MIUCC 2022), (pp. 284-288). https://www.doi.org/10.1109/MIUCC55081.2022.9781709

Johann, S. (2017). Kief Morris on Infrastructure as Code. *IEEE Software*, *34*(1), 117-120, https://www.doi.org/10.1109/MS.2017.13

Karlsson, D. (2023). *Comparison of infrastructure as code frameworks from a developer perspective*. MSc Thesis, Linköping University.

Kumara, I., Garriga, M., Romeu, A. U., Di Nucci, D., Palomba, F., Tamburri, D. A., & van den Heuvel, W. J. (2021). The do's and don'ts of infrastructure code: A systematic gray literature review. *Information and Software Technology*, *137*(March), 106593. https://www.doi.org/10.1016/j.infsof.2021.106593

L'Esteve, R. C. (2023). Applying DevOps. In: R. C. L'Esteve (Eds.), *The Cloud Leader's Handbook: Strategically Innovate, Transform, and Scale Organizations* (pp. 105-122). Apress. https://www.doi.org/10.1007/978-1-4842-9526-7_7

Manner, J. (2023, July 2-8). *A Structured Literature Review Approach to Define Serverless Computing and Function as a Service*. In: Proceedings of the IEEE International Conference on Cloud Computing, (pp. 516-522). https://www.doi.org/10.1109/CLOUD60044.2023.00068

Murphy, O. (2022). *Adoption of Infrastructure as Code (IaC) in Real World Lessons and practices from industry*. MSc Thesis, JAMK University of Applied Sciences.

Mustafa, O. (2023). Understanding DevOps Concepts. In: *A Complete Guide to DevOps with AWS: Deploy, Build, and Scale Services with AWS Tools and Techniques* (pp. 37-78). Apress. https://www.doi.org/10.1007/978-1-4842-9303-4_2

Muthoni, S., Okeyo, G., & Chemwa, G. (2021, December 9-10). *Infrastructure as Code for Business Continuity in Institutions of Higher Learning*. In: Proceedings of the International Conference on Electrical, Computer and Energy Technologies (ICECET), (pp. 1-6). https://www.doi.org/10.1109/ICECET52533.2021.9698544

Ning, A. (2023, February 24-26). *An Ansible-based Distributed Application Architecture Rapid Deployment Scheme*. In: Proceedings of the IEEE 2nd International Conference on Electrical Engineering, Big Data and Algorithms (EEBDA), (pp. 972-975). https://www.doi.org/10.1109/EEBDA56825.2023.10090753

Opdebeeck, R., Zerouali, A., Velazquez-Rodriguez, C., & Roover, C. De. (2020, September 28 - October 2). *Does Infrastructure as Code Adhere to Semantic Versioning? An Analysis of Ansible Role Evolution*. In: Proceedings of the 20th IEEE International Working Conference on Source Code Analysis and Manipulation (SCAM 2020), (pp. 238-248). https://www.doi.org/10.1109/SCAM51674.2020.00032

Opdebeeck, R., Zerouali, A., & Roover, C. De. (2023a). Infrastructure-as-Code Ecosystems. In: T. Mens, C. De Roover, & A. Cleve (Eds.), *Software Ecosystems: Tooling and Analytics* (pp. 215-245). Springer International Publishing. https://www.doi.org/10.1007/978-3-031-36060-2_9

Opdebeeck, R., Zerouali, A., & De Roover, C. (2023b, May 15-16). *Control and Data Flow in Security Smell Detection for Infrastructure as Code: Is It Worth the Effort?*. In: Proceedings of the IEEE/ACM 20th International Conference on Mining Software Repositories (MSR 2023), (pp. 534-545). https://www.doi.org/10.1109/MSR59073.2023.00079

Patni, J. C., Banerjee, S., & Tiwari, D. (2020, July 2-4). *Infrastructure as a Code (IaC) to Software Defined Infrastructure using Azure Resource Manager (ARM)*. In: Proceedings of the International Conference on Computational Performance Evaluation (ComPE 2020), (pp. 575-578). https://www.doi.org/10.1109/ComPE49325.2020.9200030

Petrović, N., Cankar, M., & Luzar, A. (2022, November 15-16). *Automated Approach to IaC Code Inspection Using Python-Based DevSecOps Tool*. In: Proceedings of the 30th Telecommunications Forum (TELFOR), (pp. 1-4). https://www.doi.org/10.1109/TELFOR56187.2022.9983681

Quattrocchi, G., & Tamburri, D. A. (2023). Infrastructure as Code. *IEEE Software*, *40*(1), 37-40. https://www.doi.org/10.1109/MS.2022.3212034

Rahman, A. (2018, May 27 - June 3). *Characteristics of defective infrastructure as code scripts in DevOps*. In: Proceedings of the International Conference on Software Engineering, (pp. 476-479). https://www.doi.org/10.1145/3183440.3183452

Rahman, A., Barsha, F. L., & Morrison, P. (2021, October 18-20). *Shhh: 12 Practices for Secret Management in Infrastructure as Code*. In: Proceedings of the IEEE Secure Development Conference (SecDev 2021), (pp. 56-62). https://www.doi.org/10.1109/SecDev51306.2021.00024

Rahman, A., Farhana, E., Parnin, C., & Williams, L. (2020, June 27 - July 19). *Gang of eight: A defect taxonomy for infrastructure as code scripts*. In: Proceedings of the International Conference on Software Engineering, (pp. 752-764). https://www.doi.org/10.1145/3377811.3380409

Rahman, A., Parnin, C., & Williams, L. (2019, May 25-31). *The Seven Sins: Security Smells in Infrastructure as Code Scripts*. In: Proceedings of the International Conference on Software Engineering, (pp. 164-175). https://www.doi.org/10.1109/ICSE.2019.00033

Rahman, A., & Williams, L. (2021). Different Kind of Smells: Security Smells in Infrastructure as Code Scripts. *IEEE Security and Privacy*, *19*(3), 33-41. https://www.doi.org/10.1109/MSEC.2021.3065190

Raj, K. A., Anand, A., & Sahana, V. (2022). DevOps and Tools Used: A Systematic Review. (Accessed: 12/11/2023) URL

Salonen, E. (2020). *Software Project Services using Infrastructure-as-Code*. MSc Thesis, University of Vaasa.

Sandobalin, J., Insfran, E., & Abrahao, S. (2017, June 25-30). *An Infrastructure Modelling Tool for Cloud Provisioning*. In: Proceedings of the IEEE 14th International Conference on Services Computing (SCC 2017), (pp. 354-361). https://www.doi.org/10.1109/SCC.2017.52

Sandobalin, J., Insfran, E., & Abrahao, S. (2019, September 15-20). *ARGON: A model-driven infrastructure provisioning tool*. In: Proceedings of the ACM/IEEE 22nd International Conference on Model Driven Engineering Languages and Systems Companion (MODELS-C 2019), (pp. 738-742). https://www.doi.org/10.1109/MODELS-C.2019.00114

Santos, A., Bernardino, J., & Correia, N. (2023). Automated Application Deployment on Multi-Access Edge Computing: A Survey. *IEEE Access*, *11*(July), 89393-89408. https://www.doi.org/10.1109/ACCESS.2023.3307023

Schwarz, J., Steffens, A., & Lichter, H. (2018, September 4-7). *Code smells in infrastructure as code*. In: Proceedings of the International Conference on the Quality of Information and Communications Technology (QUATIC 2018), (pp. 220-228). https://www.doi.org/10.1109/QUATIC.2018.00040

Shvetcova, V., Borisenko, O., & Polischuk, M. (2019, September 13-14). *Domain-Specific Language for Infrastructure as Code*. In: Proceedings of the Ivannikov Memorial Workshop (IVMEM 2019), (pp. 39-45). https://www.doi.org/10.1109/IVMEM.2019.00012

Singh, N. K., Thakur, S., Chaurasiya, H., & Nagdev, H. (2016, September 4-5). *Automated provisioning of application in IAAS cloud using Ansible configuration management*. In: Proceedings of the 1st International Conference on Next Generation Computing Technologies (NGCT 2015, September), (pp. 81-85). https://www.doi.org/10.1109/NGCT.2015.7375087

Sokolowski, D. (2022, November 14-18). *Infrastructure as code for dynamic deployments*. In: Proceedings of the 30th ACM Joint Meeting European Software Engineering Conference and Symposium on the Foundations of Software Engineering, (pp. 1775-1779). https://www.doi.org/10.1145/3540250.3558912

Sokolowski, D., & Salvaneschi, G. (2023, March 13-17). *Towards Reliable Infrastructure as Code*. In: Proceedings of the IEEE 20th International Conference on Software Architecture Companion (ICSA-C 2023), (pp. 318-321). https://www.doi.org/10.1109/ICSA-C57050.2023.00072

Sokolowski, D., Weisenburger, P., & Salvaneschi, G. (2023). Decentralizing Infrastructure as Code. *IEEE Software*, *40*(1), 50-55. https://www.doi.org/10.1109/MS.2022.3192968

Soll, M., Helmken, H., Belde, M., Schimpfhauser, S., Nguyen, F., & Versick, D. (2023, May 1-4). *Building an IT Security Laboratory for Complex Teaching Scenarios Using "Infrastructure as Code."* In: Proceedings of the IEEE Global Engineering Education Conference (EDUCON, 2023-May), (pp. 1-8). https://www.doi.org/10.1109/EDUCON54358.2023.10125250

Sorour, A., & Hamdy, A. (2022, July 21-23). *DevOps and IaC to Automate the Delivery of Hands-On Software Lab Exams*. In: Proceedings of the 6th International Conference on Computer, Software and Modeling (ICCSM), (pp. 28-35). https://www.doi.org/10.1109/ICCSM57214.2022.00012

Spielmann, D., Sokolowski, D., & Salvaneschi, G. (2023, October 22-27). *Extensible Testing for Infrastructure as Code*. In: Proceedings of the Companion Proceedings of the 2023 ACM SIGPLAN International Conference on Systems, Programming Languages, and Applications: Software for Humanity, (pp. 58-60). https://www.doi.org/10.1145/3618305.3623607

Statista (2023) Usage of cloud configuration tools worldwide in 2023, current and planned. (Accessed: 13/11/2023) URL

Surianarayanan, C., & Chelliah, P. R. (2023). Cloud Integration and Orchestration. In: *Essentials of Cloud Computing: A Holistic, Cloud-Native Perspective* (2nd ed., pp. 305-319). Springer International Publishing. https://www.doi.org/10.1007/978-3-031-32044-6_11

Tankov, V., Valchuk, D., Golubev, Y., & Bryksin, T. (2021). *Infrastructure in Code: Towards Developer-Friendly Cloud Applications*. In: 36th IEEE/ACM International Conference on Automated Software Engineering (ASE 2021), (pp. 1166-1170). https://www.doi.org/10.1109/ASE51524.2021.9678943

Terraform (2023). Terrafform documentation. (Accessed: 10/11/2023) URL

Tripathi, A. (2023). *Provisioning Secure Cloud Environment Using Policy-as-code and Infrastructure-as-code*. MSc Thesis, School of Computing National College of Ireland.

Vladusic, D., & Radolovic, D. (2020, September 1-4). *Infrastructure as Code for Heterogeneous Computing*. In: Proceedings of the 22nd International Symposium on Symbolic and Numeric Algorithms for Scientific Computing (SYNASC), (pp. 1-2). https://www.doi.org/10.1109/SYNASC51798.2020.00011

Wąsowski, A., & Berger, T. (2023). Concrete Syntax. In: *Domain-Specific Languages: Effective Modeling, Automation, and Reuse* (pp. 87-142). Springer International Publishing. https://www.doi.org/10.1007/978-3-031-23669-3_4

Witt, A., & Westling, S. (2023). *Ansible In Different Cloud Environments*. MSc Thesis, Mälardalen University.

Zadka, M. (2019). Salt Stack. In: *DevOps in Python: Infrastructure as Python* (pp. 121-137). Apress. https://www.doi.org/10.1007/978-1-4842-4433-3_10

Zhang, Y., Wu, F., & Rahman, A. (2023, March 13-17). *Practitioner Perceptions of Ansible Test Smells*. In: Proceedings of the IEEE 20th International Conference on Software Architecture Companion (ICSA-C 2023), (pp. 325-327). https://www.doi.org/10.1109/ICSA-C57050.2023.00074

Research Article GU J Sci, Part A, 10(4): 472-486 (2023) 10.54287/gujsa.1379024

Gazi University
Journal of Science
PART A: ENGINEERING AND INNOVATION
http://dergipark.org.tr/gujsa

A New Feature Selection Metric Based on Rough Sets and Information Gain in Text Classification

Rasim ÇEKİK[1] Mahmut KAYA[2*]

[1] Department of Computer Engineering, Şırnak University, Şırnak, Türkiye
[2] Department of Computer Engineering, Siirt University, Siirt, Türkiye

Keywords

Feature Selection
Text Classification
Rough Set
Dimensiomality Reduction

Abstract

In text classification, taking words in text documents as features creates a very high dimensional feature space. This is known as the high dimensionality problem in text classification. The most common and effective way to solve this problem is to select an ideal subset of features using a feature selection approach. In this paper, a new feature selection approach called Rough Information Gain (RIG) is presented as a solution to the high dimensionality problem. Rough Information Gain extracts hidden and meaningful patterns in text data with the help of Rough Sets and computes a score value based on these patterns. The proposed approach utilizes the selection strategy of the Information Gain Selection (IG) approach when pattern extraction is completely uncertain. To demonstrate the performance of the Rough Information Gain in the experimental studies, the Micro-F1 success metric is used to compare with Information Gain Selection (IG), Chi-Square (CHI2), Gini Coefficient (GI), Discriminative Feature Selector (DFS) approaches. The proposed Rough Information Gain approach outperforms the other methods in terms of performance, according to the results.

Cite

Cekik, R., & Kaya, M. (2023). A New Feature Selection Metric Based on Rough Sets and Information Gain in Text Classification. *GU J Sci, Part A, 10*(4), 472-486. doi:10.54287/gujsa.1379024

Author ID (ORCID Number)

0000-0002-7820-413X Rasim ÇEKİK
0000-0002-7846-1769 Mahmut KAYA

Article Process

Submission Date 20.10.2023
Revision Date 08.11.2023
Accepted Date 17.11.2023
Published Date 12.12.2023

1. INTRODUCTION

Several applications, such as e-commerce, social networks, location-based services, and information collecting and distribution centers, have emerged as a result of technology's rapid progress. This has resulted in the creation of big data in the digital environment. Most of this data consists of text documents. Examples of text documents include news published on news sites, tweets and posts on social media, and comments about products on e-commerce sites. However, in information gathering and distribution centers, people prefer to see only the web pages (or documents) that interest them and do not want to see irrelevant ones. Therefore, text data needs to be categorized and indexed according to their content. This allows web pages to be easily searched. But since text data has a large volume, it is impossible to process it manually. To overcome this challenge, automatic document classification methods have been proposed. This process is called text classification or categorization. One of the main problems in the field of text classification is that using one or more of each word in the document as a feature lead to high dimensional data problems. To provide a solution to this problem, feature selection methods aim to select the optimal subset in the entire feature set space. This optimal set consists of highly discriminative terms and is expected to be the subset that best represents the entire feature set. The basic purpose of feature selection methods is to select the best, most optimal set of features. Selection techniques are one of the methods that increase the performance and success of decision systems such as machine learning and reduce the execution time (Kaya et al., 2013; Kaya & Bilge, 2016; Şenol, 2023). Therefore, the success of the selection technique is an important factor in problem solving.

*Corresponding Author, e-mail: mahmutkaya@siirt.edu.tr

According to their working principles, feature selection techniques can be grouped under three headings: filter, embedding and wrapper. Filter methods calculate a score for each feature separately and work by selecting n features with the highest scores. Embedded techniques integrate the feature selection process directly into the classification algorithm and this approach is often used in certain learning algorithms. Wrapper techniques try to select the optimal subset of features using a classifier. In the literature, there are several feature selection approaches related to these different techniques. For example, improved gini index (IGI) (Shang et al., 2007), distinguishing feature selector (DFS) (Uysal & Gunal, 2012), global information gain (GIG) (Shang et al., 2013), class discriminating measure (CDM) (Chen et al., 2009), multivariate relative discrimination criterion (MRDC) (Labani et al., 2018), Fisher's discriminant ratio (Wang et al., 2009), normalized difference measure (NDM) (Rehman et al., 2017), max-min ratio (MMR) (Rehman et al., 2018) and proportional rough feature selector (PRFS) (Cekik & Uysal, 2020) are known correlation-based methods. Frequency-based, evolutionary algorithm-based and other theory-based techniques are frequently used in the literature for this purpose.

In this study, a new filter feature selector method called Rough Information Gain (RIG) based on correlation-based Rough Set Theory and Information Gain is proposed. The proposed method works by using different structures according to the three states "certain", "roughly certain" and "uncertain" in the text document information system. With the help of Rough Sets, the status of the text documents (certain, roughly certain and uncertain) is determined. If the state is uncertain, then Information Gain comes into play and a score value is calculated for the state. In other cases, Rough Sets and Information Gain work together to produce a score, and finally a score value for each feature.

2. RELATED WORKS

Feature selection is the procedure of selecting the most representative, highly discriminative features from a set of accessible features using a feature selection algorithm. This concept has been addressed in the literature with many studies investigating different feature selection approaches. For example, there are traditional methods such as Information Gain (IG), Gain Ratio (GR), Gini Index (GI), Chi2, Mutual Information (MI) (Sharmin et al., 2019) as well as recently proposed approaches such as DFS, NDM, MMR and MRDC. Many of these methods are widely used in applications such as text classification (Cekik & Uysal, 2022). The IG approach is commonly used, particularly in data and text mining. This method is centered on Shannon's information theory and thermodynamic concepts. However, if there are many different values that an attribute can take, the IG method may select it as an attribute that is easily memorized by the system. GR computes the gain ratio by dividing the discrimination information for each feature by the information gain to overcome this problem. GI is an alternative feature selection approach to IG and GR and does not use the entropy value. The Chi2 method statistically evaluates the chi-square values of all features according to their class. MI is another approach for calculating the interdependence of a feature and a class label. However, it can tend to prioritize rare features and can be sensitive to errors in probability estimation. The DP method is a widely used approach in the field of information retrieval to identify influential words and has been adapted to feature selection problems (Ogura et al., 2009). These methods offer different approaches to the feature selection process and it is important to decide which method will work better depending on the context of the problem to be applied.

DFS is one of the recently proposed novel approaches for feature selection, in addition to the traditional techniques. DFS produces a value between 0.5 and 1.0 according to the feature importance of each term. One of the recent studies, RDC, was presented by Rehman et al. (2015) as a new feature selection approach. This method takes into account the document frequencies of each term when identifying highly discriminative terms. The MRDC method was developed by Labani et al. (2018). T The fitness value for each term is calculated using Pearson correlation, and the selected term set is evaluated using a supervised learning algorithm. There is also a new text classification method called NDM proposed by Rehman et al. (2017). This approach is designed for text classification using a balanced accuracy measure. However, considering that it is not effective on imbalanced datasets with high sparsity, a new approach called MMR is proposed by the same authors. Finally, Wang and Hong (2019) proposed HRFS, a Hebb-rule feature selection model for text classification. This model considers the class and terms as neurons and focuses on selecting terms with high discriminative power. Cekik and Uysal (2022) introduces a new feature selection approach called the XY method, which effectively operates on short texts. This approach works by computing the distance between

two points in a two-dimensional plane and the XY line. This point's position is determined by the number of documents in which a phrase appears in one class versus the number of documents in which it appears in another class.

In the literature, apart from filter techniques for text classification, methods such as Linear Forward Search (LFS) (Gutlein et al., 2009), Span-Bound and RW-Bound (Weston et al., 2001) are examples of wrapper approaches, while methods such as EGA (Ghareb et al., 2016), FSS (Bermejo et al., 2012), HybridBest and HybridGreedy (Chou et al., 2010) are examples of embedded approaches. It should be noted that in the field of text classification, filter approaches are represented by more studies than other methods. This perspective is the result of the fact that filter approaches can work faster and more efficiently on high-dimensional data. Consequently, it is a fact that filter-based feature selection methods still need better and more efficient solutions. The main motivation of this work is to present new filter-based feature selection approaches that can work effectively in the field of text classification.

3. PRELIMINARIES AND BACKGROUND

3.1. Rough Set Theory

Rough Set Theory (RST) (Pawlak, 1998; Zhang et al., 2016) is a mathematical approach proposed by Pawlak (1998) that aims to make efficient inferences on incomplete and inconsistent data. This theory offers a structure that can handle verified logic, inconsistent data and imprecise latent inferences, and avoids strict limitations such as fuzzy sets. It uses both fuzzy and rough set structures to organize incomplete, inadequate and uncertain information in terms of data analysis. In rough set theory, data is stored in the form of a table containing attributes and conditional attributes and adopts the concept of equality class to divide the training data according to certain criteria. In the learning process, two types of partitions, low approximation and high approximation, are created to obtain exact and probabilistic rules. High approximation refers to elements that are unequivocally part of the set, while low approximation represents elements that are likely to belong to the set. Rough set theory plays an important role in data analysis and learning processes by handling incomplete and inconsistent data.

The rough set approach is based on two concepts, low and high approximation.

- Elements that are certain to belong to the set,
- Elements that are expected to be part of the set

Explanations of the basic concepts of rough sets are briefly stated and italicized. An example of a decision table is given in Table 1. The decision table is known as the table or information system that holds the data in Rough Sets (RS). $S = (U, A, C)$ denotes a decision table or information system, where $U = \{x_1, x_1, \dots, x_n\}$ is the universal set of objects, A is a conditional attribute set and C is a decision attribute set. For any conditional attribute subset $T \subseteq A$, the T-indistinguishability relation, denoted $IND(T)$, is defined as follows:

$$IND(T) = \{(x_i, x_j) \in U^2 | \forall a \in T, a(x_i) = a(x_j)\} \quad (1)$$

Where, the equivalence classes of the T-indistinguishability relation are expressed as $[x]_T$.

The lower and upper set approximations illustrate two essential rough set notions. The notation for T-lower and T-upper approximations of the set X over any subset $X \subseteq U$ of objects and a given subset $T \subseteq A$ of attributes is $\underline{T}X$ and $\bar{T}X$, respectively. They are also defined as follows:

$$\underline{T}X = \{x \mid [x]_T \subseteq X\}, \quad (2)$$

$$\bar{T}X = \{x \mid [x]_T \cap X \neq \emptyset\} \quad (3)$$

The pair ($\underline{T}X, \bar{T}X$), known as a rough set approximation concept, indicates whether or not a set may be roughly determined. This pair also determines the known regions in rough sets. If an object $x \in \underline{T}X$, it is known that it belongs to set X. But if $x \in \bar{T}X$, it may belong to set X, i.e. it is not certain that it belongs. For example, if $T = \{t_1, t_4\}$ and $X = \{x_1, x_2, x_5, x_7, x_8\}$ according to the decision table shown in Table 1 above, then $\underline{T}X = \{x_2, x_7\}$ and $\bar{T}X = \{x_1, x_2, x_3, x_4, x_5, x_6, x_7, x_8\}$.

Table 1. *Example of a simple decision table*

$x \in U$	t_1	t_2	t_3	t_4	d
x_1	1	2	0	2	1
x_2	0	2	1	1	1
x_3	1	1	2	2	3
x_4	2	2	2	3	4
x_5	2	2	1	3	3
x_6	1	1	2	2	2
x_7	0	1	1	1	1
x_8	2	2	0	3	2

Where, the attributes x_2 and x_7 are certain to belong to the set X, while the other attributes may belong, i.e. their belonging is not certain. The definition of Positive ($POS_T X$), Negative ($NEG_T X$) and Boundary ($BND_T X$) regions defined based on the pair ($\underline{T}X, \bar{T}X$) is given below and a representative representation is given in Figure 1.

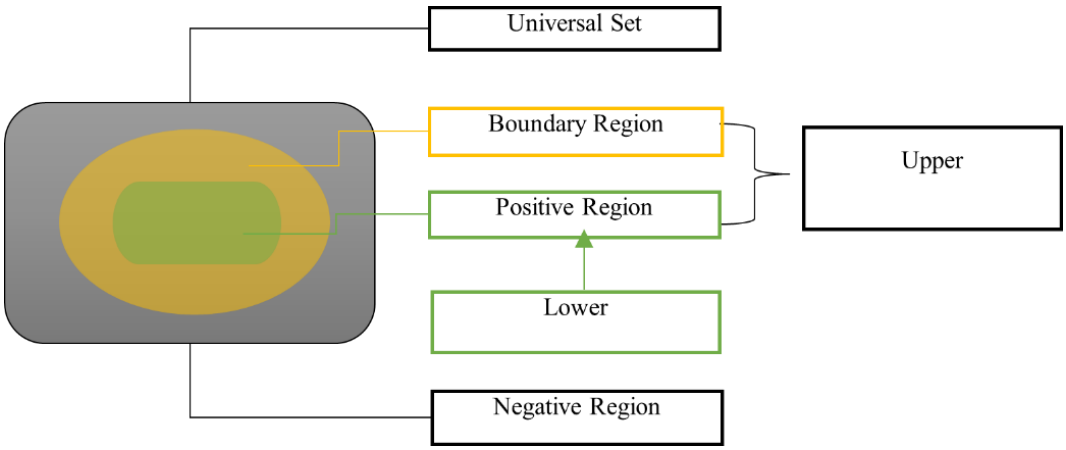

Figure 1. *The RST's regions and approximation sets*

Defining regions on sets X and T is as follows:

$$POS_T X = \underline{T}X \tag{4}$$

$$NEG_T X = U - \bar{T}X \tag{5}$$

$$BND_T X = \bar{T}X - \underline{T}X \tag{6}$$

According to RST, if the border region is not an empty set, then that set is said to be roughly determined. Otherwise, the set is said to be fully determined. For example, for sets $T = \{t_1, t_4\}$ and $X = \{x_1, x_2, x_5, x_7, x_8\}$, the regions are:

$$POS_T X = \{x_2, x_7\} \tag{7}$$

$$NEG_T X = \emptyset \tag{8}$$

$$BND_T X = \{x_1, x_3, x_4, x_5, x_6, x_8\} \tag{9}$$

The accuracy of the rough set, as expressed by Pawlak (1998), can be formulated with the following formula:

$$\lambda_T(X) = \frac{|\underline{T}(X)|}{|\overline{T}(X)|} \tag{10}$$

This is the accuracy of the rough set representation of set X, denoted as $\lambda_T(X)$. Here, $0 \leq \lambda_T(X) \leq 1$, and it represents the ratio of the number of objects that can be positively placed in set X to the number of objects that can possibly be placed in set X. This provides a measure of how closely the rough set approximates the target set. Clearly, when the upper and lower approximations are equal (i.e., the boundary region is empty), then $\lambda_T(X) = 1$, and the approximation is perfect. At the other extreme, regardless of the size of the upper approximation, if the lower approximation is empty, the accuracy is zero.

3.2. Information Gain

Information Gain (IG) (Yang & Pedersen, 1997) is a statistical information used in data and text mining that assesses the relevance of a term or word in a given text. This metric works by evaluating the salience of a term within a document and the probability that the term belongs to a specific category. It is commonly defined as the inverse of entropy. The mathematical formulation behind Information Retrieval:

$$IG(t) = -\sum_{i=1}^{M} P(C_i) log P(C_i) + P(t) \sum_{i=1}^{M} P(C_i|t) log P(C_i|t) + P(\bar{t}) \sum_{i=1}^{M} P(C_i|\bar{t}) log P(C_i|\bar{t}) \tag{11}$$

Where M represents the number of classes and $P(C_i)$ is the probability of class C_i. $P(C_i|t)$ and $P(C_i|\bar{t})$ denote the conditional probabilities of having class C_i at the same time when term t is present and having class C_i at the same time when term t is absent, respectively. Similarly, $P(\bar{t})$ and $P(t)$ denote the probabilities of t terms passing and not passing.

3.3. Preprocessing

Preprocessing is a very important and critical step in text classification. The preprocessing stage is also known as a sequence of operations on text collections, such as data cleaning, finding semantic values of words, data normalization and data integrity. In this process or stage, the following operations are generally performed:

- Cleaning unwanted (noise) data (deletion or correction of data due to spelling errors, etc.)
- Removing unnecessary words (conjunctions, prepositions, pronouns, etc.)
- Finding semantic values of words (noun, verb, adverb, etc.)
- Removing punctuation marks
- Dividing the text into sections or words
- Making lowercase to uppercase conversions
- Disassembling words into their roots (removal of suffixes, if any, etc.).

In addition to data cleaning, the preprocessing stage also aims to ensure data integrity and normalization, and to bring the data into the appropriate format. It is commonly divided into 4 categories: tokenization, stop-word removal, lowercase conversion and stemming. In this study, these operations were applied respectively.

4. THE PROPOSED METHOD

Rough Information Gain (RIG) successfully reveals the dependency of the attributes in an information system on the decision attribute and the characteristic of each attribute to the decision attribute. In this study, we compute the characteristics of each attribute with the help of upper and lower set approaches in RIG. Upper and lower approaches can understand the following characteristics of a set.

- whether it can be roughly determined.
- can be determined with certainty.
- can be determined to be uncertain.

If a set is roughly defined, a lower approach is used to obtain documents that definitely belong to that set, while a upper approach is used to obtain documents that are likely to belong to that set. With the proposed method, document sets are obtained according to the value set of each attribute. These document sets are determined whether each of them is complete, roughly complete or uncertain by upper and lower approaches. If the set is exact or rough, the characteristic value of the feature is calculated from formula (11):

$$\lambda_R(X) = \frac{|\underline{R}(X)|}{|\overline{R}(X)|} \tag{12}$$

Where R is the feature subset and X is the set of documents to be identified. $\lambda_R(X)$ is the accuracy of the set X.

If it cannot be roughly or exactly determined (uncertain) then a weight is calculated with IG (see Equation 11). The sum of the feature characteristic value and the GI value gives the weight of this set (the set allocated according to the feature) or feature:

$$RIG(t) = \lambda_R(X) + G(t) \tag{13}$$

The features are ranked according to this weight value and a total of n features are selected. The specified features are used to prepare both training and test data. As a result, now that the training and test data are ready, all that remains is to classify them with a classifier. The working mechanism of the proposed method RIG is shown in Figure 2.

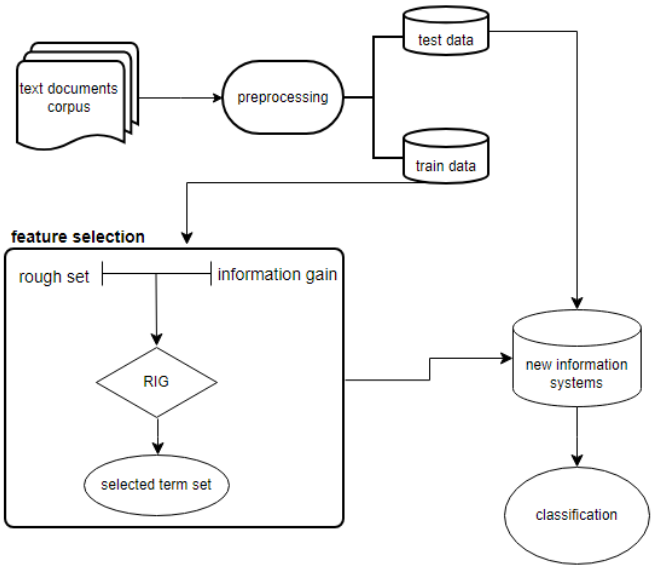

Figure 2. *The Proposed Method*

An Example:

Suppose we have 5 documents and each document belongs to either class C_1 or C_2 (C). The words in the documents are cat, dog and mouse. The following information system is given in Table 2.

Table 2. *A simple document collection*

	Terms			
Document Name	*cat*	*dog*	*mouse*	*Class Label (C)*
D_1	*1*	*0*	*0*	C_1
D_2	*1*	*1*	*0*	C_1
D_3	*1*	*2*	*1*	C_2
D_4	*1*	*1*	*0*	C_2
D_5	*1*	*0*	*1*	C_2

In the information system given in Table 2, the frequency of occurrence of each word in a document was ignored. The frequency of occurrence of the word in a document is ignored. According to the value set of each feature on Table 2, document clusters are created as follows:

- $If\ R = \{cat\}\ R = \{(D_1, D_2, D_3, D_4, D_5)\}$
- $If\ R = \{dog\}\ R = \{(D_1, D_5), (D_2, D_4), (D_3)\}$
- $If\ R = \{mouse\}\ R = \{(D_1, D_2, D_4), (D_3, D_5)\}$

Also document clusters by class;

Two separate clusters are identified as $X_1 = \{u\,|C(u) = C_1\} = \{D_1, D_2\}$ and $X_2 = \{u\,|C(u) = C_2\} = \{D_3, D_4, D_5\}$. In this case, scores can be calculated for each attribute. These are respectively:

- ***for the term cat;***

Let calculate the lower and upper set approximations of the set X_1: $\underline{R_X} = \emptyset$ and $\overline{R_X} = \{D_1, D_2, D_3, D_4, D_5\}$. Moreover, the representative set representation is shown in Figure 3a. According to this, the set X_1 cannot be determined exactly or roughly. Similarly, the lower and upper set approximations are calculated for the set X_2: $\underline{R_X} = \emptyset$ and $\overline{R_X} = \{D_1, D_2, D_3, D_4, D_5\}$. A representative cluster representation is also shown in Figure 3b. The set X_2 cannot be determined exactly or roughly. Therefore, the weight value is calculated by applying IG for cluster $\overline{R_X}$ (for documents in the upper approach):

$$IG(\overline{R_X}) = 0.9710 - 0.9710 + 0 = 0 \text{ and } \lambda_R(X) = \frac{0}{5} = 0$$

Accordingly, the score of the cat term is as follows:

$$\text{RIG(cat)} = \lambda_R(X) + IG(\overline{R_X}) = 0$$

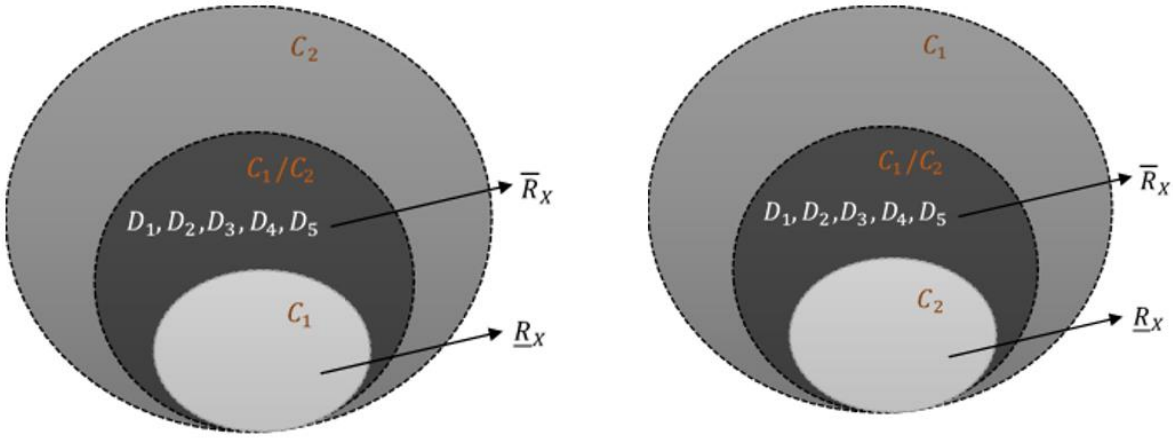

***(a)** According to set X_1* *(b) According to set X_2*

***Figure 3**. Upper and Lower sets according to cat term*

- ***for the term dog;***

Let calculate the lower and upper set approximations of the set X_1: $\underline{R}_X = \emptyset$ and $\overline{R}_X = \{D_1, D_2, D_4, D_5\}$. Accordingly, the set X_1 cannot be determined exactly or roughly. The representation is shown in Figure 4a.

$$IG(\overline{R}_X) = 1 - 0.5 - 0.5 = 0$$

For the set X_2 :$\underline{R}_X = \{D_3\}$ and $\overline{R}_X = \{D_1, D_2, D_3, D_4, D_5\}$. Accordingly, the set X_1 cannot be determined exactly or roughly. A representative cluster representation is also shown in Figure 4b.

$$\lambda_R(X_2) = \frac{1}{5} = 0.2$$

Accordingly, the score of the dog term is as follows:

$$\text{RIG(dog)} = \lambda_R(X_2) + IG(\overline{R}_X) = 0.2$$

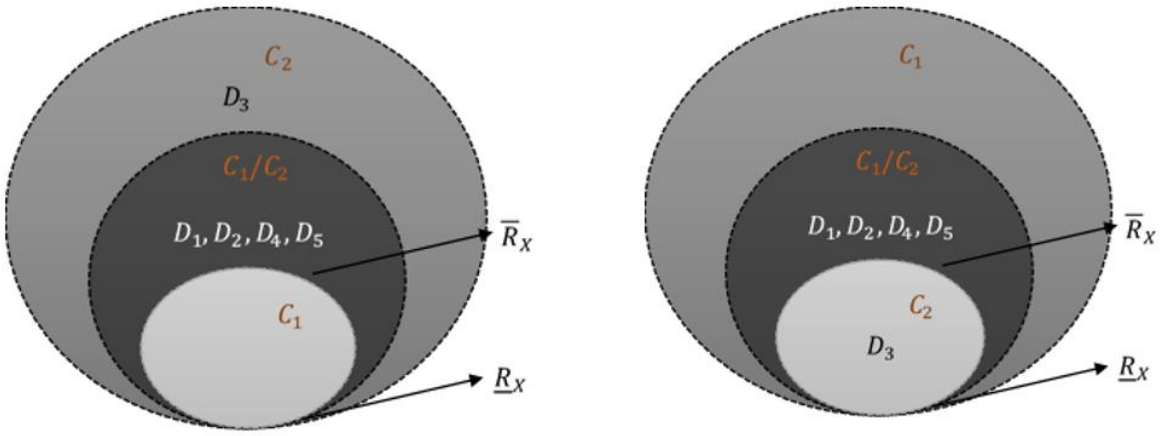

***(a)** X_1 According to set X_1* *(b) X_2 According to set X_2*

***Figure 4**. Upper and Lower sets according to dog term*

- ***for the term mouse***;

Let calculate the lower and upper set approximations of the set X_1: $\underline{R_X} = \emptyset$ and $\overline{R}_X = \{D_1, D_2, D_4\}$. Accordingly, the set X_1 cannot be determined exactly or roughly. Moreover, the representative cluster representation is shown in Figure 5a. Therefore, IG is applied for set X_1 to calculate the weight value:

$$GI(X_1) = 0.9236 - 0.9236 = 0$$

For the set X_2: $\underline{R_X} = \{D_3, D_5\}$ and $\overline{R}_X = \{D_1, D_2, D_3, D_4, D_5\}$. Moreover, the representative set representation is shown in Figure 5b. This set is a roughly determined set. Therefore, the characteristic value is calculated for the set X_2 :

$$\lambda_R(X_2) = \frac{2}{5} = 0.4$$

Accordingly, the score of the dog term is as follows:

$$\text{RIG(mouse)} = \lambda_R(X_2) + IG(\overline{R}_X) = 0 + 0.4 = 0.4$$

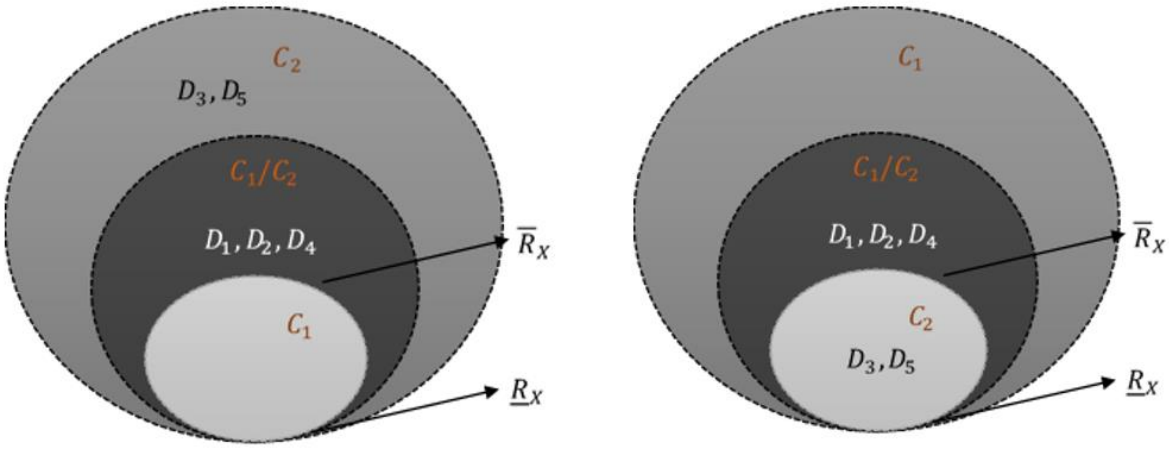

(a) X_1 *According to set* X_1 ***(b)*** X_2 *According to set* X_2

Figure 5*. Upper and Lower sets according to mouse term*

As a result, cat = 0.0, dog = 0.2, mouse = 0.4 and according to top-3, the order: $mouse > dog > cat$ is obtained.

The RIG has made an effective choice in the feature selection process in the field of text classification by utilizing the effective extraction ability of rough sets when there is not enough data. Therefore, The RIG successfully reveals the dependence of attributes in an information system on the decision attribute and the dependence of each attribute's characteristic on the decision attribute. This feature distinguishes it from other existing methods.

5. EXPERIMENTAL RESULTS

5.1. Datasets

In the experiments, Eminem and Kat Peryy datasets from the English Short Message Service (SMS) (Nuruzzaman et al., 2011) dataset and Youtube Spam Collection (Alberto et al., 2015) datasets were used. The process performed on these datasets is to determine whether an SMS is spam or not and whether the comments in the Youtube Spam Collection dataset are spam or not. The first dataset is the dataset created by Nuruzzaman

et al. (2011), which contains 425 spam and 450 non-spam English SMS text messages. The other datasets, Eminem and Kat Perry, are a general set of comments collected for spam research. They account for two of the top five most watched videos during the collection period and consist of 548 and 300 real comments, respectively. Table 3 also provides general information about the datasets.

Table 3. *Datasets*

	Spam	*Non-Spam*
SMS	*440*	*425*
Eminem	*245*	*203*
Kat Peryy	*175*	*175*

5.2. Classifiers

Classification is the process of assigning previously unlabeled data to a labeled category in a dataset. There are many approaches presented in the literature for this process. In this study, the classification methods given in Table 4 below were used.

5.3. Measure of Success

In this section, the Micro-F1 metric is chosen to evaluate the performance of feature selection approaches. In the calculation of this metric, the harmonic mean of Precision and Recall is employed in order to summarize the performance of the classifier algorithm in a more balanced way. Precision is the number of true positive examples (TP) divided by the sum of the number of true positive examples (TP) and the number of false positive examples (FP).

$$Precision = \frac{TP}{TP + FP} \tag{14}$$

Recall is defined as the ratio of true positive samples (TP) to the sum of true positive samples (TP) and false negative samples (FN).

$$Recall = \frac{TP}{TP + FN} \tag{15}$$

Precision is especially important when the cost of false positive predictions is high, and Recall is important when the cost of predicting false negatives is high.

Accordingly, Micro-F1:

$$Mikro - F1 = 2 \times \frac{Precision \times Recall}{Precision + Recall} \tag{16}$$

Table 4. *General information about classifiers used in experimental studies*

Method	Mathematical Expression	Description
Support Vector Machines (Joachims, 1998) (SVM)	$w^T x + w_0 = 0.$ $J(w, w_0, \varepsilon) = \frac{1}{2}\|\|w\|\|^2 + K\sum_{i=1}^{N}\varepsilon_i$ $w^T x + w_0 \geq 1 - \varepsilon_i \quad eğer \ x_i \in c_1$ $w^T x + w_0 \leq -1 + \varepsilon_i \quad eğer \ x_i \in c_2$ $\varepsilon_i \geq 0.$ $w = \sum_{i=1}^{N}\lambda_i y_i x_i$	Based on margin maximization, SVM is one of the most efficient and well-known classifiers. There are linear and non-linear versions available. However, the linear version is given here. Its main goal is to obtain the highest possible margin. $2/\|\|w\|\|$ is the margin width, K denotes a user-defined constant, and ε represents the margin error.
k-Nearest Neighbors (Kowsari et al., 2019) (KNN)	$\left(\sum_{i=1}^{k}(\|x_i - y_i\|)^q\right)^{1/q}$	Using distance functions such as Euclidean to find the similarity of neighbors, KNN scores category candidates based on the class of k candidates by finding the k closest neighbors of a test data among all data in the training set. It is provided the Minkowski distance computation function. In this function, if q is $q = 1$, Manhattan and $q = 2$, Euclidean functions are obtained.
Decision Tree (Aggarwal & Zhai, 2012) (DT)	$H\left(\frac{p}{n+p}, \frac{n}{n+p}\right) = -(\frac{p}{n+p} log_2 \frac{p}{n+p} + \frac{n}{n+p} log_2 \frac{n}{n+p})$ $BE(A) = \sum_{i=1}^{k}\frac{p_i + n_i}{p+n} H(\frac{p_i}{p_i + n_i}, \frac{n_i}{p_i + n_i})$ $A(BK) = H\left(\frac{p}{n+p}, \frac{n}{n+p}\right) - BE(A)$	DT, whose main working purpose is to create a tree structure of categorized data points by attribute, determines the attribute that should be at the tree root or parent level with the De Mantaras method. Where *k* denotes different values, *A* denotes the selected attribute and *E* denotes the training data, which is a subset of the training data such as $\{E_1, E_2, \dots, E_k\}$.
Naive Bayes (Pearson, 1925) (NB)	$P(A\|B) = \frac{P(B\|A)P(A)}{P(B)}$	The theoretical foundation of the strategy is Thomas Bayes' theorem, NB works according to a priori probabilities of events. Attributes are independent and the probability of each state is calculated. Classification is determined according to the highest probability value. Here, $P(A\|B)$, $P(B\|A)$, $P(A)$, and $P(B)$ denote the probability of occurrence of event A when event B occurs and the probability of occurrence of event B when event A occurs, respectively.

5.4. Success Analysis

In this study, an experimental study was conducted on three different datasets to see whether the proposed method RIG provides meaningful results. In the experiments, RIG was compared with existing feature selection approaches according to the Micro-F1 criterion with feature sizes of 50, 100, 200, 300 and 500. The best-known IG, GI, CHI2 and DFS methods were compared with RIG in terms of their impact on the performance of SVM, KNN, DT and NB classifiers. The experimental results are shown in Tables 5, Table 6, and Table 7.

Table 5 shows the Micro-F1 results for each classifier at Top-50, 100, 200, 300 and 500 dimensions on the SMS dataset. It demonstrates the classifiers' performance in several dimensions for the features chosen by the feature selection procedures. When the table is analyzed, it is seen that SVM classifier and RIG achieve the best results in all attribute sizes. Again, with KNN, it gave the best result except for dimensions 300 and 500. Similarly, the DT classifier achieved the highest values for dimensions 50, 300 and 500.

Table 5. *Micro-F1 scores results for the SMS dataset using SVM, KNN, DT, and NB*

	Accuracy results according to selected feature sizes				
SVM	50	100	200	300	500
IG	92,02	**93,54**	**91,25**	89,35	90,49
GI	93,16	91,63	**91,25**	91,25	90,49
CHI2	91,63	92,78	90,49	89,35	90,87
DFS	93,14	**93,54**	**91,25**	90,11	**91,63**
RIG	**93,25**	**93,54**	**91,25**	**91,63**	**91,63**
KNN					
IG	87,83	90,87	90,49	88,97	89,35
GI	87,45	87,83	90,78	87,07	**90,87**
CHI2	87,83	89,35	90,11	**89,35**	89,73
DFS	88,97	88,59	89,73	89,73	**90,87**
RIG	**93,93**	**92,78**	**91,25**	87,35	89,73
DT					
IG	90,87	**92,02**	**90,87**	90,11	89,35
GI	91,25	**92,02**	90,49	90,11	89,35
CHI2	91,25	**92,02**	**90,87**	90,11	89,35
DFS	91,63	90,49	**90,87**	**90,49**	89,35
RIG	**91,75**	90,97	90,35	**90,49**	**89,97**
NB					
IG	88,21	87,07	87,07	86,69	85,17
GI	84,79	88,21	85,55	84,79	85,55
CHI2	86,69	88,21	89,35	87,83	87,83
DFS	**91,63**	**93,92**	**92,78**	**93,16**	**92,78**
RIG	87,07	89,35	90,35	88,97	88,59

Table 6 shows the classifier performance according to the features presented by the feature selectors on the Eminem dataset. In the table, the RIG method, SVM, KNN and DT classifiers reached the highest value in all dimensions except dimension 100.

The performances for feature selectors on the Kat Perry dataset are shown in Table 7. The RIG method performed best with SVM in dimensions 100, 200, 300 and 500, KNN in 500, DT in all dimensions and NB in 300 and 500.

As a result, the RIG method has shown a successful performance among the existing approaches at the specified feature sizes. In particular, the RIG method performed much better with the SVM classifier.

Table 6. *Micro-F1 scores results for the Eminem dataset using SVM, KNN, DT, and NB*

	Accuracy results according to selected feature sizes				
SVM	50	100	200	300	500
IG	94,07	**94,07**	94,07	94,07	94,07
GI	94,07	**94,07**	94,07	94,07	94,07
CHI2	94,07	**94,07**	94,07	94,07	94,07
DFS	93,33	93,33	93,33	93,33	94,07
RIG	**94,81**	93,33	**94,81**	**94,81**	**95,56**
KNN					
IG	64,44	71,11	66,67	68,15	65,19
GI	68,15	68,89	68,89	68,15	69,63
CHI2	74,07	**74,81**	72,59	66,67	71,11
DFS	74,07	70,37	75,56	71,85	64,44
RIG	**77,04**	72,59	**77,78**	**76,30**	**71,85**
DT					
IG	94,07	**94,07**	94,07	94,07	94,07
GI	94,07	**94,07**	94,07	94,07	94,07
CHI2	94,07	**94,07**	94,07	94,07	94,07
DFS	93,33	93,33	93,33	93,33	93,33
RIG	**94,81**	93,33	**94,81**	**94,81**	**94,81**
NB					
IG	88,15	88,89	81,48	86,67	88,15
GI	88,15	87,41	83,70	85,19	86,67
CHI2	**93,33**	**93,33**	**93,33**	**93,33**	**94,07**
DFS	84,44	85,19	81,48	71,85	85,19
RIG	86,67	88,89	84,44	76,30	85,93

Table 7. *Micro-F1 scores results for the Kat Perry dataset using SVM, KNN, DT, and NB*

	Accuracy results according to selected feature sizes				
SVM	50	100	200	300	500
IG	**97,17**	**97,17**	**92,45**	92,45	91,51
GI	**97,17**	96,23	91,51	91,51	91,51
CHI2	**97,17**	**97,17**	**92,45**	93,40	93,40
DFS	96,23	**97,17**	**92,45**	93,40	93,40
RIG	95,28	**97,17**	**92,45**	**93,51**	**93,45**
KNN					
IG	68,87	**74,53**	68,87	**77,36**	75,47
GI	**80,19**	72,64	**76,42**	**77,36**	78,30
CHI2	69,81	**74,53**	**76,42**	76,42	75,47
DFS	70,75	69,81	75,47	76,42	76,42
RIG	72,26	71,70	68,87	70,75	**78,47**
DT					
IG	96,23	96,23	96,23	96,23	94,34
GI	96,23	96,23	96,23	96,23	96,23
CHI2	**97,17**	**97,17**	**97,17**	**97,17**	**97,17**
DFS	**97,17**	**97,17**	**97,17**	**97,17**	**97,17**
RIG	**97,17**	**97,17**	**97,17**	**97,17**	**97,17**
NB					
IG	75,28	**89,62**	92,45	83,02	77,36
GI	75,47	77,36	91,51	76,42	76,42
CHI2	**78,30**	76,42	**93,40**	75,47	73,58
DFS	68,87	71,70	**93,40**	70,75	65,09
RIG	71,32	89,43	92,51	**85,09**	**78,49**

6. CONCLUSION

A novel feature selection strategy is proposed in this paper to overcome one of the major issues in text classification, namely high dimensionality. The proposed feature selection approach utilizes the ability of Rough Sets to make effective inference in areas with incomplete and insufficient data. In addition, a hybrid structure has been created with the effective features of Rough Sets and Information Gathering. This structure distinguishes the proposed strategy from other existing filter feature selectors. Therefore, effective results were obtained in experimental studies. The proposed approach is compared with the traditional best-known method on three different textual data sets and it is observed that the approach works efficiently. Ultimately, the Rough Information Retrieval method is expected to take its place in the literature with its performance.

CONFLICT OF INTEREST

The authors declare no conflict of interest.

REFERENCES

Aggarwal, C., & Zhai, C. (2012). A survey of text classification algorithms. In: C. C. Aggarwal, & C Zhai (Eds.), *Mining text data* (pp. 163-222). https://doi.org/10.1007/978-1-4614-3223-4_6

Alberto, T. C., Lochter, J. V., & Almeida, T. A. (2015, December 9-11). *Tubespam: Comment spam filtering on youtube*. In: Proceedings of the IEEE 14th International Conference on Machine Learning and Applications (ICMLA), Miami, Florida. https://doi.org/10.1109/ICMLA.2015.37

Bermejo, P., De la Ossa, L., G´amez, J., & Puerta, J. (2012). Fast wrapper feature subset selection in highdimensional datasets by means of filter re-ranking. *Knowledge Based Systems*, *25*(1), 35-44. https://doi.org/10.1016/j.knosys.2011.01.015

Cekik, R., & Uysal, A. K. (2020). A novel filter feature selection method using rough set for short text data. *Expert Systems with Applications*, *160*, 113691. https://doi.org/10.1016/j.eswa.2020.113691

Cekik, R., & Uysal, A. K. (2022). A new metric for feature selection on short text datasets. Concurrency and *Computation: Practice and Experience*, *34*(13), e6909. https://doi.org/10.1002/cpe.6909

Chen, J., Huang, H., Tian, S., & Qu, Y. (2009). Feature selection for text classification with Naïve Bayes. *Expert Systems with Applications*, *36*(3), 5432-5435. https://doi.org/10.1016/j.eswa.2008.06.054

Chou, C., Sinha, A., & Zhao, H. (2010). A hybrid attribute selection approach for text classification. *Journal of the Association for Information Systems*, *11*(9), 491. https://doi.org/10.17705/1jais.00236

Ghareb, A., Bakar, A., & Hamdan, A. (2016). Hybrid feature selection based on enhanced genetic algorithm for text categorization. *Expert Systems with Applications*, *49*, 31-47. https://doi.org/10.1016/j.eswa.2015.12.004

Gutlein, M., Frank, E., Hall, M., & Karwath, A. (2009, March 30 - April 2). *Large-scale attribute selection using wrappers*. In: Proceedings of the IEEE Symposium on Computational Intelligence and Data Mining, (pp. 332-339), Nashville, TN. https://doi.org/10.1109/CIDM.2009.4938668

Joachims, T. (1998, April 21-23). *Text categorization with support vector machines: Learning with many relevant features*. In: Proceedings of the European conference on machine learning (pp. 137-142). Berlin, Heidelberg. https://doi.org/10.1007/BFb0026683

Kaya, M., Bilge, H. Ş., & Yildiz, O. (2013, April 24-26). *Feature selection and dimensionality reduction on gene expressions*. In: Proceedings of the 21st Signal Processing and Communications Applications Conference (SIU) (pp. 1-4), Haspolat. https://doi.org/10.1109/siu.2013.6531476

Kaya, M., & Bilge, H. Ş. (2016, May 16-19). *A hybrid feature selection approach based on statistical and wrapper methods*. In: Proceedings of the 24th Signal Processing and Communication Application Conference (SIU) (pp. 2101-2104), Zonguldak. https://doi.org/10.1109/SIU.2016.7496186

Kowsari, K., Jafari Meimandi, K., Heidarysafa, M., Mendu, S., Barnes, L., & Brown, D. (2019). Text classification algorithms: A survey. *Information*, *10*(4), 150. https://doi.org/10.3390/info10040150

Labani, M., Moradi, P., Ahmadizar, F., & Jalili, M. (2018). A novel multivariate filter method for feature selection in text classification problems. *Engineering Applications of Artificial Intelligence*, *70*, 25-37. https://doi.org/10.1016/j.engappai.2017.12.014

Nuruzzaman, M. T., Lee, C., & Choi, D. (2011, August 31 - September 2). *Independent and Personal SMS Spam Filtering*. In: Proceedings of the IEEE 11th International Conference on Computer and Information Technology, (pp. 429-435), Paphos. https://doi.org/10.1109/CIT.2011.23

Ogura, H., Amano, H., & Kondo, M. (2009). Feature selection with a measure of deviations from Poisson in text categorization. *Expert Systems with Applications*, *36*(3), 6826-6832. https://doi.org/10.1016/j.eswa.2008.08.006

Pawlak, Z. (1998). Rough set theory and its applications to data analysis. *Cybernetics & Systems*, *29*(7), 661-688. https://doi.org/10.1080/019697298125470

Pearson, E. (1925). Bayes' theorem, examined in the light of experimental sampling. *Biometrika*, *17*(3-4), 388-442. https://doi.org/10.1093/biomet/17.3-4.388

Rehman, A., Javed, K., Babri, H. A., & Saeed, M. (2015). Relative discrimination criterion–A novel feature ranking method for text data. *Expert Systems with Applications*, *42*(7), 3670-3681. https://doi.org/10.1016/j.eswa.2014.12.013

Rehman, A., Javed, K., & Babri, H. A. (2017). Feature selection based on a normalized difference measure for text classification. *Information Processing & Management*, *53*(2), 473-489. https://doi.org/10.1016/j.ipm.2016.12.004

Rehman, A., Javed, K., Babri, H. A., & Asim, M. N. (2018). Selection of the most relevant terms based on a max-min ratio metric for text classification. *Expert Systems with Applications*, *114*, 78-96. https://doi.org/10.1016/j.eswa.2018.07.028

Shang, W., Huang, H., Zhu, H., Lin, Y., Qu, Y., & Wang, Z. (2007). A novel feature selection algorithm for text categorization. *Expert Systems with Applications*, *33*(1), 1-5. https://doi.org/10.1016/j.eswa.2006.04.001

Shang, C., Li, M., Feng, S., Jiang, Q., & Fan, J. (2013). Feature selection via maximizing global information gain for text classification. *Knowledge-Based Systems*, *54*, 298-309. https://doi.org/10.1016/j.knosys.2013.09.019

Sharmin, S., Shoyaib, M., Ali, A. A., Khan, M. A., & Chae, O. (2019). Simultaneous feature selection and discretization based on mutual information. *Pattern Recognition*, *91*, 162-174. https://doi.org/10.1016/j.patcog.2019.02.016

Şenol, A. (2023). Comparison of Performance of Classification Algorithms Using Standard Deviation-based Feature Selection in Cyber Attack Datasets. International Journal of Pure and Applied Sciences, *9*(1), 209-222. https://doi.org/10.29132/ijpas.1278880

Uysal, A. K., & Gunal, S. (2012). A novel probabilistic feature selection method for text classification. *Knowledge-Based Systems*, *36*, 226-235. https://doi.org/10.1016/j.knosys.2012.06.005

Wang, H., & Hong, M. (2019). Supervised Hebb rule based feature selection for text classification. *Information Processing & Management*, *56*(1), 167-191. https://doi.org/10.1016/j.ipm.2018.09.004

Wang, S., Li, D., Wei, Y., & Li, H. (2009). *A feature selection method based on fisher's discriminant ratio for text sentiment classification*. In: Proceedings of the International Conference on Web Information Systems and Mining (pp. 88-97). Berlin. https://doi.org/10.1007/978-3-642-05250-7_10

Weston, J., Mukherjee, S., Chapelle, O., Pontil, M., Poggio, T., & Vapni, V. (2001). *Feature selection for SVMs*. Advances in neural information processing systems, Denver, CO (pp. 668-674).

Yang, Y., & Pedersen, J. O. (1997). *A comparative study on feature selection in text categorization*. 14th International Conference on Machine Learning, Nashville, USA, (pp. 412-420).

Zhang, Q., Xie, Q., & Wang, G. (2016). A survey on rough set theory and its applications. *CAAI Transactions on Intelligence Technology*, *1*(4), 323-333. https://doi.org/10.1016/j.trit.2016.11.001

Research Article GU J Sci, Part A, 10(4): 487-498 (2023) 10.54287/gujsa.1355751

Gazi University
Journal of Science
PART A: ENGINEERING AND INNOVATION
http://dergipark.org.tr/gujsa

Deep Learning Based Approach for Classification of Mushrooms

Yağmur DEMİREL[1*] Gözde DEMİREL[2]

[1] Department of Computer Engineering, Ankara University, Ankara, Türkiye

Keywords

CNN
Image Processing
Mobilenetv2
Mushrooms

Abstract

Deep learning algorithms have produced amazing results in recent years when used to identify items in digital photographs. A deep learning technique is suggested in this work to classify mushrooms in their natural habitat. The study's objective is to identify the most effective method for categorizing mushroom images produced by well-known CNN models. This study will be helpful for the field of pharmacology, mushroom hunters who gather mushrooms in the wild, and it will help to lower the number of people who are at risk of becoming ill from poisonous mushrooms. Images are taken from data labelled by INaturalist specialist. The photographs show mushrooms in their natural environment and feature a variety of backgrounds. The "Mobilenetv2_GAP_flatten_fc" model, which was the study's top performer, had a training data set accuracy of 99.99%. It was 97.20% accurate in the categorization that was done using the validation data. Using the test data set, the classification accuracy was 97.89%. This paper presents the results of a performance comparison between the best-performing model and a multitude of state-of-the-art models that have undergone prior training. Mobilenetv2_GAP_flatten_fc model greatly outperformed the trained models, according to the precision, recall, F1 Score. This illustrates how the basic training process of the suggested model can be applied to enhance feature extraction and learning.

Cite

Demirel, Y., & Demirel, G. (2023). Deep Learning Based Approach for Classification of Mushrooms. *GU J Sci, Part A*, *10*(4), 487-498. doi:10.54287/gujsa.1355751

Author ID (ORCID Number)

0009-0006-1657-1790 Yağmur DEMİREL
0009-0001-6310-8284 Gözde DEMİREL

Article Process

Submission Date 05.09.2023
Revision Date 28.10.2023
Accepted Date 22.11.2023
Published Date 13.12.2023

1. INTRODUCTION

Mushroom cultivation is a process by which people grow mushrooms for food, beverage or medicinal purposes. Mushrooms are one of the most alluring and fascinating of nature's many secrets. People who have lived in close proximity to nature for thousands of years have learned that mushrooms are not just a wonderful food but also a window into the complexity and beauty of nature. There are many different types of mushrooms in the globe, but only a small number of them are edible to humans. On the other hand, poisonous mushrooms might result in major health issues if they are not adequately identified and thrive in the same habitats. Therefore, it is crucially important to identify and categorize mushrooms. For a model to learn about thousands of items from millions of images, it needs to have a large learning capacity (Jarrett et al., 2009). The object recognition problem is so complex that it cannot be adequately described even with a dataset as extensive as ImageNet (Lee et al., 2009). Therefore, the model used in the study must incorporate a substantial amount of prior knowledge to compensate for the unavailability of certain data. Convolutional neural networks (CNNs) are a subset of deep learning models and assumptions they make about the properties of images are powerful and generally correct (Pinto et al., 2009). These assumptions can be exploited to make the network's general-purpose features more specific and optimized in a particular context (Turaga et al., 2010). Hence, CNNs possess significantly fewer connections and parameters when compared to standard feedforward neural networks of similar-sized layers, rendering them more amenable to training (Krizhevsky et al., 2012). This work offers a classification of harmful and healthy mushrooms. In order to comprehend the diversity of the

*Corresponding Author, e-mail: yagmurdemirel39@gmail.com

natural environment and minimize health hazards, mushroom taxonomy is crucial. In addition, it's crucial to comprehend how to recognize these species, what traits to look for, and why some mushroom species are poisonous to ingest in order to make mushroom gathering and consumption safer in the wild. In this study, the "Mobilenetv2_GAP_flatten_fc" network, a state-of-the-art CNN framework for the classification of mushrooms, was examined. The 'Mobilenetv2_GAP_flatten_fc' model, enriched with multiple architectural layers and a fundamental training strategy, successfully classified dangerous mushrooms. In a comparative study, our approach exhibited slightly superior results when compared to comparable pre-trained CNN models. The findings are viewed as optimistic, leading one to conclude that this research will benefit:

- Pharmacology: The study of drugs and medications.
- Mushroom hunters: Individuals who gather mushrooms, often for various purposes, such as cooking or medicinal use.
- Human health: The overall well-being and medical conditions of people.
- Mushrooms are described as a part of biodiversity, which refers to the variety of life on Earth.
- It is emphasized that precise classification of mushrooms can have a role in recognizing and safeguarding biodiversity. This implies that correctly identifying and categorizing mushrooms can contribute to the understanding and conservation of various species and ecosystems on Earth.

2. LITERATURE REVIEW

Nusrat, Zahid, and the other researchers focused on the detection of distinct mushroom species in their investigation. They classified 8190 photos of mushrooms using deep learning techniques including InceptionV3, VGG16, and Resnet50 (Zahan et al., 2021). They chose an 8:2 split between training and test data. They compared contrast-enhanced and non-contrast-enhanced approaches using InceptionV3 and the Contrast Limited Adaptive Histogram Equalization (CLAHE) method to get the maximum test accuracy. When compared to other algorithms, InceptionV3 has the greatest success rate with 88.40% accuracy. In their research, Mark and Meo created a system to categorize six mushrooms using Convolutional Neural Network (CNN) deep learning models integrated with Raspberry Pi (Sutayco & Caya, 2022). They trained 600 example mushroom images using the CNN-Inception-V3 architecture that has already been taught. For model training and validation, they used 80% and 20% of the data, respectively. The final model's total accuracy was 92.7%. In Yunnan Province, a location rich in natural mushroom resources in China, Hui, Fuhua et al. trained VGG16, Resnet18, and Googlenet models using data of diverse mushrooms with varied features and combined them with the bagging technique (Zhao et al., 2021). As a result, by adjusting to complex cues in the natural mushroom recognition process, accuracy and generalization capacity are enhanced. The model fared better than a single CNN, according to experiments. The integrated model had an accuracy of 93.1% using a 10% validation dataset, whereas the best single bagging integrated model had an accuracy of 90.8%. Wacharaphol et al. addressed the issue of finding the difference between edible and dangerous mushrooms due to their similar appearance in their study (Ketwongsa et al., 2022). They classified the toxic and edible varieties of five commonly encountered mushroom species in Thailand, including Inocybe rimosa, Amanita phalloides, Amanita citrina, Russula delica, and Phaeogyroporus portentosus, using convolutional neural networks (CNN) and region convolutional neural networks (R-CNN). The goal of this study was to lessen the amount of fatalities brought on by the intake of toxic mushrooms. Three pre-trained models—AlexNet, ResNet-50, and GoogLeNet—were compared in the study for test time and accuracy. Their suggested model required less time for testing and training while still being highly accurate. In R-CNN studies for mushroom classification, their suggested model had accuracy scores of 95.50%.

3. MATERIALS AND METHODS

3.1. Dataset

For the investigation, a sizable fungal data set made up of 224x224x3 photos of 4 distinct mushrooms was gathered. Coprinus comatus (ink mushroom), Amanita pantherina (panther mushroom), Fistulina hepatica (beefsteak mushroom), and Craterellus cornucopioides (borer mushroom) are the mushrooms utilized in the dataset. Table 1 lists the many varieties of mushrooms and their quantities.

Table 1. *Types of Mushrooms in The Dataset*

Mushroom Type	Number of Data
Coprinus comatus (ink mushroom)	1,480
Amanita pantherina (panther mushroom)	1,500
Fistulina hepatica (beefsteak mushroom)	1,500
Craterellus cornucopioides (borer mushroom)	990
Total	5,470

Images of mushrooms were gathered from the iNaturalist website. Nature lovers can submit their observations, images, and documentation of plants, animals, insects, and other living species in the database known as iNaturalist. Since different image capture tools (smartphones, digital cameras, etc.) were used to take the mushroom images, the photos' resolution and format differ. The collected mushroom data set was uploaded to the Figshare platform to be accessible to everyone under the title Mushroom Classification (Demirel & Demirel 2023). The requirement that the images be homogeneous is one of deep learning networks' essential elements. Therefore, before using any deep learning model, the raw images must go through the required preprocessing. In this experiment, A Python script first reduced each image's resolution to 224 224 3 pixels utilizing the Python Imaging module and then utilized for model training. Each image was saved in its own folder on the storage devices in the.jpg format. For standardization, the photos were then read from the storage devices and transformed into numpy arrays using the 'NumPy' package. During model training, reading and processing photos is made efficient via Numpy arrays. These 224 224 224 224 3 numpy arrays served as the input for the suggested model for feature extraction and classification. The Amanita pantherina (Panther mushroom) and Fistulina hepatica (Beefsteak mushroom) classes in this experiment have much more images than the other two classes. To improve the model's performance, increase its capacity for generalization, correct imbalances, and encourage the model to learn from a wider range of samples, data augmentation was carried out. This was done using the Python library 'Augmentor'. The altered photographs were used to create the false visuals, but the labels on the original photos were left intact. The volume and variety of the dataset were to be increased through this image augmentation. Several strategies were used for data augmentation in this study. Randomly chosen training images were rotated by 10 degrees, magnified by 10% of the width, shifted vertically by 10% of the height, and randomly shifted horizontally by 10% of the width. The data pool was thus expanded. Figure 1 shows sample images from the dataset used. Figure 2 shows the distribution rates of the data set.

Figure 1. *Analysis of the Data*

Figure 2. *Data Distribution*

3.2. Classification Approach

Currently, computer vision and pattern recognition are being advanced by deep convolutional neural networks (CNNs). CNNs have the capacity to automatically learn the differentiating characteristics of images/objects from pixel arrangements in images, in contrast to typical machine learning methods where classifiers are trained using manually created image attributes.

In this experiment, the photos were classified with the "Mobilenet-V2_GAP_flatten_fc" model, which is an improvement of the "Mobilenet-V2" CNN model, a well-known example of a modern convolutional neural network. Since MobileNetV2 is small and efficient, it can work well even on computers with limited memory and processing capacity. Using a deep learning method, this model may be applied to tasks including image categorization, object recognition, and image segmentation. A validation error rate of 2.80% and a test error rate of 2.11% were recorded during the evaluation with the "Mobilenet-V2_GAP_flatten_fc" network.

The study utilizes the Mobilenet-V2_GAP_flatten_fc model. MobileNetV2 networks are specifically designed for mobile, IoT, or low-hardware devices, offering substantial enhancements in both parameter count and computational complexity while maintaining high classification performance (Chen et al., 2020). Linear bottleneck and inverted residuals block within the architecture lead to a substantial reduction in the required memory (Zhang et al., 2019). The convolution layer is composed of depth access and point access layers (Sandler et al., 2018). Figure 3 shows the MobileNetV2 architecture (Seidaliyeva et al., 2020).

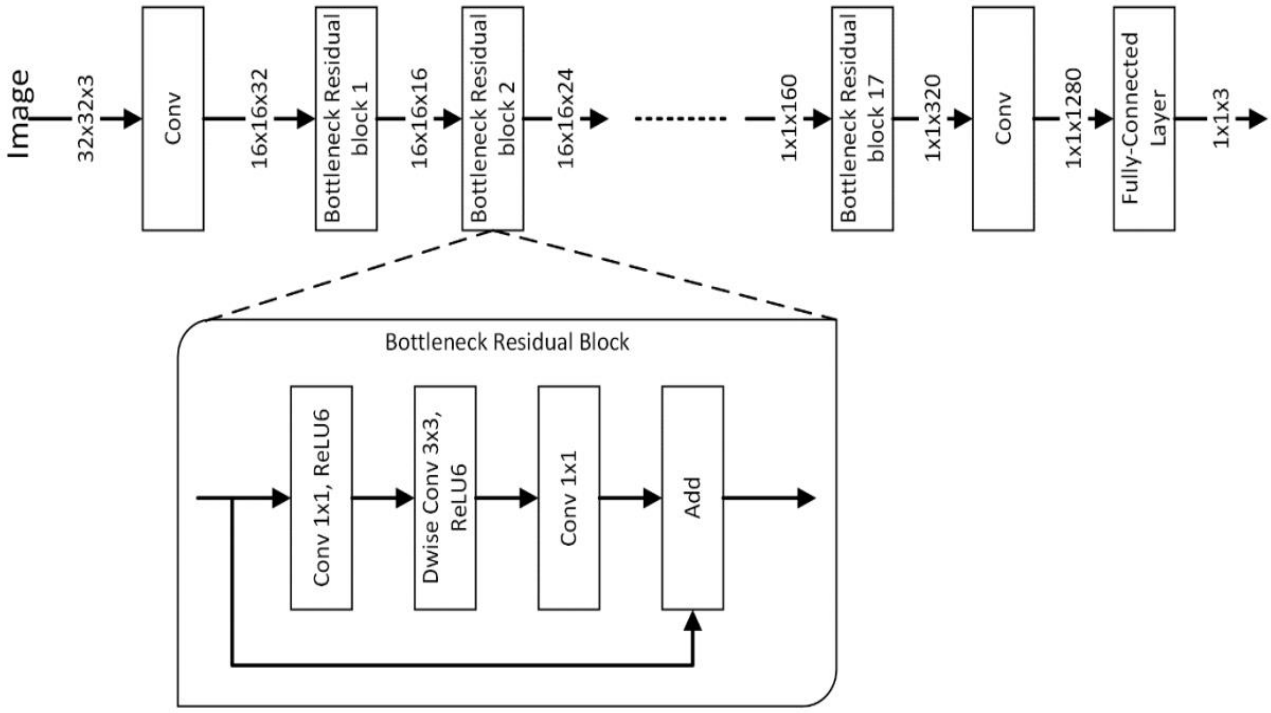

Figure 3. *MobileNetV2 Architecture*

On a field image dataset created from mushroom photographs, the models' performance was assessed and compared. A straightforward training strategy was used, in which the mushroom dataset was used to train all layers of the models. The weights were initialized randomly throughout the training phase rather than being pre-trained for the models. For both the training and validation datasets, Mobilenet-V2_GAP_flatten_fc was trained for 100 iterations. The results part included an ablation study for cycle and chunk selection.

Adam optimization was performed with a learning rate of 0.001 and default hyperparameter values. Hyperparameters utilized man optimization. 1e-3 was used as the learning rate. The training rate used throughout training was 0.000000001. The effectiveness of the suggested strategy in this research was compared to the pre-trained models. Figure 4 illustrates the model and its respective layers employed in the study.

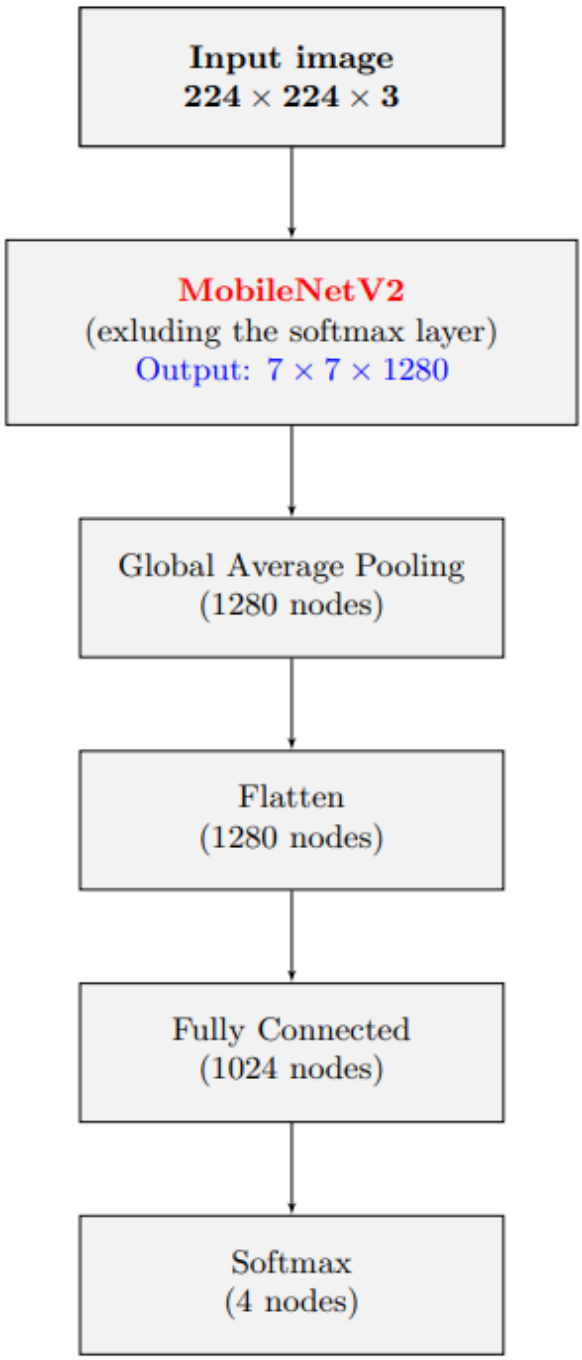

Figure 4. *MobileNetV2_GAP_flatten_fc*

3.3. Application

The Python programming language's Keras high-level TensorFlow API was used to implement each model. Table 2 provides specifics on the hardware and software configuration.

Table 2. *Hardware and Software Configuration*

Name	Parameters
Operating System	Windows 10 Home Single Language 64 bit
CPU Processor	Intel(R) Core(TM) i5-8250U CPU @ 1.60GHz 1.80 GHz
GPU (Graphics Processing Unit)	Intel(R) UHD Graphics 620
RAM	12,0 GB
Deep Learning Framework	Keras library running on TensorFlow
Deep Learning Environment	Google Colab Notebook
Programming Language	Python

4. EXPERIMENTAL RESULTS AND DISCUSSIONS

4.1. Performance Metrics

The entire dataset was split into three sections: training, validation, and test sets in order to fairly assess performance. Initially, the total dataset was split 80:20, with 80% of the data used for training and validation and 20% kept separate for testing/evaluating the models after training. Then, the remaining 80% of the data was split in half using different configurations for training-validation tasks. Table 3 provides a summary of the various training-validation setups for the dataset. To ensure that each partition had photos from both the original dataset and the enhanced dataset, the original and enhanced data were split into different partitions and then mixed. A Python script handled all data splitting. A separate 20% test dataset was used in each experiment to test the models after training and validation. It should be emphasized that photos from both the original and supplemented datasets were included in the data used to evaluate all models. Performance metrics used in the study:

Recall (Sensitivity) is calculated by the ratio of true positive classes to all the actual positive classes in the input images. Recall is calculated using the mathematical expression shown in Equation 1.

$$\text{Recall} = TP / (TP + FN) \quad (1)$$

Precision is calculated by the ratio of true positive results in the input that were correctly predicted as positive. Precision is calculated using the mathematical expression shown in Equation 2.

$$\text{Precision} = TP / (TP + FP) \quad (2)$$

Accuracy is generally used to decide whether the model is correct or not, but it is not a sufficient criterion on its own to evaluate whether the model is good or bad. Accuracy is calculated using the mathematical expression shown in Equation 3.

$$\text{Accuracy} = (TP+TN) / (TP+TN+FP+FN) \quad (3)$$

F1 Score provides a combined assessment of performance criteria such as sensitivity and accuracy. The F1 Score is calculated using the mathematical expression shown in Equation 4.

$$\text{F1 Score} = 2TP / (2TP+FP+FN) \quad (4)$$

These equations and concepts are commonly employed in the context of binary classification. In scenarios where classification involves three or more classes, performance evaluation measurements are typically averaged.

The performance of the models for mushroom-wise categorization was then determined by creating complexity matrices. The following variables are provided by the complexity matrix. The MobileNetV2_GAP_flatten_fc model evaluation results are once again shown in Table 3 along with performance metrics.

Table 3. *Performance Evaluation Results for the MobileNetV2_GAP_flatten_fc Model*

Mushroom Type	Precision	Recall	F1 Score
Coprinus comatus (Ink mushroom)	0.95	0.96	0.95
Amanita pantherina (Panther mushroom)	0.97	0.99	0.98
Fistulina hepatica (Beefsteak mushroom)	0.97	0.97	0.97
Craterellus cornucopioides (Borer mushroom)	0.96	0.92	0.94

5. COMPARATIVE ANALYSIS WİTH PREVIOUS STUDIES ON FUNGAL CLASSIFICATION

Here, a comparison of our suggested strategy and others suggested in the literature for mushroom classification is shown in Table 4. This comparison shows that, when compared to earlier studies, our suggested approach is quite successful at classifying mushrooms. Figure 5 illustrates the accuracy matrix for the MobileNetV2_GAP_flatten_fc model, while Figure 6 shows the validation matrix for the same model.

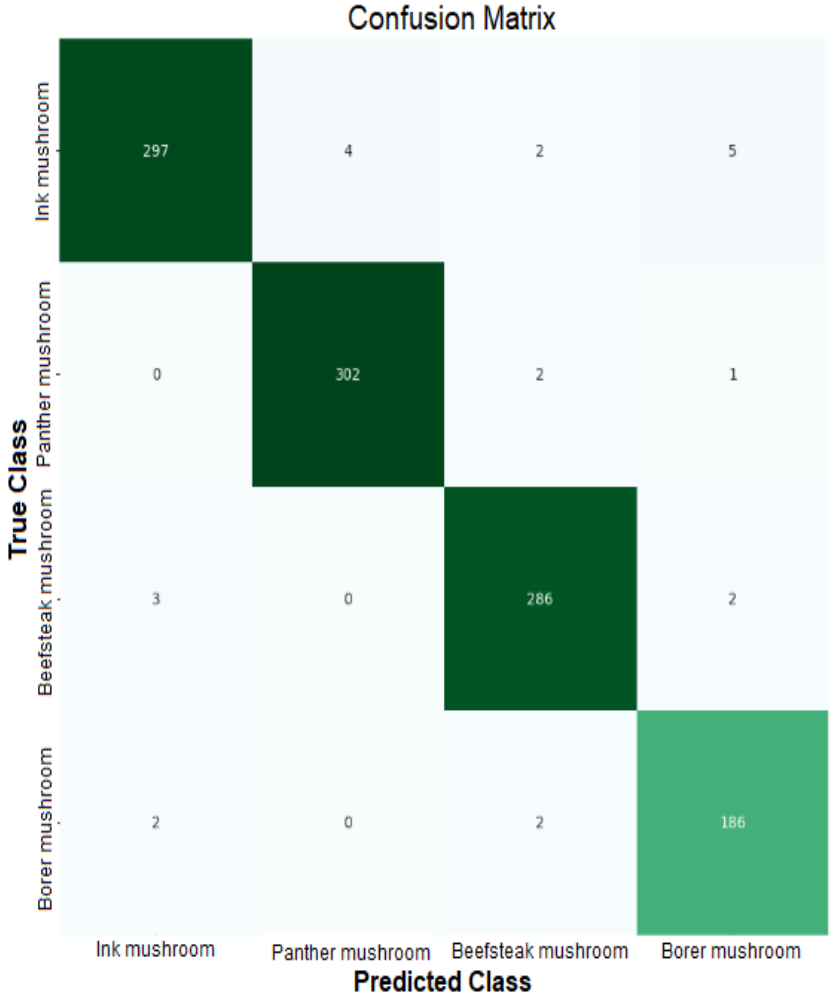

Figure 5. *Accuracy Matrix for MobileNetV2_GAP_flatten_fc Model*

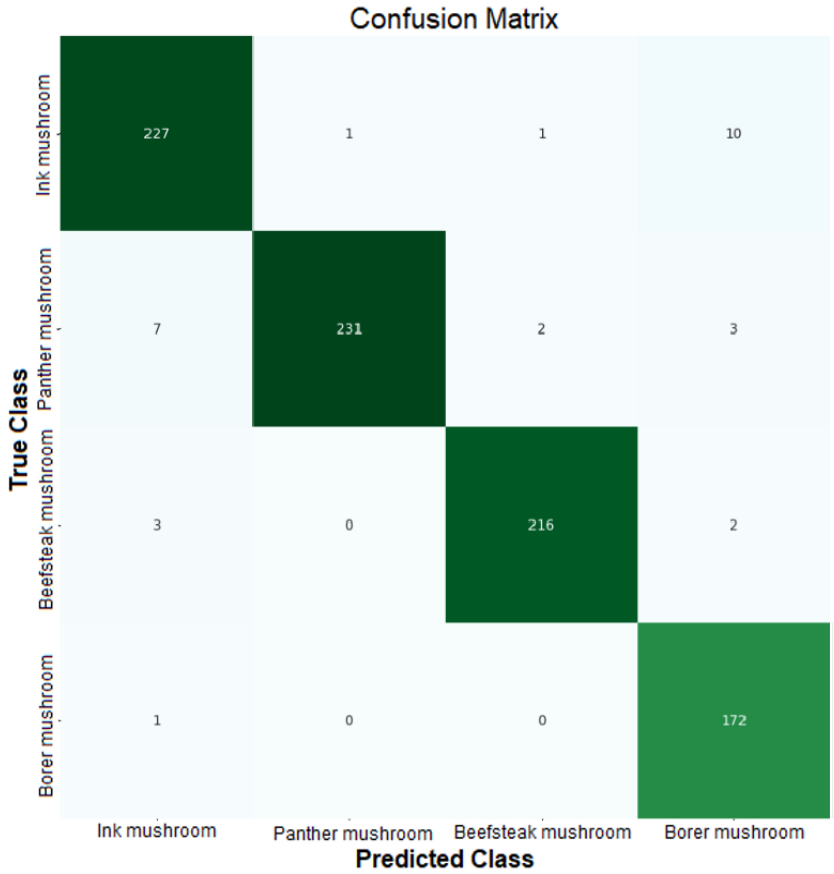

Figure 6. *Validation Matrix for MobileNetV2_GAP_flatten_fc Model*

Table 4. *Comparison of the Proposed Approach with the Approaches Found in the Literature for Mushrooms*

	Number of Images	Model	Number of Classes	Accuracy	Year
Mark and Meo	600	InceptionV3	6	%92,7	2022
Hui et al.	13.587	VGG16, ResNet18 ve GoogleNet	27	%93,1	2021
Wacharaphol et al.	623	AlexNet, ResNet-50 ve GoogLeNet	5	%95,50	2022
Boyuan	9528	Vi-T/L32	11	%95,97	2022
Nusrad, Zahid et al.	8190	InceptionV3, VGG16 ve Resnet50	45	%88,40	2021

6. ABLATION STUDIES

Several experiments were conducted on various batch sizes and epochs in order to determine the best ones to use during the model training phase. As observed in Figures 7 and Figure 8, the test accuracy rises as the training time per epoch falls up to 32 batches. Figure 8 displays the experimental outcomes of the Mobilenet-V2_GAP_flatten_fc model trained with batch sizes of 16, 32, 64, and 128 images. Test accuracy declines after 32 batches. Model training had its best performance with a batch size of 32. Test accuracy measurements for 100 model training epochs are shown in Figure 9. The test accuracy is seen to gradually rise with epoch until it approaches 100. The epoch was chosen for 100 iterations because after 100 epochs, the model begins to overfit the dataset. Figure 9 displays the training and validation success and failure for 100 epochs.

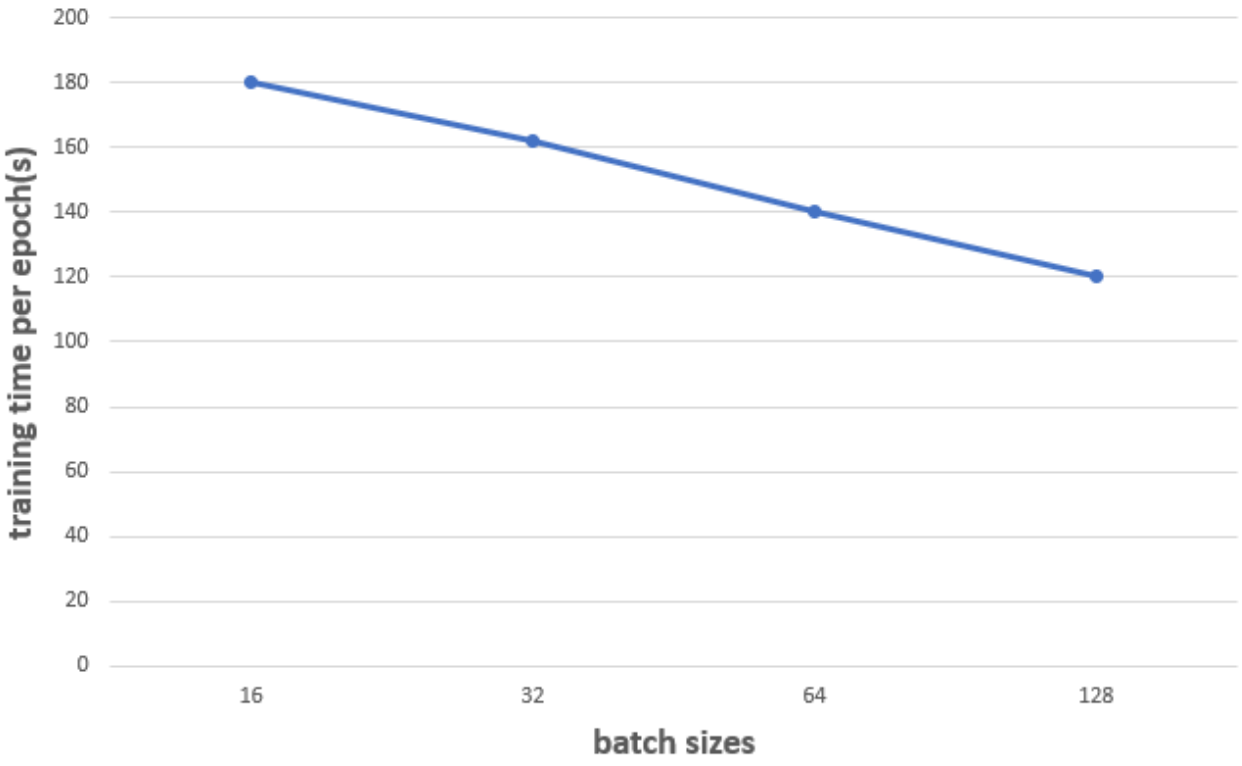

Figure 7. *Effect of Batch Sizes on the Performance of the Model*

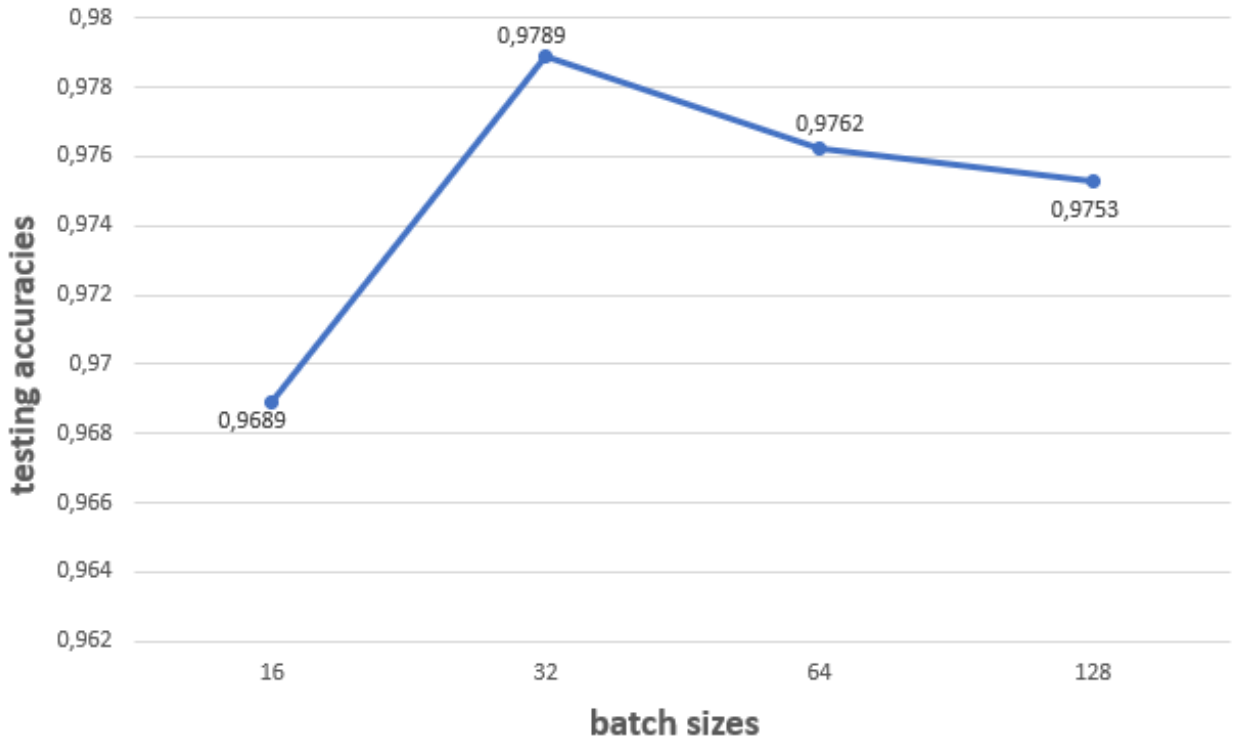

Figure 8. *Batch Size in Relation to Training Time Per Epoch and Batch Size in Relation to Model Accuracy Testing*

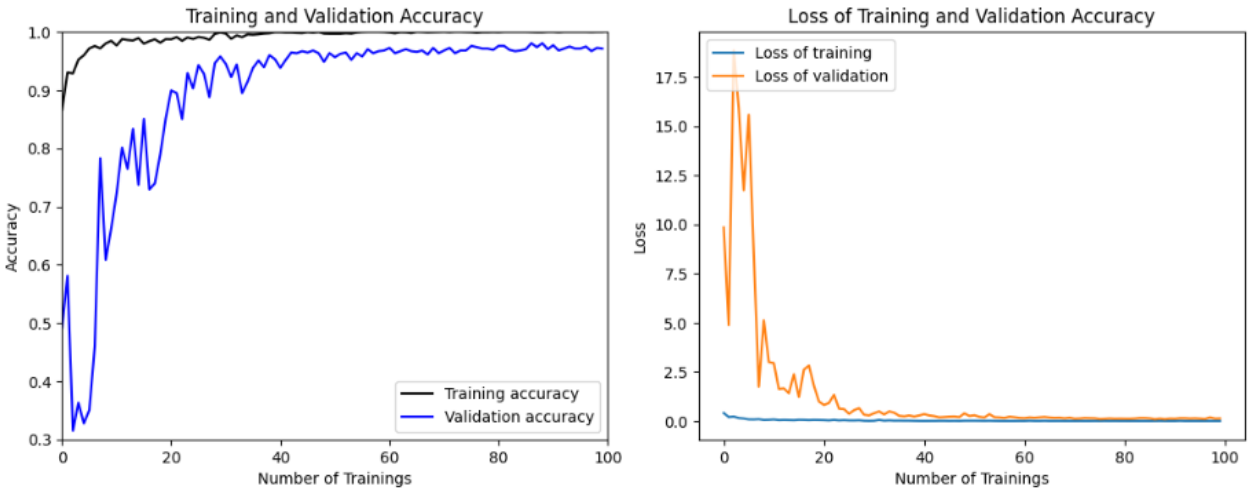

Figure 9. *Accuracy and Loss in the Training Process for the MobileNetV2 Model*

7. DISCUSSION

A thorough comparison analysis of a range of pre-trained modern facilities networks is also carried out to show the success of the suggested technique. Transfer learning was employed by utilizing pre-trained models. The comparative results demonstrate that the MobileNet-V2 model has a lower computational expenditure in terms of its training time and parameter count when compared to the pre-trained models. Nevertheless, the MobileNet-V2 model performed well in precisely categorizing mushrooms based on the attributes discovered from the studied data, in addition to having a low computational cost. It can be argued that deep CNN models can learn both low-level and high-level features from the input images during their basic training, and this training also produces impressive outcomes of the dataset under study's classification.

In the future, the envisioned model will seamlessly integrate with a mobile application, offering an advanced tool for real-time disease identification. This will make it easier for mushroom growers to automatically diagnose disease symptoms without requiring the involvement of field experts or extension workers. Thus, timely management of diseases and prevention of poisoning caused by fungi will be ensured.

8. CONCLUSION

In this article, a method based on deep convolutional neural networks is suggested to automatically recognize digital pictures of mushrooms. The training, validation, and test datasets are created by randomly dividing a collection of 5470 photos of four different types of mushrooms.

In order to provide additional evidence of the effectiveness of the proposed approach, an extensive comparative analysis of several state-of-the-art networks that have already been trained was performed Pre-trained models were employed through a transfer learning approach. Comparative results reveal that, in terms of training time and parameter count, the Mobilenet-V2_GAP_flatten_fc model exhibits a higher computational cost compared to other pre-trained models. The Mobilenet-V2_GAP_flatten_fc model performed a considerably better job of reliably diagnosing the disease symptoms utilizing learned features from the research data, despite its high computing cost. From the input photographs, it was inferred that deep CNN models trained on baseline can also extract both high-level and low-level features. It was observed also pretty good classification results on the dataset that is being studied.

The mushroom dataset's fundamental structural architecture serves as the basis for modeling the cutting-edge "Mobilenet-v2" network. In these architectures, base learning is used, and the mushroom dataset is used to train all of the computational layers. According to experimental findings, Mobilenet-V2_GAP_flatten_fc model was evaluated by looking at recall, precision, accuracy, F1 score performance evaluation criteria. In this evaluation, Macro Average values were examined for the results. As a result of the evaluation, it was seen that the best results for sensitivity, precision and F1 score in the test data set were 97.91%, 97.71%, 97.80%, respectively. In addition to accurately predicting class levels based on unobserved data, the MobileNetV2

model was effective at learning mushroom-related properties. According to this study, deep learning approaches provide highly promising outcomes for mushroom identification.

CONFLICT OF INTEREST

The authors declare no conflict of interest.

REFERENCES

Chen, T. M., Rui, J., Wang, Q. P., Zhao, Z. Y., Cui, J. A., & Yin, L. (2020). A mathematical model for simulating the phase-based transmissibility of a novel coronavirus. *Infectious Diseases of Poverty*, *9*(1), 24. https://www.doi.org/10.1186/s40249-020-00640-3

Demirel, Y., & Demirel, G. (2023). Mushrooms. *figshare*. https://www.doi.org/10.6084/m9.figshare.24470113.v1

Jarrett, K., Kavukcuoglu, K., Ranzato, M. A., & LeCun, Y. (2009, September 29 - October 2). *What is the best multi-stage architecture for object recognition?*. In: Proceedings of the International Conference on Computer Vision, (pp. 2146-2153). https://www.doi.org/10.1109/ICCV.2009.5459469

Ketwongsa, W., Boonlue, S., & Kokaew, U. (2022). A New Deep Learning Model for the Classification of Poisonous and Edible Mushrooms Based on Improved AlexNet Convolutional Neural Network. *Applied Sciences*, *12*(7), 3409. https://www.doi.org/10.3390/app12073409

Krizhevsky, A., Sutskever, I., & Hinton, E. G. (2012). ImageNet Classification with Deep Convolutional Neural Networks. *Communications of the ACM*, *60*(6), 84-90. https://www.doi.org/10.1145/3065386

Lee, H., Grosse, R., Ranganath, R., & Ng, A. Y. (2009, June 14-18). *Convolutional Deep Belief Networks for Scalable Unsupervised Learning of Hierarchical Representations*. In: Proceedings of the 26th Annual International Conference on Machine Learning, (pp. 609-616). https://www.doi.org/10.1145/1553374.1553453

Pinto, N., Doukhan, D., DiCarlo, J. J., & Cox., D. D. (2009). A high-throughput screening approach to discovering good forms of biologically inspired visual representation. *PLOS Computational Biology*, *5*(11), e1000579. https://www.doi.org/10.1371/journal.pcbi.1000579

Sandler, M., Howard, A., Zhu, M., Zhmoginov, A., & Chen, L. C. (2018, June 18-23). *MobileNetV2: Inverted residuals and linear bottlenecks*. In: Proceedings of the IEEE/CVF Conference on Computer Vision and Pattern Recognition, (pp. 4510-4520). https://www.doi.org/10.1109/CVPR.2018.00474

Seidaliyeva, U., Akhmetov, D., Ilipbayeva, L., & Matson, E. T. (2020). Real-time and accurate drone detection in a video with a static background. *Sensors (Basel)*, *20*(14), 3856. https://www.doi.org/10.3390/s20143856

Sokolova, M., & Lapalme, G. (2009). A systematic analysis of performance measures for classification tasks. *Information processing and management*, *45*(4), 427-437. https://www.doi.org/10.1016/j.ipm.2009.03.002

Sutayco, M. J. Y., & Caya M. V. C. (2022, November 22-23). *Identification of Medicinal Mushrooms using Computer Vision and Convolutional Neural Network*. In: Proceedings of the 6th International Conference on Electrical, Telecommunication and Computer Engineering (ELTICOM), (pp. 167-171). https://www.doi.org/10.1109/ELTICOM57747.2022.10038007

Turaga, S. C., Murray, J. F., Jain, V., Roth, F., Helmstaedter, M., Briggman, K., Denk, W., & Seung, H. S. (2010). Convolutional networks can learn to generate affinity graphs for image segmentation. *Neural Computation*, *22*(2), 511-538. https://www.doi.org/10.1162/neco.2009.10-08-881

Wang, B. (2022). Automatic Mushroom Species Classification Model for Foodborne Disease Prevention Based on Vision Transformer. *Journal of Food Quality*, 1173102. https://www.doi.org/10.1155/2022/1173102

Zahan, N., Hasan, M. Z., Malek, M. A., & Reya, S. S. (2021, February 27-28). *A Deep Learning-Based Approach for Edible, Inedible and Poisonous Mushroom Classification*. In: Proceedings of the International Conference on Information and Communication Technology for Sustainable Development (ICICT4SD), (pp. 440-444). https://www.doi.org/10.1109/ICICT4SD50815.2021.9396845

Zhang, X., Han, L., Dong, Y., Shi, Y., Huang, W., Han, L., González Moreno, P., Ma, H., Ye, H., & Sobeih, T. (2019). A Deep Learning-Based Approach for Automated Yellow Rust Disease Detection from High-Resolution Hyperspectral UAV Images. *Remote Sensing*, *11*, 1554. https://www.doi.org/10.3390/rs11131554

Zhao, H., Ge, F., Yu, P., & Li, H. (2021). *Identification of Wild Mushroom Based on Ensemble Learning*. In: Proceedings of the IEEE 4th International Conference on Big Data and Artificial Intelligence (BDAI), (pp. 43-47). https://www.doi.org/10.1109/BDAI52447.2021.9515225

Zheng, J. (2020). Sars-cov-2: an emerging coronavirus that causes a global threat. *International Journal of Biological Sciences*, *16*(10), 1678, 1685. https://www.doi.org/10.7150/ijbs.45053

Research Article GU J Sci, Part A, 10(4): 499-510 (2023) 10.54287/gujsa.1371904

Gazi University
Journal of Science
PART A: ENGINEERING AND INNOVATION
http://dergipark.org.tr/gujsa

Design and Co-Analysis of a Permanent Magnet Brushless DC Motor by Using Clonal Selection Principle Based Wound Healing Algorithm and Ansys-Maxwell

Yıldırım ÖZÜPAK[1*] Mehmet ÇINAR[2]

[1] Silvan Vocational School, Dicle University, Diyarbakır, Türkiye
[2] Tatvan Vocational School, Bitlis Eren University, Bitlis, Türkiye

Keywords

BLDC
WHA
Optimization
PID Controller

Abstract

This paper presents the design and analysis of a 550 W Permanent Magnet (PM) Brushless DC motor (BLDC). The finite element method (FEM) was employed to assess the motor's performance characteristics. The design and dynamic performance analysis were conducted using ANSYS/Rmxprt, while electromagnetic studies were carried out using ANSYS/Maxwell-2D. Additionally, optimization of the DC motor was achieved through a Wound Healing Algorithm (WHA). A PID controller was designed for this purpose. The paper also elaborates on the detailed design equations for creating a BLDC motor. BLDC motors are known for their high dynamic responses, efficiency, extended operating life, wide speed change intervals, and noise-free operation. The motor's geometry was modeled in the ANSYS-Maxwell-Rmxprt software tool and later imported into the Maxwell-2D environment for further analysis. The designed motor was observed to operate with 93% efficiency, meeting the specified torque value. The results of the optimization process were interpreted by comparing them with the values obtained from the ANSYS software.

Cite

Ozupak, Y., & Cinar, M. (2023). Design and Co-Analysis of a Permanent Magnet Brushless DC Motor by Using Clonal Selection Principle Based Wound Healing Algorithm and Ansys-Maxwell. *GU J Sci, Part A, 10*(4), 499-510. doi:10.54287/gujsa.1371904

Author ID (ORCID Number)

0000-0001-8461-8702 Yıldırım ÖZÜPAK
0000-0002-1542-9120 Mehmet ÇINAR

Article Process

Submission Date 05.10.2023
Revision Date 10.11.2023
Accepted Date 23.11.2023
Published Date 13.12.2023

1. INTRODUCTION

In recent years, Brushless Direct Current (BLDC) motors have garnered significant attention in the industry due to their substantial advantages. The pre-diagnosis of malfunctions is a crucial aspect in these motors since any malfunction can impact the motor's sensitivity. Recent developments in permanent magnets have facilitated their use in electrical machines. The replacement of conventional field windings in the rotor of traditional DC motors with permanent magnets enhances efficiency by reducing copper losses. These permanent magnet motors find widespread use in various industrial applications owing to their high torque, flexible design, and excellent efficiency and dynamic performance characteristics.

Studies on permanent magnet motors started in the 1990s. The detailed study of the magnetic equivalent circuit design of these motors has started to be carried out by researchers in recent years. Back electromotive force (back emf), harmonic amplitude and winding types between phases and lines have been shaped for different groove structures and magnet numbers. ANSYS-Maxwell-3D was used to design motors with different grooves and pole numbers and detailed analysis results were compared with each other (Dusane, 2016). The performance of the motors could be largely predicted even before production.

Multiple design iterations can be conducted faster and at a lower cost, creating new designs by optimizing the original parameters (Özüpak & Aslan, 2023). Precise calculation of motor parameters and features is crucial

*Corresponding Author, e-mail: yildirimozupak@gmail.com

for error-free product production (Kannojia & Chinmaya, 2023). This research details the methodology for developing a Brushless DC (BLDC) motor, presenting comprehensive design equations. The motor's geometry is generated through the RMxprt tool in ANSYS. The efficiency of the designed BLDC motor reaches 87.2%, a crucial consideration from an electric vehicle perspective (Kumar et al., 2022). The paper introduces a radial flux Brushless DC (BLDC) motor featuring a distinctive permanent magnet arrangement known as the Halbach-array magnet arrangement. In this arrangement, Halbach-array magnets are strategically positioned between the rotor poles, and their magnetization is configured to enhance the overall air gap flux density. The study conducts a performance comparison with a conventional BLDC motor, utilizing Finite Element Analysis (FEA) solutions to assess the designed configurations (Bala et al., 2020).

Furthermore, the research delves into the performance of a closed-loop BLDC motor with varied slot designs. A two-phase-based control strategy, incorporating a Proportional-Integral (PI) speed controller, is implemented on four types of BLDC motors. These motors are designed with constant slot areas using Ansys software. The study comprehensively analyzes various parameters within the closed-loop system, including dynamic speed response, electromagnetic torque, and air-gap flux waveforms (Kumar et al., 2020). In a study, a firefly algorithm based Fractional-Ordered Proportional-Integral-Derivative (FOPID) controller is proposed for torque and speed control of a Brushless DC (BLDC) motor. The research shows an effective control with low error margin, especially in Matlab/Simulink environment (Ibrahim et al., 2014). In another study, an innovative method for the optimal design of a permanent magnet BLDC motor was introduced (Bapayya & Venkata, 2020). This involves the optimization of electrical and mechanical parameters using a genetic algorithm. In another research, the use of particle swarm optimization (PSO) and bacterial search (BF) algorithms to determine the optimum parameters in a Proportional-Integral-Derivative (PID) controller for BLDC motor speed control was investigated. The study suggests a Fractional-Order PID (FOPID) controller, incorporating the artificial bee colony algorithm to enhance BLDC motor performance. Additionally, the Kalman filter is employed for speed estimation and adjustment. The obtained results are compared with other optimization algorithms, including firefly and particle swarm optimization algorithms. Moreover, a Fractional-Order PID (FOPID) is designed for DC motor speed control in a separate study, utilizing the pollination optimization algorithm. The FOPID parameters are adjusted to obtain optimum operating values, and the results are compared with those obtained from firefly and particle swarm optimization algorithms.

In this study, the design and detailed analysis of the internal magnet BLDC motor operating with a nominal speed of 1504 rpm and operating with 93% efficiency were carried out with two different methods. Transient analysis platform with ANSYS Maxwell 2D was used to obtain the performance values of the motor. The control circuit of the designed motor was designed with Ansys-Scade-Simplorer. With this program, the parameters of the motor, efficiency, speed control, torque, magnetic flux distribution, test results of the motor at full load and at no load were obtained. In addition, the parameters of the motor obtained in the ANSYS program were tried to be obtained with the PID controller designed with the help of the wound healing algorithm and the values were compared with each other.

After the introduction section of this study, the section related to materials and methods has been explained. In the third section of the study, the motor has been analyzed in the ANSYS-Maxwell environment and optimized using the developed algorithm. The fourth section presents the findings of the study as the results.

2. MATERIAL AND METHOD

2.1. Developed Algorithm (wound healing algorithm)

When a foreign substance enters the body, the immune system initiates a response, and the algorithm that leverages the characteristics of this immune response is known as the clonal selection algorithm. The clonal selection principle-based wound healing algorithm is a recently developed algorithm, and its outcomes have been compared with those of a widely used program, such as ANSYS.

$$N_c = \sum_{i=1}^{n} round\left(\frac{N}{i}\right) \quad (1)$$

N_c*:* Clone numbers that produced from each antigen

N: Solution population's total number

n: Selected antibodies number

The clonal choice principle forms the premise of the wound healing algorithm. With the assistance of equation one, the quantity of clones made is calculated. Wound healing formula was developed with the assistance α (cloning) and f (cloning acceleration factor) parameters other to (1). The ultimate state obtained is given in (4). With the assistance of the new parameters other, a lot of optimized results were tried to be obtained. Developed wound healing algorithm's flow chart is shown in Figure 1. When the initial population P is made, the choice method moves in and selects the antibodies with the most effective immunologic response (affinity) worth to get the new Pn population the essential rule. Throughout the choice process, is that the affinity worth of antibodies. Then, people within the population area unit cloned and new populations area unit created. The quantity of clones to be obtained varies in step with the affinity worth. At this stage, a brand-new population is made by applying hypermutation to the clones. within the hypermutation method, reciprocally proportional to the affinity worth, that is, a low mutation with a high affinity worth encompasses a high mutation rate with a low affinity worth. Thus, antibodies aloof from the optimum resolution area unit subjected to more mutation processes. Then, among the obtained clones, those with low similarity magnitude relation area unit replaced with new ones. As a result, the optimum results obtained with the assistance of biological research and mutation processes.

2.1.1 Solution stages of wound healing algorithm

Utilize N antibodies to form the initial population (P). Evaluate the affinity of each antibody in the P population. Choose the n antibodies (N) with the highest affinity to create a Pn population. To assess the affinity value between an antibody and an antigen, the distance between them is typically considered. This is computed using equation (2) and the Euclidean distance formula.

$$d = \sum_{i=1}^{N} (Ag_i - Ab_i)^2 \quad (2)$$

The computed value of d is compared to the threshold value λ, and the marking error E is determined according to equation (3):

$$E = d - \lambda \quad (3)$$

1. Clone the n antibodies selected in step 2 and construct N_c using (4)

$$Nc_i = \sum_{i=1}^{n} round\left(\frac{\alpha * N_s * f}{i}\right) \quad (4)$$

α : Cloning factor (value range is 0-1)

Alter the Nc clone population by introducing mutations. Define this subpopulation and calculate the affinity value for each antibody within it. Choose the antibody with the highest affinity value and incorporate it into the original population. Afterwards, replace the low-affinity antibody with new antibodies. In cases where the population value P is less than N, generate antibodies to fill the population.

2.2. Optimum PID Controller Design

There are different controller structures used in control systems. The most used ones are PID, PI, PD, phase advance or phase regression controllers. The PID controller preferred in the study has a wide range of uses due to its many advantages. The number of parameters to be calculated is low, the structure is simple, durable, and reliable, which makes these controllers stand out. PID controllers are controllers that gather the superior aspects of proportional-integral-derivative components under a single structure. While the integral component brings the steady state error closer to zero in the system, the derivative effect increases the response speed of the system. Table 1 displays the parameters WHA. The steady state structure of the PID controller is as follows:

$$U_s = \left(K_p + \frac{K_i}{s} + K_d d\right) E(s) \quad (5)$$

In (6), Kp: Proportional gain, Ki: Integral gain, Kd: Derivative gain.

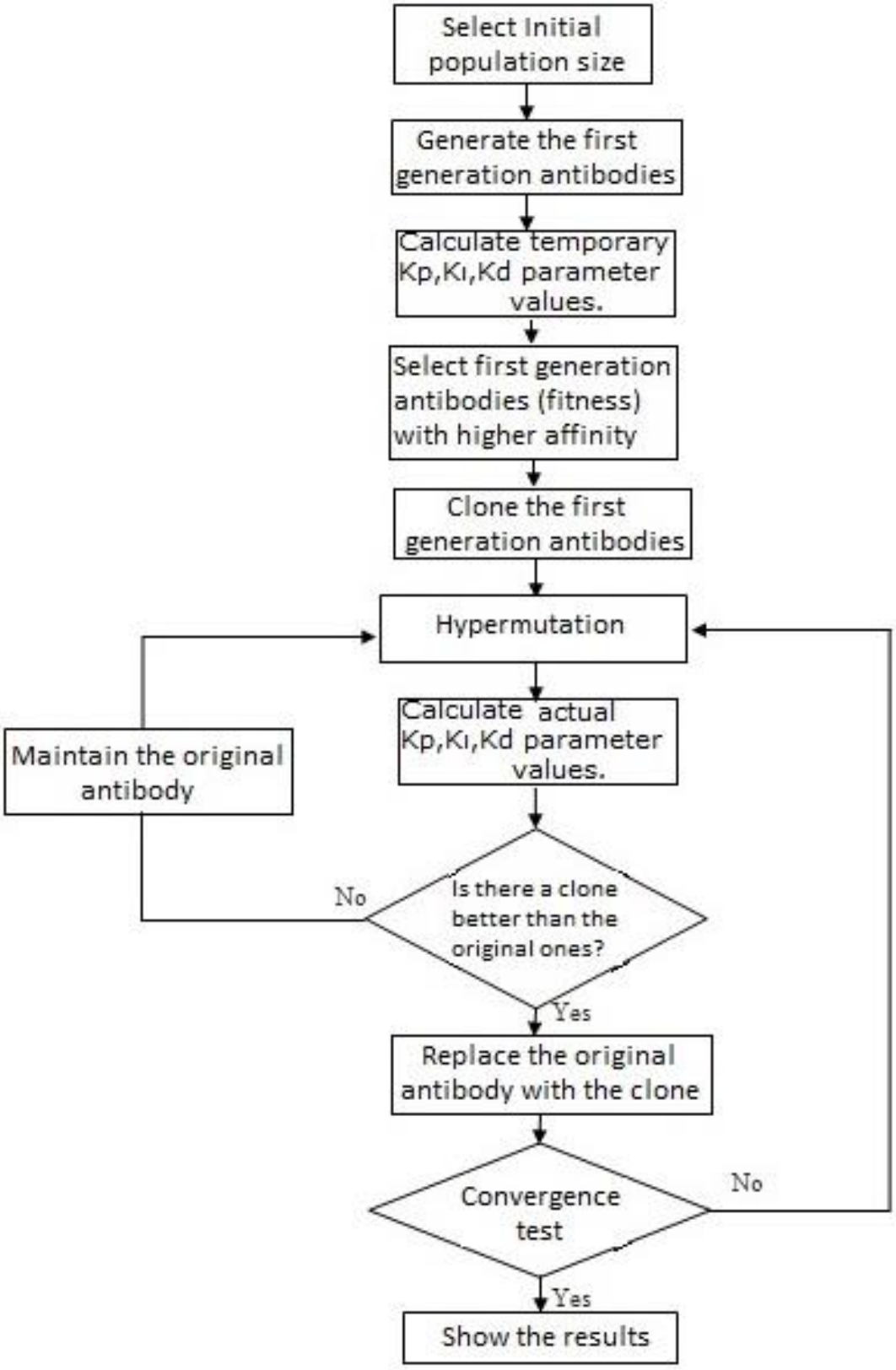

Figure 1. *Wound healing algorithm flowchart*

Table 1. *WHA parameters*

Parameter	Value
Number of Population	150
Iteration number	150
Run number	30
Healing coefficient	1.3
Affinity coefficient	1.3
Clone coefficient (α)	0.4
Clone acceleration (f)	0.95

A Matlab program was created to determine the design values of the permanent magnet brushless DC motor using a developed algorithm. Figure 2 illustrates the screen output of the program, showcasing the calculated PID controller parameter values for the optimization process.

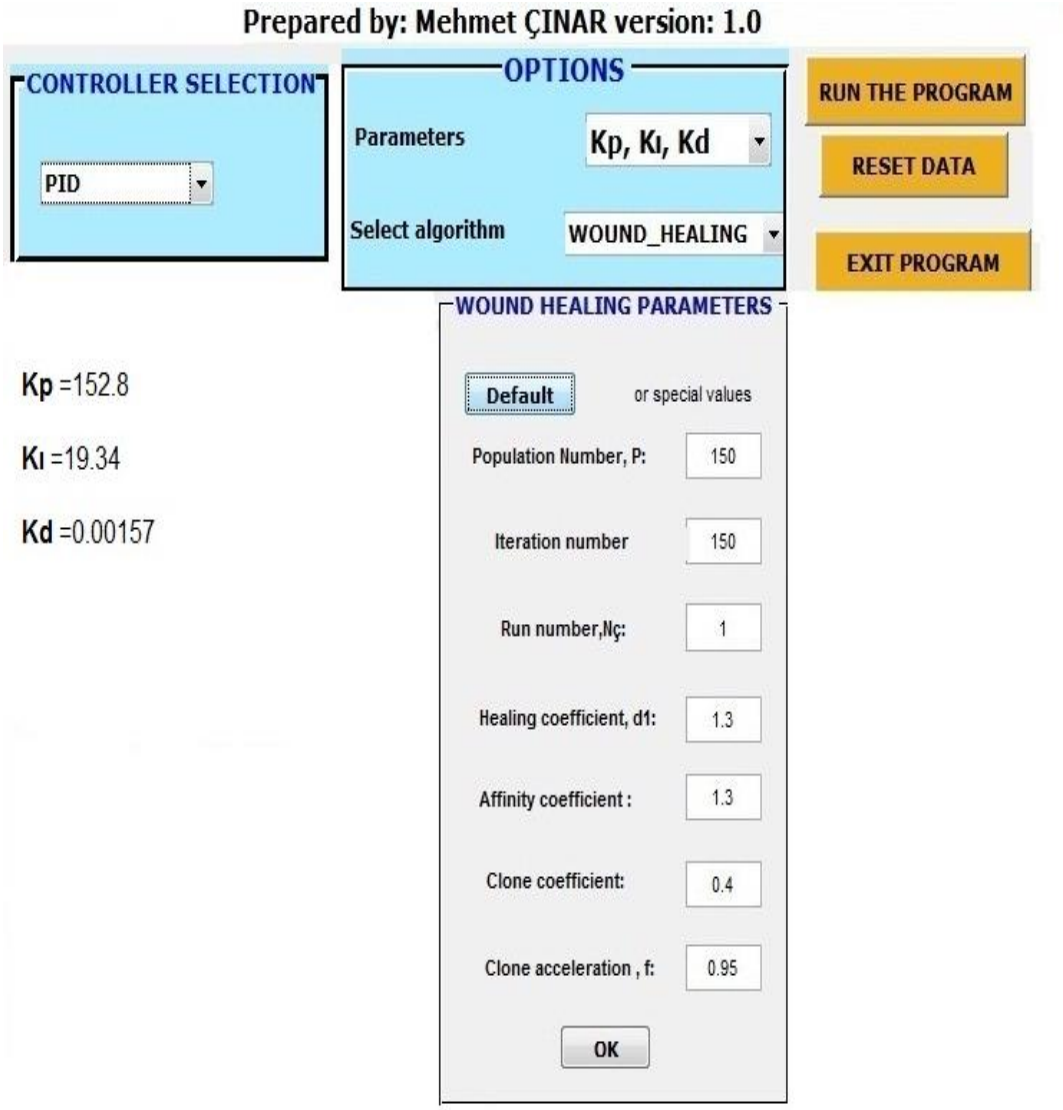

Figure 2. *The Developed Program*

2.3. Mathematical Equations of BLDC

Torque of BLDC motor is expressed by (7).

$$T = 2NN_mB_gLR_{ro}I = k_tI \quad (7)$$

In the given context, where N represents the number of turns in the groove, N_m is the number of poles, Bg is the air gap flux density, L is the length of the motor, and R_ro is the rotor outer diameter. The factor 2N takes into consideration the operation of the three-phase inverter in the 120-degree transmission mode, indicating that 2 phases carry current at any given time. Equation (8) presents the expression for the reverse electromotive force (EMF) in the Brushless DC (BLDC) motor (Bala et al., 2020).

$$E_b = 2NN_mB_gLR_{ro}W_m = k_eI \quad (8)$$

Where W_m is the angular velocity of the rotor. When the torque and reverse EMF equations are compared, it is seen that the torque and back emf constants are equal in (9).

$$k_t = k_e = 2NN_mB_gLR_{ro} \quad (9)$$

Results from the motor can be expressed in terms of main dimensions, specific electric and magnetic charges, and speed. The kVA value of the BLDC motor is given in (10).

$$S = C_oR_{ro}^2LW_m \quad (10)$$

Where, C_o is a constant and is expressed as given in (11).

$$C_o = 11B_{av}ack_w * 10^{-3} \quad (11)$$

Where, B_{av} is the magnetic charge, ac is the electrical charge and k_w is the winding factor.

Copper losses for two phases are given in P_{cu} (12).

$$P_{cu} = 2I^2\frac{\rho LN^2N_c}{K_{wb}A_g} \quad (12)$$

is expressed as. Here, ρ is the density of the copper wire, N_c is turns, K_{wb} is the filling factor of the bare wire, and A_g is the air gap. Wind and friction losses Pf are given in (13).

$$P_f = \frac{3}{100}P_{out} \quad (13)$$

The weight of the gears of the stator is defined as in equation (14). In the equation, ρ_i represents the iron density, A_t represents the cross-sectional area of the teeth, and N_s the number of grooves.

$$W_t = \rho_iA_tN_sL \quad (14)$$

The weight of the stator yoke is given by (15).

$$W_{sy} = \rho_iA_{sy}L \quad (15)$$

The weight of the rotor yoke is given as in (16).

$$W_{ry} = \rho_iA_{ry}L \quad (16)$$

Total iron weight is calculated as in (17).

$$W_{total} = W_{ry} + W_{sy} + W_t \quad (17)$$

Total iron loss is calculated by (18).

$$P_{iron} = L_{kg} * W_{total} \quad (18)$$

Here L_{kg} is the loss in Watts per kg of stator material. The power input to the motor is calculated with the help of (19).

$$P_{in} = P_{out} + P_{cu} + P_{iron} + P_f \quad (19)$$

Machine efficiency ŋ (%) is given in (20).

$$ŋ\ (\%) = \frac{P_{out}}{P_{in}} \quad (20)$$

2.4. Motor Design

The design motor was made in the Rmxprt part of and Maxwell 2D, which performs the solution with the FEM. The excitation circuit and control circuit of the motor given in Figure 3 were also created in the ANSYS environment. The parameters given in Table 2 and Table 3 are defined as the input parameters of the motor to the software. Figure 3 presents the motor control circuit.

The PID parameter values in the control circuit obtained by the ANSYS program are Kp=150, Ki=20 and Kd=0.0016. These libraries in the program environment allow the parameters and design values to be evaluated at the first stage of the design while the engine is being designed. In this subprogram, analytical parameters can be calculated easily and quickly. The designed engine model can be easily transferred to the Maxwell program in 2D/3D for numerical and electromagnetic analysis. The parameters in Table 2 and their values were used for this design.

Table 2. *Stator parameters*

Parameter	Value
Ratedpower(W)	550
Ratedvoltage(V)	220
Ratedspeed(rpm)	1500
Number of pole	4
Frictionalloss(W)	12
Windageloss(W)	0

The dimensions of the Slot parameters are presented in Table 3.

Table 3. *Slot parameters*

Parameter	Value (mm)
Hs0	0.5
Hs1	1
Hs2	8.2
Bs0	2.5
Bs1	5.6
Bs2	7.6

For the rotor permanent magnet pole, the rotor geometry among the shapes in the Rmxprt was used and the parameter values in Table 4 were used for the rotor design.

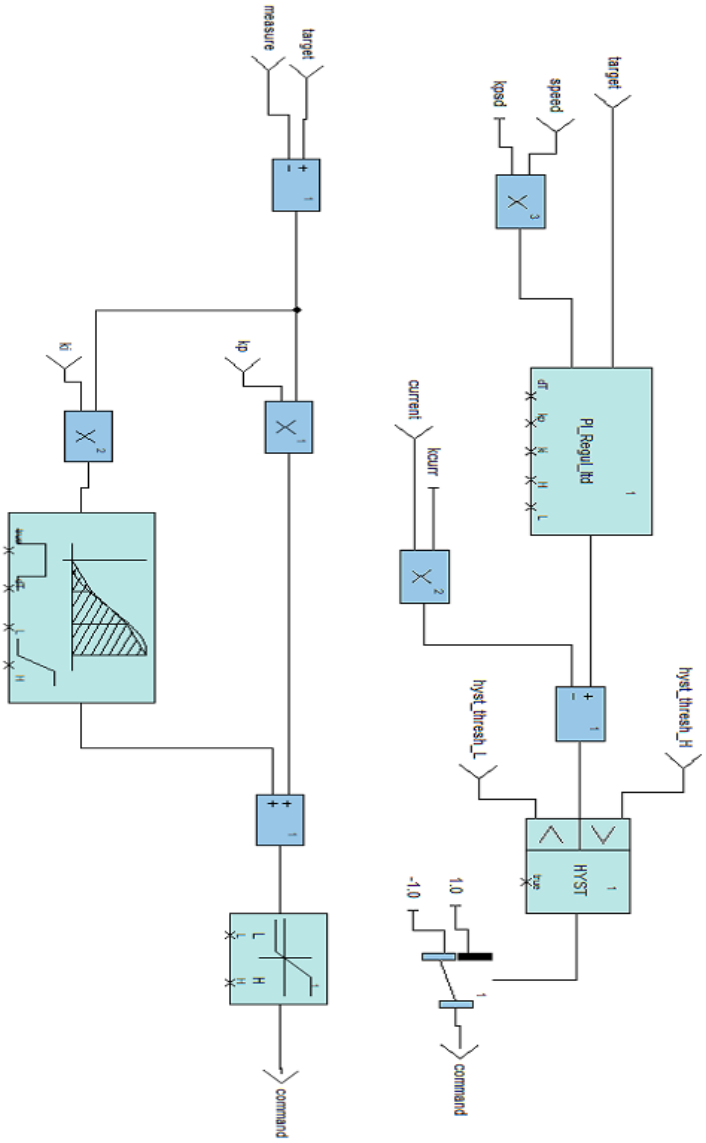

Figure 3. *Motor control circuit*

Table 4. *Rotor parameters*

Parameter	Value
Number of Slots	24
Outer Diameter (mm)	120
Inner Diameter (mm)	75
StackingFactor	0.95
SlotType	2
SkewWidth (mm)	0
Minimum airgap (mm)	1
Type of material	M19_24G
Embrace	0.7
Thickness of magnet (mm)	3.5
MagnetType	XG196/196

3. RESULTS AND DISCUSSION

3.1. Rmxprt Analysis Results

The engine design created in Rmxprt was transferred to the Maxwell-2D environment. This software is used for networking in FEM. There are some analyzes based on simulation in Maxwell 2D. The motor design created in Rmxprt was transferred to the Maxwell-2D environment. This software is used for mesh generation in FEM. Some simulation-based FEM analysis results in Maxwell 2D are presented in Figure 4, Figure 5 and Figure 6. These figures show the mesh formation, magnetic flux distribution, flux lines, speed-efficiency, current-load distribution and magnetic field intensity at a certain time of the rotor position, respectively.

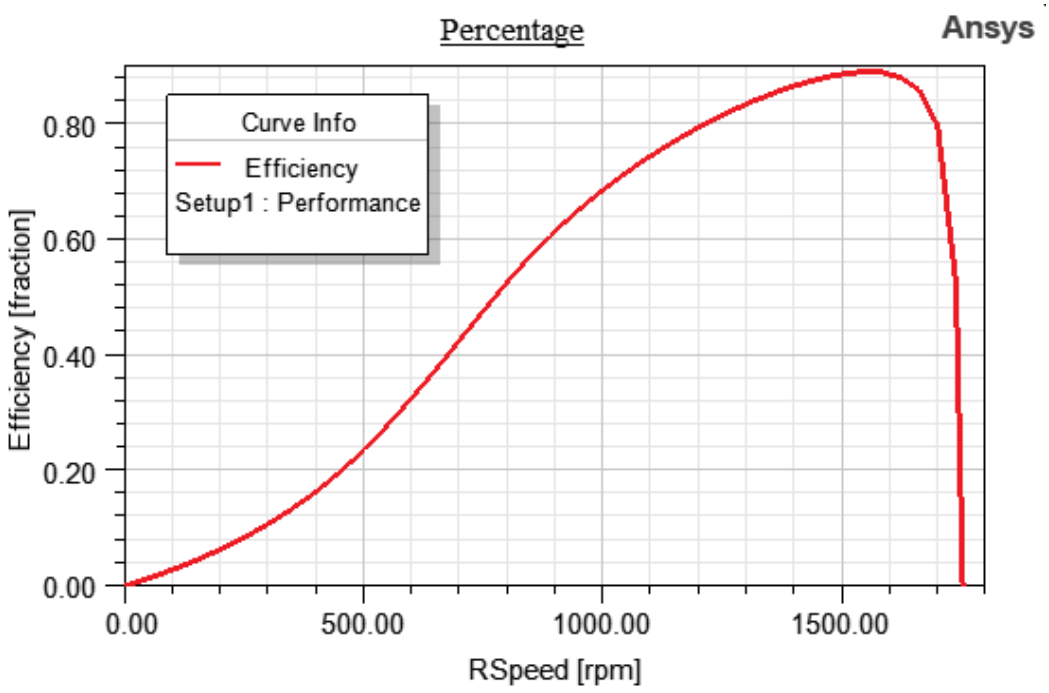

Figure 4. *Speed-efficiency graph of the motor*

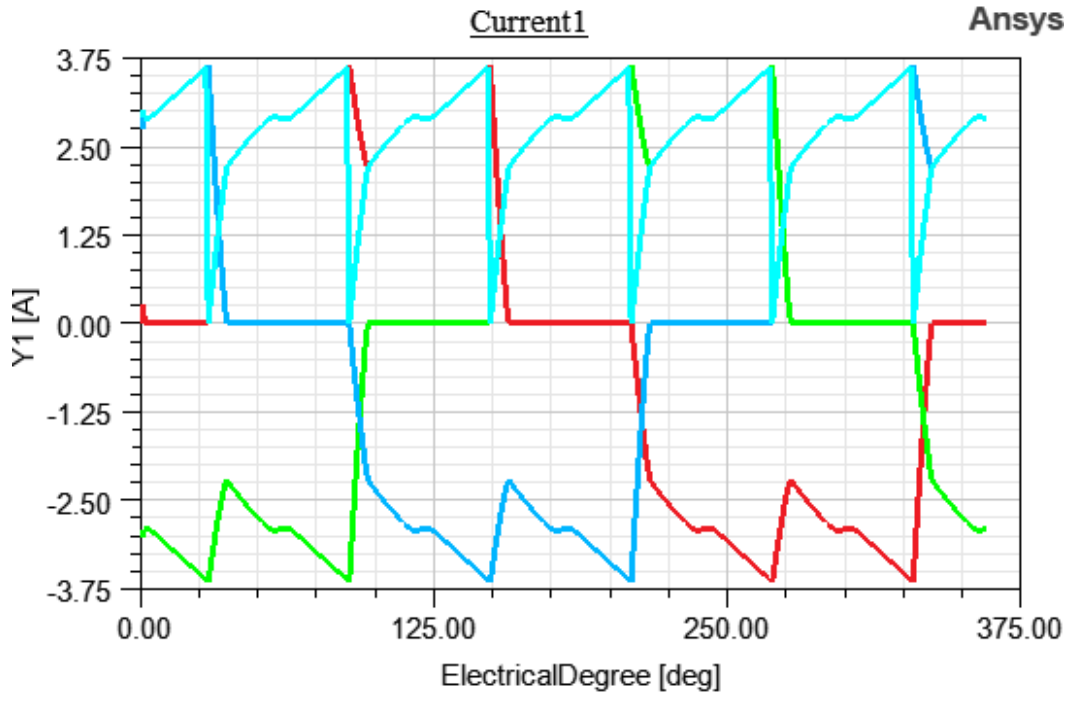

Figure 5. *Winding currents of the motor under load and variation of electrical angle graph*

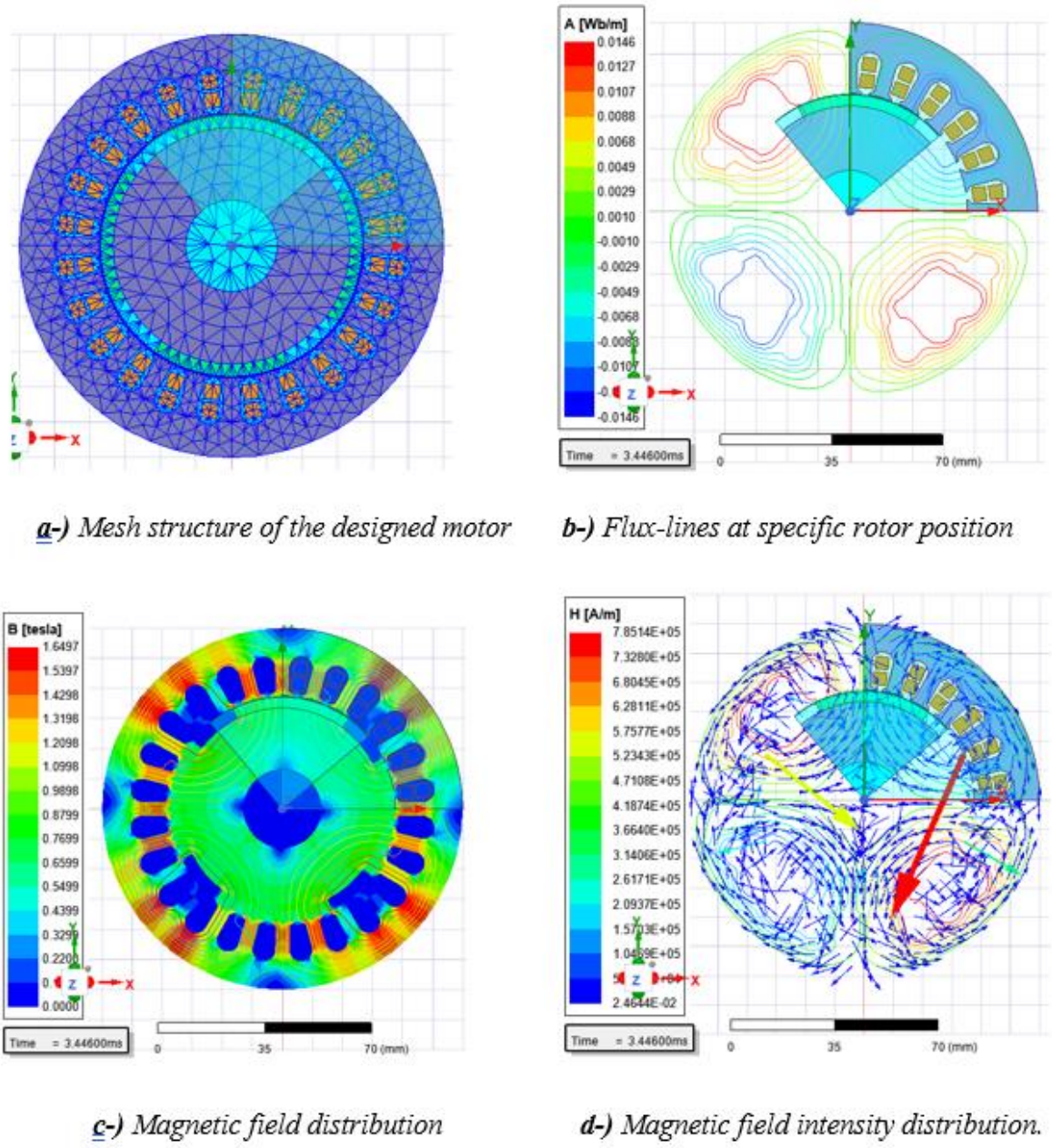

a-) Mesh structure of the designed motor *b-) Flux-lines at specific rotor position*

c-) Magnetic field distribution *d-) Magnetic field intensity distribution.*

Figure 6. *Electromagnetic Simulations results* ***a)*** *Mesh structure of the designed motor;* ***b)*** *Flux-lines at specific rotor position;* ***c)*** *Magnetic field distribution;* ***d)*** *Magnetic field intensity distribution*

After increasing the pole angle of the control circuit on the motor, the analysis is done, and the design is made when the pole angle is 0 degrees. To improve motor performance, the advance angle changes and the change in engine performance is analyzed. After changing the pole angle of the motor, the efficiency of the motor increases. The pole angle determines the induction time of the voltage. The excitation of the previous windings is due to the increase of this pole angle. The phase currents and the opposite electromotive forces of the phases have the same phase angle. Therefore, the desired torque value is obtained from BLDC machines even at low current levels.

3.2. MATLAB Analysis Results

In order to confirm the accuracy of the results obtained, the engine was reanalyzed with the program developed in the MATLAB environment. The values obtained as a result of the ANSYS program, and the results of the developed algorithm are given in Table 5. When Table 5 is examined, it is seen that the obtained values are very close to each other.

Table 5. *Results obtained as a result of the analysis*

Parameter	Value (ANSYS)	Value (Developed algorithm)
Flux Density (Tesla)	1.34	1.3125
Coercive Force(A/m)	785000	802000
Total Loss(W)	132	130.1
OutputPower(W)	512	508
InputPower(W)	550	550
Efficiency	%93	%92.3
Rated Speed (rpm)	1500	1500
RatedTorque(N-m)	4.01	4.16

4. CONCLUSION

In this paper, the basic design and analysis of the BLDC motor is carried out. Fundamentals of magnetic circuit and necessary basic equations used in electromagnetic field are obtained. BLDC motor with 550 W power and 1500 rpm has been designed. In the study, it has been observed that the efficiency of the motor at nominal torque and nominal speed is very good. The efficiency of the engine was obtained as 93%. The motor was designed in Rmxprt and electromagnetic field analyzes were performed in Maxwell-2D environment. After the motor was designed, the polar angle of the control circuit was changed and analyzes were carried out for different angle values. It has been observed that the efficiency of the BLDC motor increases when this angle is increased from 0° to 30°. It is concluded that by increasing the pole angle, the rated speed of the motor can be increased, an increase in efficiency can be achieved despite a decrease or fluctuation in the rated torque. When the motor parameters obtained in Table 5 with the help of the PID controller were examined, the efficiency of the motor was calculated as 92.3%. In addition, it is seen that the other calculated motor parameters are close to the values calculated because of the ANSYS-Maxwell.

CONFLICT OF INTEREST

The authors declare no conflict of interest.

REFERENCES

Bala, M. J., Roy, D. & Sengupta, A. (2020, 5-6 September). *The Performance Enhancement of BLDC Motor Using Halbach Array Rotor*. In: Proceedings of the 2020 IEEE 1st International Conference for Convergence in Engineering (ICCE), (pp. 405-409), Kolkata, India. https://www.doi.org/10.1109/ICCE50343.2020.9290642

Bapayya, N. K., & Venkata, R. K. (2020). Direct instantaneous torque control of Brushless DC motor using firefly Algorithm based fractional order PID controller. *Journal of King Saud University- Motorering Sciences*, *32*(2), 133-140. https://www.doi.org/10.1016/j.jksues.2018.04.007

Dusane, P. M. (2016). *Simulation of a Brushless DC Motor in ANSYS- Maxwell 3D, Prague*. MSc Thesis, Czech Technical University in Prague.

Ibrahim, H. E. A., Hassan, F. N., & Anas, O. (2014). Optimal PID control of a brushless DC motor using PSO and BF techniques. *Ain Shams Motorering Journal*, *5*(2), 391-398. https://www.doi.org/10.1016/j.asej.2013.09.013

Kannojia, P., & Chinmaya, K. A. (2023, 3-5 January). *Comparative Review and Finite Element Analysis of Energy Efficient Motors*. In: Proceedings of the International Conference on Power Electronics and Energy (ICPEE), Bhubaneswar, India. https://www.doi.org/10.1109/ICPEE54198.2023.10059611

Kumar, R., Kumar, P., Kumar, B., Singh, P., Kumar, R., & Kumar, A. (2022, 24-25 June). *Design and Analysis of High performance of a BLDC Motor for Electric Vehicle*. In: Proceedings of the 2nd International Conference on Emerging Frontiers in Electrical and Electronic Technologies (ICEFEET), Patna, India. https://www.doi.org/10.1109/ICEFEET51821.2022.984830

Kumar, A., Gandhi, R., Wilson, R. & Roy, R. (2020, 18-21 October). *The impact of different slot design of BLDC motor in a complete drive system*. In: Proceedings of the 46th Annual Conference of the IEEE Industrial Electronics Society, Singapore. https://www.doi.org/10.1109/IECON43393.2020.9255391

Özüpak, Y., & Aslan, E. (2023). Researching Inductive Power Transfer For Next Generation Electric Vehicles. *Ejons International Journal*, *7*(2), 220-232. https://www.doi.org/0.5281/zenodo.8265795

Research Article GU J Sci, Part A, 10(4): 511-523 (2023) 10.54287/gujsa.1357391

Gazi University
Journal of Science
PART A: ENGINEERING AND INNOVATION
http://dergipark.org.tr/gujsa

An Informetric View to the Negative Capacitance Phenomenon at Interlayered Metal-Semiconductor Structures and Distinct Electronic Devices

Nuray URGUN[1] Jaafar Abdulkareem Mustafa ALSMAEL[2] Serhat Orkun TAN[1*]

[1] Faculty of Technology, Karabük University, Karabük, Türkiye
[2] Faculty Engineering, Basrah University for Oil and Gas, Basrah, Iraq

Keywords

Negative Capacitance
Metal-Semiconductor Structures
Interlayer
Data Classifying
NC Devices

Abstract

Negative Capacitance (NC) phenomenon, which can be explained as the material exhibiting an inductive behavior, is often referred to as "anomalous" or "abnormal" in the literature. Especially in the forward bias/deposition region, the presence of surface states (Nss) and their relaxation times (τ), series resistance (Rs), minority carrier injection, interface charge loss in occupied states under the Fermi energy level, parasitic inductance, or poor measuring equipment calibration problems can be counted among the causes of this phenomenon. Studies on NC behavior have shown that this behavior can be observed for different frequencies, temperatures, and related parameters at forward biases. However, the NC behavior, which appears as an unidentified peak in admittance spectroscopy data, is not yet fully understood. Ultimately, this study aims to compile and analyze the NC reported in selected scientific studies, investigate the source of this phenomenon, and observe statistics in a general view.

Cite

Urgun, N., Alsmael, J. A. M., & Tan, S.O. (2023). An Informetric View to the Negative Capacitance Phenomenon at Interlayered Metal-Semiconductor Structures and Distinct Electronic Devices. *GU J Sci, Part A, 10*(4), 511-523. doi:10.54287/gujsa.1357391

Author ID (ORCID Number)

0000-0001-6574-4287 Nuray URGUN
0000-0002-2426-9421 J. Abdulkareem Mustafa ALSMAEL
0000-0001-6184-5099 Serhat Orkun TAN

Article Process

Submission Date 08.09.2023
Revision Date 28.10.2023
Accepted Date 08.11.2023
Published Date 13.12.2023

1. INTRODUCTION

The point where electronic technology has arrived currently, devices with large dimensions and slow, heavy, and rigid structures are being replaced by more compact, fast, light, and flexible ones. This rapid development draws attention to many electronic devices, especially FET, MOSFET, FinFETs, high-frequency Metal-Semiconductor (MS) Schottky Structures, several Schottky Junction Structures (SJSs) and their different interlayered types, solar cells, OLEDs, etc. Due to these structural changes in electronic devices, the negative capacitance (NC) phenomenon has been frequently observed in miniaturized electronic device applications in recent years (Joly et al., 2021; Karataş, 2021; Barkhordari et al., 2022; Liu et al., 2023; Çakıcı et al., 2023). With the Landau ferroelectric theory, ferroelectricity, which has been actively researched since the 1930s, has been employed quite commonly in the scientific community with the emergence of the negative capacitance phenomenon. Landau's theory, suitable for systems with long-range interactions such as ferroelectrics and superconductors, states that a system cannot change smoothly between two phases with different symmetries and that one phase must have higher symmetry than the other. However, negative capacitance effects were indirectly investigated but not fully revealed by researchers in the mid-1950s (Merz, 1956; Landauer, 1957).

To date, the perception of Negative capacitance has been generally described as an artificially created effect that has physical results in turn, similar to unexpected peak values in the device's electric and dielectric characteristics. NC has been explained by the feedback mechanism between applied voltage to the device and the altering value of the total device capacitance as "effective capacitance" by the polarization response of the ferroelectric material component due to the bias. Along with previous studies, in which the dielectric-

*Corresponding Author, e-mail: serhatorkuntan@karabuk.edu.tr

ferroelectric series connected capacitors approach to adjust the gate voltage of structures was employed and is based on two stable states of polarization in elastic Gibbs free energy landscape, one of the latest studies highlighted how the negative capacitance can have different behaviors in different situations by theoretical changes. They offered a new approach in ferroelectric capacitors to have all the components of NC, including *transient NC*, for a better understanding of the real existence of this phenomenon by replacing the second-order derivative of elastic Gibbs free energy with the second-order derivative of electrostatic force work in related equations (Zhang et al., 2021). The NC effect was theoretically determined in quantum well-infrared photodetectors (QWIPs) by comparing experimental results with several methods, including the Incremental Charge Approach, Sinusoidal Steady-State Analysis (SSSA), and Fourier analysis. It was concluded that the incremental charge approach was unreliable for calculating a device's characteristics since this method lacked absolute rules for separating incremental charge distribution into positive and negative parts, which is critical for devices with more than two contacts and 2D or 3D geometric devices where the incremental dopant concentration is distributed throughout the device area (Ershov et al., 1998). This method was only suitable for very small current ranges in reverse bias regions of MS/MIS/MOS structures and for capacitance values in low frequencies. Although SSSA was a convenient approximation, they noted that all equations had to be calculated at each frequency to observe the frequency dependency of the capacitance. Since observing the physical causes behind the frequency response of a device's characteristics was more noticeable in the time domain, they used Fourier analysis, which shifts between frequency and time domains. Despite the challenge of accurately selecting the sample time, they only needed to calculate the capacitance and conductance equations once for all frequencies. Their solution found a correlation between experiments and numeric models based on simulation results. They also included the negative and positive parts of the transient response and summarized the capacitance formula as follows: $c(w) = c_0 + \frac{a_1 \cdot T_1}{1+(w \cdot T_1)^2} - \frac{a_2 \cdot T_2}{1+(w \cdot T_2)^2}$ Here, a1, a2, T1, and T2 are adjustable parameters, but they do not significantly affect the main capacitance. The capacitance C(w) converges to the geometric capacitance Co at high frequencies, while C(w) can be negative at lower frequencies due to the contribution of a positive-valued time-derivative of transient current in the time domain. The researchers also clarified the confusion about parasitic effects at different frequencies and suggested that if the NC appeared in high frequencies, it could be sourced from the external circuit and was not an NC effect.

In another study, the researchers paid attention to eliminating the aforementioned external circuit effects, which can affect observed NC in results, by counting on before and after open/short circuit calibration states (Joly et al., 2021). In their work, they produced several numbers of back-to-back contact Pt/ZnO/Pt SJ diodes by ALD for a microsensor system and observed the NC in their C-V plots, offering that the main reason for this effect was due to the impact loss process-related to the hot electron injection at the MS junctions' interface trap states. The other researchers compared two diodes and observed the NC in their interlayered Schottky structure's (Ag/AgInSe$_2$/p-Si/Ag) characteristics at forward bias and low-frequency region due to additional layer's surface modification effects (Çakıcı et al., 2023). In one of the interlayered works, a p-Si MIS-structured capacitor was fabricated and investigated, using Ta2O5 as the insulating layer, ZnO as the semiconductor layer, and Al for the metal contacts (Noh et al., 2003). The researchers observed that the dielectric layer showed a negative flat band voltage due to charge trapping behavior based on the existence of positive charges in the films under the constant current applied. When they compared stress-induced leakage current (SILC) for different amounts of time, they explained why the SILC, affected by a higher stressing time of current, could be sourced from the generation of localized charges and trap states near the injection interface. So, they explained the low interface state density, which is a key element for a MIS type structure for performance, according to the combination of interlayers they employed. Researchers, then, have started to investigate alternative ways of using the "NC phenomenon" to develop device's energy consumption characteristics by designing new combinations of atoms to reduce the voltage loss rather than keeping the subthreshold swing below 60 mV, Boltzmann limit, with the help of short channel effects. In 2008, the negative capacitance was suggested to decrease the sub-threshold slope below 60 mV/decade by replacing the gate oxide with a negative capacitance material. When the compared devices' layer of HZO was changed with a pure layer of HfO_2, the new structure improved its previous, current characteristics to two times greater on ION and ten times lower on IOFF for short-channel devices (Salahuddin & Datta, 2008). Replacing the gate oxide with a negative capacitance material in conventional transistors, lessening the necessary energy for the device can be provided by reducing the supply voltage through negative capacitance (Khan, 2015).

Studies on the NC phenomenon are encountered in the literature, especially in ferroelectric-dielectric structures (Hoffmann et al., 2019; Park et al., 2019; Migita et al., 2019; Yadav et al., 2019; Luk'yanchuk et al., 2019; Hoffmann et al.,2021b; Cheema et al., 2022). These studies aim to improve sub-threshold swing and internal voltage amplification. Instead of bulky inductors, capacitors with NC values can be evaluated in many different applications, such as providing broadband impedance matching in radio frequency applications (Tade et al., 2012). However, in several studies, NC has been observed at the different low, mid, or high-frequency ranges since the point defects, N_{ss}, material types, bandgap engineering approaches, growth techniques, etc., have been changed or investigated in more detail with the help of developing tools and theoretical approaches. In one study, the NC peaks were observed at all frequencies except two individual ones (C was just negative at 30 Hz and just positive at $8.1x10^4$ Hz) for a MIS type device, while the conductance values were at all frequencies positive only (Ashery, 2022). With the classification of physics behind the basic device parameters highly connected to the temperature and frequency, it was seen that the capacitance seen at low frequencies was caused by N_{ss}, which has great effectiveness in the conduction mechanism related to TFE. One of the latest studies shows that it can be achievable to decrease the gate oxide dimensions in electronic devices below equivalent oxide thickness (EOT). The researchers used an ultrathin HfO_2-ZrO_2 superlattice gate stack for this purpose and reached a 6.5 A thickness of EOT without mobility decline. It is very promising for future electronics (Cheema et al., 2022). To stabilize the NC effect on interlayered structures, researchers have been trying different compounds of atoms for interfacial layers or adjusting different variables of a material, similar to changing the thickness of a MOSFET gate and different density percentages of dopped atoms in an interlayer or replacing the gate oxide material with new ones. In one of the previous studies, it is mentioned that researchers changed the gate dielectric material of a Si-based MOSFET from SiO_2 to SiON so they could achieve decreasing the dimension of gate oxide below the EOT for lowering the switch voltage between on and off by increasing the ε_r. In the following years, even the usage of dielectric materials became the new "necessity" to provide a higher ε_r to continue for better scaling of EOT (Hoffmann et al.,2021a). However, the physical limitations of the nature of structures have not allowed this reduction by changing the dimensions to below minimum according to loss of reliability and implementation of device characteristics until the new founds on ultrathin superlattice gate material of transistors (Cheema et al., 2022). In another study, researchers explored Al/Ag/Al_2O_3/TiN structure for two different thicknesses at 20 nm and 5 nm, respectively, and reached the results that different thicknesses of Al_2O_3 can change the switching performance and dipole uniformity of a CBRAM according to its changing ferroelectric characteristics. So, with the help of this rising ferroelectricity by reducing the thickness of the Al_2O_3 because of the more diffusing ionized Ag atoms into the thinner layer. So, this layer shows NC effects because of the phase change rather than geometric capacitance. And as a result, this ferroelectric behavior will help many kinds of memory units to store big data and fast controllability (Senapati et al., 2020). Several researchers have also been interested in modeling or determining the NC and finding numerical models for predictions on materials, which can be favorable for usage and production of what technology brings next in non-linear behavioral structures. Since many NC observed structures in literature generally have a common tendency to have NC at lower frequencies and forward bias, a model modification was offered on Barna and Horelick (BH) recombination diode model, employing a variable series resistance effect, which may stem from the reducing intrinsic carrier concentration after comparing the surface states and BH model due to its adaptation is more flexible to related solar cell structures (Bisquert, 2011). In a recent work, the authors used Miller Model (MM) combined with Poisson equations to make a blueprint model of how the NC effects can be changed and observed by means of the MM since it has more flexibility compared to the LM which cannot catch or present the different directional switches by fitting on just one S curve (Lee & Yoon, 2022). To do so, for a FE–DE capacitor, they divided, as a theoretical/numerical approach, the structure into local polarization zones into an aligned dots-like shape for better investigation. So, they would be able to observe the average polarization response around a dot to the applied field in scale determined. They did not include domain interactions between these little dots since the FE layer of the FE-DE combination would exhibit almost a uniform electric field. They concluded that if the ferroelectric layer is used with a dielectric layer, the FE will have more sudden polarization changes resulting in increased effects of NC behavior. Also, the FE layer's dimensions can be considered an improvement in NC when it is thicker due to simulation. Other findings were that the smaller the coercive field (EC) and remnant polarization (PR) values, the narrower the hysteresis curve range was. As long as the polarization can be manipulated, which in turn will make it possible to get a higher effective capacitance and a lower bias necessity and so a smaller SS in the ferroelectric material's structures by the help of domain walls' energy or other parameters mostly effective on switching directions and spin moment and so on, not only Boltzmann limit can be achieved, but also other

limitations will be able to overcome. This concept within a study, was achieved a hysteresis-free transition behavior at a subthreshold swing (SS) as small as 9.7 mV without a DE layer attached to the structure's FE layer (Song et al., 2022). In another study, the researchers explored Pt nanosheets' effects on MgSe thin films, revealing enhancements in light absorbability, energy band red-shift, and decreased dielectric constants, while sandwiching MgSe between Pt layers enabled the creation of tunneling-type diodes with negative capacitance properties, indicating potential applications in parasitic capacitance mitigation, noise reduction, and microwave resonance (Algarni et al., 2022).

When it was first searched for the negative capacitance in this study, it was realized that this phenomenon is strongly related to all these structures: MS, MPS, MIS, MFS(MFMIS, MFIS, and so on), and it was expected that it has the potential to be a building block property for many others which have not been invented or fabricated yet. All these structures need insulating or interfacial dielectric layers, except just directly MS contact ones like some Schottky barrier diodes. In the literature, mostly III-V or II-VI groups of compounds from the periodic table have been used when Schottky structures are prepared. Moreover, hafnium zirconium oxide (HZO) related variations of interlayers have been generally preferred for ferroelectric-based structures like NC-Fets and capacitors, as well as in ferroelectric tunnel junctions (FJTs) according to both industrial background and good features (Khosla & Sharma, 2021; Li et al., 2021; Segatto et al., 2022). Also, polyvinyl alcohol (PVA) has been lately attracting researchers and thought for usage in Organic field-effect transistors (OFETs), MPS-type structures, and capacitors for its capability of thin- film fabrication, specialties in usage processes such as effortlessly dissolving in water or alcohol, and by being nontoxic, a wide range of crystallinity, having high dielectric strength, and reasonable charge storage capacity, and fast eliminating the oxidation of surfaces specialty for better conduction by its formation. (Ashery et al., 2021; Demirezen & Yerişkin, 2021; Kaur et al., 2020; Alsmael et al., 2022). In 2021, researchers investigated a PVA/nSi Schottky barrier device for its electrical characteristics dependent on temperature. Some results, which are highly related to NC, showed that the increase in barrier height and ideality factor values could be sourced from the specific characterization of the interface situations (Ashery et al., 2021). In another study, the use of PVC and PVC:SnS interlayers in MPS-based SBDs was found to contribute to the observed negative capacitance at low frequencies, a phenomenon attributed to the presence of these doped or undoped interlayers, as well as the saturation effect of interfacial trap levels at the crossover frequency and the differential effect of the electric charge (Q) (Barkhordari et al., 2022).

Recently, a study group made one of the most straightforward explanations for the act of NC by directly measuring it in a Pt/BTO/Si/Pt structure with a total capacitance change by an interplay between geometric capacitance and additional capacitance, which is formed due to the bias change that is effective on charge moves related to oxygen vacancy migration, interface charge injection, interface depletion layer, and polarization switching (Liu et al., 2023). They presented the total capacitance changes according to altering relaxation components and bias response of charges from small to large scale of polarizations for both positive,0, and negative voltages on device response and observed the tunable NC effect under low frequency and large polarization. They concluded that the total capacitance can be tuned by adjusting the contribution of relaxation parameters with different voltages, specifically on the ferroelectric/semiconductor part.

In light of all these findings, it has become a necessity to determine the ratio of the produced, simulated, or modeled structure publications related to MS-NC among themselves in order to understand the general trend and its causes in the main structures in which NC is observed. In this study, basic subgroup classification was made with the help of a support vector machine (SVM) algorithm in order to see under which structure the existing studies in the literature are gathered.

2. MATERIAL AND METHOD

The data was acquired from the Web of Science (WOS) database for the last 20 years, excluding pre-prints, as a result of scanning the academic studies on NC behavior in certain electronic devices worldwide and in Türkiye and were transferred to an excel file and analyzed with statistical distributions by years, sub-structures, and countries. We prepared the training data according to most related terms in categories or sub-categories related to literature. Initially, the FNC filter (just NC terms) was applied to identify all NC studies, resulting in 2613 NC-related records. Subsequently, the FMS filter (NC and MS, MIS, MFS, MPS terms) yielded 276 records related to both NC and MS. These studies were then further sorted in the WOS database: the 2613

records were reduced to 2483 records by cleaning unrelated or repeating ones, while the 276 records were categorized using a more specific method. Since all 2483 records have both MS-NC and other types of NC-related structures, mostly including FET data, we did not share that classification results of the 2483 records distribution in this study. Since sorting searches were giving interwoven sub-categories of structures all together in databases, it was necessary to cluster them into more precise numbers of categories to determine the most realistic record numbers. So, these studies were categorized using a classification code, which is given below, into their sub-structures to investigate how the differently structured materials show NC behavior. We preferred to use a SVM since when K-means is used, it will only give the numbers of random labels no matter what they are. It is necessary to say when trained SVD and then K-means are used together or just K-means and elbow method are used in the algorithm they give closer numbers to WOS results but since the labels should be clear up to the sub-categories, it was not preferred. Since a study showed that a combination of SVD and SVM algorithms gave better accuracy when used together than just SVM used itself, we preferred a similar way as in their work by employing the favors of SVD by dimension reduction (., & Rarasati , 2022). When using the data tables for both training and testing, we employed the same index terms for training as the same as in the WOS search. For the classification of the datasets, text data in two columns of records for each study were used as “article title” and “abstract.” other data of records (except publication years), like authors, etc., were excluded since they did not have the necessary information in them. Other details can be accessed from the supplementary document. The study process is given in Figure 1 below. This work primarily focused on drawing a general picture of the NC observations and how related studies are distributed statistically. However, since it is a general view for specifically count on MS-NC studies, it was not mentioned how the FETs, high-k materials, ferroelectric behavior basics, spintronics, and other approaches to the field have been affecting, which may be a topic for another paper.

Classifying script’s Pseudocode Steps:

1. Import necessary libraries such as: Pandas, TruncatedSVD, TfidfVectorizer, and SVM.
2. Read in the training and testing data from Excel files using Pandas read_excel function.
3. Train a TruncatedSVD model on the training data. TfidfVectorizer is used to convert the text data into a matrix of TF-IDF features. TruncatedSVD is then applied to the transformed training data to reduce the number of dimensions to n=13(n selected for best accuracy according to feature numbers).
4. Apply the trained TruncatedSVD on the testing data.
5. Use SVM to classify the testing data. An SVM model is trained on the reduced training data using the SVM class from scikit-learn with a linear kernel.(rbf, poly, sigmoid were also tried besides linear kernel but empirically ‘linear’ gave better results than rest). The trained SVM model is then used to make predictions on the reduced test data.
6. Map predicted label numbers to their corresponding names using a dictionary.
7. Create a Pandas DataFrame of the predicted labels and write to an Excel file named 'Predictions.xlsx'.
8. Print the count of each predicted label.
9. Evaluation of the classifier through comparing the predicted labels and true labels.

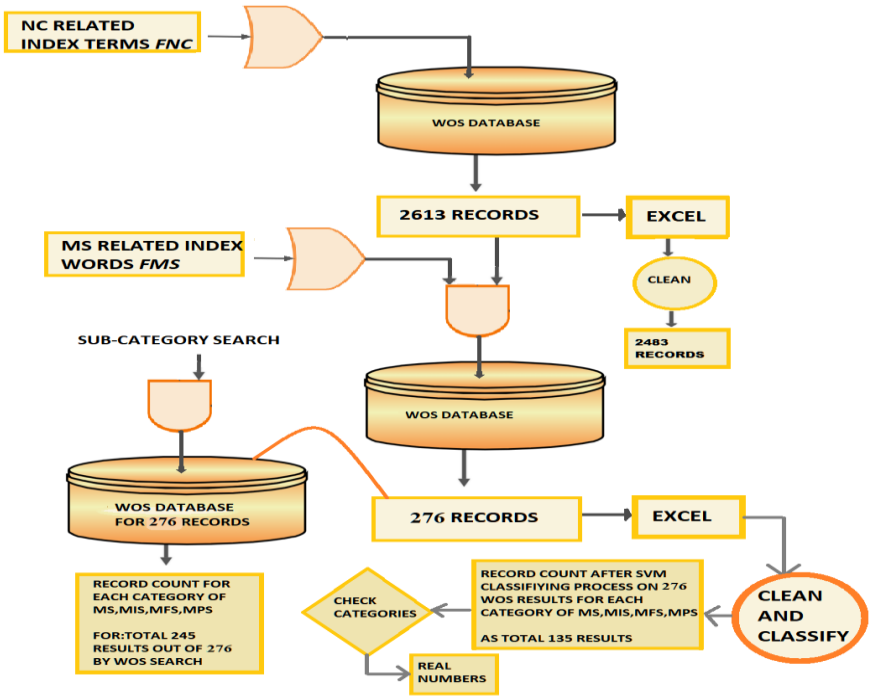

Figure 1. *Study research process with our filtering terms in the WOS index and classifying in script*

3. RESULTS AND DISCUSSION

The NC phenomenon, whose presence in MS structures was previously attributed to parameters such as surface states and series resistance as well as instrumental problems, noticed as an ill-defined peak and described as an abnormal and explained as an inductive behavior of the material, has become increasingly popular in the scientific community, thanks to a better understanding of its origin and advantageous properties especially at ferroelectric-based devices in recent years (Tan et al., 2017). From this point of view, this study sheds light on the meaning of the presence of NC in both MS structures and other structures, and the statistical distribution of studies in this field is interpreted with the figures below. In the last fifteen years, especially after 2015, the prominence of advantageous features such as reduce subthreshold swing and power supply voltage, improve static noise margin, voltage gating, low power dissipation and low threshold voltage has enabled the intensification of scientific studies on the NC phenomenon.

The small differences between record counts in Figure 2 are sourced from cleaning unrelated or repeating articles for corrections in articles. Figure 3 and Figure 4 show that MS-related (generally comprised of interlayered structures like diodes, solar cells, capacitors, and heterostructures excluding most of the 3-leg devices) NC studies have increased over the years. However, the ratio of the rising number of studies in these plots is lower than the general NC studies in Figure 2, since most researchers have been focusing on new materials related to multi-layered structures (like FETs and so on) in general NC works. Moreover, the MS-related search result of WOS also had unrelated records in Figure 3; after a small data cleaning, we obtained 135 directly related records out of 276 total results in Figure 4. In these records, many heterostructures were not described as a specific structure in their data columns, and they were included or excluded according to their consistency of metal and semiconductor parts in a structure somewhat together. So, the 135 records distribution in Figure 4 has only MS-related NC records. Also, the number of studies is expected to be higher by the end of this year since this work includes the dataset until August 2023.

The rapid increase after 2015, seen in both Figure 2, Figure 3, and Figure 4, started to rise cumulatively due to the findings of a previous study by the researchers (Salahuddin & Datta, 2008). After achieving SS reduction, the academy and the industry have turned their interests into different device designs with ferroelectric materials and other new compounds to employ in heterostructures to develop these re-discovered figures of merits, specifically for the polarized-layered structures. So, the rising trend in Figure 2 explains the ferroelectric behavior based on complex devices' designs, fabrications, and investigations (Iwashige et al.,

2023). Also, they include other types of devices, like MS-based ones, but with a slight impact on the statistics. When looking at Figure 4, the MS-NC studies become prominent in the statistics. They shape this rising trend in records due to the employing of new or non-used materials, fabrication methods, and materials already in use for the aforementioned re-discovered field (Saghrouni et al., 2015; Poklonski et al., 2023).

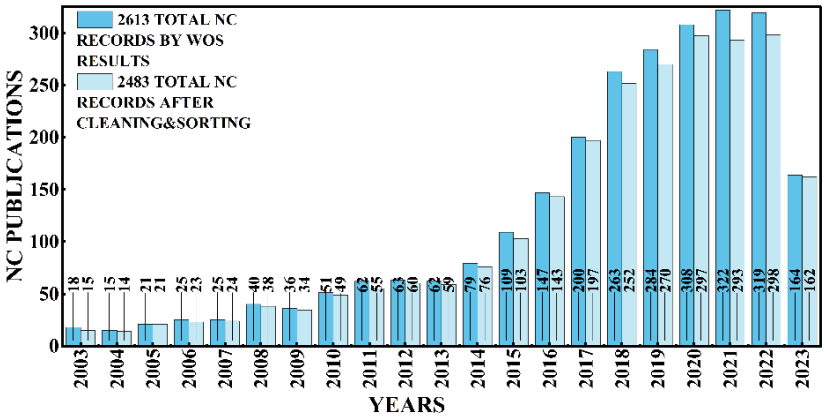

Figure 2. *The Publication counts on general NC studies*

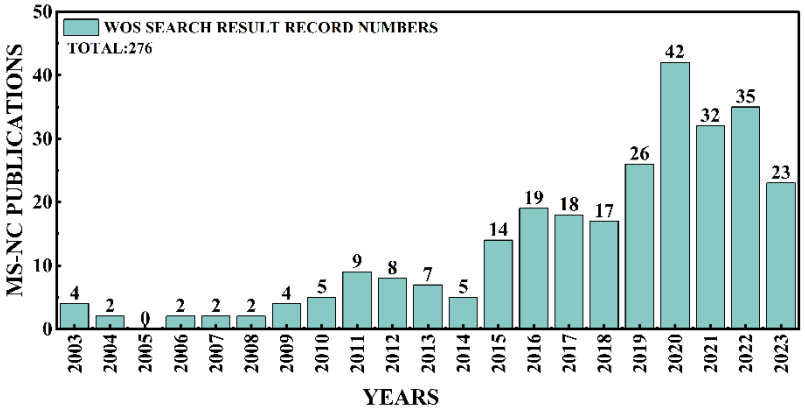

Figure 3. *Total 276 WOS results for MS-NC studies*

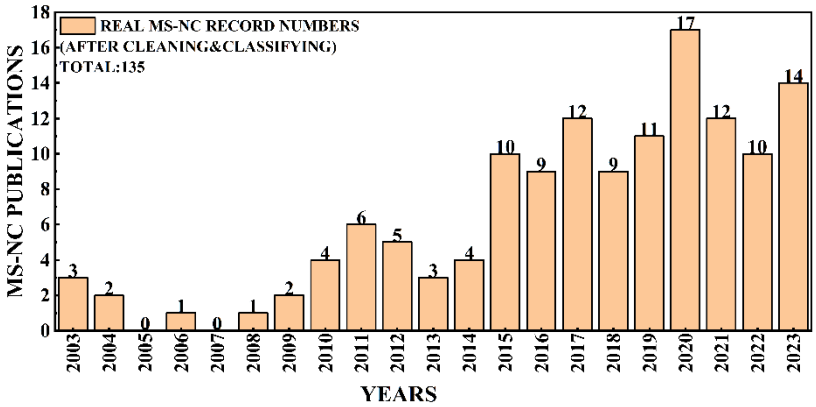

Figure 4. *Total 135 results for MS-NC studies after cleaning and classifying*

As seen in Figure 5, China is at the top of the countries studying NC by 867 records. Moreover, the USA and India follow, respectively. The most important reason for this may be the excess number of researchers and research opportunities in these three countries and the amount of field marketplace. Türkiye ranks 8th among the countries in general NC publications, which shows that the researchers in Türkiye are interested in non-linear behaviors like NC of interlayered structures. This result may arise from the fact that the follow-up project funds are getting broader for this field or that the universities find this sub-field more attractive due to the

developments of these fundamental structures having an interplay in future mass production opportunities.

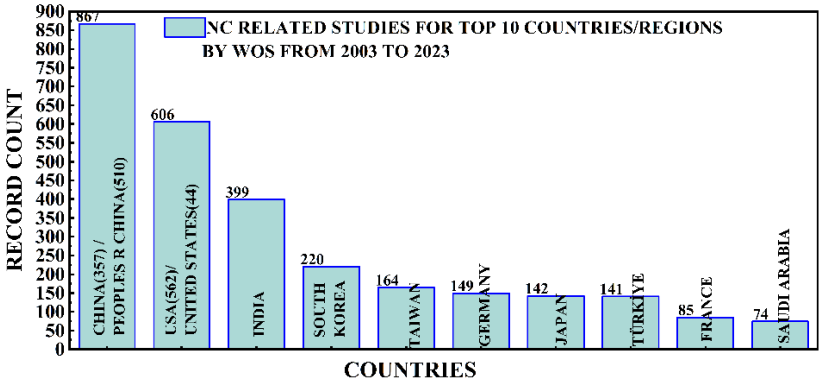

Figure 5. *The Publication counts by top 10 countries on general NC studies*

Figure 6 shows that Türkiye is focused on metal-semiconductor structures and has observed NC-related behavior 68 times in MS-NC studies so far among the other countries. At the same time, China has the first seat with 69 total records, and India is in the third seat with 63 publications.

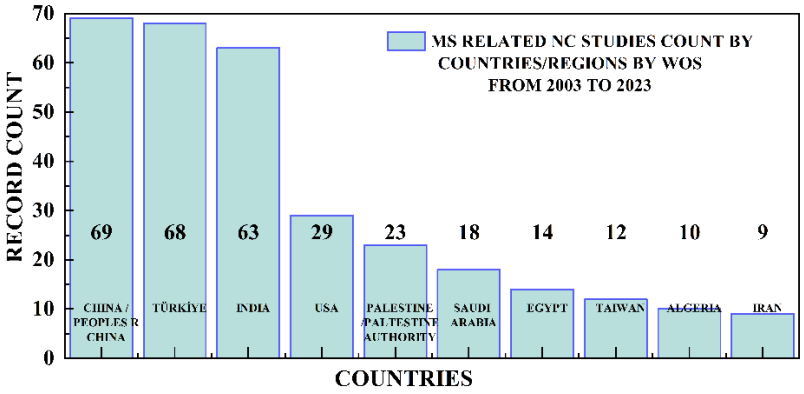

Figure 6. *MS related NC works distribution by countries*

Figure 7 shows that in Türkiye, this phenomenon *NC* takes more attention with time. The reason for that may be considered as the "surface states" come with the results of rising studies of interlayered MS structures, specifically reported Schottky structures studied in Türkiye.

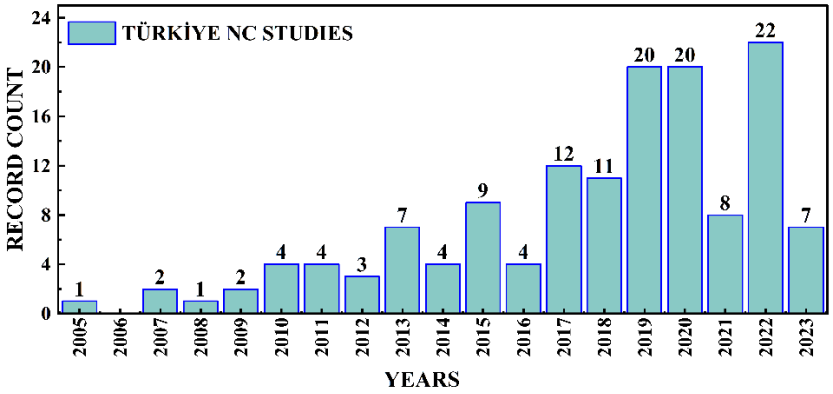

Figure 7. *The NC Publication counts in Türkiye by years*

The giant pies for NC studies in Figure 8 belong to the fields of Engineering, Physics, and Materials Science. The reason engineering is on the highest side of the group may be the developments related to memory devices'

sub-parts, like all kinds of switching components with different gate designs. However, with surface/additive engineering studies, optics and computer science are growing, too. The rise of the tendency to search for NC and ferroelectricity among scientists is promising for future applications. Nevertheless, it is still underrated compared to other research areas in semiconductor-related fields. As seen in Figure 9, Physics has a key role in MS-NC works since the structures' modeling, fabrication, and investigation processes employ many inter-disciplines, such as with the Physics theorems from ion-scattering, even more from electron's spin moment, quantum mechanics approaches to the compounds, interlayers, defects. Thus, this field has the highest second-record number among the others on MS-NC. Also, of course, all these research areas have intertwined with each other. The difference in the research field distribution up to MS and MS-NC Figure 8 and Figure 9 might be attributed to the fact that engineering is more interested in using devices that are more complicated and multilayered, such as FETs, as building blocks for bigger device systems, which has a big pie in literature, while physics is more interested in solving the basics behind why all these structures have different or similar characteristics or their tendency to develop new basic structures as samples for better options to use in more complicated ones. Also, computer-aided design developments should have contributed to this result.

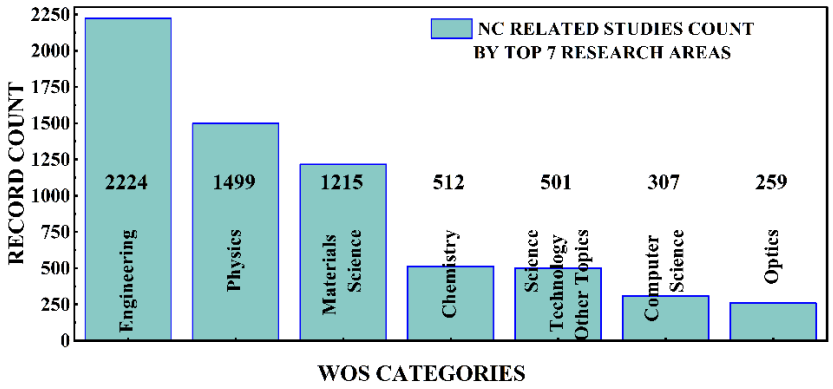

Figure 8. *The distribution of publications on distinct research areas in WOS categories for general NC studies*

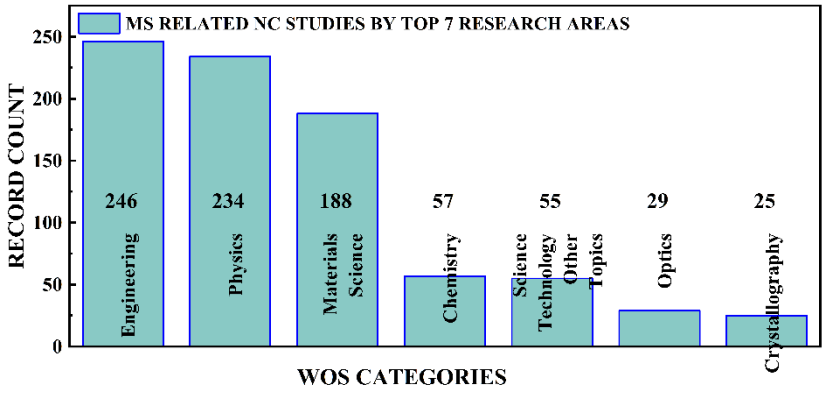

Figure 9. *The distribution of publications on distinct research areas in WOS categories for MS related NC studies*

This study showed that NC-MS-related studies have been chiefly on MS and MIS-type structures in Figure 10. However, one shall notice that MS structures have a big pie in all statistics because most structures have metal and semiconductor contacts, so the ratio of the sub-structures is manipulated by common MS terms in databases since MS includes all other categories. It also shows that Schottky barrier junction studies can have a big pie in this sub-research field. The deviation in the WOS search, which gives 276 results for MS-NC studies for a total and 245 for a total of each subcategory, is because these 276 studies have unrelated records like specific ferroelectric or polymer or another type of multi-layered structures that belong to another sub-field of NC-related works. Also, these structures have interwoven categories, so the actual numbers of records are not clearly represented in general database searches. According to these compared results, researchers have

studied 135 MS-NC-related works. The deviation of WOS from the actual MIS records numbers may stem from MIS structures that can include MPSs and MFSs. The deviation of classification from real numbers in MIS stems from mismatching with MS structures since MS has common terms for all categories, while the datasets for abstracts and titles need more specified unique keywords for testing. Also, the WOS deviation in MFS may stem from ferroelectric material configuration-based FET-like miscategorized structures that exist in the database when they should have been excluded instead. The deviation in MFS for classification results stems from the ferroelectric-based words, which are not used in the proper configuration as ferroelectric between M and S layers, while the text data still has these materials in as a whole combination. Also, the non-functional word groups in texts affect the training SVD since some of them are specifically necessary to define a structure like the word "with" as a matrix feature; pointing on an "interlayer" cannot be used as stop words to eliminate in algorithm while many of them are useless in the rest of the text.

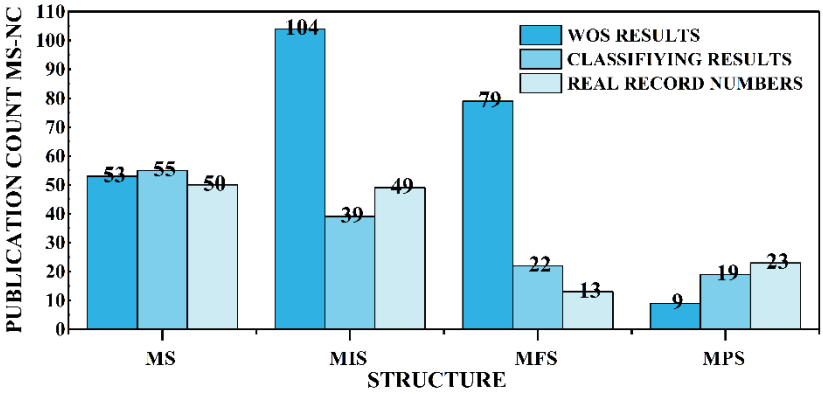

Figure 10. *The distribution comparison of MS-NC publications as MS,MIS,MPS,MFS by WOS search, classifying and real records after label checking*

Perovskite oxides mainly contribute to MFS interlayers in capacitors, solar cells, and gate stacks, while PVC/PVA-related materials are essential for MPS structures besides high-tech carbon orderings. MIS structures have a broad range of interlayers, primarily employing oxide compounds, while they also share the structure type of mainly SBDs with the MPS group. A detailed list of publications generally presented in Figure 11, including these materials, can be reached directly from the WOS database, or supporting documentation.

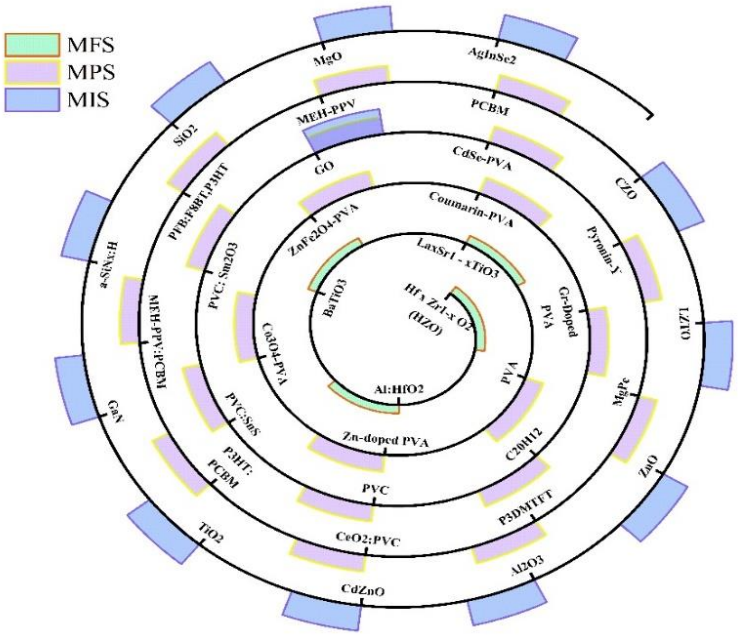

Figure 11. *Interlayer materials used in MS-NC studies for three sub-categories*

4. CONCLUSION

In this study, a general statement was given for NC observed MS publications with the help of statistical analyses made by an SVM algorithm, finding a realistic distribution of publications besides employing database statistics up to August 2023. After explaining the existence of NC and its advantages clearly, statistical data emphasized that the number of publications related to NC worldwide and in Turkey has increased over the years. It was observed that 5.68% of the total 2483 records in NC are publications containing Turkey's contribution. With a total of 65 publications, with 53 directly studied in Türkiye and 12 contributions to other countries, Türkiye has a share of 48,15% on MS-related-NC records in a total of 135 classified works. These ratios can be interpreted as a result of the high number of study groups working on NC in MS structures in Türkiye and the fact that the NC phenomenon has become a popular field of study in recent years. Based on the examined MS-related articles in the literature, it can be concluded that NC appears mostly at forward bias and low frequencies due to dipole relaxation times. Surface states affect NC appearance at low frequencies, and decreasing sub-threshold voltage has been a game changer in low power consumption and speed switch applications. NC has been used as a manufacturing parameter for memory-cell production and investigated for filament formations and breakages in resistive switching. The specific arrangement and thickness of layers in a Schottky diode can determine its electrical characteristics, and Spintronics research can also be relevant. Scientific studies on NC are expected to increase and NC phenomenon is expected to play a critical role in electronics technology.

ACKNOWLEDGEMENT

Some part of this study was presented at MSNG 2022 Conference.

CONFLICT OF INTEREST

The authors declare no conflict of interest.

REFERENCES

., N., & Rarasati, D. B. (2022). Recommendation for Classification of News Categories Using Support Vector Machine Algorithm with SVD. *Ultimatics : Jurnal Teknik Informatika*, *13*(2), 72-80. https://www.doi.org/10.31937/ti.v13i2.1854

Algarni, S. E., Qasrawi, A. F., & Khusayfan, N. M. (2022). Enhanced Optical and Electrical Interactions at the Pt/MgSe Interfaces Designed for 6G Communication Technology. *Crystal Research and Technology*, *58*(1), 2200185. https://www.doi.org/10.1002/crat.202200185

Alsmael, J. A. M. , Urgun, N. , Tan, S. O. & Tecimer, H. (2022). Effectuality of the Frequency Levels on the C&G/ω–V Data of the Polymer Interlayered Metal-Semiconductor Structure. *Gazi University Journal of Science Part A: Engineering and Innovation*, *9*(4), 554-561. https://www.doi.org/10.54287/gujsa.1206332

Ashery, A. (2022). Novel Negative Capacitance Appeared in all Frequencies in Au/AlCu/SiO2/p-Si/Al Structure. *Silicon*, *14*, 11061-11078. https://www.doi.org/10.1007/s12633-022-01850-0

Ashery, A., Gad, S. A., & Turky, G. M. (2021). Analysis of Electrical and Capacitance–Voltage of PVA/nSi. *Journal of Electronic Materials*, *50*(6), 3498-3516. https://www.doi.org/10.1007/s11664-021-08867-y

Barkhordari, A., Altındal, Ş., E., Pirgholi-Givi, G., Mashayekhi, H., Özçelik, S., & Azizian-Kalandaragh, Y. (2022). The Influence of PVC and (PVC:SnS) Interfacial Polymer Layers on the Electric and Dielectric Properties of Au/n-Si Structure. *Silicon*, *15*(2), 855-865. https://www.doi.org/10.1007/s12633-022-02044-4

Bisquert, J. (2011). A variable series resistance mechanism to explain the negative capacitance observed in impedance spectroscopy measurements of nanostructured solar cells. *Physical Chemistry Chemical Physics*, *13*(10), 4679. https://www.doi.org/10.1039/c0cp02555k

Cheema, S. S., Shanker, N., Wang, L. C., Hsu, C.-H., Hsu, S.-L., Liao, Y.-H., San Jose, M., Gomez, J., Chakraborty, W., Li, W., Bae, J.-H., Volkman, S. K., Kwon, D., Rho, Y., Pinelli, G., Rastogi, R., Pipitone, D., Stull, C., Cook, M., Salahuddin, S. (2022). Ultrathin ferroic HfO_2–ZrO_2 superlattice gate stack for advanced transistors. *Nature*, *604*, 65-71. https://www.doi.org/10.1038/s41586-022-04425-6

Çakıcı, T., Ajjaq, A., Çağırtekin, A. O., Barin, Ö., Özdal, M., & Acar, S. (2023). Surface activation of Si-based Schottky diodes by bacterial biosynthesized $AgInSe_2$ trimetallic alloy nanoparticles with evidenced negative capacitance and enhanced electro-dielectric performance. *Applied Surface Science*, *631*, 157522. https://www.doi.org/10.1016/j.apsusc.2023.157522

Demirezen, S., & Yerişkin, S. A. (2021). Frequency and voltage-dependent dielectric spectroscopy characterization of Al/(Coumarin-PVA)/p-Si structures. *Journal of Materials Science: Materials in Electronics*, *32*, 25339-25349. https://www.doi.org/10.1007/s10854-021-06993-1

Ershov, M., Liu, H., Li, L., Buchanan, M., Wasilewski, Z., & Jonscher, A. (1998). Negative capacitance effect in semiconductor devices. *IEEE Transactions on Electron Devices*, *45*(10), 2196-2206. https://www.doi.org/10.1109/16.725254

Hoffmann, M., Fengler, F. P. G., Herzig, M., Mittmann, T., Max, B., Schroeder, U., Negrea, R., Pintilie, L., Slesazeck, S., & Mikolajick, T. (2019). Unveiling the double-well energy landscape in a ferroelectric layer. *Nature*, *565*, 464-467. https://www.doi.org/10.1038/s41586-018-0854-z

Hoffmann, M., Slesazeck, S., & Mikolajick, T. (2021a). Progress and future prospects of negative capacitance electronics: A materials perspective. *APL Materials*, *9*(2), 020902. https://www.doi.org/10.1063/5.0032954

Hoffmann, M., Gui, M., Slesazeck, S., Fontanini, R., Segatto, M., Esseni, D., & Mikolajick, T. (2021b). Intrinsic Nature of Negative Capacitance in Multidomain $Hf_{0.5}Zr_{0.5}O_2$-Based Ferroelectric/Dielectric Heterostructures. *Advanced Functional Materials*, *32*(2), 2108494. https://www.doi.org/10.1002/adfm.202108494

Iwashige, K., Toprasertpong, K., Takenaka, M., & Takagi, S. (2023). Effect of $Hf_x Zr_{1-x} O_2$/Ge metal–ferroelectrics–insulator–semiconductor interfaces on polarization reversal behavior. *Japanese Journal of Applied Physics*, *62*(SC), SC1093. https://www.doi.org/10.35848/1347-4065/acb829

Joly, R., Girod, S., Adjeroud, N., Grysan, P., & Polesel-Maris, J. (2021). Evidence of negative capacitance and capacitance modulation by light and mechanical stimuli in pt/zno/pt schottky junctions. *Sensors*, *21*(6), 2253. https://www.doi.org/10.3390/s21062253

Karataş, Ş. (2021). Temperature and voltage dependence C–V and G/ω–V characteristics in Au/n-type GaAs metal–semiconductor structures and the source of negative capacitance. *Journal of Materials Science: Materials in Electronics*, *32*(1), 707-716. https://www.doi.org/10.1007/s10854-020-04850-1

Kaur, R., Arora, A., & Tripathi, S. K. (2020). Fabrication and characterization of metal insulator semiconductor Ag/PVA/GO/PVA/n-Si/Ag device. *Microelectronic Engineering*, *233*, 111419. https://www.doi.org/10.1016/j.mee.2020.111419

Khan, A. I. (2015). *Negative Capacitance for Ultra-low Power Computing*. PhD Thesis, University of California, Berkeley.

Khosla, R., & Sharma, S. K. (2021). Integration of Ferroelectric Materials: An Ultimate Solution for Next-Generation Computing and Storage Devices. *ACS Applied Electronic Materials*, *3*(7), 2862-2897. https://www.doi.org/10.1021/acsaelm.0c00851

Landauer, R. (1957). Electrostatic Considerations in $BaTiO_3$ Domain Formation during Polarization Reversal. *Journal of Applied Physics*, *28*(2), 227-234. https://www.doi.org/10.1063/1.1722712

Lee, H., & Yoon, Y. (2022). Simulation of Negative Capacitance Based on the Miller Model: Beyond the Limitation of the Landau Model. *IEEE Transactions on Electron Devices*, *69*(1), 237-241. https://www.doi.org/10.1109/ted.2021.3124475

Li, J., Si, M., Qu, Y., Lyu, X., & Ye, P. D. (2021). Quantitative Characterization of Ferroelectric/Dielectric Interface Traps by Pulse Measurements. *IEEE Transactions on Electron Devices*, *68*(3), 1214-1220. https://www.doi.org/10.1109/ted.2021.3053497

Liu, L., Lei, L., Lu, X., Xia, Y., Wu, Z., & Huang, F. (2023). Direct Measurement of Negative Capacitance in Ferroelectric/Semiconductor Heterostructures. *ACS Applied Materials & Interfaces*, *15*(7), 10175-10181. https://www.doi.org/10.1021/acsami.2c19930

Luk'yanchuk, I., Tikhonov, Y., Sené, A., Razumnaya, A., & Vinokur, V. M. (2019). Harnessing ferroelectric domains for negative capacitance. *Communications Physics*, *2*(22). https://www.doi.org/10.1038/s42005-019-0121-0

Merz, W. J. (1956). Switching time in ferroelectric $BaTiO_3$ and its dependence on crystal thickness. *Journal of Applied Physics*, *27*(8), 938-943. https://www.doi.org/10.1063/1.1722518

Migita, S., Ota, H., & Toriumi, A. (2019). Design points of ferroelectric field-effect transistors for memory and logic applications as investigated by metal-ferroelectric-metal-insulator-semiconductor gate stack structures using $Hf_{0.5}Zr_{0.5}O_2$ films. *Japanese Journal of Applied Physics*, *58*(SL), SLLB06. https://www.doi.org/10.7567/1347-4065/ab389b

Noh, Y. S., Chatterjee, S., Nandi, S., Samanta, S. K., Maiti, C. K., Maikap, S., & Choi, W. K. (2003). Characteristics of MIS capacitors using Ta_2O_5 films deposited on ZnO/p-Si. *Microelectronic Engineering*, *66*(1-4), 637-642. https://www.doi.org/10.1016/s0167-9317(02)00976-0

Park, H. W., Roh, J., Lee, Y. B., & Hwang, C. S. (2019). Modeling of Negative Capacitance in Ferroelectric Thin Films. *Advanced Materials*, *31*(32), 1805266. https://www.doi.org/10.1002/adma.201805266

Poklonski, N. A., Kovalev, A. I., Usenko, K. V., Ermakova, E. A., Gorbachuk, N. I., & Lastovski, S. B. (2023). Inductive Type Impedance of Mo/*n*-Si Barrier Structures Irradiated with Alpha Particles. *Devices and Methods of Measurements*, *14*(1), 38-43. https://www.doi.org/10.21122/2220-9506-2023-14-1-38-43

Saghrouni, H., Jomni, S., Belgacem, W., Elghoul, N., & Beji, L. (2015). Temperature dependent electrical and dielectric properties of a metal/Dy_2O_3/n-GaAs (MOS) structure. *Materials Science in Semiconductor Processing*, *29*, 307-314. https://www.doi.org/10.1016/j.mssp.2014.05.039

Salahuddin, S., & Datta, S. (2008). Use of negative capacitance to provide voltage amplification for low power nanoscale devices. *Nano Letters*, *8*(2), 405-410. https://www.doi.org/10.1021/nl071804g

Segatto, M., Fontanini, R., Driussi, F., Lizzit, D., & Esseni, D. (2022). Limitations to Electrical Probing of Spontaneous Polarization in Ferroelectric-Dielectric Heterostructures. *IEEE Journal of the Electron Devices Society*, *10*, 324-333. https://www.doi.org/10.1109/jeds.2022.3164652

Senapati, A., Roy, S., Lin, Y. F., Dutta, M., & Maikap, S. (2020). Oxide-Electrolyte Thickness Dependence Diode-Like Threshold Switching and High on/off Ratio Characteristics by Using Al_2O_3 Based CBRAM. *Electronics*, *9*(7), 1106. https://www.doi.org/10.3390/electronics9071106

Song, J., Qi, Y., Xiao, Z., Wang, K., Li, D., Kim, S. H., Kingon, A. I., Rappe, A. M., & Hong, X. (2022). Domain wall enabled steep slope switching in MoS_2 transistors towards hysteresis-free operation. *Npj 2D Materials and Applications*, *6*, 77. https://www.doi.org/10.1038/s41699-022-00353-1

Tade, O. O., Gardner, P., & Hall, P. S. (2012). *Negative impedance converters for broadband antenna matching*. In: Proceedings of the 42nd European Microwave Conference, Amsterdam, Netherlands, (pp. 613-616). https://www.doi.org/10.23919/eumc.2012.6459295

Tan, S. O., Tecimer, H. U., Çiçek, O., Tecimer, H., & Altındal. (2016). Frequency dependent C–V and G/ω–V characteristics on the illumination-induced Au/ZnO/n-GaAs Schottky barrier diodes. *Journal of Materials Science: Materials in Electronics*, *28*, 4951-4957. https://www.doi.org/10.1007/s10854-016-6147-0

Yadav, A. K., Nguyen, K. X., Hong, Z., García-Fernández, P., Aguado-Puente, P., Nelson, C. T., Das, S., Prasad, B., Kwon, D., Cheema, S., Khan, A. I., Hu, C., Íñiguez, J., Junquera, J., Chen, L. Q., Muller, D. A., Ramesh, R., & Salahuddin, S. (2019). Spatially resolved steady-state negative capacitance. *Nature*, *565*, 468-471. .doi.org/10.1038/s41586-018-0855-y

Zhang, Y., Ma, X., Wang, X., Xiang, J., & Wang, W. (2021). *Revisiting the definition of ferroelectric negative capacitance based on Gibbs free energy*. In: Proceedings of the 5th IEEE Electron Devices Technology & Manufacturing Conference (EDTM), (pp. 1-3), Chengdu, China. https://www.doi.org/10.1109/edtm50988.2021.9420889

Research Article GU J Sci, Part A, 10(4): 524-541 (2023) 10.54287/gujsa.1357247

Gazi University
Journal of Science
PART A: ENGINEERING AND INNOVATION
http://dergipark.org.tr/gujsa

Investigation of Turkey's Climate for Service Lifetime of Photovoltaic Modules: A Mapping Approach

Abdulkerim GOK[1*]

[1] Department of Materials Science and Engineering, Gebze Technical University, Gebze, Kocaeli, Türkiye

Keywords

PV Modules
Standard Testing
Degradation
Reliability
Service Lifetime

Abstract

The longevity of photovoltaic systems during real-world operation is a concern that needs to be addressed. Polymeric materials used in module constructions, particularly encapsulants, are susceptible to hydrolysis, which can lead to cell metallization corrosion and result in power loss and shortened service lifetime. One of the test protocols within the current certification standard of IEC 61215 is damp heat exposure, which subjects the modules to constant temperature and humidity level for a specific duration (85°C/85%RH for 1000 hours). However, its effectiveness as a reliability test for long-term durability is often debated. This study applies a methodology for calculating the equivalent damp heat testing time that corresponds to a targeted service lifetime (i.e., 30 years) in real-world conditions. The results are presented in the form of a country map, focusing on Turkey, illustrating the variations in testing times across different regions due to local climate conditions. This study shows that applying a single set of conditions for a fixed duration, as applied in the damp heat testing, to all modules with different components and for all climate conditions poses substantial risks when it comes to predicting service lifetime.

Cite

Gok, A. (2023). Investigation of Turkey's Climate for Service Lifetime of Photovoltaic Modules: A Mapping Approach. *GU J Sci, Part A, 10*(4), 524-541. doi:10.54287/gujsa.1357247

Author ID (ORCID Number)

0000-0003-3433-7106 Abdulkerim GOK

Article Process

Submission Date 08.09.2023
Revision Date 06.12.2023
Accepted Date 26.12.2023
Published Date 31.12.2023

1. INTRODUCTION

Over the past decade, the installation of photovoltaic (PV) systems has experienced tremendous growth. The improved cell/module efficiencies and the reduction in manufacturing and electricity generation costs have been the key factors for this robust adoption of PV systems (IEA PVPS, 2022). While the global cumulative capacity of installed PV systems has reached 1.2 TW at the end of 2022, it stands around 9.5 GW in Turkey (IEA PVPS, 2023). However, to ensure sustainable growth, it is crucial to enhance the durability and reliability of PV modules to extend their service lifetime. In the current market, a 30-year power performance warranty is provided for PV modules which guarantees a maximum of 20% power loss by the end of the warranty period. The challenge lies in the fact that this warranty applies universally to all PV modules irrespective of the diverse climate conditions they are installed in. In real-world, PV modules are subjected to a range of environmental stress factors such as heat, humidity, ultraviolet light, and mechanical stresses. Therefore, these varying conditions necessitate the selection of appropriate materials and material combinations for module lamination to enhance the PV modules' durability and reliability. Recent studies not only focus on understanding the degradation mechanisms and failure modes in the currently installed PV modules and systems (Gok et al., 2019; Aghaei et al., 2022), but also search for alternative materials and lamination strategies for improved service lifetime (López-Escalante et al., 2018; Oreski et al., 2020; Adothu et al., 2021). In economic and environmental terms, extending service lifetime will lead to reduced levelized cost of electricity and greenhouse gas emissions for a more sustainable future.

*Corresponding Author, e-mail: agok@gtu.edu.tr

A conventional crystalline silicon (c-Si) PV module, as shown in Figure 1 (GSES, 2023), is constructed using a tempered front glass, solar cells with metallization elements embedded in two layers of encapsulant polymers, a polymeric multi-layer backsheet, a junction box, and an aluminum frame. Encapsulant and backsheet films are known as the packaging polymers that play a crucial role in providing electrical insulation, environmental protection, and mechanical stability to the cells and cell metallization. The most commonly used encapsulant material is ethylene-vinyl acetate (EVA), but it is susceptible to hydrolytic degradation (Oreski et al., 2019), leading to discoloration, delamination, and the corrosion of cell metallization, ultimately reducing the power performance and service lifetime of PV modules.

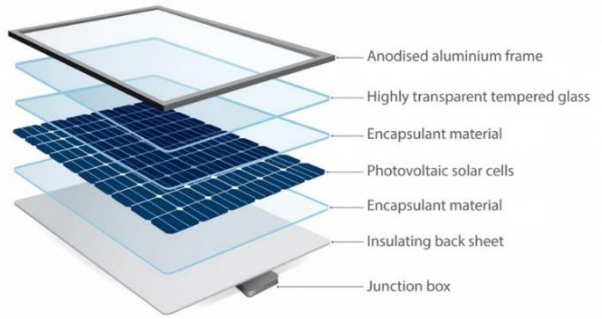

Figure 1. *PV module components*

The IEC 61215 standard (IEC, 2021) for design qualification and type approval for terrestrial PV modules lays down requirements for long-term operation in open-air climates. According to the standard, "the useful service lifetime of modules so qualified will depend on their design, their environment, and the conditions under which they are operated". While it helps identify the premature failures that might occur in the field due to design, processing, and manufacturing flaws, it should not be solely relied upon as a reliability test for estimating service lifetime as explicitly stated by the standard. This standard includes a damp heat exposure protocol to assess the long-term effects of humidity ingress into the module construction. As part of this protocol, PV modules are exposed to a constant temperature of 85°C and a relative humidity level of 85% for 1000 hours. However, passing this test under certain criteria is often mistakenly interpreted as an indication of service lifetime. Given the complexities of the real-world conditions and differences in module constructions, the standard's ability to accurately predict long-term performance has become a topic of intense debate within the PV community (Weiß et al., 2022).

The effect of heat and humidity is one of the most important stressor factors for PV modules in real-world conditions. They particularly contribute to the decline in power performance due to the degradation of polymeric encapsulant materials and corrosion of the cell metallization. Even though the damp heat conditions, especially the level of applied temperature, are criticized, a translation of real-world conditions into the laboratory-based testing conditions, or vice versa, is required in order to achieve a successful service lifetime estimation. Koehl et al. (2012, 2017) have proposed a methodology that enables the calculation of equivalent damp heat testing time needed to achieve a targeted service lifetime, taking the activation energy of power degradation caused by humidity-driven reactions during damp heat testing into account. Using the same methodology, this study aims to calculate and map the equivalent damp heat testing times across Turkey in order to examine the variations in climate conditions in different regions and their impact on the corresponding equivalent damp heat testing times. Turkey stands out as one of the unique countries in Europa not only with its gigantic solar energy potential but also with its diverse geographical regions and climate conditions, both of which have tremendous effects on the performance and service lifetime of PV modules.

Like many countries, Turkey is concerned about environmental issues and the impact of conventional energy sources on air quality and climate change. By setting ambitious targets and introducing various regulations and incentives, increasing the share of renewable energy in the total energy mix, including solar PV, is part of the strategy to mitigate these environmental concerns. Recent studies on solar energy research, focusing on Turkey, have mostly deal with solar radiation and energy generation potential forecasts for a specific location (Turan et al., 2023) and, in rare cases, for the entire country (Salmanoğlu & Çetin, 2022), including

performance analysis and economic perspectives of PV systems (Er, 2023). The effect of environmental stress factors on PV system performance and lifetime; however, has been studied either for individual stress factors such as temperature (Çabuk, 2022) or for specific systems and locations (Tirmikçi et al., 2021). Since the installation of PV systems in Turkey has started after the year 2014, there are limited number of experimental and statistical studies dealing with long-term durability and reliability of these systems under real-world conditions.

Instead of specific systems, locations, or stress factors, the mapping approach applied in this study helps us have better insights into the impacts of local climate conditions on the performance of PV systems in the entire country and unveil the risks linked to the application of standard conditions for a certain period of time to all kinds of module constructions and climatic conditions for service lifetime estimation. By considering the specific characteristics of different PV modules and the diverse climatic conditions, this study seeks to contribute to the ongoing discussions within the PV community regarding the accuracy of the existing standard test protocols in determining the long-term performance of PV modules. Although the standard damp heat conditions (85°C and 85%RH) are used, since the analysis workflow is automated, it can be used for the application of different temperature and humidity levels as well.

2. MATERIALS AND METHODS

2.1. Calculation of the Equivalent Damp Heat Testing Times

The analysis process for the calculation of equivalent damp heat testing time for a given location, as outlined by Koehl et al. (2012, 2017), involves the following steps:

1. Calculating the module temperature using the well-known Faiman Model (Faiman, 2008) according to Equation 1 as follows:

$$T_{mod} = T_{amb} + \frac{G_{POA}}{U_0 + U_1 \cdot WS} \tag{1}$$

where T_{amb} and T_{mod} are the ambient and module temperatures (°C), respectively, G_{POA} is the plane or array irradiance (W/m^2), U_0 is the constant heat transfer coefficient (25 W/m^{2}K), U_1 is the convective heat transfer coefficient (6.84 W/m^{3}sK), and WS is the wind speed (m/s).

2. Calculating the surface relative humidity at the module surface and temperature (referred to as micro-climate) according to Equation 2 as follows:

$$RH(T_{mod}) = RH(T_{amb}) \times \frac{p_{sat}(T_{amb})}{p_{sat}(T_{mod})} \tag{2}$$

where $RH(T_{amb})$ and $RH(T_{mod})$ are the surface relative humidity (%) values at the ambient and module temperatures, respectively, and $p_{sat}(T_{amb})$ and $p_{sat}(T_{mod})$ are the water vapor saturation pressures at the ambient and module temperatures, respectively. Water vapor saturation pressure values can be calculated according to Equation 3 as follows:

$$p_{sat} = 10^{0.66077+7.5\times\frac{T}{237.3+T}} \tag{3}$$

where T is either the ambient temperature (°C) for $p_{sat}(T_{amb})$ or the module temperature (°C) for $p_{sat}(T_{mod})$.

3. Calculating the effective surface relative humidity at the module surface and temperature (referred to as sigmoidal model) according to Equation 4 as follows:

$$RH_{eff} = \frac{1}{\left[1 + 98 \times \exp\left(-9.4 \cdot RH(T_{mod})\right)\right]} \tag{4}$$

Koehl et al. (2012, 2017) showed that the sigmoidal model was the best model to represent the impact of the effective surface humidity of PV modules on degradation processes. In this model expression, the factor of 9.4 is a free parameter in the predicted model fitted to the experimental observed test data.

4. Calculating the time periods (Δt_{85}) corresponding to 85% relative humidity as a function of the module temperature according to Equation 5 as follows:

$$\Delta t_{85}(85\%RH, T_{mod}) = \Delta t_{mon} \times \frac{RH_{eff}}{0.85} \tag{5}$$

where Δt_{mon} is the monitored time interval during which the effective relative humidity levels that are assessed are transformed to a contribution of the time period of high relative humidity levels (i.e., here, it is set to 85% relative humidity for the standard testing condition).

5. Applying a time transformation to a constant test temperature and performing integration to calculate the equivalent testing time for a given location required for a specific service lifetime using the Arrhenius relationship according to Equation 6 as follows:

$$\Delta t_{ref} = \sum_{1}^{N} \Delta t_i \cdot \exp\left[\left(-\frac{E_a}{R}\right)\left(\frac{1}{T_i} - \frac{1}{T_{ref}}\right)\right] \tag{6}$$

where Δt_{ref} is the time period in the standard (reference) test conditions, Δt_i is the time interval, E_a is the activation energy of the damp heat driven power degradation processes, which is a free parameter used to investigate the effect of module construction on the equivalent damp heat testing times, T_i is the transient temperature at time intervals of Δt_i, and T_{ref} is the standard (reference) temperature of 85 °C. The calculated testing time (Δt_{ref}) is then multiplied by the number of years anticipated as the service lifetime, i.e., 30 years.

This methodology can be viewed as a means of translating real-world climate conditions into equivalent constant damp heat conditions. When calculating the module temperature, it takes air temperature, irradiance, and wind speed into account, and when calculating the effective surface relative humidity, it treats relative humidity as a dose. As the first step, the analysis workflow assesses the frequency distribution of 85% relative humidity based on module temperature at a given location, and as the second step, it calculates the acceleration factors using the activation energies of power degradation processes. Koehl et al. (2012, 2017) effectively demonstrated this procedure by incorporating four different relative humidity models: (i) ambient relative humidity model accounts for the overall relative humidity in the surrounding environment, (ii) surface relative humidity (or micro-climate) model takes the relative humidity in close proximity to the module surface, acknowledging the influence of the immediate surrounding of the module, and thus, differs from the ambient relative humidity as it is affected by the module temperature, (iii) squared surface relative humidity (or squared micro-climate) model incorporates the hydrolysis kinetics of polymeric materials as some exhibit second-order kinetics with water content, and (iv) effective surface relative humidity (sigmoidal) model represent the sigmoidal shape of the water sorption isotherms of the polymeric encapsulant material, providing more accurate representation of the humidity content in the module construction. By considering these relative models, they conducted the analysis across various selected locations spanning different climate zones. Here, in this study, instead of specific point locations, a more comprehensive approach is applied to produce a country map in order to achieve more thorough understanding of the effects of local climate conditions on the equivalent damp heat testing times and gain more detailed insights into the effect of heat and humidity on different PV module constructions with varying activations energies in different environments.

2.2. Data Preparation

In order to calculate equivalent testing times for precise point locations in Turkey, typical meteorological year (TMY) data were obtained from the Photovoltaic Geographical Information System (PVGIS, 2023) database at a resolution of 0.05 in both latitude and longitude, which corresponds approximately to 5.5 km and 4.3 km in real-scale, respectively. This is the highest resolution provided by the PVGIS database, ensuring accurate spatial representation of the data, aggregating to a total of 43,000 coordinate numbers for Turkey. The TMY

data obtained includes hourly measurements of various meteorological parameters such as global horizontal irradiance (GHI), direct normal irradiance (DNI), diffuse horizontal irradiance (DHI), air pressure, dry-bulb temperature, wind speed and direction, relative humidity, and long-wave downwelling infrared radiation. It provides a comprehensive set of data necessary for the analysis of the climate conditions, however, it is important to note that the data is provided at an hourly resolution, which poses a limitation for the analysis. To address this limitation and ensure robustness, a wider area is covered with closely spaced data points. This approach compensates for the hourly resolution and allows for a more comprehensive assessment.

For each data point, the TMY data was initially retrieved from the PVGIS database and thoroughly examined for any potential corrupt or missing values. Once the data quality is ensured, the processing is carried out in accordance with the aforementioned analysis workflow: (i) evaluation of the frequency distribution of 85% relative humidity as a function of the module temperature, and (2) calculation of the equivalent damp heat testing times for 30 years of service lifetime based on varying activation energies. Since the activation energies for power degradation in PV modules due to humidity driven reactions under the damp heat conditions fall within the range of 0.5 eV to 0.7 eV, as reported in Koehl et al. (2012, 2017), for standard glass/backsheet modules with EVA-based encapsulants, an average activation energy of 0.6 eV is selected for the mapping purposes. The resulting dataset consists of three columns: longitude, latitude, and the corresponding equivalent testing time. It is noteworthy that the computation time for processing the dataset at a resolution of 0.05 was nearly 10 hours without employing any parallelization techniques. This relatively long processing time can be attributed to the size of the dataset, the intricacies of data retrieval, and processing at such high resolution.

2.3. Interpolation Method

The selection of an appropriate interpolation method for mapping requires careful consideration of different approaches and resolutions. Due to the complexity of the task, making the right decision usually needs a lot of experience and specialization in the field, but extensive experimentation with the dataset with various methods and evaluating their performances is usually a reliable strategy. Thus, several interpolation methods and data resolutions are examined, and ultimately, the Inverse Distance Weighting (IDW) method (Watson & Philip, 1985), combined with a dataset resolution of 0.1 in both latitude and longitude, is found to be the most optimal approach in terms of accuracy and computational efficiency. Efficiency is crucial as the study area expands, and time and hardware requirements do not increase linearly.

IDW is a relatively simple interpolation method that assumes a linear relationship between two data points, assigning higher weights to points closer to the target location. This results in a smooth transition of colors in the interpolated map, providing visually appealing and informative representation of data. In comparison, Kriging (Matheron, 1963), another commonly used interpolation method in mapping applications, utilizes a variogram to model the spatial autocorrelation of the data. Nevertheless, the variogram analysis conducted for the dataset indicates a lack of significant spatial autocorrelation, hence rendering Kriging impractical in this study for the mapping process. Furthermore, Kriging exhibits slow computational performance when applied to the dataset of 43,000 data points. Other interpolation methods are also tested, but the results do not significantly differ from IDW, considering the high density and regular arrangement of data points. Therefore, IDW is selected as the appropriate interpolation method due to its ease of use and computational efficiency.

Once the interpolation method is assessed, resolution studies are conducted to optimize the mapping process. It is found that a coordination resolution of 0.1 is sufficient, as it yields similar results compared to a resolution of 0.05, while significantly reducing the data acquisition time, leading to a more efficient mapping process.

2.4. Visualization

For visualization purposes, the dataset of equivalent damp heat testing times is transformed into an informative and visually appealing country map, allowing for a clear representation of the variations across different regions of Turkey. In order to accomplish this task, the following steps are applied using an open-source Geographic Information System (QGIS, 2023) tool: (i) the resulting dataset containing latitude, longitude, and the corresponding equivalent testing time is uploaded into QGIS along with the Turkey's shapefile (EEA, 2023), ensuring that the proper coordinate reference system is used to maintain accurate spatial representation, (ii) the IDW interpolation is applied to the dataset, setting the power constant to four in order to control the

influence of nearby points on the interpolated values and raster sizes of X and Y pixels to 0.05 in order to achieve the desired level of detail in the interpolated map, (iii) the interpolated layer is masked using the shapefile of Turkey, removing any excess parts of the interpolated map that fall outside the boundaries of the country, ensuring that the visualization solely focuses on the relevant area, (iv) the render type is set to single-band pseudo-color to enhance the visualization, allowing for the representation of different values using a color ramp, (v) the interpolation is discretized to provide a more distinct representation of the values, and early resampling techniques are applied to optimize the rendering performance, and (vi) a legend is generated based on the frequency of the values, enabling viewers to interpret the colors in the map.

3. RESULTS AND DISCUSSION

In order to exemplify the analysis workflow for relative humidity frequency profiles in Section 3.1 and equivalent damp heat testing time calculations in Section 3.2, twelve cities located in different geographical regions across the country are selected as examples of location-dependent climate conditions in Turkey. Then, Section 3.3 will follow for the mapping discussion.

3.1. Relative Humidity Frequency Profiles

Figure 2 illustrates the distribution of hours with 85% RH in relation to module temperature considering the four different humidity models for the selected cities. Analyzing diverse geographical regions reveals distinguishable frequency distributions of 85% RH in dry and humid climates, highlighting the importance of the local climate conditions. Significantly higher frequencies are seen in humid climates such as Adana, Antalya, Istanbul, Izmir, Samsun, and Trabzon, and considerably lower frequencies are seen in dry climates such as Ankara, Erzurum, Konya, Sanliurfa, Sivas, and Van. When the ambient temperature, and consequently the module temperature, is low, the humidity levels are high, leading to similar frequency distributions across the different humidity models. On the contrary, as the ambient and module temperatures increase, the humidity levels decrease, resulting in varying frequency distributions among the different humidity models. For hot and humid locations, the peak frequency is observed at the module temperature of around 15°C, but on the other hand, this temperature is around 5°C for mild and dry locations.

3.2. Equivalent Damp Heat Testing Times

Figure 3 illustrates the corresponding equivalent damp heat testing times at 85°C/85%RH for a service lifetime of 30 years as a function of activation energy considering the four different humidity models for the selected cities. It can be noticed that the equivalent damp heat testing times vary tremendously with changing activation energies, highlighting the importance of the module construction. When the activation energy is low, reaction kinetics will be faster, and therefore, the required testing time for the targeted service lifetime will be higher. Similarly, when the activation energy is high, reaction kinetics will be slower, and therefore, the required testing time for the targeted service lifetime will be lower. Regarding the behavior of the different humidity models, a similar conclusion made for the frequency distributions can be drawn here as well. The variation between the models is larger for hot and humid climates, especially at higher activation energies, than that for mild and dry climates.

For further discussion, only the results obtained from the sigmoidal humidity model are presented, as it is established as the most suitable model for estimating the degradation impacts of the effective surface relative humidity on PV module performance.

Table 1 provides the comprehensive list of the equivalent damp heat testing times (in hours) at 85°C/85%RH for a service lifetime of 30 years as a function of activation energy for the effective surface relative humidity (sigmoidal) model for all cities in Turkey. Here, it is to be noted that the official latitude and longitude values of each city are used. Although the calculations are performed for the activation energies of 0.2 eV to 1.4 eV (with 0.1 eV increments), as seen in Figure 3., only the activation energies of 0.3 eV to 0.9 eV are included here due to limited space. As expected, humid climates exhibit higher humidity levels, leading to longer equivalent testing times compared to dry climates. For instance, for an activation energy of 0.6 eV, while only 1268 hours of testing under the damp heat conditions is sufficient to ensure 30 years of lifetime in Sanliurfa (hot and dry climate), 3109 hours of exposure is required for the same lifetime in Adana (hot and humid

climate). The same situation is also true for Van and Izmir. Only 792 hours of testing under the damp heat conditions is adequate to represent 30 years of lifetime in Van (mild and dry climate) for an activation energy of 0.6 eV, whereas Izmir (hot and humid climate) requires 2283 hours of testing for the same lifetime. It is interesting to see that Istanbul necessities more testing time than Trabzon, i.e., 2686 hours for the former and 2153 hours for the latter. Trabzon is known for heavy rainfalls in the country; however, Istanbul has higher humidity content, higher temperature, and higher wind speed conditions than Trabzon. All these factors affect module temperature, and hence the effective humidity levels at the module surface, indicating the importance of the type and the magnitude of effective stress factors.

The findings in Table 1 also demonstrate the strong dependence of the equivalent damp heat testing times on the activation energies for power degradation, and thus, the module construction. For instance, in Konya, the city with the highest installed PV capacity due to irradiation conditions, land availability, and dry climate conditions, the testing time is approximately 1112 hours with an activation energy of 0.6 eV (representing a standard glass/backsheet module construction with an EVA-based encapsulant), but this testing time reduces to around 113 hours with an activation energy of 0.9 eV (representing a double glass module construction with impermeable edge-seal for minimal humidity ingress). This discrepancy highlights that the testing time of 1000 hours, as required by the standard, seems to be reasonable for this specific location. It is still inadequate to accurately represent a service lifetime of 30 years for the former scenario and it is quite excessive for the latter scenario, leading to over-aging.

It is important to note that if the targeted service lifetime is extended beyond the current 30-year period, these testing times, reported in Table 1, will need to be adjusted accordingly. A simple conversion procedure suffices for this task: a testing time is divided by 30 in order to obtain the testing time needed for a 1-year period, and then, multiplied by the desired service lifetime, i.e., 40 years. For instance, 1112 hours of testing time for Konya, for a service lifetime of 30 years with an activation energy of 0.6 eV, are brought up to 1483 hours for a service lifetime of 40 years.

Figure 4 depicts how equivalent damp heat testing times are distributed across all cities in Turkey. It is to be noted that only the activation energies of 0.5 eV, 0.6 eV, and 0.7 eV are included in this density plot for visualization purposes. Regardless of the activation energies, all density curves are characterized by a global maximum at lower equivalent testing times, representing the interior regions in the country with lower humidity levels, and a local maximum at higher equivalent testing times, representing the areas close to coastal regions with higher humidity levels. For 0.6 eV, these correspond approximately to 1200 and 2100 hours, respectively. As the activation energy decreases, population density decreases with a broader distribution.

Figure 5 delineates the similarities and the differences between the cities in the form of a dendrogram generated using the hierarchical clustering method. It is one of the most popular and widely used methods to analyze data in which nodes (i.e., cities) are compared with another based on their similarities (i.e., equivalent damp heat testing times). It is an unsupervised machine learning technique that arranges data points into clusters by progressively merging similar clusters together. This creates a tree-like diagram called a dendrogram, capturing data relationships at different levels of detail. The process continues until either all data points are in one cluster (Johnson, 1967). In the dendrogram, there are two main branches: one with small number of cities with higher temperature and humidity levels, and thus higher testing times, representing the coastal regions, and the other with large number of cities with lower humidity levels, representing mostly the interior regions. In the former, Adana seems to be unique with its harsh climate conditions. In the latter, there are two sub-branches: one with cities close to coastal regions with relatively higher humidity levels, and the other with cities mostly located in the central part of the country, away from coastal regions, with relatively lower humidity levels. The dendrogram also presents one obvious and one interesting fact. The obvious fact is that the neighboring cities (or cities within the same geographical regions or in close proximity to each other) are grouped together as they are expected to have very similar climate conditions. The pairs of Istanbul/Kocaeli, Van/Sirnak, Bingol/Tunceli, Edirne/Tekirdag, and Agri/Erzurum can be given as examples. The interesting fact is that there are clusters with cities from different geographical regions (in distant proximity to each other). This is also expected if they have similar climate conditions specifically in terms of temperature and humidity levels. The pairs of Konya/Kars, Igdir/Afyonkarahisar, Bolu/Yozgat, Kutahya/Sanliurfa, and Hatay/Yalova

can be given as examples. This dendrogram is constructed using the data with an activation energy of 0.6 eV; however, similar dendrograms can be obtained with varying activation energies as grouping will not change.

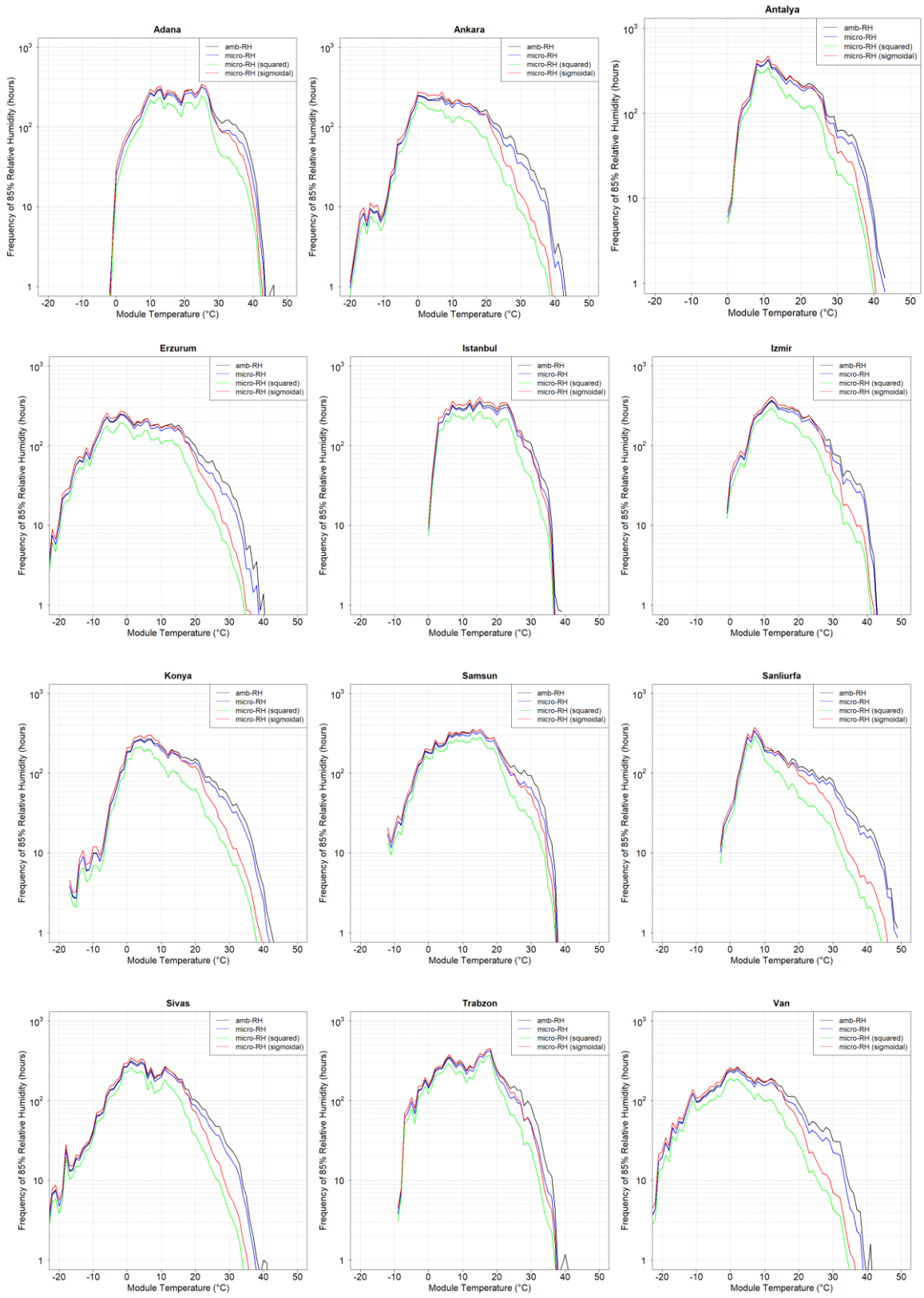

Figure 2. *Frequency distributions of 85% relative humidity in hours as a function of module temperature for the four different humidity models for the selected cities*

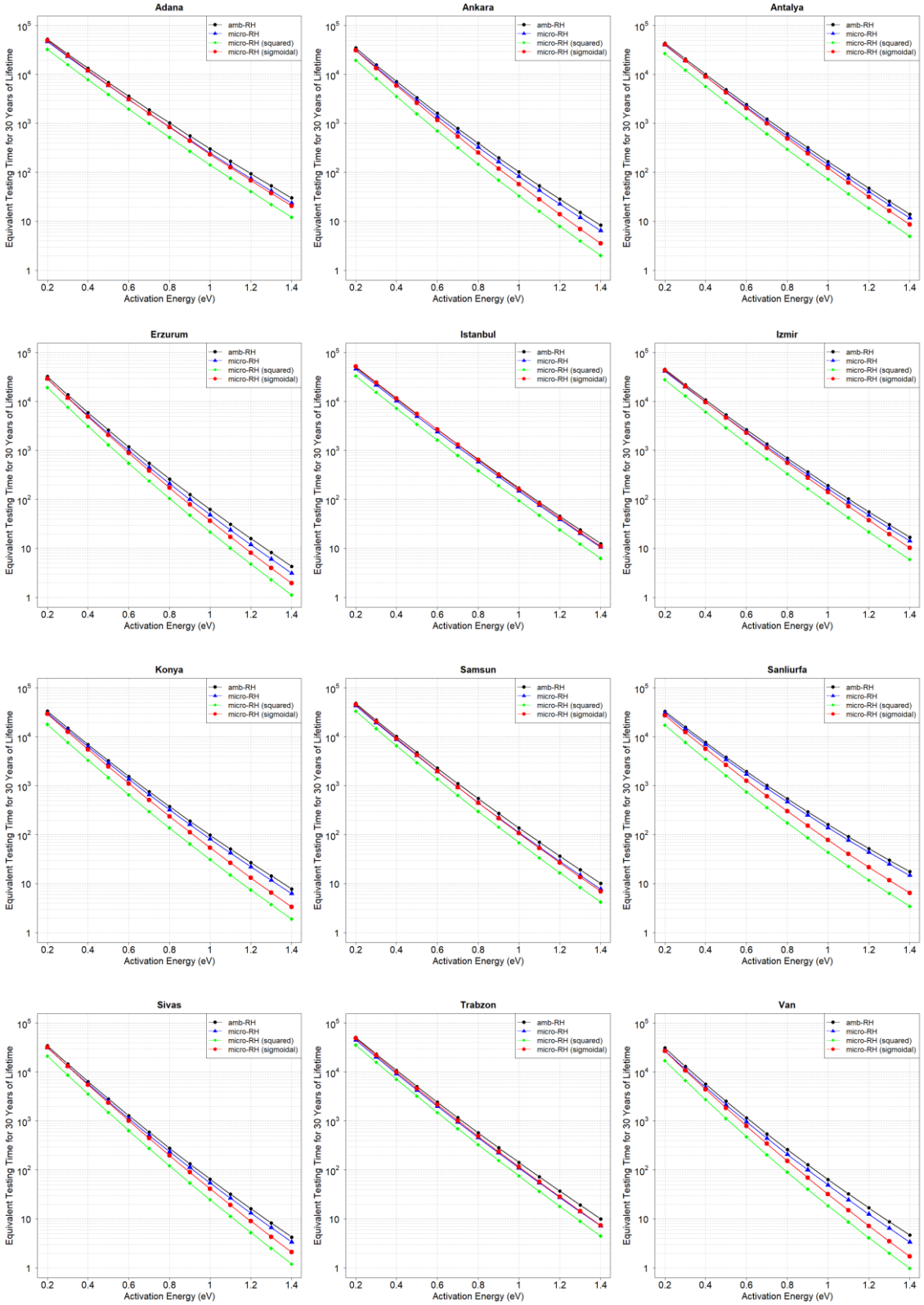

Figure 3. *Equivalent damp heat testing times at 85°C/85%RH for a service lifetime of 30 years as a function of activation energy with the four different humidity models for the selected cities*

Table 1. *Equivalent damp heat testing times at 85°C/85%RH for a service lifetime of 30 years with varying activation energies with the sigmoidal model for all cities in Turkey*

Location	Activation Energy (eV)						
	0.3	0.4	0.5	0.6	0.7	0.8	0.9
Adana	24402.2	12127.6	6103.5	3109.4	1602.8	835.6	440.3
Adiyaman	13655.2	6168.4	2829.1	1317.9	623.7	299.9	146.6
Afyonkarahisar	14206.7	6146.4	2700.9	1205.5	546.5	251.6	117.6
Agri	12329.7	5054.8	2110.8	897.6	388.6	171.2	76.8
Aksaray	11923.8	5201.2	2303.2	1035.8	473.1	219.5	103.5
Amasya	18085.0	8333.5	3898.2	1849.9	890.0	433.8	214.1
Ankara	13455.4	5885.6	2617.0	1182.7	543.1	253.4	120.0
Antalya	19251.3	9039.7	4290.9	2059.4	999.5	490.6	243.5
Ardahan	14581.1	6041.0	2552.4	1098.6	481.3	214.4	97.0
Artvin	18243.2	8270.0	3820.8	1796.7	858.7	416.7	205.0
Aydin	15145.5	6966.2	3247.5	1534.7	735.2	357.1	175.9
Balikesir	19745.3	9222.1	4369.3	2099.1	1022.1	504.1	251.7
Bartin	19709.4	8835.8	4025.7	1863.3	875.6	417.4	201.7
Batman	11434.9	5147.4	2357.3	1099.5	522.8	253.6	125.6
Bayburt	12934.9	5385.0	2286.6	988.9	435.0	194.5	88.2
Bilecik	18528.0	8530.7	3990.0	1894.2	912.0	445.0	219.9
Bingol	12179.3	5131.3	2204.2	964.6	429.6	194.6	89.6
Bitlis	11361.6	4739.6	2012.9	870.5	383.4	172.0	78.5
Bolu	15705.8	6655.6	2869.0	1257.3	559.8	253.0	116.0
Burdur	14199.9	6189.9	2737.4	1228.2	559.0	258.0	120.8
Bursa	19807.6	9072.5	4216.4	1987.1	948.9	458.9	224.6
Canakkale	22211.2	10333.2	4871.7	2326.3	1124.4	549.8	271.8
Cankiri	12774.1	5500.0	2408.4	1072.3	485.3	223.1	104.2
Corum	15478.8	6851.1	3076.4	1401.3	647.2	303.1	143.8
Denizli	13673.8	6308.8	2953.1	1402.8	676.4	331.1	164.5
Diyarbakir	12252.3	5483.9	2498.9	1160.8	550.2	266.4	131.8
Duzce	21622.3	9914.0	4611.0	2174.0	1038.5	502.2	245.8
Edirne	20742.9	9694.9	4581.8	2189.3	1057.6	516.4	254.9
Elazig	12961.2	5702.9	2547.9	1156.2	533.0	249.6	118.7
Erzincan	12434.3	5145.7	2170.4	932.5	407.9	181.5	82.1
Erzurum	11871.1	4894.2	2062.3	887.3	389.3	174.1	79.2
Eskisehir	13782.6	6068.2	2708.2	1225.3	562.1	261.4	123.2
Gaziantep	15714.1	7395.5	3532.8	1712.9	842.8	420.7	213.0
Giresun	16337.7	6812.2	2892.2	1249.4	548.8	244.8	110.9
Gumushane	14034.8	5935.2	2557.3	1121.8	500.6	227.1	104.6
Hakkari	9879.9	3925.6	1590.3	657.0	276.8	118.9	52.1
Hatay	21876.2	10509.6	5105.5	2508.1	1245.8	625.7	317.6
Igdir	13493.2	5916.2	2651.0	1212.3	564.8	267.7	128.9
Isparta	15451.0	6792.4	3026.3	1366.2	624.8	289.4	135.7
Istanbul	24522.0	11611.1	5556.1	2686.2	1311.6	646.6	321.7

Table 1. *(continued)*

Location	Activation Energy (eV)						
	0.3	0.4	0.5	0.6	0.7	0.8	0.9
Izmir	20587.2	9785.4	4701.5	2283.4	1121.1	556.3	279.1
Kahramanmaras	15242.7	6962.9	3228.6	1519.2	725.1	350.9	172.1
Karabuk	18398.2	8249.5	3757.1	1737.3	815.3	388.0	187.1
Karaman	12191.3	5328.0	2360.3	1060.1	482.8	222.9	104.4
Kars	14112.4	5938.9	2549.1	1114.9	496.4	224.8	103.5
Kastamonu	15907.0	6917.3	3055.2	1370.2	623.8	288.1	135.0
Kayseri	12045.9	4996.5	2111.6	909.0	398.3	177.6	80.6
Kirikkale	12294.9	5409.9	2424.8	1107.1	514.8	243.8	117.5
Kirklareli	22328.8	10322.1	4835.6	2294.2	1101.6	535.0	262.6
Kirsehir	12298.8	5359.3	2376.1	1071.6	491.4	229.0	108.4
Kilis	16117.9	7582.4	3616.6	1749.0	857.5	426.2	214.6
Kocaeli	24076.2	11394.1	5468.9	2660.5	1311.0	653.9	330.0
Konya	12651.3	5538.3	2462.6	1112.4	510.5	238.0	112.8
Kutahya	14710.3	6415.3	2840.7	1276.8	582.3	269.4	126.4
Malatya	11643.9	5147.9	2312.7	1055.9	490.1	231.2	110.8
Manisa	16725.2	7616.3	3511.9	1639.6	774.9	370.7	179.5
Mardin	11842.7	5352.6	2461.3	1152.2	549.5	267.1	132.3
Mersin	15822.5	7037.9	3176.8	1454.9	675.8	318.2	151.8
Mugla	19340.2	9129.8	4362.1	2109.7	1032.7	511.7	256.5
Mus	12126.6	5157.4	2235.1	986.7	443.4	202.8	94.3
Nevsehir	14390.8	6361.5	2855.9	1302.2	603.0	283.6	135.4
Nigde	11816.5	4971.8	2130.3	929.1	412.3	186.0	85.3
Ordu	20472.0	9193.5	4195.3	1944.6	915.1	436.9	211.5
Osmaniye	21255.1	10353.0	5113.3	2559.8	1298.4	666.9	346.8
Rize	17427.9	7353.6	3149.9	1369.6	604.3	270.5	122.7
Sakarya	22787.7	10643.2	5041.5	2420.5	1177.2	579.7	288.8
Samsun	20413.7	9241.6	4247.2	1980.6	936.7	449.0	218.0
Siirt	11380.8	4967.4	2206.1	997.7	459.7	216.0	103.5
Sinop	18360.7	8201.6	3722.4	1715.6	802.4	380.6	182.9
Sivas	13205.5	5529.2	2352.4	1016.7	446.2	198.8	89.9
Sanliurfa	12429.8	5709.7	2666.8	1267.6	613.7	302.7	152.2
Sirnak	8893.0	3791.9	1649.6	732.9	332.9	154.7	73.5
Tekirdag	20956.1	9735.9	4583.8	2186.6	1056.4	516.7	255.7
Tokat	16561.7	7261.5	3235.3	1463.6	671.7	312.6	147.4
Trabzon	21998.1	10000.8	4610.4	2153.8	1019.0	488.0	236.3
Tunceli	11978.6	5065.8	2187.0	963.4	432.8	198.2	92.5
Usak	12728.8	5614.3	2514.1	1143.2	527.9	247.5	117.9
Van	10788.1	4422.9	1852.4	792.0	345.4	153.6	69.6
Yalova	23066.5	10892.5	5209.3	2522.3	1235.9	612.6	307.0
Yozgat	14288.9	6255.9	2783.1	1257.7	577.1	268.8	127.0
Zonguldak	22312.9	10295.2	4820.1	2288.9	1101.7	537.3	265.3

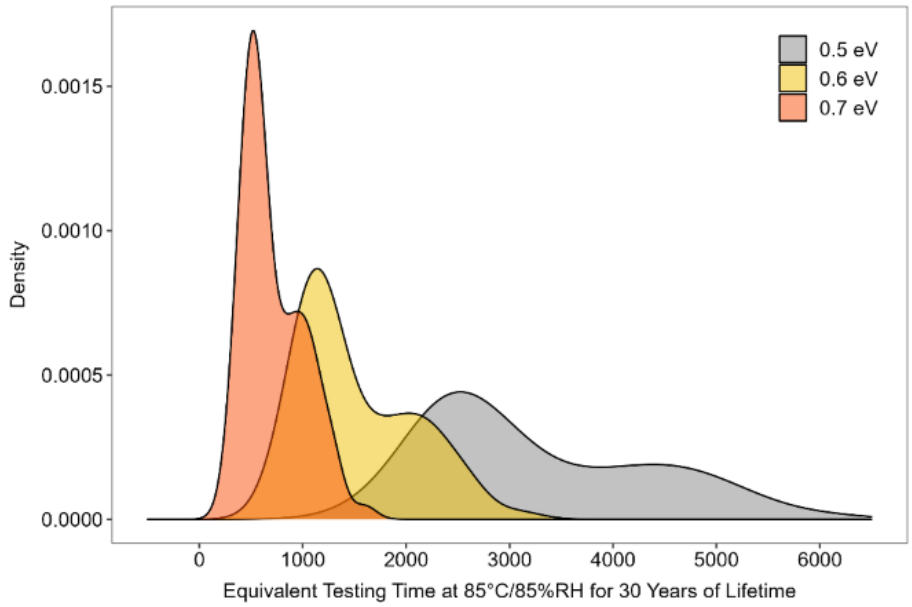

Figure 4. *Distribution of equivalent damp heat testing times at 85°C/85%RH for a service lifetime of 30 years with varying activation energies with the sigmoidal model all cities in Turkey*

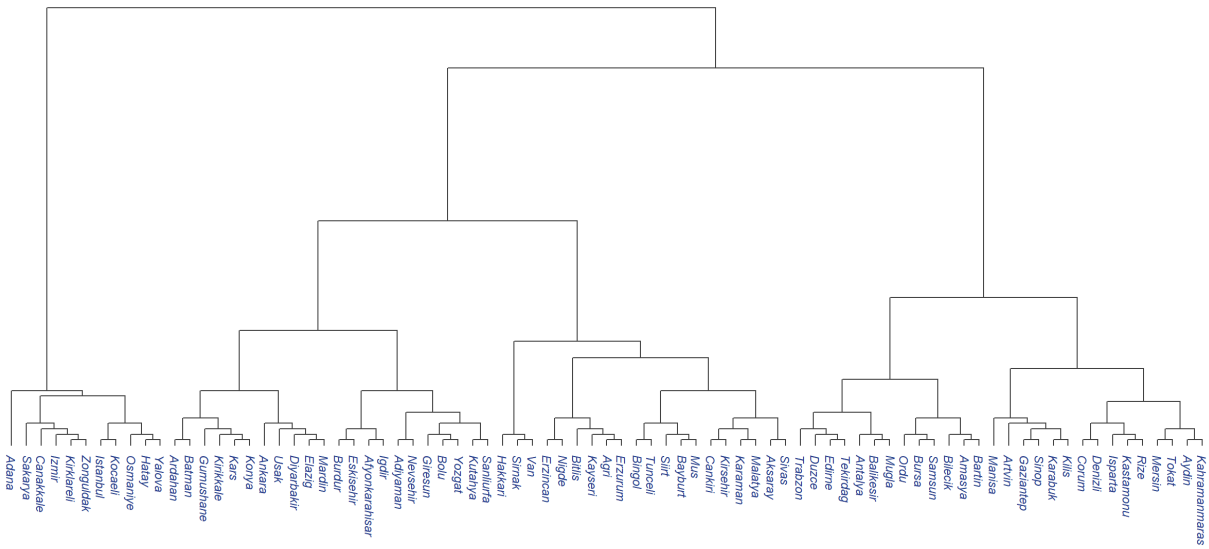

Figure 5. *Hierarchical clustering dendrogram of cities in Turkey, showing their similarities in terms of equivalent damp heat testing times*

3.3. Equivalent Damp Heat Testing Time Map of Turkey

Since the degradation of power in typical glass/backsheet PV modules with EVA-based encapsulants, caused by hydrolytic reactions under the damp heat conditions, exhibits activation energies ranging from 0.5 eV to 0.7 eV, an average activation energy of 0.6 eV is applied for the visualization purposes in mapping procedure. Figure 6 illustrates the map of Turkey, displaying the equivalent testing times required under the standard damp heat conditions (at 85°C/85%RH) for a service lifetime of 30 years generated by using the sigmoidal model for the effective surface relative humidity with an activation energy of 0.6 eV for power degradation. The coastal areas, characterized by higher relative humidity levels, with hot and humid climate conditions, necessitate longer testing times to achieve the desired service lifetime compared to the interior regions with mild/hot and dry climate conditions. This is particularly notable in the Southern, Western, and Northwestern regions. Surprisingly, despite the expectation of longer testing times in the coastal areas of the Northern region, the lower temperature values in this area result in shorter testing times compared to the Southern and Western

coasts. While the central parts show moderate testing times, Eastern and Southeastern regions, as anticipated due to their dry climate conditions, exhibit the shortest testing times in the country.

It is seen that the equivalent testing times exhibit a strong dependence on the location, given the significant variations in local climate conditions, specifically temperature and relative humidity, even within this relatively small country. Best places for PV installations seem to be the Southern-Central, Southeastern-Central, Eastern, and Southeastern regions, characterized by blue areas, followed by mostly interior regions, that are away from the coasts with high humidity content, characterized by the green areas. However, in order for this observation to be completely true, additional factors, such as the irradiation conditions, must be considered. Irradiation condition is, of course, the most important factor for modules to produce electricity. Terrain information is also essential because lands to be used for PV systems, particularly for utility scales, should be feasible for installation, for which urban/residential areas, forests, crop fields, etc., are out of option.

While the current study focuses on providing a country-specific map, our future endeavors encompass a more comprehensive approach. We aim to generate a worldwide map that takes varying activation energies associated with different module constructions and desired service lifetimes into account. By expanding our scope, we aspire to provide a broader understanding of the intricate relationship between module construction, climatic conditions, and the necessary testing durations for PV modules on a global scale. Multi-level maps, combining climatic conditions, irradiation conditions, and terrain information, should also be generated for a more complete understanding of the trade-offs between the performance, reliability, and service lifetime issues.

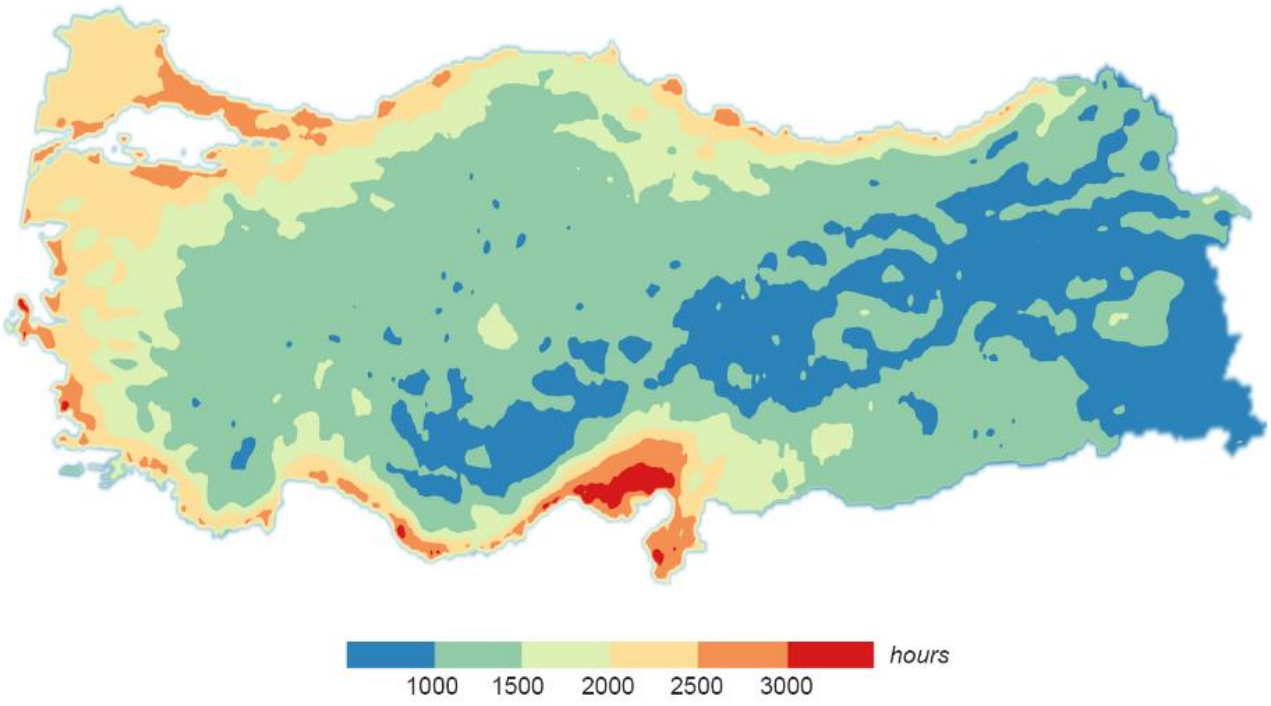

Figure 6. *Equivalent damp heat testing times map of Turkey for a service lifetime of 30 years with an activation energy of 0.6 eV for the effective surface relative humidity (sigmoidal) model*

3.4. The Drawbacks of Standard Testing for Service Lifetime Prediction

Lab-based standard accelerated testing usually involves single and/or constant stress factors applied at elevated intensity levels for a relatively short time frames (compared to the expected service lifetime in real-world operation). Three testing protocols, concerning the durability of module packaging materials and laminated structure, in the IEC 61215 standard, are worth mentioning. Damp heat testing, which is the main focus of this study, is applied to determine the ability of the module construction to withstand the effects of long-term penetration of humidity. In this protocol, temperature and humidity levels are kept constant at 85°C and 85%RH for 1000 hours. Thermal cycling (TC200) testing, on the other hand, is applied to determine the ability of the module construction to withstand thermal mismatch, fatigue and other stresses caused by repeated

changes of temperature. In this protocol, modules are subjected to thermal cycles between -40°C and 85°C (with no humidity content) for 200 times. Similarly, humidity-freeze (HF10) testing is applied to determine the ability of the module construction to withstand the effects of high temperature and humidity followed by sub-zero temperatures. In this protocol, modules are subjected to thermal cycles between -40°C (with no humidity control) and 85°C (with 85% humidity content) for 10 cycles. In the latter two protocols that involve thermal cycles, maximum cycle times, minimum dwell times at each temperature level, and the heating and cooling rates are specified by the standard. There also exist protocols for testing mechanical stability, such as static mechanical load test to determine the ability of the module construction to withstand wind, snow, static or ice loads, and hail test (as a dynamic mechanical impact test) to verify that the module construction is capable of withstanding the impact of hailstones. Other than the protocols for determining characteristic module parameters, the standard also consists of test protocols to investigate the other aspects of failures, mostly related to safety and performance of electrical components, such as insulation test, wet leakage current test, robustness of terminations, hot-spot endurance test, and bypass diode thermal test. Procedures for each testing and requirements for qualification are determined by the standard.

The primary purpose of standard testing for PV modules is to assess the overall construction integrity for design approval and qualification. While it is effective in identifying design and processing flaws that could lead to early failures and safety issues in the field, with its pass/fail nature lacking experimental depth, it offers limited insight into module behavior over the intended service lifetime of 30 years in real-world conditions. Unlike standard testing, which uses single or constant stress factors, actual PV module operation involves multiple, uncontrolled, and cyclic stress factors acting simultaneously with varying intensities during real-world operation. Fielded modules often exhibit various concurrent degradation mechanisms (IEA PVPS, 2014) due to interactions among different stress factors, resulting in complex degradation pathways. The overall degradation or performance loss in this case depends on the integrated effects of all stress factors. Standard testing, accelerated for quick observations, only assesses how modules perform under specific stress conditions and fails to consider the diverse degradation mechanisms active throughout the lifetime. Owing to its simplicity, cost-effectiveness, and shorter test durations, standard testing is preferred over real-world testing to assure reliability for market introduction. Osterwald and McMahon (2009) emphasize that despite aspirations, the conventional standards are not designed as service lifetime tests and argue that establishing a universal test or series of tests for service lifetime prediction of any arbitrary module for 30 years would be impractical. Of course, as they state, this challenge is not unique to the field of PV as various other industries dealing with durable, high-value products, that are expected to maintain long-term performance, like building materials, confront comparable issues. Therefore, there is a growing debate within the PV community about the standard's effectiveness to be used as an indicator of service lifetime. Predicting a service lifetime of 30 years based on lab-based exposures may seem practical and advantageous, but it carries risks due to intensified and more aggressive stress levels that can overstress modules and thus trigger unrealistic degradation mechanisms that cannot be observed in the field instead of initializing and stimulating realistic ones to a greater extent. Manufacturers may take unnecessary measures to meet stringent requirements solely to pass standards without improving performance of modules in real-world. The study by Jordan et al. (2017) reveals the impacts of climate and module construction on the observed field failures with a comprehensive survey of older and newer installations. They reported that (1) modules installed in hot and humid climates exhibited a broader range of degradation mechanisms compared to those other climates, (2) delamination and diode/junction-box problems were also more prevalent in hot and humid climates, (3) encapsulant discoloration emerged as the most common degradation mechanisms especially in older systems, and (4) newer modules primarily suffered from hot spots, followed by discoloration in internal circuitry. The debate about the usefulness of standard testing for predicting service lifetime therefore revolves mainly around the complexity of real-world conditions, diverse module constructions, and various mounting configurations. While some of the current installations might share similarities with their designs and bill-of-materials that have been in use for maybe 20+ years, considering the history of commercial installations, many of today's modules have distinct differences, probably using lower cost components, from those with a documented history. On that account, it is uncertain whether modules installed today will continue to operate effectively for 30 years.

Numerous studies in the literature have also unveiled the drawbacks associated with utilizing damp heat testing as a predictor for the service lifetime of modules and module materials. For instance, Pickett (2015) investigated the degradation behavior of polyethylene terephthalate (PET) and polycarbonate (PC) polymers

under the standard damp heat conditions of 85°C and 85%RH. Although PET degraded more quickly than PC under these conditions, extrapolating the results to an ambient temperature of 25°C using the Arrhenius relationship revealed that PET outlasted PC due to their distinct activation energies. Both polymers exceeded the standard required lifetime by a significant margin. Similarly, Kempe and Wohlgemuth (2013) explored the hydrolysis kinetics of PET used in PV backsheets, finding that 1000 hours of damp heat testing equated to 150 years of real-world exposure in Bangkok, Thailand. This location is known for its very harsh climate conditions for PV modules with very high levels of temperature and humidity content, suggesting that testing time could be extended to thousands of years in milder climates. Using micro-climate data and finite elements analysis, Hülsmann and Weiss (2015) found that humidity content in the encapsulant polymer between the cells and front glass, induced by damp heat testing, was twice as high as real-world weathering over 20 years. Similarly, Reisner et al. (2006) determined that 1000 hours of damp heat was equivalent to only 16 years in a tropical climate, but to over 100 years in a moderate climate, for the degradation of polyurethane-type encapsulant material in rear-insulated PV modules which usually run 25°C hotter than free-standing modules in mild climates. The correlation between damp heat testing and real-world exposure was found to be inconsistent in the study by Whitfield et al. (2012). They observed higher failure rates under damp heat conditions due to elevated relative humidity content compared to real-world conditions, suggesting a lower overall risk of field failure. After reviewing failures occurred in the field and under damp heat testing, Wohlgemuth and Kempe (2013) asserted that failures driven by field conditions cannot be accurately reproduced by damp heat testing. Additionally, Kempe et al. (2015) explored equivalent damp heat testing times for various module constructions under diverse climate conditions by conducting damp heat testing at various temperature and relative humidity levels and using finite element analysis with real-world meteorological data to predict and compare humidity ingress profiles. For example, 3700 hours of testing (for an open-rack mounted glass/backsheet module with an activation energy of around 0.57 eV) was found to be required to represent a service lifetime of 25 years in a tropical climate. This finding aligns well with the results obtained within this work. Further study by Fan et al. (2018), using empirical kinetics modeling and gamma processes, demonstrated that service life approximations of 20 to 25 years can be achieved under conditions of 50°C/45%RH, underling the severity of the standard damp heat conditions of 85°C/85%RH. Likewise, Kimball et al. (2016) estimated damp heat acceleration factors for a service lifetime of 25 years for over 2500 locations worldwide using empirical kinetics modeling and real-world meteorological data. They concluded that 1000 hours of damp heat adequately represented most locations, even in tropical climates, for humidity-resistant module constructions with an activation energy of around 0.9 eV. Similar to our work, the significant impact of activation energy on testing times was evident in this study as well. On this topic, Laronde et al. (2012) emphasized the need for precise identification of activation energy as a 10% variation in activation energy was shown to alter the estimated service lifetime by 30%.

Warranties for module performance, universally applied to all kinds of modules deployed in all climates, are solely based on established standards. However, findings from this and other studies in the literature clearly indicate that the uncertainty arising from standard damp heat testing results poses a significant challenge in predicting the service lifetime. This is particularly concerning given the intricacies of real-world conditions, diverse module constructions, and varying mounting configurations. To effectively address the reliability issues and improve the performance and service lifetime of PV modules, understanding of degradation mechanisms and failure modes specific to different module types and climate conditions and developing standards that can closely simulate real-world conditions are essential.

4. CONCLUSION

In this study, the analysis of equivalent damp heat testing times to simulate a service lifetime of 30 years for PV modules in Turkey was conducted. With a meticulous approach, the calculations were performed with a resolution of 0.1 in both latitude and longitude values. The obtained results were then presented in the form of a country map, employing an interpolation technique. By mapping, the variations in climatic conditions, and consequently, the effective stress factors were identified, underlining the influence of these factors on the required damp heat testing times necessary to achieve a desired service lifetime for PV modules.

The outcomes of this investigation have shed light on the risks associated with relying solely on standard testing procedures for predicting service lifetime of PV modules across diverse module constructions and

climatic conditions. It has become evident that the durability and reliability of PV modules in real-world scenarios is significantly influenced by both the specific module construction, as it directly affects the kinetics of degradation processes, and the prevailing climatic conditions, as they directly impact the effective stress factors experienced by the PV modules.

As a future work, instead of a country-specific map, a worldwide map to capture the global picture of the service lifetime issues is anticipated. A multi-level mapping, that involves both climate and irradiation conditions, along with the terrain information, to pinpoint the best possible locations for PV system installations for increased performance and reliability can further be persuaded.

ACKNOWLEDGEMENT

This work is conducted as part of the Solar-Era.NET project: PV40+ and supported by the funding from The Scientific and Technological Research Council of Turkey (TUBITAK) under the Grant No: 120N520. The author would like to thank Vahit A. Yenigul for helping with the mapping procedure.

CONFLICT OF INTEREST

The author declares no conflict of interest.

REFERENCES

Adothu, B., Costa, F. R., & Mallick, S. (2021). Damp heat resilient thermoplastic polyolefin encapsulant for photovoltaic module encapsulation. *Solar Energy Materials and Solar Cells*, *224*, 111024. https://www.doi.org/10.1016/j.solmat.2021.111024

Aghaei, M., Fairbrother, A., Gok, A., Ahmad, S., Kazim, S., Lobato, K., Oreski, G., Reinders, A., Schmitz, J., Theelen, M., Yilmaz, P., & Kettle, J. (2022). Review of degradation and failure phenomena in photovoltaic modules. *Renewable and Sustainable Energy Reviews*, *159*, 112160. https://www.doi.org/10.1016/j.rser.2022.112160

Çabuk, A. S. (2022). Comparison of innovative and traditional method for optimizing the efficiency of photovoltaic panels. *International Journal of Energy Applications and Technologies*, *9*(2), 45-49. https://www.doi.org/10.31593/ijeat.1082277

EEA (European Environmental Agency). (2023). Turkey shapefile. (Accessed:27/07/2023) URL

Er, Z. (2023). Solar Radiation Forecasts and a Tiny House PV Off-Grid System. *Avrupa Bilim ve Teknoloji Dergisi*, (47), 7-12. https://www.doi.org/10.31590/ejosat.1234216

Faiman, D. (2008). Assessing the outdoor operating temperature of photovoltaic modules. *Progress in Photovoltaics: Research and Applications*, *16*(4), 307-315. https://www.doi.org/10.1002/pip.813

Fan, J., Qian, Z., & Wang, J. (2018, November 6-8). *Photovoltaic Modules Power Degradation and Lifetime Prediction under Accelerated Damp-heat Conditions Based on Gamma Process*. In: Proceedings of the International Conference on Power System Technology (POWERCON), (pp. 93-100). https://www.doi.org/10.1109/POWERCON.2018.8601560

Gok, A., Gordon, D. A., Wang, M., French, R. H., & Bruckman, L. S. (2019). Degradation Science and Pathways in PV Systems. In: H. Yang, L. S. Bruckman, & R. H. French (Eds.), *Durability and Reliability of Polymers and Other Materials in Photovoltaic Modules* (pp. 47-95). William Andrew Publishing. https://www.doi.org/10.1016/B978-0-12-811545-9.00003-3

GSES (Global Sustainable Energy Solutions). (2023). Recycling Solar Panels. (Accessed:27/07/2023) URL

Hülsmann, P., & Weiss, K.-A. (2015). Simulation of water ingress into PV-modules: IEC-testing versus outdoor exposure. *Solar Energy*, *115*, 347-353. https://www.doi.org/10.1016/j.solener.2015.03.007

IEA PVPS. (2014). Review of Failures of Photovoltaic Modules (No. IEA-PVPS T13-01:2014). International Energy Agency (IEA) Photovoltaic Power Systems Programme (PVPS). (Accessed:27/07/2023) URL

IEA PVPS. (2022). Trends in Photovoltaic Applications 2022 (No. IEA PVPS T1-43:2022). International Energy Agency (IEA). (Accessed:27/07/2023) URL

IEA PVPS. (2023). Snapshot of Global PV Markets 2023 (No. IEA-PVPS T1-44:2023). International Energy Agency (IEA) Photovoltaic Power Systems Programme (PVPS). (Accessed:27/07/2023) URL

IEC (International Electrotechnical Society). (2021). IEC 61215-2:2021: Terrestrial photovoltaic (PV) modules—Design qualification and type approval—Part 2: Test procedures. (Accessed:27/07/2023) URL

Johnson, S. C. (1967). Hierarchical clustering schemes. *Psychometrika*, *32*(3), 241-254. https://www.doi.org/10.1007/BF02289588

Jordan, D. C., Silverman, T. J., Wohlgemuth, J. H., Kurtz, S. R., & VanSant, K. T. (2017). Photovoltaic failure and degradation modes. *Progress in Photovoltaics: Research and Applications*, *25*(4), 318-326. https://www.doi.org/10.1002/pip.2866

Kempe, M. D., Panchagade, D., Reese, M. O., & Dameron, A. A. (2015). Modeling moisture ingress through polyisobutylene-based edge-seals: Polyisobutylene-based edge-seals. *Progress in Photovoltaics: Research and Applications*, *23*(5), 570-581. https://www.doi.org/10.1002/pip.2465

Kempe, M. D., & Wohlgemuth, J. H. (2013, June 16-21). *Evaluation of temperature and humidity on PV module component degradation*. In: Proceedings of the IEEE 39th Photovoltaic Specialists Conference (PVSC), (pp. 0120-0125). https://www.doi.org/10.1109/PVSC.2013.6744112

Kimball, G. M., Yang, S., & Saproo, A. (2016, June 5-10). *Global acceleration factors for damp heat tests of PV modules*. In: Proceedings of the IEEE 43rd Photovoltaic Specialists Conference (PVSC), (pp. 0101-0105). https://www.doi.org/10.1109/PVSC.2016.7749557

Koehl, M., Heck, M., & Wiesmeier, S. (2012). Modelling of conditions for accelerated lifetime testing of Humidity impact on PV-modules based on monitoring of climatic data. *Solar Energy Materials and Solar Cells*, *99*, 282-291. https://www.doi.org/10.1016/j.solmat.2011.12.011

Koehl, M., Hoffmann, S., & Wiesmeier, S. (2017). Evaluation of damp-heat testing of photovoltaic modules. *Progress in Photovoltaics: Research and Applications*, *25*(2), 175-183. https://www.doi.org/10.1002/pip.2842

Laronde, R., Charki, A., & Bigaud, D. (2012). Lifetime Estimation of a Photovoltaic Module Subjected to Corrosion Due to Damp Heat Testing. *Journal of Solar Energy Engineering*, *135*(021010). https://www.doi.org/10.1115/1.4023101

López-Escalante, M. C., Fernández-Rodríguez, M., Caballero, L. J., Martín, F., Gabás, M., & Ramos-Barrado, J. R. (2018). Novel encapsulant architecture on the road to photovoltaic module power output increase. *Applied Energy*, *228*, 1901-1910. https://www.doi.org/10.1016/j.apenergy.2018.07.073

Matheron, G. (1963). Principles of geostatistics. *Economic Geology*, *58*(8), 1246-1266. https://www.doi.org/10.2113/gsecongeo.58.8.1246

Oreski, G., Omazic, A., Eder, G. C., Voronko, Y., Neumaier, L., Mühleisen, W., Hirschl, C., Ujvari, G., Ebner, R., & Edler, M. (2020). Properties and degradation behaviour of polyolefin encapsulants for photovoltaic modules. *Progress in Photovoltaics: Research and Applications*, *28*(12), 1277-1288. https://www.doi.org/10.1002/pip.3323

Oreski, G., Ottersböck, B., & Omazic, A. (2019). Degradation processes and mechanisms of encapsulants. In: H. E. Yang, R. H. French, & L. S. Bruckman (Eds.), *Durability and Reliability of Polymers and Other Materials in Photovoltaic Modules* (pp. 135-152). William Andrew Publishing. https://www.doi.org/10.1016/B978-0-12-811545-9.00006-9

Osterwald, C. R., & McMahon, T. J. (2009). History of accelerated and qualification testing of terrestrial photovoltaic modules: A literature review. *Progress in Photovoltaics: Research and Applications*, *17*(1), 11-33. https://www.doi.org/10.1002/pip.861

Pickett, J. E. (2015). Hydrolysis Kinetics and Lifetime Prediction for Polycarbonate and Polyesters in Solar Energy Applications. In: C. C. White, J. Martin, & J. T. Chapin (Eds.), *Service Life Prediction of Exterior*

Plastics (pp. 41-58). Cham: Springer International Publishing. https://www.doi.org/10.1007/978-3-319-06034-7_3

PVGIS (Photovoltaic Geographical Information System). (2023). (Accessed:27/07/2023) URL

QGIS. (2023). Open Source Geographic Information System (GIS). (Accessed:27/07/2023) URL

Reisner, E. U., Stollwerck, G., Peerlings, H., & Shafiq, F. (2006). Humidity in a Solar Module—Horror Vision or Negligible? 2058-2060. Dresden, Germany.

Salmanoğlu, F., & Çetin, N. S. (2022). An Approach on Developing a Dynamic Wind-Solar Map for Tracking Electricity Production Potential and Energy Harvest. *Gazi University Journal of Science Part A: Engineering and Innovation*, *9*(2), 62-78. https://www.doi.org/10.54287/gujsa.1085005

Tirmikçi, C. A., Yavuz, C., & Gümüş, T. E. (2021). Investigating the Effects of Temperature and Relative Humidity on Performance Ratio of a Grid Connected Photovoltaic System. *Academic Platform - Journal of Engineering and Science*, *9*(3), 427-432. https://www.doi.org/10.21541/apjes.894390

Turan, V., Karakuş, C., & Üstün, İ. (2023). Installation of solar power plant in Adıyaman region and analysis of solar energy potential. *International Journal of Energy Applications and Technologies*, *10*(1), 21-25.

Watson, D. F., & Philip, G. M. (1985). A Refinement of Inverse Distance Weighted Interpolation. *Geoprocessing*, *2*(4), 315-327.

Weiß, K.-A., Klimm, E., & Kaaya, I. (2022). Accelerated aging tests vs field performance of PV modules. *Progress in Energy*, *4*(4), 042009. https://www.doi.org/10.1088/2516-1083/ac890a

Whitfield, K., Salomon, A., Yang, S., & Suez, I. (2012, June 3-8). *Damp heat versus field reliability for crystalline silicon*. In: Proceedings of the 38th IEEE Photovoltaic Specialists Conference, (pp. 001864-001870). https://www.doi.org/10.1109/PVSC.2012.6317957

Wohlgemuth, J. H., & Kempe, M. D. (2013, June 16-21). Equating damp heat testing with field failures of PV modules. In: Proceedings of the IEEE 39th Photovoltaic Specialists Conference (PVSC), (pp. 0126-0131). Tampa, FL, USA: IEEE. https://www.doi.org/10.1109/PVSC.2013.6744113

Research Article GU J Sci, Part A, 10(4): 542-554 (2023) 10.54287/gujsa.1384048

Gazi University
Journal of Science
PART A: ENGINEERING AND INNOVATION
http://dergipark.org.tr/gujsa

Enhancing Software Process Assessment with an Ontology-Based Tool: Integrating CMMI, SPICE, and TMMI Models

Rukiye BAŞKARA[1*] Ahmet COŞKUNÇAY[2]

[1] Yildiz Technical University, İstanbul, Türkiye
[2] Atatürk University, Erzurum, Türkiye

Keywords

Software Process Reference Model
Process Assessment Tool
Semantic Web Tool
Software Process Improvement

Abstract

Software process reference models like Capability Maturity Model Integration (CMMI) and Software Process Improvement and Capability Determination (SPICE) have played a crucial role in evaluating processes for several decades. Their adoption by institutions has become essential for consistently delivering software projects to customers on time and with expected quality. However, conducting software process assessments demands considerable time, effort, and skilled personnel. This research introduces an ontology-based tool that facilitates software process assessment for organizations by integrating widely used process reference models, namely CMMI, SPICE, and Test Maturity Model Integration (TMMI). The development of this tool involves multiple stages: creating ontologies for each process reference model, integrating them into the tool, enabling querying capabilities, and visualizing the ontologies. Through a validation study in a selected organization, two sets of processes were assessed using the Ontology-Based Software Process Assessment Tool (OSPAT). The results demonstrated that organizations can benefit from OSPAT in evaluating their software development processes across diverse reference models, thereby enhancing overall process efficiency and quality.

Cite

Coşkunçay, A., & Başkara, R. (2023). Enhancing Software Process Assessment with an Ontology-Based Tool: Integrating CMMI, SPICE, and TMMI Models. *GU J Sci, Part A*, *10*(4), 542-554. doi:10.54287/gujsa.1384048

Author ID (ORCID Number)

0009-0007-5408-208X Rukiye BAŞKARA
0000-0002-7411-310X Ahmet COŞKUNÇAY

Article Process

Submission Date 31.10.2023
Revision Date 06.12.2023
Accepted Date 26.12.2023
Published Date 31.12.2023

1. INTRODUCTION

Software organizations have long relied on software process reference models like CMMI and SPICE to assess their existing processes. Through process assessment, institutions gain valuable insights into the strengths, weaknesses, and potential gaps in their software process implementations (15504, 2003). Furthermore, process reference models enable organizations to gauge the competence and maturity of their processes. By evaluating software project processes using internationally recognized frameworks, organizations can identify and address process shortcomings.

Failure to improve processes based on process assessments using reference models can lead to challenges in delivering software projects to customers as planned, with expected quality. In such cases, organizations may struggle to measure project efficiency, identify deficiencies, and monitor process compliance across multiple reference models, making it more difficult to understand deviations between them (Gazel et al., 2009). To streamline the assessment process with different models, there is a pressing need for an intuitive and comprehensive assessment tool.

The advent of the semantic web has empowered machines to comprehend the meaning of data and address associated problems using well-defined ontologies (Türkyılmaz & Yaşar, 2008). Ontologies present

*Corresponding Author, e-mail: rukiye.baskara@yildiz.edu.tr

promising solutions for computer-aided software process assessment (Feloni & Braga, 2015). As they are expressed in machine-understandable language, ontologies facilitate the identification and maintenance of mappings between process reference models and an organization's processes (Mora et al., 2010). Utilizing existing ontologies from the literature saves researchers time compared to creating ontologies from scratch.

However, despite some preliminary studies on CMMI, SPICE, and TMMI models, no tools in the literature support both ontology-based modeling and these specific process reference models. The primary goal of this article is to develop a comprehensive tool that facilitates the overall process assessment of organizations by unifying the CMMI, SPICE, and TMMI models into a common ontology. The use of a shared ontology allows for easy comparison of assessment results obtained from different models within the same organization. The ontologies created in this research will serve as a valuable resource for professionals in the field of software process assessment, aiding in understanding the models, identifying relationships between concepts, and discerning similarities and differences among the models. Besides these, other main contributions of the paper are to focus on the ability of the developed tool to support different process reference models by providing flexibility to organizations and to make process evaluations more effective by facilitating data access and increasing information sharing using semantic web technologies.

1.1. Literature Review

The results of assessments with software process reference models can be extensive and complex. In a study, they contributed to the development of 5 different software companies by measuring the CMMI maturity levels quickly and easily through a survey (Yucalar & Erdoğan, 2009). However, it was mentioned that this survey study is not suitable for large-scale companies. They also said that it does not claim to replace an official CMMI assessment. Therefore, there is a need to develop more reliable and effective methods or tools that measure the maturity levels of companies. In another study, the WMSC model for project management knowledge domains was presented, but it was found that there was a need to develop a generalizable expert system that would provide real-time dynamic solutions for maturity assessment (Göçmen, 2021). In addition, one study analysed the Smart Grid Maturity Model (SGMM), which is proposed as a maturity model in the field of smart grid. After the use of the SGMM, it has been revealed that there is a need for a model where practices are specialised according to the roles in the sector, can change according to different market structures, has clear scoring and criteria, can be easily used by everyone and has different maturity levels (İlisulu et al., 2020).

In addition to this, Due to the large number of process improvement models, observation, modification and validation of the models are time consuming and error prone. Therefore, although the SPI-CMMI ontology in the literature has many benefits for this purpose, it has been revealed that it needs to be further developed in terms of functions (Zaied et al., 2021). The need for tool support may be necessary to simplify, comprehend and analyze the results (Hunter et al., 1997). Such tools allow software development organizations to evaluate project processes quickly and accurately. A computer-assisted assessment tool is more cost-effective, easier to change and update, and can be used without requiring external consultants (Soydan & Kokar, 2006). Tools such as these are meant to help institutions reduce the costs associated with assessment and increase the reliability of assessment reports. As part of the process assessment, software tools were used to support the data collection phase and to monitor compliance with the software processes of the institutions (Gazel et al., 2012). Process assessment tools that support a single model are rarely sufficient to meet the needs of many organizations. By using tools that evaluate using different models, the results of the assessment can be compared. To put it another way, institutions may want to determine how they compare to different models by evaluating their processes against different process models. A software process assessment tool with diverse features should also enable the definition of a new model with a comprehensive meta-model (Yürüm, 2014). In one study, CMMI_Dev version 3.1 and PMBOK presented an ontological approach to represent, guide and analyse knowledge (Silega et al., 2023). However, they mentioned that there is a need to extend the ontology to represent the knowledge of various standards and to identify common concepts between different standards. They stated that the new methodology created by combining TMMI and PRISMA methodologies will increase the efficiency and effectiveness of the testing process in terms of time and budget (Aktaş et al., 2021).

The fact that most of the tools in the literature are non-ontology-based software process assessment tools indicates a deficiency in this area. Because, if making process assessments using an ontology-based tool is compared with doing it manually, assessments can be made in a shorter time with an ontology-based tool (Athiththan et al., 2018). In one study, they examined whether the ontological approach used significantly reduced the analysis time and found that the analysis of code defects with the ontological-based approach was 10 times faster than other methods (Castellano et al., 2023). By using ontology, the information about software development standards is represented. However, in order to increase its benefits, there is a need to represent more than one standard on this ontology and to define common concepts between different standards (Silega et al., 2023). In addition, since ontologies have computer-executable semantics, inferences can be made about the maturity level of models of companies based on some data provided by the institution (Soydan & Kokar, 2006). Among the related studies, the Ontology-based CMMI Mapping and Query Tool (OCMQT) is a software process assessment tool developed to support the data collection phase of process assessment and to observe its compliance with the CMMI model and is an add-on to an open-source EPF-based process management tool (Gazel et al., 2012). This tool supports the need to search for process definitions and CMMI-related information. However, the OCMQT tool is not capable of making inferences about the assessment rating. GSPA, on the other hand, is a meta-model process assessment tool created using class diagrams to integrate the most widely used process reference models, CMMI and ISO 15504, into a single model. Although this tool supports process assessment with two models, it is not an ontology-based tool (Yürüm, 2014). In one of the studies on the use of ontologies in different fields in the literature, the ontology was used in a supply chain assessment application because it has the advantages of easy extensibility and fast querying between different databases. However, in this study, it is mentioned that there is a need to work on some more adaptive tools based on ontology-based knowledge representation in order to make a more user-friendly application, access accurate information, increase its efficiency and process knowledge in modifiable format (Zhang et al., 2022). In another study, the necessity of using ontologies to make the information about Agile applications easier to understand by non-experts and people without prior knowledge was mentioned. Thus, an ontology-based user-friendly simplification tool called OBAMA was developed (Kiv et al., 2022). When the current process assessment tool studies are examined, it is observed that no ontology-based tool provides assessment and comparison with three different models. In this article, an ontology-based software process assessment tool is proposed by combining three different models in a common ontology. They developed the Software Integration Model (SIM) by combining the CMMI, IMM and SOVRM models to help organizations evaluate and improve their activities related to software integration in global software development (Haider et al., 2023). However, it has been observed that there should be a tool that can perform various activities and produce different evaluation reports for organizations.

According to the literature, the use of ontologies in various fields has increased in recent years. However, in order to solve the semantic, visual and analysis problems faced by organizations in software process evaluation, the need for a support tool that can perform evaluation with various models using ontologies has emerged.

2. MATERIAL AND METHOD

CMMI, SPICE, and TMMI, which are widely used software process reference models that play a crucial role in software quality assurance, have been examined as suitable for use in the process assessment tool. Considering the similarities between the process descriptions and applications of these three models, it was appropriate to match the three models. Due to their common features, these three models share similar concepts. The first step was to create ontologies for the three models. Ontologies were created based on questions about their purpose, which questions they would answer, and who would use them. Ontologies will be able to address and provide answers to the questions some of which are listed below. Defining and limiting the scope of ontologies is achieved through these questions.

- What are the purposes of the SPICE, TMMI, and CMMI models?
- What are the scopes and constraints of SPICE, TMMI, and CMMI models?
- What risk factors do SPICE, TMMI, and CMMI carry?

- What practices do SPICE, TMMI, and CMMI include?
- What work products do SPICE, TMMI, and CMMI suggest?
- What are the assessment methods used by SPICE, TMMI, and CMMI models?
- What are the roles of SPICE, TMMI, and CMMI models?
- What maturity/capability levels do SPICE, TMMI, and CMMI include?
- What types of projects are SPICE, TMMI, and CMMI used for?
- What are the process and process areas of the SPICE, TMMI, and CMMI models? To what goals do these processes, concepts, and relationships belong?

Table 1 illustrates how concepts belonging to Process reference models are matched (Vanamali et al., 2008). Despite the different names of some concepts in this table, it has been observed that they have a similar meaning. Moreover, since the TMMI model is derived from the CMMI model, it was easy to match as they share the same concepts. A concept found only in the CMMI model called Continuous Capability is absent in the TMMI model.

Table 1. *Matching the Concepts of the Models*

CMMI	SPICE	TMMI
Process Area	Process	Process Area
Purpose	Process Purpose	Purpose
Specific Goal	Process Outcomes	Specific Goal
Specific Practice	Base Practices	Specific Practice
Subpractices	-	Subpractices
Typical Work Products	Output Work Products	Typical Work Products
-	Work Product Characteristics	-
Generic Goal	Process Attributes	Generic Goal
Generic Practice	Generic Practices	Generic Practice
Generic Practice Elaborations	-	Generic Practice Elaborations
-	Generic Resources	-
Examples	-	Examples
Amplifications	-	Amplifications
Continuous Capability	-	-
Staged Capability	-	Staged Capability
Capability Levels	Capability Levels	Capability Levels

After creating the ontology of the three models, the common classes, and relationships of the 3 models were taken into account while creating the common YGOM ontology. While matching ontology, it is given the importance that the concepts of the models have the same function. In light of these questions, classes, subclasses, and relations of the models were created. In Figure 1, the conceptual scheme of YGOM drawn in the Draw.io [1]program is given.

In this ontology in Figure 1, the various concepts and the relationships between them denote the YGOM. Here are the concepts and relationships in this schema: ContinuousRepresentation and StagedRepresentation: These refer to the maturity levels of an organization. ContinuousRepresentation presents a continuous

[1] Draw.io: https://app.diagrams.net

development model, while StagedRepresentation focuses on specific stages or levels. Representation: This is a meta-concept that combines the above two concepts into a general category. Level and MaturityLevel: These represent different aspects of an organization's process maturity. Level refers to a general level and MaturityLevel refers to a specific level in terms of maturity. Organization: This represents the organization being assessed or to which the model is applied. Projects: Indicates the projects the organization is working on. Assessment: This represents the process of assessing the organization's processes ProcessArea: Refers to the different process areas within the organization. CapabilityLevel: Indicates the capability or maturity level of a process area. AssessmentOutput: Represents the assessment result, which is usually an output related to the capability level of a process. Goal, SpecificGoal, and GenericGoal: These concepts refer to the general and specific goals that the organization aims to achieve. Practice: Represents the methods or practices applied to achieve specific goals. The different links between relations (e.g. "isA", "hasA", "ownedBy", "consistOf") show how these concepts are interconnected and how they contribute to each other. For example, an Organization can be seen to be owned by Projects, which in turn are composed of ProcessAreas, and these ProcessAreas are themselves related to Goals and Practices. In Table 2, the concepts of the three models and the relationships between them are defined with their meanings in the conceptual schemes.

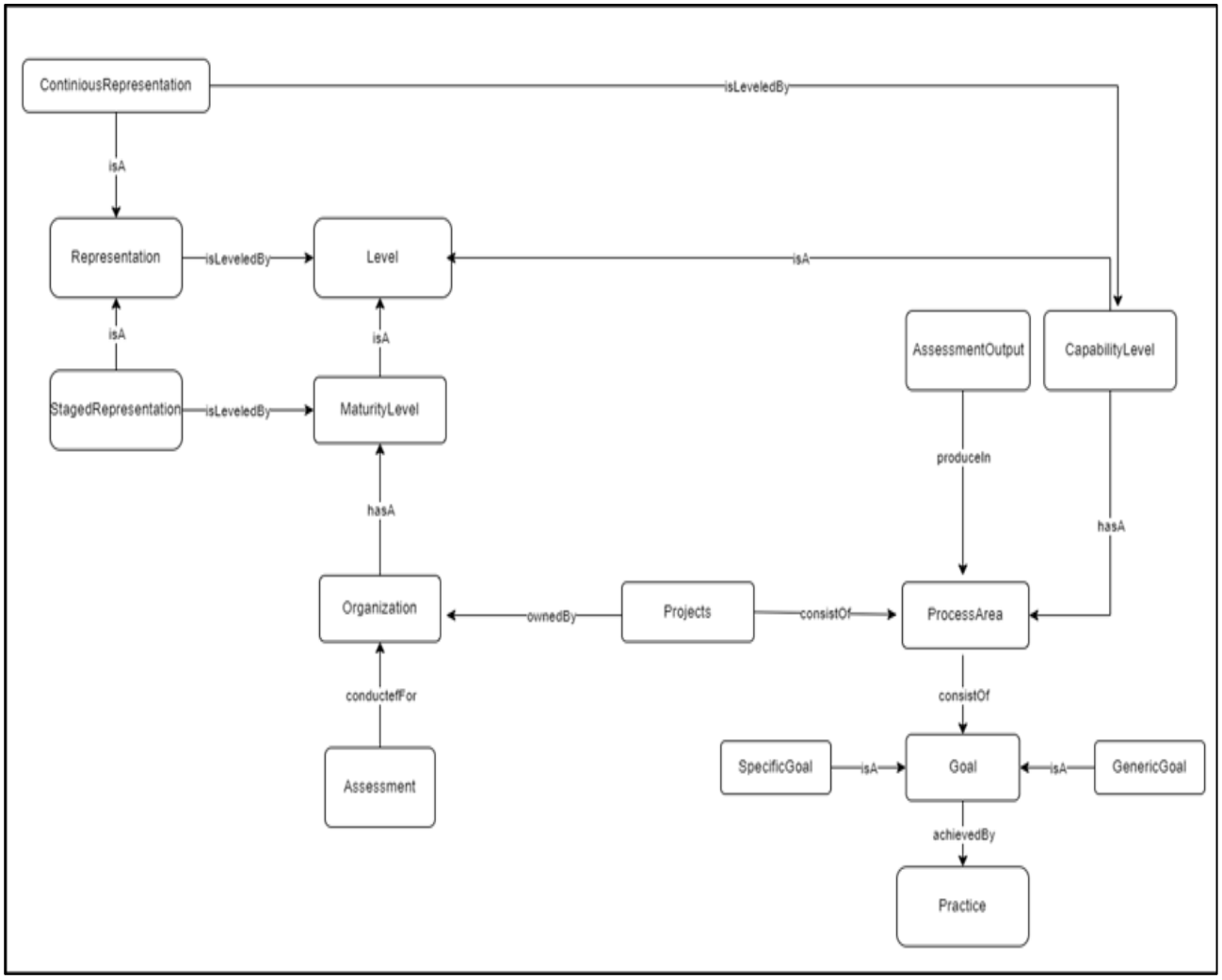

Figure 1. *YGOM Diagram*

Table 2. *Description of relationships in diagrams*

Relationships Between Concepts		**Example Relationships From Diagrams**
1	ownedBy	Organizations own the projects.
2	ConsistOf	Processes are included in projects.
3	ConductedFor	Assessments are made for organizations
4	isA	Generic practice is a Practice. It is used in superclass-subclass (Inheritance) relationships.
5	achievedBy	When all practices of a goal result in success, it is specified in the model it belongs to.
6	representedBy	Represented in the presentation from the process area
7	producedIn	Assessment output produced in the Process Area
8	isLeveledBy	Impressions rated by maturity level
9	satisfiedBy	Goals fulfilled by process areas
10	outputOf	Work products are the output of projects
11	developedBy	Progressive representation enhanced by Maturity Level
12	subClassOf	Process dimension is a subclass of Process.
13	fulfilledBy	Assessment Output produced in assessment
14	associatedWith	Work products associated with Process output
15	Uses	Generic resources are used by applications
16	hasLevel	Assessments have skill levels
17	sameAs	Artifacts are the same as work products

2.1. OSPAT (Ontology-Based Software Processes Assessment Tool)

2.1.1 Development of the Tool

Java was chosen as the programming language for the tool because it proved most suitable as several Java ontology libraries exist. Java is an open-source language with free libraries for developing semantic web applications, which has played a major role in its selection. The interface of the application was created using Java Swing, which is part of the Java AWT package and provides all the tools necessary to develop Graphical User Interfaces (GUIs) using Java. As the development platform, the open-source Eclipse[2] or Netbeans IDEs, which provide a Java-based application development environment, were suitable. Despite Netbeans' AWT and Swing graphical user interface support, the Eclipse environment has been preferred because it is more convenient to test the previously created frame codes. To integrate the ontology support, the Java framework Jena[3] Library was used. Jena was chosen because it provides full support for the JAVA language that we use in ontology-based development, because it can work in harmony with other components, and because it is an open source library for building Semantic Web applications. In this way, the information kept in the ontology was transferred to the Eclipse environment with the Jena Library. After the ontologies are loaded, SPARQL[4] , a standard rich query language similar to SQL, is used to access RDF files, that is, classes, properties, and individuals in ontologies through the interface. In Eclipse, Java codes were used to load the desired data from the imported ontology using SPARQL queries. These queries

[2] Eclipse: https://www.eclipse.org/
[3] Jena: https://jena.apache.org
[4] SPARQL: https://www.w3.org/TR/rdf-sparql-query/

transfer the information stored in the ontologies and present it over the interface. By using queries, information about process areas, applications, and work products can be retrieved from the OWL files of the models. The OWLGrEd[5] editor is used to visualize the ontologies. OWL files can be opened in this editor, providing the ability to visualize ontologies with OWLGrEd and distribute the formal information held in ontologies. The visualizer might make the tool easy to understand and easy to use, even for those who are "ontology illiterate".

2.1.2 Properties of the Tool

OSPAT supports assessments based on CMMI, SPICE, and TMMI models. The tool aims to ensure that the assessment results would be brought together in a common ontology. The ability to make process assessments with these different models contributes to the flexibility of the tool. OSPAT also can report different assessment results to the organizations by keeping and querying the assessment data. The fact that the tool is suitable for assessment across three models provides the opportunity to make comparisons by observing the assessment results of the three models. To compare the process assessments of the three models in the same organization, it is necessary to align the processes that have similar contexts whether they are named the same or not.

This ontology-based tool, which allows assessment with more than 25 process areas, contains the quality level of the organizations based on the processes assessed. This tool performs many functions such as entering grades that should be used during assessment for the models it supports, entering success percentages, and entering work products. In the interface of the tool, short explanations about the process areas in the CMMI, SPICE, and TMMI models and the practices in a process area are given for the convenience of the users. By using SPARQL, queried data is listed through the tool interface by using the ontologies, and a query function is added to the tool. With the queries information such as the process areas of the models, the applications of the process areas, and the work products of the applications are listed. For the sake of completeness, the concepts added through the interface are added to the OWL files connected with other concepts. It is also possible to read the ontologies created with the Protégé through the interface. Another feature of this tool is that it keeps data safe so that we can reuse the results during assessment and reporting and make comparisons with subsequent assessments. It is reliable in its ability to store assessments permanently. Finally, this tool has a simple and visual user interface to allow assessment by non-expert users. For process assessment tools quality and efficiency are important aspects (Lok & Walker, 1997). OSPAT is designed by conforming to Lok and Walker's (1997) quality characteristics.

2.1.3 Validation of the Tool

After the development of OSPAT, validation of it was carried out at a state university. This university has been found suitable for software process assessment-based validation due to the size of the software projects it has. An Ethics Committee approval was obtained to carry out the study. The university has an understanding of quality based on continuous improvement but has not yet documented itself with international standards or models in terms of its software development processes. First, a preliminary interview was held about the processes included in the university's software projects. Two groups of processes were selected for assessment. For these selected groups of processes, the common process areas of the three models are shown in Table 3. For matching the models and their processes, we referred to Vanamali et al.'s (2008) work. Software Requirements Analysis and Requirements Management processes do not have a corresponding process in the TMMI model, so no requirements related assessment is planned for TMMI as the blank cell in Table 3 indicates.

A software project was selected to make the assessment. Interviews were made with the System Analyst who worked on the selected project. First, demographic questions were asked in these interviews to gather information about the organization and the analyst participating in the assessment. After the demographic questions during the interview, questions about five selected process areas were asked and so the process

[5] OWLGrEd: http://owlgred.lumii.lv/

assessment started. These questions are the regular assessment questions on the processes of the selected models (Kalaycı, 2007).

During the assessment, notes regarding the processes in the project were taken. Data such as the strengths and weaknesses of the application were entered into the tool by making inferences from the answers given to the application questions related to the selected process areas during the interview. The work product information is also added. After entering data, process achievements were evaluated. In Figure 2, the interface for process achievement evaluation, and work products belonging to the Software Requirements Analysis process, which is one of the SPICE process reference model processes, is given.

Figure 3 shows the interface where the assessment data can be added to the OWL file and the previously added assessment can be deleted after the information is entered regarding the Software Requirements Analysis Process during the assessment.

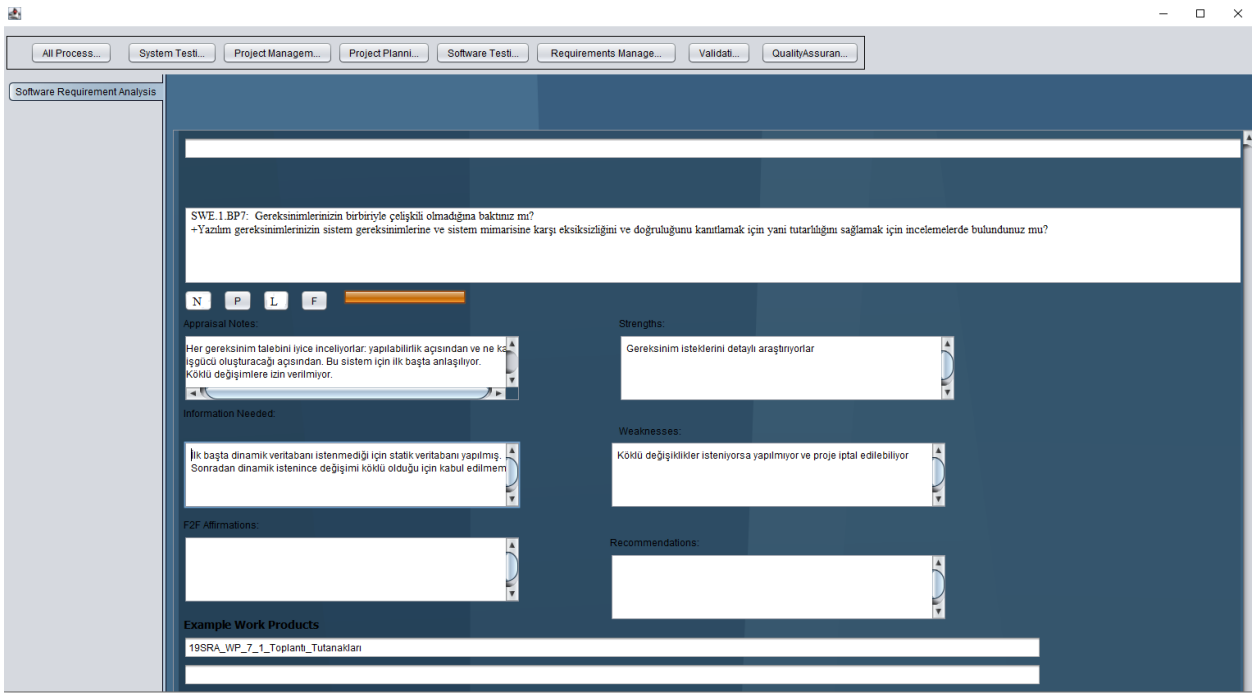

Figure 2. *The Interface for Assessing the Software Requirements Analysis Process*

Table 3. *The Matching Processes of the Models*

Groups Of Processes	**SPICE**	**CMMI**	**TMMI**
1st group of processes	Project Management	Project Planning	Test Planning
2nd group of processes	Software Requirements Analysis	Requirements Management	-

Using this interface, individuals and features can be added by entering data to the OWL file. The achievement rate of the Software Requirements Analysis process was 75%. The name of the assessment made in the university (i.e. Organization1) is Assessment1 and the name of the evaluated project is entered as Project1. The process work products were added as individuals through the interface. The achievement rate of the Requirements Management process is 70%. Based on the 1st group of process assessment, there is a 5% difference between the Requirements Management Process of the CMMI model and the Software Requirements Analysis Process of the SPICE model. This data shows that the assessment results of the two models are close to each other. According to the process reference models, both process areas of Organization1 achieve a good achievement rate. As a result of this assessment, the organization's process competence in the requirements management process is rated.

After the data added through the interface of the Software Requirements Analysis process is transferred to the OWL file, the work products and success percentage are displayed in Protégé as in Figure 5.

With the assessment of the processes in the 2nd group, the achievement rate of the Project Planning process was 76%. The achievement rate of the Project Management process was 78%. When the assessment of the Project Planning of the CMMI model and the Project Management process of the SPICE model are compared, there is a 2% difference between the two processes. This shows that the assessment results of the two models are very close to each other. Furthermore, both process areas of Organization1 achieve high achievement percentages based on the process reference models. The practices are applied sufficiently in these processes. Test planning, however, is assessed in the TMMI model with a 42% achievement rate. This low score shows that this organization has deficiencies in its practices in the Test Planning process area and that there is a need for improvement. The results of the achievement rates resulting from the validations are shown in Figure 4 for better comparison.

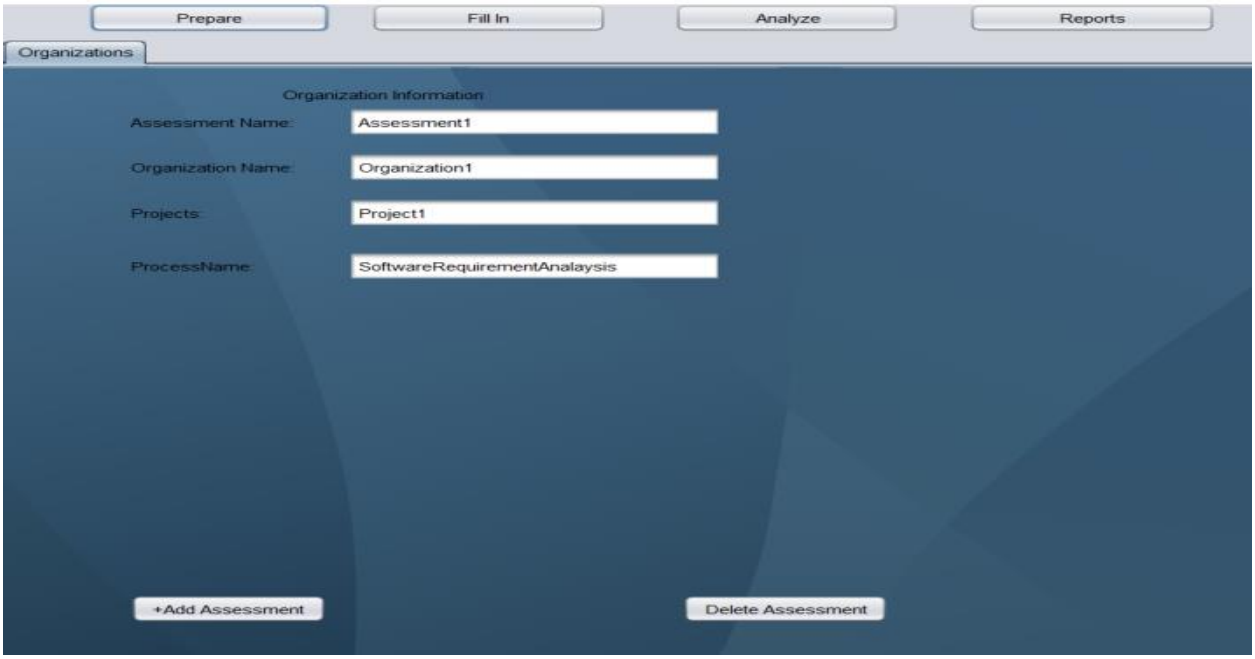

Figure 3. *The interface for entering and updating the assessment data kept in the ontology*

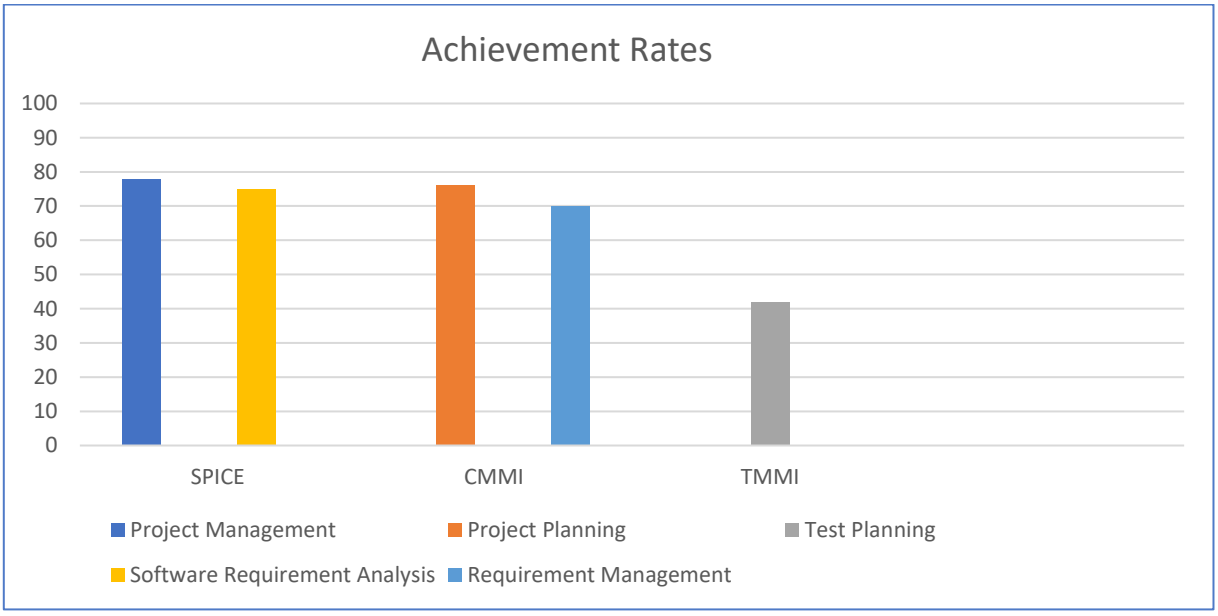

Figure 4. *Achievement Rates of Validation Results*

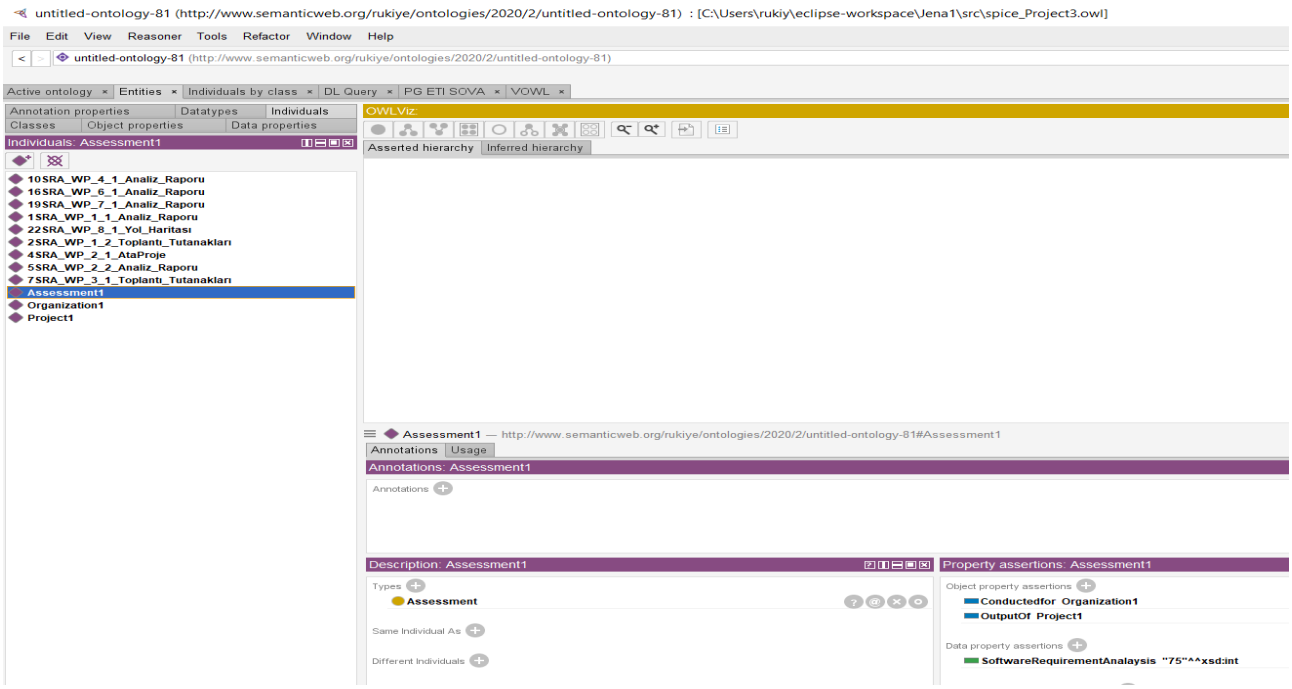

Figure 5. *Display of individuals added to the OWL file in the Protégé editor of the Software Requirements Analysis process after assessment*

Finally, with the OWLGrEd editor used, users are provided with the features to visualize the classes, properties, and individuals of the selected ontologies. The visualization is provided for CMMI, SPICE, TMMI, and YGOM ontologies and their instances associated with the assessments. In this way, instead of examining the complex and long OWL file, it is possible to see the entire ontology at once with the visualization editor, which is easy to understand and use even for those who are not "ontology literate". OWLGrEd provides visualizations that are similar to UML Class Diagrams by displaying OWL classes as UML classes, data properties as class attributes, object properties as associations, and individuals as objects.

For the objective evaluation of the interface of the OSPAT tool, an independent user was surveyed after performing a process evaluation. The questions in Table 4 were asked and answers were obtained (Charfi et al., 2015).

Table 4. *User Interface Survey Questions and Answers*

Number	User interface survey questions	Strongly agree	I agree	I don't know	Disagree	Strongly disagree
1	Did you realize what you wanted to do?		x			
2	Was the interface easy to use?	x				
3	Have you waited for something in the user interface and can't find it?				x	
4	Is the definition of each process area and application well defined?	x				
5	Did the tool guide you correctly in carrying out an action?		x			
6	Is it easy to read the content of the interface pages?	x				

3. RESULTS AND DISCUSSION

We have developed an advanced, ontology-based tool for general process assessment, combining three widely utilized models for evaluating software development processes within organizations. The integration of the model ontologies within the tool has resulted in a unified, common ontology, enabling seamless querying of assessment data and model information. Users benefit from a visual representation of the ontologies, facilitating comprehension, verification, and updates. Since ontologies are expressed in a formal, machine-intelligible, and shareable language (Gazel, 2009), the assessment information generated by the tool is equally precise and supported.

To validate the tool's effectiveness, a partial software process assessment was conducted using the three reference models to assess different groups of processes within a university project. The tool proves to be versatile, accommodating software process assessments across multiple reference models. Its ontology-based architecture ensures low effort requiring updates for incorporating new models or integrating changes into existing ones. During the evaluation process, the tool provided assessment results for each of the three process reference models, allowing the organization to compare its performance against each model individually. Additionally, by supporting assessments with multiple models, the tool facilitates comparisons of assessment results from different models within the same organization, enabling comprehensive process evaluation across various projects.

The OSPAT tool is designed for self-assessment purposes and, though comprehensive, lacks an automatic assessment feature. Nevertheless, it effectively fulfills its intended features, displaying a user-friendly design. However, there are opportunities for further enhancing its functionality. Notably, the tool presently lacks the ability to assess multiple processes simultaneously within a project. To overcome this limitation, introducing a parallel assessment capability would enable organizations with single or multiple assessment teams to evaluate multiple projects simultaneously. Such an improvement could significantly streamline and expedite the assessment process (Yürüm, 2014). Overall, the OSPAT tool demonstrates promising potential in aiding organizations with their process assessment needs and can be further refined to better accommodate complex project evaluations.

4. CONCLUSION

This paper presents the development of a new ontology-based software process evaluation tool called OSPAT. The tool offers the capability to perform evaluation based on three process reference models, and to validate the effectiveness of the tool, a partial software process evaluation was performed on a university software project, whose process achievement rates are shown in Figure 4. As an ontology-based tool, OSPAT was conceived in response to the lack of a process assessment support tools capable of incorporating various reference models with the ontology models it uses.

By leveraging OSPAT, users can retrieve queries results from the ontologies of three process reference models and conduct assessments in a unified manner. The tool's ability to display all three models on a single platform facilitates comparisons of assessments made on the same project with different models. In order to objectively evaluate the interface of the OSPAT tool, a survey was conducted on an independent real user. In line with the answers given, the usefulness of the tool was also verified. The visual representation of ontologies, including classes, subclasses, relations, properties and individuals, was facilitated using the OWLGrEd editor and helped to support the decision-making process for people using the tool by increasing clarity.

The tool demonstrated the possibility of integrating three models into a single ontology and highlighted similarities among the matched process areas. Moreover, it provided a glimpse into the potential of unifying diverse reference models within a shared ontology, promoting open-source accessibility and dissemination of valuable model information to interested experts.

Organizations can benefit from this tool as it facilitates the comparison of results from regular process assessments, enabling them to track their progress in software process assessments. Ultimately, OSPAT presents a promising advancement in ontology-based software process assessment, streamlining assessments

across multiple models and fostering a more efficient and insightful assessment process for software projects. Furthermore, the ontology used makes it easier to model complex relationships between software standards, process areas and other related concepts. This allows the tool to perform more comprehensive analyses and evaluate different aspects of projects in more depth. With this ontology, a flexible and extensible software evaluation tool has been developed. This means that the information in the tool can be updated when new concepts arise during the evaluation process.

5. FUTURE WORK

In this study, validation was conducted within a single organization, allowing for the evaluation of processes across different projects. However, due to time constraints, verifications on multiple projects were not feasible. To enhance the tool's validation, it is planned to extend assessments to multiple projects and involve diverse organizations. Additionally, the tool can be expanded by incorporating assessment features for other software process reference models beyond the three selected in this study.

Notably, the OSPAT tool is well-suited to support process assessments based on SPICE, CMMI, and TMMI as these reference models share similar concepts. In the current research, ontologies were developed based on the v1.3 version of the CMMI process reference model. However, to keep the tool up-to-date, future studies can integrate changes from the CMMI v2.0 version into the ontologies.

By extending validation efforts to multiple organizations and incorporating updates from newer versions of relevant process reference models, the OSPAT tool can continue to evolve and remain a valuable asset for efficient and comprehensive software process assessments across various projects and organizations.

CONFLICT OF INTEREST

The authors declare no conflict of interest.

REFERENCES

15504, A. I. I. (2003). Information Technology–Process Assessment.

Aktaş, A. Z., Yağdereli, E., & Serdaroğlu, D. (2021). An introduction to software testing methodologies. *Gazi University Journal of Science Part A: Engineering and Innovation*, *8*(1), 1-15.

Athiththan, K., Rovinsan, S., Sathveegan, S., Gunasekaran, N., Gunawardena, K. S., & Kasthurirathna, D. (2018, December). *An ontology-based approach to automate the software development process*. In: Proceedings of the 2018 IEEE International Conference on Information and Automation for Sustainability (ICIAFS) (pp. 1-6). IEEE.

Castellano, I. L., Aguilar, G. F. C., Silega, N., Kamal, T., Al-Gaashani, M., Samee, N. A., & Alabdulhafith, M. (2023). An Ontology-Based Approach to Reduce the Negative Impact of Code Smells in Software Development Projects. *IEEE Access*, *11*, 100146-100153 https://www.doi.org/10.1109/ACCESS.2023.3300575

Charfi, S., Ezzedine, H., & Kolski, C. (2015). RITA: a useR Interface evaluaTion frAmework. *Journal of Universal Computer Science*, *21*(4), 526-560.

Feloni, D., & Braga, R. T. V. (2015). Methodologies for Evaluation and Improvement of Software Processes in the Context of Quality and Maturity Models: a Systematic Mapping. In CIbSE (p. 123).

Gazel, S. (2009). *"CMMI-DEV" için bir ontoloji ve CMMI esaslı süreç değerlendirmenin ontoloji tabanlı bir araç ile desteklenmesi*. MSc Thesis, Hacettepe University.

Gazel, S., Sezer, E. A., & Tarhan, A. (2012). An ontology based infrastructure to support CMMI-based software process assessment. *Gazi University Journal of Science*, *25*(1), 155-164.

Gazel, S., Tarhan, A., & Sezer, E. (2009). A CMMI ontology for an ontology-based software process assessment tool, Proceedings of the 16th EuroSPI2 Conference.

Göçmen, E. (2021). A maturity model for assessing sustainable project management knowledge areas: A case study within a logistics firm. *Journal of Advanced Research in Natural and Applied Sciences*, *7*(4), 536-555.

Haider, W., Ilyas M., Khalid S., & Ali, S. (2023). Factors influencing sustainability aspects in crowdsourced software development: A systematic literature review. *Journal of Software: Evolution and Process*, e2630. https://www.doi.org/10.1002/smr.2630

Hunter, R., Robinson, G., & Woodman, I. (1997). Tool support for software process assessment and improvement. *Software Process: Improvement and Practice*, *3*(4), 213-223.

İlisulu, F., Kolukısa, A., & Kavak, K. (2020). Akıllı Şebeke Olgunluk Modelinin Dünya Çapındaki Uyarlamaları ve Türkiye için Öneriler. *Bilişim Teknolojileri Dergisi*, *13*(2), 123-136. https://www.doi.org/10.17671/gazibtd.533221

Kalaycı, O. (2007). Yöneticiler için Doğru Sorular CMMI. Shamrock Süreç İyileştirme ve Yenilikçilik, Kanada.

Kiv, S., Wautelet, Y., Heng, S., & Kolp, M. (2022). OBAMA, an Ontology-Based Software Tool for Agile Method Adoption. arXiv preprint arXiv:2206.02207.

Lok, R. H., & Walker, A. (1997). *Automated tool support for an emerging international software process assessment standard*. In: Proceedings of the IEEE International Symposium on Software Engineering Standards. IEEE, (pp. 25-35).

Mora, M., Cervantes-Pérez, F., Garrido, L., Wang, F., & Angel-Sicilia, M. (2010). On KM, KMS and ontology-based KMS in the domain of SwE standards and models of processes: A conceptual survey. *Intelligent Decision Technologies*, *4*(1), 75-98.

Silega, N., Castro Aguilar, G. F., Martillo Alcívar, I., Faggioni, K. M., Rogozov, Y. I. ,& Lapshin, V. S. (2023). An ontology-based approach to support the knowledge management of software quality standards. *Enfoque UTE*, *14*(3), 49-56. https://www.doi.org/10.29019/enfoqueute.946

Soydan, G. H., & Kokar, M. (2006). An OWL ontology for representing the CMMI-SW model, Workshop on Semantic Web Enabled Software Engineering (SWESE). Citeseer.

Türkyılmaz, İ., & Yaşar, C. (2008). Semantik web teknolojileri. Akademik Bilişim 2008.

Vanamali, B., Bella, F., & Hörmann, K. (2008). From CMMI to SPICE-Experiences on How to Survive a SPICE Assessment Having Already Implemented CMMI, 2008 32nd Annual IEEE International Computer Software and Applications Conference. IEEE, pp. 1045-1052.

Yucalar, F., & Erdoğan, Ş. Z. (2009). A questionnaire based method for CMMI level 2 maturity assessment. *Journal of Aeronautics and Space Technologies*, *4*(2), 39-46.

Yürüm, O. R. (2014). *GSPA: A generic software process assessment tool*. MSc Thesis, Middle East Technical University.

Zaied, A. N., H., Eldrandaly, K., & Tantawy, A. (2021). An OWL-Based Ontology Structure for representing Multimodel Process Improvement Framework. *Kafrelsheikh Journal of Information Sciences*, *2*(1), 1-11. https://doi.org/10.21608/kjis.2021.22087.1007

Zhang, L., Olsen, A., & Lobov, A. (2022). An ontology-based KBE application for supply chain sustainability assessment. *Resources, Environment and Sustainability*, *10*, 100086.

Research Article GU J Sci, Part A, 10(4): 555-570 (2023) 10.54287/gujsa.1386488

Gazi University
Journal of Science
PART A: ENGINEERING AND INNOVATION
http://dergipark.org.tr/gujsa

Kantorovich Stancu Type Operator Including Generalized Brenke Polynomials

Gürhan İÇÖZ[1] Shamsullah ZALAND[2*]

[1] Department of Mathematics, Faculty of Science, Gazi University, Ankara, Türkiye
[2] Graduate School of Natural and Applied Science, Gazi University, Ankara, Türkiye

Keywords

Stancu-Type Operators

Kantorovich Type of the Operators

Kantorovich Stancu Type Linear Positive Operators

Abstract

This article is concerned with the sequence of operators of Stancu's-type, involving extended Brenke polynomials. We apply Korovkin's theorem to the sequence of positive linear operators, discuss the uniform approximation of continuous functions on closed bounded intervals by known tools theory, and also consider the second modulus of continuity, Peetre's K-functional and Lipschitz class, which are essential concepts in approximation theory.

Cite

İçöz, G., & Zaland, S. (2023). Kantorovich Stancu Type Operator Including Generalized Brenke Polynomials. *GU J Sci, Part A*, *10*(4), 555-570. doi:10.54287/gujsa.1386488

Author ID (ORCID Number)

0000-0003-1204-9517 Gürhan İÇÖZ
0000-0002-7548-9483 Shamsullah ZALAND

Article Process

Submission Date 05.11.2023
Revision Date 25.12.2023
Accepted Date 27.12.2023
Published Date 31.12.2023

1. INTRODUCTION

The idea of approximating functions with polynomials is not only a fundamental aspect of mathematical analysis, but gives valuable mathematical instrument for a wide range of practical fields. The Weierstrass theorem asserts that any function f, is able to expressed using a polynomial series that is uniformly convergent on $[a, b]$. Bernstein provided definitive proof of the Weierstrass approximation theory using a probabilistic construction.

The following operators S_n are introduced and investigated by Szász and known as Szász Mirakjan operators. Agrawal et al. (2018) and Aktaş et al. (2013).

$$S_n(f;x) := e^{-nx} \sum_{k=0}^{\infty} \frac{(nx)^k}{k!} f\left(\frac{k}{n}\right) \tag{1.1}$$

Where $n \in N,\ x \geq 0$ and $f \in C[0,\infty)$ whenever the sum mentioned above convergence. These operators are generalizations of Bernstein polynomials to the infinite interval. Several authors have investigated and discussed some approximation properties of the S_n operators.

Varma and Sucu (2022) have given the operators, as follows, (Sucu & Varma, 2019).

$$W_n^*(f;x) = \frac{n}{A(1)\Upsilon(n^2x^2B(1) + nxC(1) + D(1))} \sum_{k=0}^{\infty} \phi_i(nx) \int_{\frac{k}{n}}^{\frac{k+1}{n}} f(\varphi)d\varphi,$$

*Corresponding Author, e-mail: shamszaland102@gmail.com

where

$$A(\vartheta)=\sum_{i=0}^{\infty}a_i t^i\ ,\quad B(\vartheta)=\sum_{i=0}^{\infty}b_i t^{i+1}\ ,\quad C(\vartheta)=\sum_{i=0}^{\infty}c_i t^{i+1}\ ,\quad D(\vartheta)=\sum_{i=0}^{\infty}d_i t^{i+3}\ ,\quad \Upsilon(\vartheta)=\sum_{i=0}^{\infty}\tau_i t^i$$

are analytic functions on the disc $|z|<\chi$, $\chi>1$. And $a_0\neq 0$, $c_0\neq 0$, $\tau_0\neq 0$. The polynomials ϕ_i are generated by following relation

$$A(1)\Upsilon\left(x^2B(1)+xC(1)+D(1)\right)=\sum_{k=0}^{\infty}\phi_i(x)t^i.$$

Under the assumption $p_k(x)\geq 0$ for $x\epsilon[0,\infty)$, the linear positive operators $P_n(f;x)$ are introduced by Jakimovski and Leviatan (1969), İçöz et al. (2016), Çekim et al. (2019) and Varma (2013).

$$P_n(f;x):=\frac{e^{-nx}}{g(1)}\sum_{k=0}^{\infty}p_k(nx)f\left(\frac{k}{n}\right), \tag{1.2}$$

where $p_k(x)$ is Appell polynomials and for $n\epsilon N$ and gave the approximation properties of these operators with the help of Szász's method.

The generating functions of the Brenke-type polynomials are as follow Chaggaraa and Gahami (2023) and Atakut and Büyükyazcı (2016).

$$A(t)B(t)=\sum_{k=0}^{\infty}p_k\,(x)t^k,$$

where $p_k(x)$ is Brenke polynomials, A and B are analytic functions by

$$A(t)=\sum_{k=0}^{\infty}a_k t^k\ ,\qquad a_0\neq 0\ ,$$

$$B(t)=\sum_{k=0}^{\infty}b_k\,t^k\ ,\quad b_0\neq 0\ (k\geq 0)\ .$$

The following linear positive operators are introduced by Varma et al. (2012) including the Brenke type polynomials (Cheney & Sharma, 1964).

$$\mathcal{L}_n(f;x):=\frac{1}{A(1)B(nx)}\sum_{k=0}^{\infty}p_k\,(nx)f\left(\frac{k}{n}\right), \tag{1.3}$$

where $x\geq 0$ and $n\epsilon\mathbb{N}$. Taking into consideration that

$$g(z)=\sum_{j=0}^{\infty}g_j z^j\qquad ,(g_0\neq 0)$$

the function g is analytic on the set $\{z:|z|<Q\ ,\ \ Q>1\}$, and also $g(1)\neq 0$. If polynomials π_k fulfill the subsequent relation

$$g(z)e^{ux}=\sum_{k=0}^{\infty}\pi_k(x)t^k,$$

then it is called Appell polynomials (İçöz & Çekim, 2015). The previously mentioned polynomials hold significant importance as special functions, finding diverse applications in engineering and mathematical analysis.

If $\pi_k(x)$ satisfies the following relation

$$\partial_1\big(g(t)\big)\partial_2\big(xg(t)\big) = \sum_{k=0}^{\infty} \pi_k(x)t^k, \tag{1.4}$$

then it is called generalized Brenke polynomials. İçöz & Çekim (2016a) and Rao et al. (2021), where ∂_1 , ∂_2 and h are functions that are analytic within the specified set

$$\{t: |t| < G\,, \quad G > 1\},$$

such that

$$\begin{aligned} \partial_1(t) &= \sum_{k=0}^{\infty} r_{1,k}t^k\,, \qquad (r_{1,0} \neq 0) \\ \partial_2(t) &= \sum_{k=0}^{\infty} r_{2,k}t^k\,, \qquad \big(r_{2,0} \neq 0\big) \\ h(t) &= \sum_{k=0}^{\infty} h(t)t^k\,, \qquad (h(1) \neq 0) \end{aligned} \tag{1.5}$$

under the following assumptions:

(i) $\partial_1(1) \neq 0, \dfrac{a_{k-\tau}b_\tau}{\partial(1)} \geq 0, \quad 0 \leq \tau \leq k, \quad k = 0,1,2,\ldots$

(ii) $B: [0,\infty) \longrightarrow (0,\infty)$

(iii) (1.6) and (1.7) converge for $|t| < G, (G > 1)$ where

$$\partial(t) = \sum_{\tau=0}^{\infty} r_\tau t^\tau\,, \qquad r_0 \neq 0 \tag{1.6}$$

$$B(t) = \sum_{\tau=0}^{\infty} b_\tau t^\tau\,, \qquad b_\tau \neq 0\ (\tau \geq 0) \tag{1.7}$$

are analytic functions, and the Kantorovich type of the operators. İçöz & Çekim (2016b), under the above assumptions, is defined as

$$K_n(f;x) \coloneqq \frac{n}{\partial(1)B(nx)} \sum_{k=0}^{\infty} p_k\,(nx) \int_{\frac{k}{n}}^{\frac{k+1}{n}} f(t)\,dt$$

where $n \in \mathbb{N}$, $x \geq 0$, $f \in C[0,\infty)$, and $p_k(x)$ is the Brenke type polynomials.

Sucu (2022) has given sequence of operators $\{L_n^{(\sigma_1,\sigma_2)}\}_{n\geq 1}$, $\sigma_1, \sigma_2 \geq 0$ as follows:

$$L_n^{(\sigma_1,\sigma_2)}(f;x) \coloneqq \frac{1}{\partial_1\big(g(1)\big)\partial_2\big(nxg(1)\big)} \sum_{k=0}^{\infty} \pi_k\,(nx) f\left(\frac{k+\sigma_1}{n+\sigma_2}\right), \tag{1.8}$$

$\pi_k(x)$ polynomials are given by (1.4), and also the polynomials $\pi_k(x)$ and function h satisfies these conditions $h'(1) = 1$, $\pi_k(x) \geq 0$.

Motivated by the above-mentioned works, we consider the Kantorovich Stancu type linear positive operators as follows:

$$L_m^{*(\sigma_1,\sigma_2)}(f;x) \coloneqq \frac{m+\sigma_2}{\partial_1\big(g(1)\big)\partial_2\big(mxg(1)\big)} \sum_{k=0}^{\infty} \pi_k\,(mx) \int_{\frac{k+\sigma_1}{m+\sigma_2}}^{\frac{k+\sigma_1+1}{m+\sigma_2}} f(\varphi)d\varphi. \tag{1.9}$$

Where $f \epsilon C[0,\infty)$ and $x \epsilon [0,\infty)$.

Here, we assume that

(i) $\partial_1, \partial_2: \mathbb{R} \longrightarrow (0,\infty)$

(ii) (1.4) and (1.5) converge for $|t| < G, (G > 1)$.

This article focuses on the operators of Stancu-type, containing extended Brenke polynomials. the secound part provides, some results which are essential for $L_m^{*(\sigma_1,\sigma_2)}$ and in the third section, we employ Korovkin theorem, we are discussing and considering the second modulus of continuity, Peetre's K- functional in the continuous functions space and Lipschitz class, which are fundamental concepts in approximation theory.

2. SOME RESULTS OF THE OPERATORS $L_m^{*(\sigma_1,\sigma_2)}$

Before that, to apply the Korovkin-type theorem to the sequence of operators $\{L_m^{*(\sigma_1,\sigma_2)}\}_{m\geq 1}$ we need to have some essential lemmas.

Lemma 2.1. If π_k is polynomials fulfilling the equality (1.4), then

$$(i)\quad \sum_{k=0}^{\infty}\pi_k(mx)=\partial_1\big(g(1)\big)\partial_2\big(mxg(1)\big)$$

$$(ii)\quad \sum_{k=0}^{\infty}k\pi_k(mx)=\partial'_1\big(g(1)\big)\partial_2\big(mxg(1)\big)+mx\partial_1\big(g(1)\big)\partial'_2\big(mxg(1)\big)$$

$$(iii)\quad \sum_{k=0}^{\infty}k^2\pi_k(mx)=\big[(g''(x)+1)\partial'_1\big(g(1)\big)+\partial''_1\big(g(1)\big)\big]\partial_2\big(mxg(1)\big)$$
$$+\big[2\partial'_1\big(g(1)\big)+(g''(1)+1)\partial_1\big(g(1)\big)\big]\partial'_2\big(mxg(1)\big)mx$$
$$+\partial_1(g(1))\partial''_2\big(mxg(1)\big)(mx)^2$$

Proof. Using the relation given by(1.4), we have

$$\partial_1\big(g(t)\big)\partial_2\big(mxg(t)\big)=\sum_{k=0}^{\infty}\pi_k(mx)t^k.$$

For $t=1$ we have

$$\partial_1\big(g(1)\big)\partial_2\big(xmg(1)\big)=\sum_{k=0}^{\infty}\pi_k(mx).$$

From the relation $\sum_{k=0}^{\infty}\pi_k(mx)t^k=\partial_1\big(g(t)\big)\partial_2\big(mxg(t)\big)$, we take the derivative from the both side of equality and get

$$\sum_{k=0}^{\infty}k\pi_k(mx)t^{k-1}=g'(t)\partial'_1\big(g(t)\big)\partial_2\big(mxg(t)\big)+mxg(t)\partial_1\big(g(t)\big)\partial'_2\big(mxg(t)\big).$$

If $t=1$and $g'(1)=1$, then we obtain

$$\sum_{k=0}^{\infty}k\pi_k(mx)=\partial_2\big(mxg(1)\big)\partial'_1\big(g(1)\big)+mx\partial_1\big(g(1)\big)\partial'_2\big(mxg(1)\big).$$

As we know

$$\sum_{k=0}^{\infty}k\pi_k(mx)t^{k-1}=g'(t)\partial'_1\big(g(t)\big)\partial_2\big(mxg(t)\big)+mxg'(t)\partial_1\big(g(t)\big)\partial'_2\big(mxg(t)\big),$$

then we have

$$\sum_{k=0}^{\infty} k(k-1)\pi_k(mx)t^{k-2} = \partial''_1(g(t))g'(t)\partial_2(mxg(t)) + \partial'_1(g(t))g''(t)\partial_2(mxg(t))$$
$$+\partial'_1(g(t))g'(t)mxg'(t)\partial'_2(mxg(t)) + mxg''(t)\partial_1(g(t))\partial'_2(mxg(t))$$
$$+mxg'(t)g'(t)\partial'_1(g(t))\partial'_2(mxg(t))$$
$$+(mx)^2g'(t)\partial_1(g(t))g'(t)\partial''_2(mxg(t)).$$

If $t = 1$and $g'(1) = t$, then we acquire

$$\sum_{k=0}^{\infty} k^2\pi_k(mx) - \sum_{k=0}^{\infty} k\pi_k(mx) = \partial''_1(g(1))\partial_2(mxg(1)) + \partial'_1(g(1))g''(1)\partial_2(mxg(1))$$
$$+mx\partial'_1(g(1))\partial'_2(mxg(1)) + mxg''(1)\partial_1(g(1))\partial'_2(mxg(1))$$
$$+mx\partial'_1(g(t))\partial'_2(mxg(1)) + (mx)^2\partial_1(g(1))\partial''_2(mxg(1)).$$

So, we win

$$\sum_{k=0}^{\infty} k^2\pi_k(mx) = \partial''_1(g(1))\partial_2(mxg(1)) + \partial'_1(g(1))h''(1)\partial_2(mxg(1))$$
$$+mx\partial'_1(g(1))\partial'_2(mxg(1)) + mxg''(1)\partial_1(g(1))\partial'_2(mxg(1))$$
$$+mx\partial'_1(g(t))\partial'_2(mxg(1)) + (mx)^2\partial_1(g(1))\partial''_2(mxg(1)) + \sum_{k=0}^{\infty} k\pi_k(mx)$$

$$\sum_{k=0}^{\infty} k^2\pi_k(mx) = \partial_2(mxg(1))\partial''_1(g(1)) + g''(1)\partial'_1(g(1))\partial_2(mxg(1))$$
$$+mx\partial'_1(g(1))\partial'_2(mxg(1)) + mxg''(1)\partial_1(g(1))\partial'_2(mxg(1))$$
$$+mx\partial'_1(g(t))\partial'_2(mxg(1)) + (mx)^2\partial_1(g(1))\partial''_2(mxg(1))$$
$$+\partial'_1(g(1))\partial_2(mxg(1)) + mx\partial_1(g(1))\partial'_2(mxg(1))$$
$$= [\partial'_1(g(1))(g''(1)+1) + \partial''_1(g(1))]\partial_2(mxg(1))$$
$$+[2\partial'_1(g(1)) + \partial_1(g(1))(g''(1)+1)]\partial'_2(mxg(1))mx$$
$$+\partial_1(g(1))\partial''_2(mxg(1))(mx)^2.$$

Lemma 2.2. For $m \geq 1$ we notch-up the following identities:

(i) $L_m^{*(\sigma_1,\sigma_2)}(1;x) = 1,$

(ii) $L_m^{*(\sigma_1,\sigma_2)}(s;x) = \frac{1}{m+\sigma_2}\left(\frac{m\partial'_2(mxg(1))}{\partial_2(mxg(1))}x + \frac{\partial'_1(g(1))}{\partial_1(g(1))} + \frac{2v_1+1}{2}\right),$

(iii) $L_m^{*(\sigma_1,\sigma_2)}(s^2;x) = \frac{1}{(m+\sigma_2)^2}\left\{\frac{m^2\partial''_2(mxg(1))}{\partial_2(mxg(1))}x^2\right.$

$$+\left(\frac{mg'_2(mxg(1))\left[\partial'_1(g(1))+(g''(1)+1)\partial_1(d(1))\right]}{\partial_1(g(1))\partial_2(mxg(1))}\right)x$$
$$+\frac{(g''(1)+1)\partial'_1(g(1))+\partial''_1(g(1))+(2\sigma_1+1)\partial'_1(g(1))}{\partial_1(g(1))}+\frac{3\sigma_1^2+3\sigma_1+1}{3}\Bigg\}.$$

Proof. Using the operator given by (1.9), we have

$$L_m^{*(\sigma_1,\sigma_2)}(1;x)=\frac{m+\sigma_2}{\partial_1(g(1))\partial_2(mxg(1))}\sum_{k=0}^{\infty}\pi_k(mx)\int_{\frac{k+\sigma_1}{m+\sigma_2}}^{\frac{k+\sigma_1+1}{m+\sigma_2}}d\varphi$$
$$=\frac{m+\sigma_2}{\partial_1(g(1))\partial_2(mxg(1))}\sum_{k=0}^{\infty}\pi_k(mx)\left(\varphi\Big|_{\frac{k+\sigma_1}{m+\sigma_2}}^{\frac{k+\nu_1+1}{m+\sigma_2}}\right)$$
$$=\frac{m+\sigma_2}{\partial_1(g(1))\partial_2(mxg(1))}\sum_{k=0}^{\infty}\pi_k(mx)\frac{1}{m+\sigma_2}.$$

As we know from Lemma 2.1.

$$\partial_1(g(1))\partial_2(mxg(1))=\sum_{k=0}^{\infty}\pi_k(mx),$$

then we attain

$$L_m^{*(\nu_1,\nu_2)}(1;x)=1.$$

Using the operator (1.9), we get.

$$L_m^{*(\sigma_1,\sigma_2)}(s;x)=\frac{m+\sigma_2}{\partial_1(g(1))\partial_2(mxg(1))}\sum_{k=0}^{\infty}\pi_k(mx)\int_{\frac{k+\sigma_1}{m+\sigma_2}}^{\frac{k+\sigma_1+1}{m+\sigma_2}}\varphi\,d\varphi$$
$$=\frac{m+\sigma_2}{\partial_1(g(1))\partial_2(mxg(1))}\sum_{k=0}^{\infty}\pi_k(mx)\frac{1}{2}\left(\varphi^2\Big|_{\frac{k+\sigma_1}{m+\sigma_2}}^{\frac{k+\nu_1+1}{m+\nu_2}}\right)$$
$$=\frac{m+\sigma_2}{\partial_1(g(1))\partial_2(mxg(1))}\sum_{k=0}^{\infty}\pi_k(mx)\left\{\frac{k}{(m+\sigma_2)^2}+\frac{2\sigma_1+1}{2(m+\sigma_2)^2}\right\}$$
$$=\frac{m+\sigma_2}{\partial_1(g(1))\partial_2(mxg(1))}\left\{\sum_{k=0}^{\infty}\pi_k(mx)\frac{k}{(m+\sigma_2)^2}+\sum_{k=0}^{\infty}\pi_k(mx)\frac{2\sigma_1+1}{2(m+\sigma_2)^2}\right\}$$
$$=\frac{m+\sigma_2}{\partial_1(g(1))\partial_2(mxg(1))}\left\{\frac{1}{(m+\sigma_2)^2}\sum_{k=0}^{\infty}k\pi_k(mx)+\frac{2\nu_1+1}{2(m+\nu_2)^2}\sum_{k=0}^{\infty}\pi_k(mx)\right\}$$

$$=\frac{1}{\partial_1(g(1))\partial_2(mx(1))}\left\{\frac{1}{m+\sigma_2}\left(\partial'_1(h(1))\partial_2(mxh(1))+mx\partial'_1(g(1))\,\partial'_2(mxg(1))\right)\right.$$
$$\left.+\frac{2\sigma_1+1}{2(m+\sigma_2)}\partial_1(g(1))\partial_2(mxhg)\right\}$$

$$= \frac{\partial'_1(\mathcal{g}(1))}{\partial_1(\mathcal{g}(1))(m+\sigma_2)} + \frac{m\partial'_2(mx\mathcal{g}(1))}{\partial_2(mx\mathcal{g}(1))(m+\sigma_2)}x + \frac{2\sigma_1+1}{2(m+\sigma_2)}$$

$$= \frac{1}{m+\sigma_2}\left(\frac{\partial'_1(\mathcal{g}(1))}{\partial_1(\mathcal{g}(1))} + \frac{m\partial'_2(mx\mathcal{g}(1))}{\partial_2(mx\mathcal{g}(1))}x + \frac{2\sigma_1+1}{2}\right).$$

From (1.9), we come by

$$L_m^{*(\sigma_1,\sigma_2)}(s^2;x) = \frac{m+\sigma_2}{\partial_1(\mathcal{g}(1))\partial_2(mx\mathcal{g}(1))}\sum_{k=0}^{\infty}\pi_k(mx)\int_{\frac{k+\sigma_1}{m+\sigma_2}}^{\frac{k+\sigma_1+1}{m+\sigma_2}}\varphi^2\,d\varphi$$

$$= \frac{m+\sigma_2}{\partial_1(\mathcal{g}(1))\partial_2(mx\mathcal{g}(1))}\sum_{k=0}^{\infty}\pi_k(mx)\frac{1}{3}\left(\varphi^3\Big|_{\frac{k+\sigma_1}{m+\sigma_2}}^{\frac{k+\sigma_1+1}{m+\sigma_2}}\right)$$

$$= \frac{m+\sigma_2}{\partial_1(\mathcal{g}(1))\partial_2(mx\mathcal{g}(1))}\sum_{k=0}^{\infty}\pi_k(mx)\left\{\frac{k^2}{(m+\sigma_2)^3} + \frac{k(2\sigma_1+1)}{(m+\sigma_2)^3} + \frac{3\sigma_1^2+3\sigma_1+1}{3(m+\sigma_2)^3}\right\}$$

$$= \frac{1}{\partial_1(h(1))\partial_2(mxh(1))}\left\{\frac{1}{(m+\sigma_2)^2}\sum_{k=0}^{\infty}k^2\pi_k(mx) + \frac{2\sigma_1+1}{(m+\sigma_2)^2}\sum_{k=0}^{\infty}k\pi_k(mx) + \frac{3\sigma_1^2+3\sigma_1+1}{3(m+\sigma_2)^2}\sum_{k=0}^{\infty}\pi_k(mx)\right\}$$

If we put the values from the Lemma 2.1 in the last equality, then we get

$$L_m^{*(\sigma_1,\sigma_2)}(s^2;x) = \frac{1}{(m+\sigma_2)^2}\left\{\frac{m^2\partial''_2(mx\mathcal{g}(1))}{\partial_2(mxh(1))}x^2 + \left(\frac{m\partial''_2(mx\mathcal{g}(1))\left[\partial'_1(\mathcal{g}(1)) + (\mathcal{g}''(1)+1)\partial_1(\mathcal{g}(1))\right]}{\partial_1(\mathcal{g}(1))\partial_2(mx\mathcal{g}(1))} + \frac{m(2\sigma_1+1)\partial'_2(mx\mathcal{g}(1))}{\partial_2(mx\mathcal{g}(1))}\right)x + \frac{(\mathcal{g}''(1)+1)\partial'_1(\mathcal{g}(1)) + \partial''_1(\mathcal{g}(1)) + (2\sigma_1+1)\partial'_1(\mathcal{g}(1))}{\partial_1(\mathcal{g}(1))} + \frac{3\sigma_1^2+3\sigma_1+1}{3}\right\}.$$

Lemma 2.3. Let $L_m^{*(v_1,v_2)}$ be operators which are defined by (1.9), then it follows that:

$$(i)\quad L_m^{*(\sigma_1,\sigma_2)}(s-x;x) = \frac{1}{m+\sigma_2}\left\{\left(\frac{m\partial'_2(mx\mathcal{g}(1))}{\partial_2(mx\mathcal{g}(1))} - (m+\sigma_2)\right)x + \frac{\partial'_1(\mathcal{g}(1))}{\partial_1(\mathcal{g}(1))} + \frac{2\sigma_1+1}{2}\right\}$$

$$(ii)\quad L_n^{*(\sigma_1,\sigma_2)}((s-x)^2;x) = \left(\frac{m^2\partial''_2(mx\mathcal{g}(1))}{\partial_2(mx\mathcal{g}(1))(m+\sigma_2)^2} - \frac{2m\partial'_2(mx\mathcal{g}(1))}{\partial_2(mx\mathcal{g}(1))(m+\sigma_2)} + 1\right)x^2 + \left(\frac{m\left[\partial'_1(\mathcal{g}(1)) + (\mathcal{g}''(1)+1)\partial''_2(mx\mathcal{g}(1))\right]}{\partial_1(\mathcal{g}(1))\partial_2(mx\mathcal{g}(1))(m+\sigma_2)^2} + \frac{m(2\sigma_1+1)\partial'_2(mx\mathcal{g}(1))}{(m+\sigma_2)^2\partial_2(mx\mathcal{g}(1))} - \frac{2\partial'_1(\mathcal{g}(1))}{(m+\sigma_2)\partial_1(\mathcal{g}(1))} - \frac{2\sigma_1+1}{m+\sigma_2}\right)x + \frac{(\mathcal{g}''(1)+1)\partial_1(\mathcal{g}(1)) + (\mathcal{g}''(1)+1)\partial''_1(\mathcal{g}(1)) + (2\sigma_1+1)\partial'_1(\mathcal{g}(1))}{(m+\sigma_2)^2\partial_1(\mathcal{g}(1))} + \frac{3\sigma_1^2+3\sigma_1+1}{3(m+\sigma_2)^2}.$$

Proof. According to the principle of linearity of $L_m^{*(\sigma_1,\sigma_2)}$ operators and applying Lemma 2.2

$$L_m^{*(\sigma_1,\sigma_2)}(s-x;x) = L_m^{*(\sigma_1,\sigma_2)}(s;x) - L_m^{*(\sigma_1,\sigma)}(x;x) = L_m^{*(\sigma_1,\sigma_2)}(s;x) - xL_m^{*(\sigma_1,\sigma_2)}(1;x)$$
$$= \left(\frac{m\partial'_2(mxg(1))}{\partial_2(mxh(1))}x + \frac{\partial'_1(g(1))}{\partial_1(h(1))} + \frac{2\sigma_1+1}{2}\right)\frac{1}{m+\sigma_2} - x$$
$$= \left(\frac{m\partial'_2(mxg(1))}{\partial_2(mxg(1))(m+\sigma_2)} - 1\right)x + \frac{1}{m+\sigma_2}\left(\frac{\partial'_1(g(1))}{\partial_1(g(1))} + \frac{2\sigma_1+1}{2}\right),$$

and

$$L_m^{*(\sigma_1,\sigma_2)}((s-x)^2;x) = L_m^{*(\sigma_1,\sigma_2)}(s^2 - 2sx + x^2;\ x)$$
$$= L_m^{*(\sigma_1,\sigma_2)}(s^2;x) - 2xL_m^{*(\sigma_1,\sigma_2)}(s;x) + x^2$$
$$= \frac{1}{(m+\sigma_2)^2}\left\{\frac{m^2\partial''_2(mxg(1))}{\partial_2(mxg(1))}x^2\right.$$
$$+\left(\frac{m[\partial'_1(g(1)) + (g''(1)+1)\partial_1(g(1))]\partial''_2(mxg(1))}{\partial_1(g(1))\partial_2(mxg(1))}\right.$$
$$\left.+\frac{m(2\sigma_1+1)\partial'_2(mxg(1))}{\partial_2(mxh(1))}\right)x$$
$$+\frac{(g''(1)+1)\partial'_1(g(1)) + \partial''_1(g(1)) + (2\sigma_1+1)\partial'_1(g(1))}{\partial_1(g(1))}$$
$$\left.+\frac{3\sigma_1^2+3\sigma_1+1}{3}\right\}$$
$$-\frac{2}{m+\sigma_2}\left(\frac{m\partial'_2(mxg(1))}{\partial_2(mxg(1))}x^2 + \frac{\partial'_1(g(1))}{\partial_1(g(1))}x + \frac{2\sigma_1+1}{2}x\right) + x^2$$
$$= \left(\frac{m^2\partial''_2(mxg(1))}{\partial_2(mxg(1))(m+\sigma_2)^2} - \frac{2m\partial'_2(mxg(1))}{\partial_2(mxg(1))(m+\sigma_2)} + 1\right)x^2$$
$$+\left(\frac{m[\partial'_1(g(1)) + (g''(1)+1)\partial''_2(mxg(1))]}{\partial_1(g(1))\partial_2(mxg(1))(m+\sigma_2)^2} + \frac{m(2\sigma_1+1)\partial'_2(mxg(1))}{(m+\sigma_2)^2\partial_2(mxg(1))}\right.$$
$$\left.-\frac{2\partial'_1(g(1))}{(m+\sigma_2)\partial_1(g(1))} - \frac{2\sigma_1+1}{m+\sigma_2}\right)x$$
$$+\frac{(g''(1)+1)\partial_1(g(1)) + (g''(1)+1)\partial''_1(g(1)) + (2v_1+1)\partial'_1(g(1))}{(m+\sigma_2)^2\partial_1(g(1))}$$
$$+\frac{3\sigma_1^2+3\sigma_1+1}{3(m+\sigma_2)^2}.$$

Now we define

$$M_{1,m}^{(\sigma_1,\sigma_2)} := L_m^{*(\sigma_1,\sigma_2)}(s-x;x)$$
$$M_{2,m}^{(\sigma_1,\sigma_2)} := L_m^{*(\sigma_1,\sigma_2)}((s-x)^2;x) \qquad (2.1)$$

Now we define $\tilde{C}[0,\infty)$ and $C_B[0,\infty)$ to represent the set of all uniformly continuous functions and bounded, continuous functions on $[0,\infty)$ respectively. With this we can now determine the arrange of approximation for the functions within the space $\tilde{C}[0,\infty) \cap E$ where

$$E = \left\{ f : \frac{f(x)}{1+x^2} \ is\ convergent\ as\ x \longrightarrow \infty \right\}.$$

Theorem 2.1. Let $f:[0,\infty) \longrightarrow \mathbb{R}$ be a continuous function which belongs to class E and

$$\lim_{y\to\infty} \frac{\partial'_2(y)}{\partial_2(y)} = 1 \quad and \quad \lim_{y\to\infty} \frac{\partial''_2(y)}{\partial_2(y)} = 1. \tag{2.2}$$

Then we see that

$$L_m^{*(\sigma_1,\sigma_2)}(f;x) \longrightarrow f(x)$$

uniformly as $m \longrightarrow \infty$ over every limited subset within the interval $[0,\infty)$.

Proof. Under the assumption of (2.2) and using Lemma 2.2 for $i = 0,1,2$, we acquire the subsequent equality

$$L_m^{*(\sigma_1,\sigma_2)}(s^i;x) \longrightarrow x^i$$

for $i = 0$ which is

$$L_m^{*(\sigma_1,\sigma_2)}(s^i;x) = L_m^{*(\sigma_1,\sigma_2)}(1;x) = 1.$$

So, we have

$$\lim_{m\to\infty} \left\{ L_m^{*(\sigma_1,\sigma_2)}(1;x) \right\} = 1.$$

For $i = 1$

$$L_m^{*(\sigma_1,\sigma_2)}(s^i;x) = L_m^{*(\sigma_1,\sigma_2)}(s;x) = \frac{1}{m+\sigma_2}\left(\frac{m\partial'_2(mxg(1))}{\partial_2(mxg(1))}x + \frac{\partial'_1(g(1))}{\partial_1(g(1))} + \frac{2\sigma_1+1}{2} \right),$$

and we come off

$$\lim_{m\to\infty} \left\{ L_m^{*(\sigma_1,\sigma_2)}(s;x) \right\} = \lim_{m\to\infty} \left\{ \frac{1}{m+\sigma_2}\left(\frac{m\partial'_2(mxg(1))}{\partial_2(mxg(1))}x + \frac{\partial'_1(g(1))}{\partial_1(g(1))} + \frac{2\sigma_1+1}{2} \right) \right\}$$

$$= \lim_{m\to\infty} \frac{\partial'_2(mxg(1))}{\partial_2(mxg(1))}x = x \lim_{y\to\infty} \frac{\partial'_2(y)}{\partial_2(y)} = x.$$

Finally, for $i = 2$

$$\lim_{m\to\infty} \left\{ L_m^{*(\sigma_1,\sigma_2)}(s^2;x) \right\} = \lim_{m\to\infty} \frac{1}{(m+\sigma_2)^2} \left\{ \frac{m^2\partial''_2(mxg(1))}{\partial_2(mxg(1))}x^2 \right.$$

$$+ \left(\frac{m\left[\partial'_1(g(1)) + (g''(1)+1)\partial_1(g(1))\right]\partial''_2(mxg(1))}{\partial_1(g(1))\partial_2(mxg(1))} \right.$$

$$\left. + \frac{m(2\sigma_1+1)\partial'_2(mxg(1))}{\sigma_2(mxg(1))} \right) x$$

$$\left. + \frac{(g''(1)+1)\partial'_1(g(1)) + \partial''_1(g(1)) + (2\sigma_1+1)\partial'_1(g(1))}{\partial_1(g(1))} + \frac{3\sigma_1^2+3\sigma_1+1}{3} \right\}$$

$$= \lim_{m\to\infty} \frac{\partial''_2(mxg(1))}{\partial_2(mxg(1))} x^2 = x^2 \lim_{m\to\infty} \frac{\partial''_2(y)}{\partial_2(y)} = x^2.$$

In the result, we come off

$$L_m^{*(\sigma_1,\sigma_2)}(s^i;x) \longrightarrow x^i \ , \qquad i = 0,1,2.$$

3. APPROXIMATION TO FUNCTIONS USING $L_m^{*(\sigma_1,\sigma_2)}$ OPERATORS

Theorem 3.1. Let f be a function within the class $f \in \tilde{C}[0,\infty) \cap E$, then

$$\left|L_m^{*(\sigma_1,\sigma_2)}(f;x) - f(x)\right| \le 2\omega\left(f;\delta_m(x)\right),$$

where $\delta_m(x) = \sqrt{M_{2,m}^{(\sigma_1,\sigma_2)}(x)}$ and $\omega(f;.)$ is modulus of continuity of the function f.

Proof. By using the operator (1.9), we have

$$\left|L_m^{*(\sigma_1,\sigma_2)}(f;x) - f(x)\right| = \left| \frac{1}{\partial_1(g(1))\partial_2(mxg(1))} \sum_{k=0}^{\infty} \pi_k(mx) \int_{\frac{k+\sigma_1}{m+\sigma_2}}^{\frac{k+\sigma_1+1}{m+\sigma_2}} \left(f(\varphi) - f(x)\right) d\varphi \right|$$

$$\le \frac{1}{\partial_1(g(1))\partial_2(mxg(1))} \sum_{k=0}^{\infty} \pi_k(mx) \int_{\frac{k+\sigma_1}{m+\sigma_2}}^{\frac{k+\sigma+1}{m+\sigma}} |f(\varphi) - f(x)| d\varphi.$$

By using the property of the modulus of continuity, we have

$$\left|L_m^{*(\sigma_1,\sigma_2)}(f;x) - f(x)\right| \le \frac{1}{\partial_1(g(1))\partial_2(mxg(1))} \sum_{k=0}^{\infty} \pi_k(mx) \int_{\frac{k+\sigma_1}{m+\sigma_2}}^{\frac{k+\sigma_1+1}{m+\sigma_2}} \left(1 + \frac{1}{\delta}|\varphi - x|\right) \omega(f;\delta) d\varphi$$

$$= \frac{\omega(f;\delta)}{\partial_1(g(1))\partial_2(mxg(1))} \left(\sum_{k=0}^{\infty} \pi_k(mx) \int_{\frac{k+\sigma_1}{m+\sigma_2}}^{\frac{k+\sigma_1+1}{m+\nu_2}} d\varphi \right.$$

$$\left. + \sum_{k=0}^{\infty} \pi_k(mx) \frac{1}{\delta} \int_{\frac{k+\sigma_1}{m+\sigma_2}}^{\frac{k+\sigma_1+1}{m+\sigma_2}} |\varphi - x| d\varphi \right)$$

$$= \left(L_m^{*(\sigma_1,\sigma_2)}(1;x) + \frac{1}{\delta} L_m^{*(\sigma_1,\sigma_2)}(|s-x|;x) \right) \omega(f;\delta)$$

$$= \left(1 + \frac{1}{\delta} L_m^{*(\sigma_1,\sigma_2)}(|s-x|;x)\right) \omega(f;\delta)$$

$$= \left(1 + \frac{1}{\delta}\delta\right) \omega(f;\delta) = 2\omega(f;\delta_m(x)).$$

In the result, we get

$$\left|L_m^{*(\sigma_1,\sigma_2)}(f;x) - f(x)\right| \le 2\omega\left(f;\delta_m(x)\right).$$

Definition 1. If for $0 < \alpha \leq 1$ and $M > 0$ function f satisfy the following inequality, then it is called to be Lipschitz property of arrange α

$$|f(t) - f(x)| \leq M|t - x|^{\alpha}, \quad t, x \in [0, \infty)$$

the set of all function that belongs to Lipschitz class functions is given as follows (Srivasta et al., 2019).

$$Lip_M(\alpha) = \{f: |f(t) - f(x)| \leq M|t - x|^{\alpha}, \qquad t, x \in [0, \infty)\}.$$

Theorem 3.2. Let f be a function of set $Lip_M(\alpha)$, then for $x \geq 0$

$$\left|L_m^{*(\sigma_1,\sigma_2)}(f;x) - f(x)\right| \leq M\delta_m^{\alpha}(x)$$

where $\delta_m(x) = \sqrt{M_{2,m}^{(\sigma_1,\sigma_2)}(x)}$.

Proof. By using the operator (1.9), we have

$$\left|L_m^{*(\sigma_1,\sigma_2)}(f;x) - f(x)\right| = \left|L_m^{*(\sigma_1,\sigma_2)}(f(s) - f(x);x)\right|$$

$$= \left|\frac{1}{\partial_1(\mathcal{g}(1))\partial_2(mx\mathcal{g}(1))}\sum_{k=0}^{\infty}\pi_k(mx)\int_{\frac{k+\sigma_1}{m+\sigma_2}}^{\frac{k+\sigma_1+1}{m+\sigma_2}}(f(\varphi) - f(x))d\varphi\right|$$

$$\leq \frac{1}{\partial_1(\mathcal{g}(1))\partial_2(mx\mathcal{g}(1))}\sum_{k=0}^{\infty}\pi_k(mx)\int_{\frac{k+\sigma_1}{m+\sigma_2}}^{\frac{k+\sigma_1+1}{m+\sigma_2}}|f(\varphi) - f(x)|d\varphi.$$

As f is a function of $Lip_M(\alpha)$ then

$$\left|L_m^{*(\sigma_1,\sigma_2)}(f;x) - f(x)\right| \leq \frac{1}{\partial_1(\mathcal{g}(1))\partial_2(mx\mathcal{g}(1))}\sum_{k=0}^{\infty}\pi_k(mx)\int_{\frac{k+\sigma_1}{m+\sigma_2}}^{\frac{k+\sigma_1+1}{m+\sigma_2}}M|\varphi - x|^{\alpha}d\varphi.$$

By application of Holder`s inequality we obtain

$$\left|L_m^{*(\sigma_1,\sigma_2)}(f;x) - f(x)\right| \leq M\left\{\frac{1}{\partial_1(\mathcal{g}(1))\partial_2(mx\mathcal{g}(1))}\sum_{k=0}^{\infty}(\pi_k(mx))^{\frac{2-\alpha}{2}}(\pi_k(mx))^{\frac{\alpha}{2}}\int_{\frac{k+\sigma_1}{m+\sigma_2}}^{\frac{k+\sigma_1+1}{m+\sigma_2}}|\varphi - x|^{\alpha}d\varphi\right\}$$

$$\leq M\left\{\frac{1}{\partial_1(\mathcal{g}(1))\partial_2(mx\mathcal{g}(1))}\left[\partial_1(\mathcal{g}(1))\partial_2(mx\mathcal{g}(1))\right]^{\frac{2-\alpha}{2}}\right.$$

$$\times\left[\frac{1}{\partial_1(\mathcal{g}(1))\partial_2(mx\mathcal{g}(1))}\sum_{k=0}^{\infty}\pi_k(mx)\right]^{\frac{2-\alpha}{2}}\left[\partial_1(\mathcal{g}(1))\partial_2(mx\mathcal{g}(1))\right]^{\frac{\alpha}{2}}$$

$$\left.\times\left[\frac{1}{\partial_1(\mathcal{g}(1))\partial_2(mx\mathcal{g}(1))}\sum_{k=0}^{\infty}\pi_k(mx)\int_{\frac{k+\sigma_1}{m+\sigma_2}}^{\frac{k+\sigma_1+1}{m+\sigma_2}}|\varphi - x|^2d\varphi\right]^{\frac{\alpha}{2}}\right\}$$

$$\leq M\left\{L_m^{*(\sigma_1,\sigma_2)}(1;x)\right\}^{\frac{2-\alpha}{2}}\left\{L_m^{*(\sigma_1,\sigma_2)}((s-x)^2;x)\right\}^{\frac{\alpha}{2}}$$

$$= M\left(\sqrt{M_{2,m}^{(\sigma_1,\sigma_2)}(x)}\right)^{\alpha}.$$

In the result, we get

$$\left|L_m^{*(\sigma_1,\sigma_2)}(f;x) - f(x)\right| \leq M\delta_m^{\alpha}(x).$$

Definition 2. If $f \in C_B[0,\infty)$, then the Peetre's K- functional for f is defined by

$$K(f;\delta) = inf\left\{||f-g|| + \delta||g||_{C_B^2[0,\infty)}\right\}$$

where $C_B^2[0,\infty) = \{g \in C_B[0,\infty): g', g'' \in C_B[0,\infty)\}$ with the norm

$$||g||_{C_B^2[0,\infty)} = ||g||_{C_B[0,\infty)} + ||g'||_{C_B[0,\infty)} + ||g''||_{C_B[0,\infty)}.$$

A norm of linear space $C_B[0,\infty)$ is defined by Sucu et al. (2012),

$$||f||_{C_B[0,\infty)} = \sup_{x\in[0,\infty)} |f(x)|.$$

Definition 3. The second modulus of continuity of the function $f \in C_B[0,\infty)$ is defined by

$$\omega_2 := \sup_{0<t\leq\delta} \|f(.+2t) - 2f(.+t) + f(.)\|_{C_B[0,\infty)}.$$

It is known that there exists a constant $C > 0$ such that (İçöz & Eryiğit, 2020).

$$K(f;\delta) \leq C\omega_2\left(f;\sqrt{\delta}\right). \tag{3.1}$$

Theorem 3.3. Suppose $f \in C_B[0,\infty)$ and $x \in [0,\infty)$. Then

$$\left|L_m^{*(\sigma_1,\sigma_2)}(f;x) - f(x)\right| \leq 2K\left(f;\lambda_m(x)\right)$$

where

$$\lambda_m(x) = \frac{1}{2}\left[M_{1,m}^{(\sigma_1,\sigma_2)}(x) + M_{2,m}^{(\sigma_1,\sigma_2)}(x)\right]$$

and $K(f;.)$ represents the Peetre's K -functional for the function f.

Proof. Suppose $f \in C_B^2[0,\infty)$ with respect to x applying Taylor's theorem, we receive

$$\psi(s) = \psi(x) + (s-x)\psi'(x) + \frac{\psi''(\eta)}{2}(s-x)^2, \quad \eta \in (x,s).$$

This results in

$$L_m^{*(\sigma_1,\sigma_2)}(\psi;x) - \psi(x) = \psi'(x)M_{1,m}^{(\sigma_1,\sigma_2)}(x) + \frac{\psi''(\eta)}{2}M_{2,m}^{(\sigma_1,\sigma_2)}(x).$$

From this, it follows easily that.

$$\begin{aligned}\left|L_m^{*(\sigma_1,\sigma_2)}(\psi;x) - \psi(x)\right| &\leq \left|\psi'(x)M_{1,m}^{(\sigma_1,\sigma_2)}(x) + \frac{\psi''(\eta)}{2}M_{2,m}^{(\sigma_1,\sigma_2)}(x)\right| \\ &\leq \left[M_{1,m}^{(\sigma_1,\sigma_2)}(x) + M_{2,m}^{(\sigma_1,\sigma_2)}(x)\right]\|\psi\|_{C_B[0,\infty)}^2. \end{aligned} \tag{3.2}$$

With Lemma 2.2. and (2.1) equality, the estimation can be written as

$$\left|L_m^{*(\sigma_1,\sigma_2)}(f;x) - f(x)\right| = \left|L_m^{*(\sigma_1,\sigma_2)}(f;x) - L_m^{*(\sigma,\sigma_2)}(\psi;x) + L_m^{*(\sigma,\sigma_2)}(\psi;x) - \psi(x) - f(x) + \psi(x)\right|$$

$$\leq \left|L_m^{*(\sigma_1,\sigma_2)}(f-\psi;x)\right| + \left|L_m^{*(\sigma_1,\sigma_2)}(\psi;x)-\psi(x)\right| + |f(x)-\psi(x)|$$
$$\leq 2\|f-\psi\|_{C_B[0,\infty)} + \left|L_m^{*(\sigma_1,\sigma_2)}(\psi;x)-\psi(x)\right|$$
$$\leq 2\|f-\psi\|_{C_B[0,\infty)} + 2\delta_m(x)\|\psi\|_{C_B^2[0,\infty)}$$
$$= 2\left(\|f-\psi\|_{C_B[0,\infty)} + \delta_m(x)\|\psi\|_{C_B^2[0,\infty)}\right).$$

By finding the infimum among all $\psi \in C_B^2[0,\infty)$ and combining it with the definition of $K(f;.)$, we can deduce the intended result from the last inequality

$$\left|L_m^{*(\sigma_1,\sigma_2)}(f;x)-f(x)\right| \leq 2K\big(f;\lambda_m(x)\big).$$

Theorem 3.4. Suppose $f \in C_B[0,\infty)$. Then

$$\left|L_m^{*(\sigma_1,\sigma_2)}(f;x)-f(x)\right| \leq C\omega_2\left(f;\sqrt{\mu_m(x)}\right) + \omega\left(f;M_{1,m}^{(\sigma_1,\sigma_2)}(x)\right)$$

here C is a positive constant and

$$\mu_m(x) = \frac{1}{8}\left\{M_{1,m}^{(\sigma_1,\sigma_2)}(x) + \left[M_{2,m}^{(\sigma_1,\sigma_2)}(x)\right]^2\right\},$$

and $\omega_2(f;.)$ denote the second order modulus of smoothness of function f.

Proof. Here we take the operators $F_m^{(\sigma_1,\sigma_2)}$ given by

$$F_m^{(\sigma_1,\sigma_2)}(f;x) = L_m^{*(\sigma_1,\sigma_2)}(f;x) - f\left(L_m^{*(\sigma_1,\sigma_2)}(s;x)\right) + f(x). \tag{3.3}$$

We can also derive this From Lemma 2.2.

$$F_m^{(\sigma_1,\sigma_2)}(s-x;x) = 0. \tag{3.4}$$

Furthermore, $\psi \in C_B^2[0,\infty)$ the subsequent equality can be derived using the Taylor formula,

$$\psi(s) = \psi(x) + (s-x)\psi'(x) + \int_x^s (s-u)\,\psi''(u)du\,.$$

If we use the operator which is defined by (3.3), then

$$\left|F_m^{(\sigma_1,\sigma_2)}(\psi;x)-\psi(x)\right| = \left|F_m^{(\sigma_1,\sigma_2)}\left(\int_x^s (s-u)\,\psi''(u)du;x\right)\right|$$
$$= \left|L_m^{*(\sigma_1,\sigma_2)}\left(\int_x^s (s-u)\,\psi''(u)du;x\right)\right.$$
$$\left. - \int_x^{L_m^{*(\sigma_1,\sigma_2)}(s;x)} \left(L_m^{*(\sigma_1,\sigma_2)}(s;x)-u\right)\psi''(u)du + \int_x^x (s-u)\,\psi''(u)du\right|$$
$$\leq \left|L_m^{*(\sigma_1,\sigma_2)}\left(\int_x^s (s-u)\,\psi''(u)du;x\right)\right|$$
$$+ \left|\int_x^{L_m^{*(\sigma_1,\sigma_2)}(s;x)} \left(L_m^{*(\sigma_1,\sigma_2)}(s;x)-u\right)\psi''(u)du\right|.$$

If we use the relation which is defined by (2.1), then

$$\left|F_m^{(\sigma_1,\sigma_2)}(\psi;x)-\psi(x)\right| \leq \frac{1}{2}\left\{M_{2,m}^{(\sigma_1,\sigma_2)}(x)+\left[M_{1,m}^{(\sigma_1,\sigma_2)}(x)\right]^2\right\}\|\psi''\|_{C_B[0,\infty)}$$
$$\leq 4\mu_m(x)\|\psi\|_{C_B^2[0,\infty)}. \quad (3.5)$$

Combining the definition of the operator $F_n^{(\sigma_1,\sigma_2)}$, Lemma 2.2 and (3.5), we acquire the estimation

$$\left|L_m^{*(\sigma_1,\sigma_2)}(f;x)-f(x)\right| = \left|F_m^{(\sigma_1,\sigma_2)}(f-\psi;x)-(f-\psi)(x)+F_m^{(\sigma_1,\sigma_2)}(\psi;x)-\psi(x)\right.$$
$$\left.+f\left(L_m^{*(\sigma_1,\sigma_2)}(s;x)\right)-f(x)\right|.$$

Using the triangle inequality

$$\left|L_m^{*(\sigma_1,\sigma_2)}(f;x)-f(x)\right| \leq \left|F_m^{(\sigma_1,\sigma_2)}(f-\psi;x)-(f-\psi)(x)\right|+\left|F_m^{(\sigma_1,\sigma_2)}(\psi;x)-\psi(x)\right|$$
$$+\left|f\left(L_m^{*(\sigma_1,\sigma_2)}(s;x)\right)-f(x)\right|$$
$$\leq 4\|f-\psi\|_{C_B[0,\infty)}+4\mu_m(x)\|\psi\|_{C_B^2[0,\infty)}+\omega\left(f;L_m^{*(\sigma_1,\sigma_2)}(s-x;x)\right)$$
$$\leq 4\|f-\psi\|_{C_B[0,\infty)}+4\mu_m(x)\|\psi\|_{C_B^2[0,\infty)}+\omega\left(f;M_{1,m}^{(\sigma_1,\sigma_2)}(x)\right).$$

Considering the relation between $K(f;.)$ and $\omega_2(f;.)$ which is given by (3.1), then we have

$$\left|L_m^{*(\sigma_1,\sigma_2)}(f;x)-f(x)\right| \leq 4K\left(f;\mu_m(x)\right)+\omega\left(f;M_{1,m}^{(\sigma_1,\sigma_2)}(x)\right)$$
$$\leq C\omega_2\left(f;\sqrt{\mu_m(x)}\right)+\omega\left(f;M_{1,m}^{(\sigma_1,\sigma_2)}(x)\right).$$

4. CONCLUSION

In this paper, a brief introduction is provided for the Szász operator. This operator serves as the foundation for exploring various approximation properties, leading to the creation of additional operators and polynomials. One such operator is the Cheney and Sharma (1964) operator, giving rise to the emergence of orthogonal polynomials. Subsequently, a model involving Appell polynomials is devised by Jakimovski and Leviatan (1969). Following this, a study focusing on Brenke polynomials is conducted by Varma et al. (2012). Additionally, a Kantorovich operator containing Brenke polynomials is introduced, along with an exploration of the operator which is defined by Waterman incorporating generalized Brenke polynomials by Sucu (2022). These operators, with their distinct formulations, are presented in a different format, specifically expressed as (1.9) and encompassing an expansion of Brenke polynomials.

5. RESULT

In this paper, we have generalized the operators that are defined by Sucu (2022), and we defined them in different shapes, it is shown as (1.9), where we call them Stancu Kantorovich type operators, including generalized Brenke polynomials. Also, the approximation of functions is discussed. As mentioned in the introduction section, with the motivation of these newly defined operators, we believe that it will be helpful and valuable for the readers.

REFERENCES

Agrawal, P. N., Baxhaku, B., & Chauhan, R. (2018). Quantitative Voronovskaya-and Grüss-Voronovskaya-type theorems by the blending variant of Szász operators including Brenke-type polynomials. *Turkish Journal of Mathematics*, *42*(4), 1610-1629. https://doi.org/10.3906/mat-1708-1

Aktaş¸ R., Çekim, B., & Taşdelen, F. (2013). A Kantorovich-Stancu Type Generalization of Szász Operators including Brenke Type Polynomials. *Journal of Function Spaces and Applications*, 935430. https://doi.org/10.1155/2013/935430

Atakut, Ç., & Büyükyazcı, İ. (2016). Approximation by Kantorovich-Szász type operators based on Brenke type polynomials. *Numerical Functional Analysis and Optimization*, *37*(12), 1488-1502. https://doi.org/10.1080/01630563.2016.1216447

Chaggaraa, H., & Gahami, A. (2023). Classification of 2-Orthogonal Polynomials with Brenke Type Generating Functions. *Mathematical Physics*. https://doi.org/10.48550/arXiv.2310.11734

Cheney, E. W., & Sharma, A. (1964). Bernstein power series. *Canadian Journal of Mathematics*, *16*, 241-252. https://doi.org/10.4153/CJM-1964-023-1

Çekim, B., Aktaş, R., & İçöz, G. (2019). Kantrovich-Stancu type operators including Boas-Buck type polynomials. *Hacettepe Journal of Mathematics and Statistics*, *48*(2), 460-471. https://doi.org/10.15672/HJMS.2017.528

İçöz, G., & Çekim, B. (2015). Dunkl generalization of Szász operators via q-calculus. *Journal of Inequalities and Applications*, *284*. https://doi.org/10.1186/s13660-015-0809-y

İçöz, G., & Çekim, B. (2016a). Stancu type generalization of Dunkl analogue of Szász Kantorovich operators. *Mathematical Methods in the Applied Sciences*, *39*(7), 1803-1810. https://doi.org/10.1002/mma.3602

İçöz, G., & Çekim, B. (2016b). Stancu-type generalization of the Chan-Chyan-Srivastava operators. *Filomat*, *30*(14), 3733-3742. https://doi.org/10.2298/FIL1614733I

İçöz, G., & Eryigit, H. (2020). Beta generalization of Stancu-Durrmeyer operators involving a generalization of Boas-Buck type polynomials. *Gazi University Journal of Science*, *33*(3), 715-724. https://doi.org/10.35378/gujs.597272

İçöz, G., Varma, S., & Sucu, S. (2016). Approximation by operators including Generalized Appell polynomials. *Filomat*, *30*(2), 429-440. https://doi.org/10.2298/FIL1602429I

Jakimovski, A., & Leviatan, D. (1969). Generalized Szász operators for the approximation in the infinite interval. *Mathematica (Cluj)*, *11*(34), 97-103.

Rao, N., Heshamuddin, Md., Shadab, M., & Srivastava A. (2021). Approximation Properties of Bivariate Szász Durrmeyer Operators via Dunkl Analogue. *Filomat*, *35*(13), 4515-4532. https://doi.org/10.2298/FIL2113515R

Srivasta, N., İçöz, G., & Çekim, B. (2019). Approximation properties of on extended family of the Szász Mirakjan Beta type operators. *Axioms*, *8*(4), 111. https://doi.org/10.3390/axioms8040111

Sucu, S. (2022). Stancu type operators including generalized Brenke polynomials. *Filomat*, *36*(07), 2381-2389. https://doi.org/10.2298/FIL2207381S

Sucu, S., & Varma, S. (2019). Approximation by sequence of operators involving analytic functions. *Mathematics*, *7*(2), 188. https://doi.org/10.3390/math7020188

Sucu, S., İçöz, G., & Varma, S. (2012). On some extensions of Szász operators including Boas-Buck-type polynomials. *Abstract and Applied Analysis*, 680340. https://doi.org/10.1155/2012/680340

Varma, S. (2013). On a generalization of Szász operators by multiple Appell polynomials. *Stud. Univ. Babeş-Bolyai Math*, 58(3), 361-369

Varma, S., & Sucu, S. (2022). Operators obtained by using certain generating function for approximation. *Mathematics*, *10*(13), 2239. https://doi.org/10.3390/math10132239

Varma, S., Sucu, S., & İçöz, G. (2012). Generalization of Szász operators involving Brenke type polynomials. *Computers and Mathematics with Applications*, *64*(2), 121-127. https://doi.org/10.1016/j.camwa.2012.01.025

Research Article GU J Sci, Part A, 10(4): 571-592 (2023) 10.54287/gujsa.1393092

Gazi University
Journal of Science
PART A: ENGINEERING AND INNOVATION
http://dergipark.org.tr/gujsa

Comparative Analysis of Optimal Control Strategies: LQR, PID, and Sliding Mode Control for DC Motor Position Performance

Hakan KIZMAZ[1*]

[1] Department of Electrical and Electronics Engineering, Faculty of Engineering and Architecture, Batman University, Batman, Türkiye

Keywords

DC Motor
Linear Quadratic Regulator
Optimal Control
Optimal PID
Optimal Integral Sliding Mode Control

Abstract

This study applies these control methods to the DC motor system to examine the robustness and performance of four optimal control methods. Optimal controllers aim to control the system to minimize a selected performance index. These control methods offer advantages such as improving energy efficiency, reducing costs, and enhancing system security. The Linear Quadratic Regulator (LQR) based controller is the primary optimal control method. Two well-known traditional control techniques include the Proportional-Integral-Derivative (PID) and Integral Sliding Mode Controller (ISMC). However, they do not usually contain optimal properties. In this study, the optimal control algorithms, defined by obtaining controller parameters through the Riccati equation, are applied to achieve accurate position-tracking control in a DC motor system using Matlab/Simulink. The integral term-based algorithms seem to be robust and eliminate steady-state errors. The optimal PID controller could not provide the minimum performance index, unlike the other controllers in the study. LQR and optimal ISMC algorithms could allow the performance index to be a minimum. An illustrative comparison of the performances of all optimal control algorithms has been presented through graphical representation, along with corresponding interpretations.

Cite

Kizmaz, H. (2023). Comparative Analysis of Optimal Control Strategies: LQR, PID, and Sliding Mode Control for DC Motor Position Performance. *GU J Sci, Part A, 10*(4), 571-592. doi:10.54287/gujsa.1393092

Author ID (ORCID Number)

0000-0001-7680-7191 Hakan KIZMAZ

Article Process

Submission Date 19.11.2023
Revision Date 13.12.2023
Accepted Date 26.12.2023
Published Date 31.12.2023

1. INTRODUCTION

DC motors are extensively utilized in applications involving velocity and position control, especially robotics (He et al, 2023). They actuate components in various electronic projects, including inverted pendulum systems (Mondal & Dey, 2020), self-balancing robots (Feng et al., 2023), and uncrewed vehicles (Tanveer & Ahmad, 2023). DC motors are preferred over their AC counterparts due to their lower power consumption and ease of maintenance. However, achieving precise control over the angular position of a DC motor remains challenging.

Position control of DC motors has been thoroughly investigated in the literature, resulting in well-defined system transfer functions and state space equations. When working with such systems, controllers that utilize the known system model for control law derivation offer significant advantages in design simplicity, hardware implementation, and adaptability. DC motors are favored for their cost-effectiveness, low power consumption, and precision in servo applications. However, the main challenge in controlling systems with DC motors is accurately calculating the necessary electrical power to attain the desired motor angular position or speed.

An optimal control system seeks to maximize system benefit while minimizing costs, involving a viable control strategy within defined constraints to optimize a system's performance. In a controlled dynamic system, the goal is to find the best control plan from a set of permissible plans, enabling the system to transition from its initial state to a desired target state while enhancing system performance. In linear systems, optimal control

*Corresponding Author, e-mail: hakan.kizmaz@batman.edu.tr

typically translates into a linear-quadratic problem. This approach is widely acknowledged for systematically designing controllers to optimize performance according to a specified index. In the literature, there are studies in the field of optimal control of DC motors using various artificial neural networks (Khomenko et al., 2013; Wang et al., 2019) or metaheuristic algorithms (Mamta & Singh, 2020; Rasheed, 2020). However, despite yielding successful results, these algorithms come with a high computational burden.

The (LQR) is a linear optimal controller that harnesses the state space model to derive the control, utilizing state variables of the system for control law formulation. LQR is formulated to minimize both the square of the error and the energy required to attain the same objective concurrently. Solving the algebraic Riccati equation results in the optimal control law, characterized by a steady gain matrix for linear time-invariant systems. After selecting the appropriate weighting matrices in the performance index, the state feedback gain can be tailored to meet specific requirements. However, the robustness of a state feedback control system relying solely on a constant gain matrix cannot be guaranteed. To ensure robustness in LQR control, we employ the integral of the output variable within the control system. This type of control function, known in the literature as LQR with integral action, exhibits robustness against system uncertainties and steady-state errors (Ruderman et al., 2008).

PID controllers are a straightforward and effective way to regulate plants. The PID controller is widely used in control engineering for its simplicity and effectiveness, and it has a rich history in the field. The three controller gain parameters are typically set as constants. Nonetheless, manual fine-tuning of the PID controller demands substantial human intervention, constituting a significant limitation. PID controller parameters are usually determined to achieve the desired system behaviour using pole placement. The desired behaviour of the system can be in terms of settling time for system state variables or optimizing energy consumption within the system. An alternative but more complex approach involves using optimal controllers, which seek the optimal solution by solving the algebraic Riccati equation. These strategies require a linear system and complete state feedback for implementation. However, a system incorporating a PID controller can be transformed into a feedback system where the Riccati equation can be applied through specific mathematical manipulations. Mukhopadhyay (1978) includes such a study.

Sliding mode control (SMC) theory, initially developed for variable structure systems, has since become emblematic of this class of control systems. During its early development, SMC theory was secondary to linear control theory. Recent efforts have refocused on variable structure control strategies using sliding-mode techniques for DC servo drive systems. SMC offers distinct advantages, including robust performance in unmodeled dynamics, insensitivity to parameter variations, and resilience against external disturbances. These benefits find practical application in controlling position and speed in DC servo systems (Durdu & Dursun, 2019; Eli et al., 2023; Saputra, et al., 2023).

The SMC design process consists of two primary stages. Initially, a sliding surface is selected to represent the desired closed-loop performance. Subsequently, a control strategy is formulated to guide the system state trajectory towards this surface. The period before reaching the sliding surface is called the "reaching phase." External disturbances, including matched ones, affect the system during this reaching phase. An Integral Sliding Mode was introduced to eliminate the reaching phase and maintain a sliding mode. ISMC is mainly employed in cases where a steady-state error in the system needs correction. An integrator-term compensator is added to the sliding surface expression to eliminate the steady-state error. Adding a compensator to the SMC system introduces extra dynamics, increasing the system's order compared to the original setup. Typically, performance evaluation involves quadratic functions of state variables and control inputs. Solving the algebraic Riccati equation provides the optimal control law for a linear time-invariant system with a constant gain matrix. Once weighting matrices are chosen, the feedback gain can be customized for specific needs. However, the robustness of the optimal gain may not match that of the pole-placement gain. Integrating LQR design principles into the SMC framework is crucial. This situation is presented in by Utkin (1977).

In Yu et al. (2004), a method that integrates LQR and SMC techniques is proposed for the design of the DC motor position control system. A. Yosef (2011) proposed an integral control-based SMC for DC motor servo control. In Gorczyca et al. (2011) presented a work about optimal control of the linear and the nonlinear DC motor model. The nonlinear optimal control solutions are obtained using the mean square error method.

Marva et al. proposed a controller strategy comprising the optimal control law and integral sliding mode (Jouini et al., 2019). Maghfiroh et al. (2022) improved the LQR control of the DC motor. Their study was about the optimization of the LQR algorithm. Aravind et al. (2017) deal with implementing linear quadratic Gaussian and extended Kalman filters for DC motors. Xiang and Wei (2021) made a work about a DC motor position tracking system based on LQR. Pratama et al. (2022) employed an optimal quadratic regulator PID for DC motor angular velocity control.

In this article, some of the mentioned optimal control algorithms may require a different number of measurable state variables than others. This study has not analyzed the algorithms' need for measurable state variables. Readers searching for a solution in this regard can refer to the topics of observers and estimators in control and system theory. Observers like Luenberger (Davis, 2002) and Kalman (Simon, 2006) are the most used algorithms for estimating unmeasurable state variables.

This study presents a comparative simulation analysis that centres on implementing four distinct optimal control methods for the positional control of a DC motor. Notably, all methods commonly employ the Riccati equation as a fundamental component. Furthermore, these algorithms are formulated to minimize or maximize a designated performance index. The study meticulously explores the impact of these algorithms on the state variables and performance indices of the DC motor model. The findings are effectively illustrated through comparative graphs. This unique methodology serves the purpose of discerning the practical efficacy of these methods in the context of DC motor applications, thus offering a valuable contribution to industrial and automation literature.

This paper is structured in the following manner: The section titled 'Preliminaries and Mathematical Background' provides an overview of a range of optimal control algorithms rooted in the Riccati equation and conventional control methods. The section titled 'DC Servo Machine Mathematical Model' offers an in-depth exposition of the mathematical underpinnings of the DC machine model. The section 'Computational Findings' details the numerical computations associated with the optimal control algorithms. The section on 'Simulation Results' presents the outcomes of the aforementioned optimal control approaches. Finally, the 'Conclusions' section offers a summarization of the paper.

2. PRELIMINARIES AND MATHEMATICAL BACKGROUND

This section summarizes the theories and mathematical expressions used in this paper. Consider the following linear system,

$$\dot{\mathbf{x}}(t) = \mathbf{A}\mathbf{x}(t) + \mathbf{B}\mathbf{u}(t) \tag{1}$$

where $\mathbf{A}\in\Re^{n\times n}$ is the state matrix, $\mathbf{B}\in\Re^{n\times r}$ the system input matrix, $\mathbf{x}\in\Re^{n\times 1}$ is the state vector and $\mathbf{u}\in\Re^{r\times 1}$ is system input vector. The indices *n* and *r* refer to the number of state variables and the number of system inputs, respectively. The output equation of a linear system,

$$\mathbf{y}(t) = \mathbf{C}\mathbf{x}(t) \tag{2}$$

where $\mathbf{C}\in\Re^{m\times n}$ is output matrix. The indices *m* is referred to the number of outputs.

The optimal control problem can be calculated as a control input $\mathbf{u}(t)$ that satisfies the system to follow an optimal state variables trajectory. An initial cost function is established. The control input must minimize the cost function as much as possible.

Dreyfus (1962) offered a method for deriving a series of differential equations that exhibit boundary condition properties, referred to as the Euler-Lagrange equations. The exact boundary conditions can be provided using the Hamiltonian function, employing the Pontryagin (1986) maximum principle.

Hamilton-Jacobi-Bellman (HJB) partial differential equation is one of the main approaches to solving optimal control problems (Kirk, 1998). The optimality problem with linear quadratic performance criterion is generally solved by Hamilton-Jacobi equations. Solutions of the equations take the form of the matrix Riccati equation. When the system is controllable, that equation provides an optimal control law as a linear function of the state vector components.

The most usable quadratic performance index is as follows.

$$J = \int_{t_0}^{t_1} (\mathbf{x^T Q x} + \mathbf{u^T R u}) dt \tag{3}$$

where J is a scalar quantity, $\mathbf{Q} \in \Re^{n \times n}$ and $\mathbf{R} \in \Re^{r \times r}$ the state and control weighting matrices, respectively. Besides, they are always symmetric, positively defined, and square. Optimal control problems include crucial performance criteria such as settling time and the consumed energy for system control. These two criteria have the opposite operating mentality. When the weight entries of the **Q** matrix are selected as equal to the weights of the **R** matrix, the system's energy consumption has equal importance with the settling time. When the **Q** matrix weights are selected bigger than the **R** matrix weights, the settling time is more important than energy consumption. Namely, to reduce the settling time, the energy consumption is ignored. When the **Q** matrix weights are selected less than the **R** matrix weights, the energy consumption is as low as possible.

2.1. Linear Quadratic State Feedback Controller

Upon consideration of Eq. (1) and (3), application of the Hamiltonian theorem to these equations yields the following expression (Kirk, 1998; Burns, 2001),

$$\mathbf{u}_{lqr} = -\mathbf{K}_{lqr}\mathbf{x} = -\mathbf{R}^{-1}\mathbf{B}^T\mathbf{P}_{lqr}\mathbf{x} \tag{4}$$

where $\mathbf{u}_{lqr}$ is the optimal control input, $\mathbf{P}_{lqr} \in \Re^{n \times n}$ is a square symmetric adjoint matrix, $\mathbf{P}_{lqr}(t)$ are found by Eq. (5).

$$\dot{\mathbf{P}}_{lqr} = -\mathbf{P}_{lqr}\mathbf{A} - \mathbf{A}^T\mathbf{P}_{lqr} - \mathbf{Q}_{lqr} + \mathbf{P}_{lqr}\mathbf{B}\mathbf{R}^{-1}\mathbf{B}^T\mathbf{P}_{lqr} \tag{5}$$

As time integration in a backward direction advance, Kalman demonstrated that $\mathbf{P}_{lqr}(t)$ solutions stabilize at constant values. In that case, Eq. (5),

$$0 = -\mathbf{P}_{lqr}\mathbf{A} - \mathbf{A}^T\mathbf{P}_{lqr} - \mathbf{Q}_{lqr} + \mathbf{P}_{lqr}\mathbf{B}\mathbf{R}^{-1}\mathbf{B}^T\mathbf{P}_{lqr} \tag{6}$$

Eq. (5)-(6) are continuous solutions of the matrix Riccati equation. Solving Eq. (6) yields the $\mathbf{P}_{lqr}$ matrix. Substituting the $\mathbf{P}_{lqr}$ matrix into Eq. (4) concluded optimal control input with feedback matrix $\mathbf{K}_{lqr}$. The linear feedback control system is considered in Figure 1. When the matrix $\mathbf{K}_{lqr}$ is substituted into Figure 1, the control system becomes a linear quadratic feedback control system or LQR (Burns, 2001). Attention should be drawn to the existence of state feedback in Figure 1. It should be noted that the state feedback algorithms may need to possess observable state variables or use an observer for such situations.

It is commonly assumed that LQRs, as depicted in Figure 1, are primarily used for scenarios where the set point is equal to zero. However, the set point regulation requires driving the system states to the desired set point state vector $\mathbf{x}_d$ from any initial state and under disturbance. The set point regulation is generally proposed in industrial applications. This paper aims to use the linear quadratic techniques for set point regulation processes. As a first step, the calculation of the desired control input, $\mathbf{u}_d$, that needs to be applied to obtain the desired state vector is required. The derivative terms within Eq. (1) are equated to zero, resulting in the calculation of the control input, $\mathbf{u}_d$, corresponding to the obtained $\mathbf{x}_d$ vector is derived.

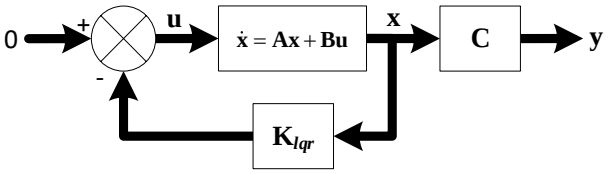

***Figure 1**. LQR block diagram*

$$0 = \mathbf{A}\mathbf{x}_d + \mathbf{B}\mathbf{u}_d \tag{7}$$

where $\mathbf{x}_d$ is a constant steady-state vector, also called system equilibrium point. Considering matrix **B** has full rank, the desired control input, $\mathbf{u}_d$, is determined as,

$$\mathbf{u}_d = -(\mathbf{B}^T\mathbf{B})^{-1}\mathbf{B}^T\mathbf{A}\mathbf{x}_d \tag{8}$$

The desired state vector, $\mathbf{x}_d$, might be feasible by directly applying the control input, $\mathbf{u}_d$, to the open-loop system. However, open-loop applications would not ensure slight overshoot or robustness against disturbances. Utilizing a feedback control algorithm is a dependable approach to improve system transient behaviour and reject disturbances. The control algorithm necessitates the determination of the system's error dynamics as follows,

$$\left.\begin{array}{l} \tilde{\mathbf{x}} = \mathbf{x} - \mathbf{x}_d, \Longrightarrow \mathbf{x} = \tilde{\mathbf{x}} + \mathbf{x}_d \\ \tilde{\mathbf{u}} = \mathbf{u} - \mathbf{u}_d \Longrightarrow \mathbf{u} = \tilde{\mathbf{u}} + \mathbf{u}_d \end{array}\right\} \tag{9}$$

Differentiating state error expression in Eq. (9) and substituting in (1) provides the following,

$$\dot{\mathbf{x}} = \dot{\tilde{\mathbf{x}}} + \dot{\mathbf{x}}_d = \mathbf{A}(\tilde{\mathbf{x}} + \mathbf{x}_d) + \mathbf{B}(\tilde{\mathbf{u}} + \mathbf{u}_d) \tag{10}$$

Here, $\mathbf{x}_d$ is the equilibrium point and contains constant entries. Since the derivative of a constant is zero, by substituting $\dot{\mathbf{x}}_d = 0$ and Eq. (7) into Eq. (10), the following expression is derived,

$$\dot{\tilde{\mathbf{x}}} = \mathbf{A}\tilde{\mathbf{x}} + \mathbf{B}\tilde{\mathbf{u}} \tag{11}$$

Eq. (11) defines the error dynamics and allows for direct application of an LQR algorithm.

$$J_{lqr} = \int_{t_0}^{t_1} (\tilde{\mathbf{x}}^{\mathbf{T}}\mathbf{Q}\tilde{\mathbf{x}} + \tilde{\mathbf{u}}^{\mathbf{T}}\mathbf{R}\tilde{\mathbf{u}})dt \tag{12}$$

The following form of the feedback control optimizes the cost function Eq. (12)

$$\tilde{\mathbf{u}} = -\mathbf{K}_{lqr}\tilde{\mathbf{x}} \tag{13}$$

where the matrix $\mathbf{K}_{lqr}$ is defined by

$$\mathbf{K}_{lqr} = \mathbf{R}^{-1}\mathbf{B}^T\mathbf{P} \tag{14}$$

Incorporating Eq. (13) into Eq. (11), the closed-loop system equation is obtained as follows,

$$\dot{\tilde{\mathbf{x}}} = (\mathbf{A} - \mathbf{B}\mathbf{K}_{lqr})\tilde{\mathbf{x}} \tag{15}$$

The eigenvalues of $\mathbf{A}$-$\mathbf{BK}_{lqr}$ are placed in the left half of the complex s-plane. That proves the system is asymptotically stable and provides a steady state. In the steady state, the system state $\mathbf{x}$ becomes $\mathbf{x}_d$. Substituting Eq. (9) into Eq. (15) yields the following equation,

$$\dot{\mathbf{x}} = (\mathbf{A} - \mathbf{BK}_{lqr})\mathbf{x} - (\mathbf{A} - \mathbf{BK}_{lqr})\mathbf{x}_d \tag{16}$$

The error variables Eq. (8)-(9) and the feedback control Eq. (13) satisfy the following equation.

$$\mathbf{u} = -\left[(\mathbf{B}^T\mathbf{B})^{-1}\mathbf{B}^T - \mathbf{K}_{lqr}\right]\mathbf{x}_d - \mathbf{K}_{lqr}\mathbf{x} \tag{17}$$

In summary, the equilibrium point at the set point is calculated first. Then, the processes defined by Eq. (6),(8), and Eq. (14) are executed, respectively. Finally, optimal control input Eq. (17) is obtained. The entire algorithm is executed as depicted in Figure 2 (Naidu, 2002; Anderson & Moore, 2007).

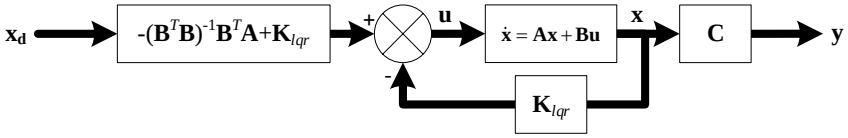

Figure 2*. LQR tracking control block diagram*

2.2. LQR With Integral Control Action (LQRI)

Control algorithms aim to achieve stability, the desired transient response, and minimize steady-state error. The LQR algorithm may not eliminate steady-state error if there are no closed-loop system poles at the origin of the complex plane. The same situation arises when the DC gain of the closed-loop system with a state feedback controller differs from unity.

Steady-state error elimination decreases the disparity between the system's input and output. This action is provided by adding an integral term of the open-loop system. This section discusses using integral terms with a linear quadratic feedback controller (Dorf & Bishop, 2010; Ogata, 2010).

The basic mentality here is to enlarge the original closed-loop system with a linear quadratic controller. Substituting Eq. (4) into Eq. (1) concluded the following equation.

$$\dot{\mathbf{x}} = (\mathbf{A} - \mathbf{BK}_{lqr})\mathbf{x} \tag{18}$$

Eq. (18) is stable when the eigenvalues of $\mathbf{A}$-$\mathbf{BK}_{lqr}$ expression are at the left half complex plane. Linear quadratic state feedback controller enables stabilization. However, comprehensive control of steady-state error is achieved by implementing the following procedures.

The integration of error between output and reference input, $\mathbf{x}_i$, is as follows,

$$\mathbf{x}_i = \int (\mathbf{r} - \mathbf{y})dt = \int (\mathbf{r} - \mathbf{Cx})dt \tag{19}$$

where the reference control input vector of the system is $\mathbf{r}$, the integration error is taken as a new state variable. The derivative of Eq. (19) is as follows,

$$\dot{\mathbf{x}}_i = \mathbf{r} - \mathbf{Cx} \tag{20}$$

By combining Eq. (20) with the original system equations (1) and (2), the augmented state space system is obtained as follows.

$$\begin{bmatrix}\dot{\mathbf{x}}\\ \dot{\mathbf{x}}_i\end{bmatrix}=\begin{bmatrix}\mathbf{A} & 0_{n\times m}\\ -\mathbf{C} & 0_{m\times m}\end{bmatrix}\begin{bmatrix}\mathbf{x}\\ \mathbf{x}_i\end{bmatrix}+\begin{bmatrix}\mathbf{B}\\ 0_{m\times r}\end{bmatrix}\mathbf{u}+\begin{bmatrix}0_{n\times m}\\ \mathbf{I}_{m\times m}\end{bmatrix}\mathbf{r}$$
$$\mathbf{y}=\begin{bmatrix}\mathbf{C} & 0_{m\times m}\end{bmatrix}\begin{bmatrix}\mathbf{x}\\ \mathbf{x}_i\end{bmatrix} \quad (21)$$

$\mathbf{I}_{m\times m}$ is the $m\times m$ dimensional identity matrix. Eq. (21) includes a new state space vector. In this situation, the state-feedback controller has the following form.

$$\mathbf{u}=-\underbrace{\begin{bmatrix}\mathbf{K}_x & \mathbf{K}_{in}\end{bmatrix}}_{\mathbf{K}_{lqri}}\begin{bmatrix}\mathbf{x}\\ \mathbf{x}_i\end{bmatrix}=-\mathbf{K}_x\mathbf{x}-\mathbf{K}_{in}\mathbf{x}_i \quad (22)$$

the $\mathbf{K}_x\in\Re^{r\times n}$ is the original state feedback control matrix, and $\mathbf{K}_{in}\in\Re^{r\times m}$ is the integral control feedback matrix. $\mathbf{K}_x$ and $\mathbf{K}_{in}$ form the matrix $\mathbf{K}_{lqri}\in\Re^{r\times(m+n)}$. The extended system matrices are as in Eq. (23).

$$\mathbf{x}_{lqri}=\begin{bmatrix}\dot{\mathbf{x}}\\ \dot{\mathbf{x}}_i\end{bmatrix},\ \mathbf{A}_{lqri}=\begin{bmatrix}\mathbf{A} & 0_{n\times m}\\ -\mathbf{C} & 0_{m\times m}\end{bmatrix},\ \mathbf{B}_{lqri}=\begin{bmatrix}\mathbf{B}\\ 0_{m\times r}\end{bmatrix},\ \mathbf{C}_{lqri}=\begin{bmatrix}\mathbf{C} & 0_{m\times m}\end{bmatrix},\ \mathbf{B}_r=\begin{bmatrix}0_{n\times m}\\ \mathbf{I}_{m\times m}\end{bmatrix} \quad (23)$$

Substituting Eq. (22) into Eq. (21) yields

$$\dot{\mathbf{x}}_{lqri}=\left(\mathbf{A}_{lqri}-\mathbf{B}_{lqri}\mathbf{K}_{lqri}\right)\mathbf{x}_{lqri}+\mathbf{B}_r\mathbf{r} \quad (24)$$

The eigenvalues of $\mathbf{A}_{lqri}$-$\mathbf{B}_{lqri}\mathbf{K}_{lqri}$ are placed in the left half of the complex s plane for asymptotically stable. The cost function related to the augmented state-space system is defined as follows.

$$J_{lqri}=\int_{t_0}^{t_1}\left(\mathbf{x}_{lqri}^{T}\mathbf{Q}_{lqri}\mathbf{x}_{lqri}+\mathbf{u}^{\mathbf{T}}\mathbf{R}\mathbf{u}\right)dt \quad (25)$$

The matrices are substituted in Eq. (26), and the extended costate $\mathbf{P}_{lqri}$ matrix is calculated.

$$0=-\mathbf{P}_{lqri}\mathbf{A}_{lqri}-(\mathbf{A}_{lqri})^T\mathbf{P}_{lqri}-\mathbf{Q}_{lqri}+\mathbf{P}_{lqri}\mathbf{B}_{lqri}(\mathbf{R})^{-1}(\mathbf{B}_{lqri})^T\mathbf{P}_{lqri} \quad (26)$$

$\mathbf{Q}_{lqri}$ extended state weight matrix, $\mathbf{P}_{lqri}$ matrix is used in Eq. (27), and feedback control matrix $\mathbf{K}_{lqri}$ is obtained.

$$\mathbf{K}_{lqri}=\begin{bmatrix}\mathbf{K}_x & \mathbf{K}_{in}\end{bmatrix}=\mathbf{R}^{-1}\mathbf{B}_{lqri}^{T}\mathbf{P}_{lqri} \quad (27)$$

$\mathbf{R}$ and $\mathbf{B}_{lqri}$ matrices are extended control weight and system input matrices.

All obtained matrices $\mathbf{K}_x$ and $\mathbf{K}_{in}$ are replaced in Figure 3, and the control system is executed (Ogata, 2010; Nise, 2011).

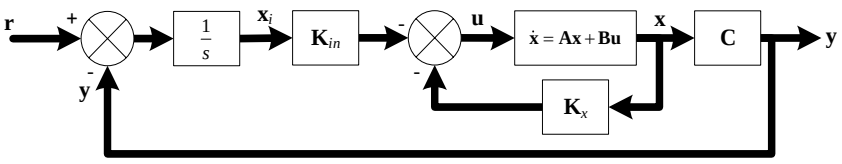

Figure 3*. LQR with integral action*

2.3. Optimal PID Controller

The algorithms given under the subheadings so far use state variables. This case necessitates observable state variables. The state observers are employed for this purpose. Lüenberger observer, reduced order observer, or

Kalman estimator can be employed to estimate any observed state variables of any system (Davis, 2002; Simon, 2006).

However, the PID controller may not need any observer since it is an output-based controller, as seen in Figure 4. The feedback is implemented from output to input. The PID controller requires a smaller number of measurable outputs (**y**) of the system. The input signal **u** is a three-term controller as follows (Paraskevopoulos, 2002; Franklin et al., 2009; Ogata, 2010):

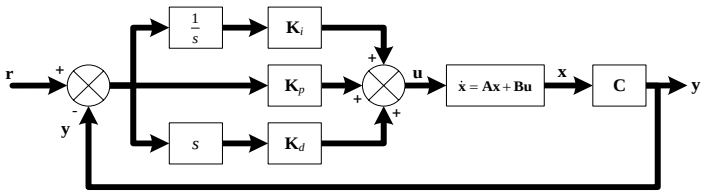

Figure 4*. PID control system*

$$\mathbf{u} = -\mathbf{K}_p(\mathbf{r}-\mathbf{y}) - \mathbf{K}_i\int_0^t(\mathbf{r}-\mathbf{y})dt - \mathbf{K}_d(\dot{\boldsymbol{r}}-\dot{\boldsymbol{y}}) \tag{28}$$

where $\mathbf{K}_p \in \Re^{m\times r}$, $\mathbf{K}_i \in \Re^{m\times r}$ and $\mathbf{K}_d \in \Re^{m\times r}$ are proportional, integral, and derivative feedback gain matrices. Considering the help of Eq. (1)-(2) and Eq. (28), Eq. (29) is obtained (Mukhopadhyay, 1978; Pratama, et al., 2022)

$$\begin{aligned}\mathbf{u} &= \left(\mathbf{K}_p\mathbf{r} + \mathbf{K}_i\int \mathbf{r}dt + \mathbf{K}_d\dot{\mathbf{r}} + \right) - \mathbf{K}_p\mathbf{C}\mathbf{x} - \mathbf{K}_i\int \mathbf{y}dt - \mathbf{K}_d\mathbf{C}(\mathbf{A}\mathbf{x}+\mathbf{B}\mathbf{u}) \\ &= \mathbf{u}_r - \bar{\mathbf{K}}_p\mathbf{x} - \bar{\mathbf{K}}_i\int_{\mathbf{0}}^{\boldsymbol{t}}\mathbf{y}dt\end{aligned} \tag{29}$$

Here the gains $\bar{\mathbf{K}}_p$, $\bar{\mathbf{K}}_i$ and the input residue $\mathbf{u}_r$ are all defined as

$$\bar{\mathbf{K}}_p = (\mathbf{I}_m + \mathbf{K}_d\mathbf{C}\mathbf{B})^{-1}\left(\mathbf{K}_p\mathbf{C} + \mathbf{K}_d\mathbf{C}\mathbf{A}\right) \tag{30}$$

$$\bar{\mathbf{K}}_i = (\mathbf{I}_m + \mathbf{K}_d\mathbf{C}\mathbf{B})^{-1}\mathbf{K}_i \tag{31}$$

$$\mathbf{u}_r = \left(\mathbf{K}_p\mathbf{r} + \mathbf{K}_i\int \mathbf{r}dt + \mathbf{K}_d\dot{\mathbf{r}} + \right) \tag{32}$$

Eq. (29) demonstrates that the output feedback with the PID controller resembles any state feedback controller. However, the integral term ∫**y**dt appears as a new state variable in Eq. (29). The new state variable is then defined as follows.

$$\mathbf{x}_{new} = \int_0^t \mathbf{y}dt \tag{33}$$

The variable then

$$\dot{\mathbf{x}}_{new} = \mathbf{y} = \mathbf{C}\mathbf{x} \tag{34}$$

The augmented state vector of the system is defined as

$$\bar{\mathbf{x}} = \begin{bmatrix}\mathbf{x} \\ \mathbf{x}_{new}\end{bmatrix} \tag{35}$$

The augmented system may now be described as

$$\dot{\bar{\mathbf{x}}} = \bar{\mathbf{A}}\bar{\mathbf{x}} + \bar{\mathbf{B}}\mathbf{u} \tag{36}$$

The augmented system matrix $\bar{\mathbf{A}}$ and $\bar{\mathbf{B}}$ are described by

$$\bar{\mathbf{A}} = \begin{bmatrix} \mathbf{A} & 0_{n\times m} \\ \mathbf{C} & 0_{m\times m} \end{bmatrix}, \bar{\mathbf{B}} = \begin{bmatrix} \mathbf{B} \\ 0_{m\times r} \end{bmatrix} \tag{37}$$

The substituting Eq. (35) into the control input Eq. (29) is then,

$$\mathbf{u} = \mathbf{u}_r - \mathbf{K}_{pid}\bar{\mathbf{x}} \tag{38}$$

where $\mathbf{K}_{pid} = \begin{bmatrix} \bar{\mathbf{K}}_p & \bar{\mathbf{K}}_i \end{bmatrix}$. Substituting the Eq. (42) into (36) gives

$$\dot{\bar{\mathbf{x}}} = \left(\bar{\mathbf{A}} - \bar{\mathbf{B}}\mathbf{K}_{pid}\right)\bar{\mathbf{x}} + \bar{\mathbf{B}}\mathbf{u}_r \tag{39}$$

The eigenvalues of $\bar{\mathbf{A}} - \bar{\mathbf{B}}\mathbf{K}_{pid}$ are placed in the left half of the complex s-plane for asymptotically stable. The performance index of the form given by Eq. (36)

$$J_{pid} = \int_{t_0}^{t_1} (\bar{\mathbf{x}}^T\bar{\mathbf{Q}}\bar{\mathbf{x}} + \mathbf{u}^T\mathbf{R}\mathbf{u})dt \tag{40}$$

the desired optimal control

$$\mathbf{u}^* = -\mathbf{R}^{-1}\bar{\mathbf{B}}^T\bar{\mathbf{P}}\bar{\mathbf{x}} \tag{41}$$

where the matrix $\bar{\mathbf{P}}$ is defined as

$$\bar{\mathbf{P}}\bar{\mathbf{A}} + \bar{\mathbf{A}}^T\bar{\mathbf{P}} - \bar{\mathbf{P}}\bar{\mathbf{B}}\mathbf{R}^{-1}\bar{\mathbf{B}}^T\bar{\mathbf{P}} + \bar{\mathbf{Q}} = 0 \tag{42}$$

where $\bar{\mathbf{Q}} \in \Re^{(n+m)\times(n+m)}$ extended state weight matrix. Comparing the Eq. (29) and Eq. (41) concluded

$$\begin{bmatrix} \bar{\mathbf{K}}_p & \bar{\mathbf{K}}_i \end{bmatrix} = \mathbf{R}^{-1}\bar{\mathbf{B}}^T\bar{\mathbf{P}} \tag{43}$$

where $\bar{\mathbf{K}}_p \in \Re^{r\times n}$ and $\bar{\mathbf{K}}_i \in \Re^{r\times m}$. Once Eq. (43) is obtained, the controller coefficients are all calculated as following expressions

$$[\mathbf{K}_p \quad \mathbf{K}_d] = \bar{\mathbf{K}}_p\bar{\mathbf{C}}^T(\bar{\mathbf{C}}\bar{\mathbf{C}}^T)^{-1} \tag{44}$$

where $\bar{\mathbf{C}} = \begin{bmatrix} \mathbf{C}^T & \left(\mathbf{CA} - \mathbf{CB}\bar{\mathbf{K}}_p\right)^T \end{bmatrix}^T$ and

$$\mathbf{K}_i = (\mathbf{I}_m + \mathbf{K}_d\mathbf{CB})\bar{\mathbf{K}}_i \tag{45}$$

The last two equations conclude optimal PID controller parameters.

2.4. Controller with Optimal Sliding Mode

In this section, it will be demonstrated only how to provide optimality to the sliding mode controller. Variable structure system control theory is a relatively comprehensive subject. The most pioneer works on this subject belong to Utkin (1977, 1992, 1993) and Utkin and Parnakh (1978).

SMC involves bringing the instantaneous states of the system onto the sliding or switching surface created from state variables and keeping them there. The integrated error dynamics should be considered by appending them to the error variable vector. ISMC's subject is concerned with the robustness of the SMC. Readers are referred to Utkin et al. (2009) for details. The augmented error dynamic vector is as follows.

$$\tilde{\mathbf{x}}_{ismc} = \begin{bmatrix} \tilde{\mathbf{x}} \\ \int \tilde{\mathbf{x}} dt \end{bmatrix} \tag{46}$$

The error dynamics equation then becomes as follows by combining integrated error, $\int \tilde{\mathbf{x}} dt$, and Eq. (11).

$$\underbrace{\frac{d}{dt}\begin{bmatrix} \tilde{\mathbf{x}} \\ \int \tilde{\mathbf{x}} dt \end{bmatrix}}_{\dot{\tilde{\mathbf{x}}}_{ismc}} = \underbrace{\begin{bmatrix} \mathbf{A} & 0_{n\times n} \\ \mathbf{I}_{n\times n} & 0_{n\times n} \end{bmatrix}}_{\mathbf{A}_{ismc}} \underbrace{\begin{bmatrix} \tilde{\mathbf{x}} \\ \int \tilde{\mathbf{x}} dt \end{bmatrix}}_{\tilde{\mathbf{x}}_{ismc}} + \underbrace{\begin{bmatrix} \mathbf{B} \\ 0_{n\times r} \end{bmatrix}}_{\mathbf{B}_{ismc}} \tilde{\mathbf{u}} \tag{47}$$

The regular form is the most canonic form used for SMC for linear systems. Consider the nominal linear model error dynamic and their integrated variables are given by Eq. (47). ($\mathbf{A}_{ismc}$, $\mathbf{B}_{ismc}$) is a controllable pair and rank($\mathbf{B}_{ismc}$)=η. The sliding surface function

$$s(t) = \boldsymbol{\sigma}\tilde{\mathbf{x}}_{ismc}(t) \tag{48}$$

where $\boldsymbol{\sigma} \in \Re^{\eta\times 2n}$ is the sliding surface coefficient vector and $s(t)$ is a scalar function.

The dynamic equation of the linear system, defined by Eq. (1)-(2), may be separated into subsystems; only one includes a control signal. A non-singular transformation is used with an orthogonal matrix **T**, to transform the system into the regular form,

$$\mathbf{z}(t) = \mathbf{T}\tilde{\mathbf{x}}_{ismc}(t) \tag{49}$$

Taking derivatives of Eq. (49) and substituting into (47), the following regular form obtained

$$\dot{\mathbf{z}}_1(t) = \mathbf{A}_{11}\mathbf{z}_1(t) + \mathbf{A}_{12}\mathbf{z}_2(t) \tag{50}$$

$$\dot{\mathbf{z}}_2(t) = \mathbf{A}_{21}\mathbf{z}_1(t) + \mathbf{A}_{22}\mathbf{z}_2(t) + \mathbf{B}_2\mathbf{u}(t) \tag{51}$$

where $\mathbf{A}_{11} \in \Re^{(2n-\eta)\times(2n-\eta)}$, $\mathbf{A}_{12} \in \Re^{(2n-\eta)\times 2\eta}$ and $\mathbf{A}_{21} \in \Re^{\eta\times(2n-\eta)}$, $\mathbf{A}_{22} \in \Re^{\eta\times\eta}$ are all sub-block matrices of transformed **A** matrix. $\mathbf{B}_2$ is η dimensional matrix. $\mathbf{z}_1 \in \Re^{(2n-\eta)\times 1}$ and $\mathbf{z}_2 \in \Re^{\eta\times 1}$ are sub-block vectors. This method is called the decoupling principle as well. The matrix sub-blocks in Eq. (50)-(51),

$$\mathbf{T}\mathbf{A}_{ismc}\mathbf{T}^T = \begin{bmatrix} \mathbf{A}_{11} & \mathbf{A}_{12} \\ \mathbf{A}_{21} & \mathbf{A}_{22} \end{bmatrix}, \qquad \mathbf{T}\mathbf{B}_{ismc} = \begin{bmatrix} 0 \\ \mathbf{B}_2 \end{bmatrix} \tag{52}$$

Transformation matrix **T** is an orthogonal matrix and can be calculated by QR decomposition (Golub & Loan, 2013). This is useful to get the decomposition of the input matrix. The sliding surface is written as

$$s(t) = \underbrace{\boldsymbol{\sigma}\mathbf{T}^T}_{\mathbf{S}}\mathbf{z} = \mathbf{S}\mathbf{z} = [\mathbf{S}_1 \quad \mathbf{S}_2]\begin{bmatrix}\mathbf{z}_1\\ \mathbf{z}_2\end{bmatrix} = \mathbf{S}_1\mathbf{z}_1(t) + \mathbf{S}_2\mathbf{z}_2(t) \tag{53}$$

where the $\mathbf{S}_1 \in \Re^{\eta\times(2n-\eta)}$ and $\mathbf{S}_2 \in \Re^{\eta\times\eta}$ sub-vector of $\mathbf{S}$.

The switching function $s(t)$ equals zero during the sliding motion. Eq. (53) is then equal to zero.

$$\mathbf{S}_1\mathbf{z}_1(t) + \mathbf{S}_2\mathbf{z}_2(t) = 0 \tag{54}$$

The variable $\mathbf{z}_2$ is left alone,

$$\mathbf{z}_2 = -\mathbf{S}_2^{-1}\mathbf{S}_1\mathbf{z}_1 \tag{55}$$

Eq. (55) is substituted into the Eq. (50) yields,

$$\dot{\mathbf{z}}_1 = [\mathbf{A}_{11} - \mathbf{A}_{12}\mathbf{S}_2^{-1}\mathbf{S}_1]\mathbf{z}_1 \tag{56}$$

To provide asymptotically stability of the system given by Eq. (56), the eigenvalues of $[\mathbf{A}_{11} - \mathbf{A}_{12}\mathbf{S}_2^{-1}\mathbf{S}_1]$ partition must be at the left-half s-plane. The unknown partition $\mathbf{S}_2^{-1}\mathbf{S}_1$ can be calculated by employing the pole placement or optimal control methods. $\mathbf{S}_2$ may be chosen as a non-singular matrix and calculated according to $\mathbf{S}_1$. The equation below will be employed for the calculation of $\boldsymbol{\sigma}$ vector

$$s(t) = \mathbf{S}\mathbf{z} = \underbrace{\mathbf{S}\mathbf{T}}_{\boldsymbol{\sigma}}\tilde{\boldsymbol{x}}_{ismc} = \boldsymbol{\sigma}\tilde{\boldsymbol{x}}_{ismc} \tag{57}$$

When the state variables are not on the sliding surface, there is a need for a reaching rule to drive the state variables onto the sliding surface. In Gao and Hung (1993) proposed a reaching law called a constant plus proportional rate.

$$\dot{s}(t) = -\rho \cdot sign\big(s(t)\big) - k \cdot s \tag{58}$$

where ρ>0 and k>0. The constant parameter k within the signum function balances the convergence rate during the reaching phase and the magnitude of oscillations experienced during the sliding phase. The introduction of the proportional component enhances convergence rates for larger sliding variable values, allowing for a reduction in the coefficient ρ without compromising the favorable aspects during the reaching mode. Conversely, as the sliding surface is approached, the impact of the proportional term diminishes, effectively mitigating the potential for increased oscillations during the sliding phase.

Eq. (58) will equal zero, while the state variables are on the sliding surface. Eq. (47) is substituted into the derivative of Eq. (57). The resulting outcome is equated with Eq. (58). The control input $\mathbf{u}_{ismc}$ is then left alone by considering $\tilde{\mathbf{u}} = \mathbf{u}_{ismc} - \mathbf{u}_d$, and the SMC input rule is obtained as follows.

$$\mathbf{u}_{ismc} = \mathbf{u}_d - (\boldsymbol{\sigma}\mathbf{B}_{ismc})^{-1}[\boldsymbol{\sigma}(k\mathbf{I} + \mathbf{A}_{ismc})\tilde{\mathbf{x}}_{ismc} + \rho \cdot sign(s)] \tag{59}$$

where $\mathbf{u}_d$ is defined by Eq. (8).

This subsection discusses the calculation of the $\mathbf{S}$ vector according to the minimizing cost function criterion. Utkin and Yang (1978) proposed this method as quadratic minimization. It is possible to reach the details (Utkin, 1992; Edwards & Spurgeon, 1998).

SMC action includes two modes: the first is to bring state variable values onto the switching surface. The second mode is to keep all state variables at the sliding surface. Once the second mode is satisfied, the sliding surface equation equals zero. Sliding mode motion does not depend on control input and is defined by the equation of sliding surface. Eq. (3) is not suited to the sliding motion optimality criterion. Control-independent the functional optimality criterion,

$$J_{ismc} = \int_{t_0}^{t_1} (\tilde{\mathbf{x}}_{ismc})^T \mathbf{Q}_{ismc} \tilde{\mathbf{x}}_{ismc} dt \tag{60}$$

It is presumed that the system's state at time t_0, $\mathbf{x}(t_0)$ is a known initial condition and is such that $\mathbf{x}(t)\rightarrow 0$ as $t\rightarrow\infty$. It is needed to be determined that the optimal m-dimensional control system Eq. (50)-(51) with vector $\mathbf{z}_2=(\mathbf{S}_2)^{-1}\mathbf{S}_1\mathbf{z}_1$ as control and criterion (60) is represented according to (49) transformation.

$$\mathbf{T}\mathbf{Q}_{ismc}\mathbf{T}^T = \begin{bmatrix} \mathbf{Q}_{11} & \mathbf{Q}_{12} \\ \mathbf{Q}_{21} & \mathbf{Q}_{22} \end{bmatrix}, \quad \mathbf{Q}_{21} = \mathbf{Q}_{12}^T \tag{61}$$

The optimality criterion (60) may then be expressed regarding the **T** transformation.

$$J_{ismc} = \int_{t_0}^{t_1} (\mathbf{z}_1^T \mathbf{Q}_{11} \mathbf{z}_1 + 2\mathbf{z}_1^T \mathbf{Q}_{12} \mathbf{z}_2 + \mathbf{z}_2^T \mathbf{Q}_{22} \mathbf{z}_2) dt \tag{62}$$

It is required to reform Eq. (62) in the standard LQR problem as Eq. (3). Thus, it is necessary to eliminate the cross term $2(\mathbf{z}_1)^T\mathbf{Q}_{12}\mathbf{z}_2$. The last two in Eq. (62) may be regarded as yield.

$$2\mathbf{z}_1^T \mathbf{Q}_{12} \mathbf{z}_2 + \mathbf{z}_2^T \mathbf{Q}_{22} \mathbf{z}_2 = (\mathbf{z}_2 + \mathbf{Q}_{22}^{-1}\mathbf{Q}_{21}\mathbf{z}_1)^T \mathbf{Q}_{22} (\mathbf{z}_2 + \mathbf{Q}_{22}^{-1}\mathbf{Q}_{21}\mathbf{z}_1) - \mathbf{z}_1^T \mathbf{Q}_{21}^T \mathbf{Q}_{22}^{-1} \mathbf{Q}_{21} \mathbf{z}_1 \tag{63}$$

It is forthright to authenticate that Eq. (62) can be reformed as

$$J_{ismc} = \int_{t_s}^{\infty} \left(\mathbf{z}_1^T (\mathbf{Q}_{11} - \mathbf{Q}_{12}\mathbf{Q}_{22}^{-1}\mathbf{Q}_{21}) \mathbf{z}_1 + (\mathbf{z}_2 + \mathbf{Q}_{22}^{-1}\mathbf{Q}_{21}\mathbf{z}_1)^T \mathbf{Q}_{22} (\mathbf{z}_2 + \mathbf{Q}_{22}^{-1}\mathbf{Q}_{21}\mathbf{z}_1) \right) dt \tag{64}$$

Define

$$\acute{\mathbf{Q}} = \mathbf{Q}_{11} - \mathbf{Q}_{12}\mathbf{Q}_{22}^{-1}\mathbf{Q}_{21} \tag{65}$$

$$\mathbf{v} = \mathbf{z}_2 + \mathbf{Q}_{22}^{-1}\mathbf{Q}_{21}\mathbf{z}_1 \tag{66}$$

Eq. (64) can then be written as

$$J_{ismc} = \int_{t_s}^{\infty} \left(\mathbf{z}_1^T \acute{\mathbf{Q}} \mathbf{z}_1 + \mathbf{v}^T \mathbf{Q}_{22} \mathbf{v} \right) \tag{67}$$

Recall the original transformed Eq. (50). Taking $\mathbf{z}_2$ alone in Eq. (66) and substituting it into Eq. (50),

$$\dot{\mathbf{z}}_1 = (\mathbf{A}_{11} - \mathbf{A}_{12}\mathbf{Q}_{22}^{-1}\mathbf{Q}_{21})\mathbf{z}_1 + \mathbf{A}_{12}\mathbf{v} \tag{68}$$

Hence, the problem turns into minimizing the Eq. (67) subject to the system (68). The problem also can be interpreted as a standard LQR problem. The positive definiteness of $\mathbf{Q}_{ismc}$ ensures that $\mathbf{Q}_{22}>0$ so that the pair ($\mathbf{A}_{ismc}$, $\mathbf{B}_{ismc}$) is controllable. Thus, matrix $\mathbf{P}_{ismc}$ being the unique solution to the matrix Riccati equation,

$$\begin{aligned} \mathbf{P}_{ismc}(\mathbf{A}_{11} - \mathbf{A}_{12}\mathbf{Q}_{22}^{-1}\mathbf{Q}_{12}^T) + (\mathbf{A}_{11} - \mathbf{A}_{12}\mathbf{Q}_{22}^{-1}\mathbf{Q}_{12}^T)^T \mathbf{P}_{ismc} - \mathbf{P}_{ismc}\mathbf{A}_{12}\mathbf{Q}_{22}^{-1}\mathbf{A}_{12}^T\mathbf{P}_{ismc} \\ + (\mathbf{Q}_{11} - \mathbf{Q}_{12}\mathbf{Q}_{22}^{-1}\mathbf{Q}_{12}^T) = 0 \end{aligned} \tag{69}$$

The optimal **v** minimizing Eq. (67) is as follows,

$$\mathbf{v} = -\mathbf{Q}_{22}^{-1}\mathbf{A}_{12}^{T}\mathbf{P}_{ismc}\mathbf{z}_1 \tag{70}$$

This expression is substituted into (66)

$$\mathbf{z}_2 = -\mathbf{Q}_{22}^{-1}(\mathbf{A}_{12}^{T}\mathbf{P}_{ismc} + \mathbf{Q}_{21})\mathbf{z}_1 \tag{71}$$

Comparing Eq. (71) with (55) yields,

$$\mathbf{S}_2^{-1}\mathbf{S}_1 = \mathbf{Q}_{22}^{-1}(\mathbf{A}_{12}^{T}\mathbf{P}_{ismc} + \mathbf{Q}_{21}) \quad \Longrightarrow \quad \mathbf{S}_1 = \mathbf{S}_2\mathbf{Q}_{22}^{-1}(\mathbf{A}_{12}^{T}\mathbf{P}_{ismc} + \mathbf{Q}_{21}) \tag{72}$$

The non-singular $\mathbf{S}_2$ is chosen arbitrarily, and then $\mathbf{S}_1$ is calculated. Finally, matrix $\mathbf{S}$= [$\mathbf{S}_1$ $\mathbf{S}_2$] is created, and the optimal sliding surface is obtained by substituting **S** into Eq. (57).

In summary, all calculation step by step is as follows: First, the orthogonal transformation matrix **T** is determined. The regular form of the system equation (47) is determined by Eq. (49)-(51). The sub-matrices are determined by Eq. (52). The sub-matrices of the transformed matrix $\mathbf{Q}_{ismc}$ are determined by Eq. (61). The matrix Riccati Eq. (69) concerning $\mathbf{P}_{ismc}$ is solved. By considering $\mathbf{S}_2$ as an identity matrix, Eq. (72) is solved, and **S** is obtained. The optimal surface vector $\boldsymbol{\sigma}$ is determined by Eq. (57). Finally, the positive constants k and ρ are chosen large enough, and all findings are substituted into Eq. (59).

3. DC SERVO MACHINE MATHEMATICAL MODEL

The linear quadratic algorithms discussed in this paper are all implemented in linear systems. DC servo motor is one of the prevalent devices used to control a system. The performance of the algorithms can be examined by implementing any DC servo motor. Under this heading, the mathematical model of the DC motor is discussed.

DC servo motor consists of two separate partitions. The stator includes field windings. The other partition has armature windings. The right sight of Figure 5 presents the armature circuit partition of the DC motor. The other side presents the field circuit partition (Krishnan, 2001; Krause et al., 2002).

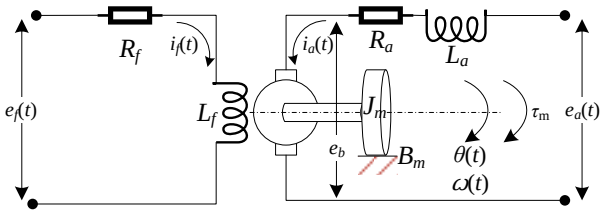

Figure 5*. DC servo motor electromechanical diagram*

Air gap flux Φ is proportional to field current i_f,

$$\Phi = K_{fd}i_f \tag{73}$$

where K_{fd} is the constant between field current, i_f, and gap flux Φ, namely field coil constant. The rotor shaft generates τ_m torque, proportional to the product of air gap flux and the armature current.

$$\tau_m(t) = \Phi K_{am}i_a(t) \tag{74}$$

where K_{am} is the armature coil constant. Substituting (73) into (74) yields

$$\tau_m(t) = K_a i_a(t) \tag{75}$$

where the overall armature constant K_a is

$$K_a = K_{fd} K_{am} i_f \tag{76}$$

The armature behaves like a generator which produces a back electromotive force $e_b(t)$ while the armature is rotating. It is also proportional to the shaft angular velocity $\omega(t)$.

$$e_b(t) = K_b \frac{d\theta(t)}{dt} = K_b \omega(t) \tag{77}$$

where K_b is back electromotive force constant. There is a potential difference between the armature windings leads.

$$e_a(t) - e_b(t) = L_a \frac{di_a}{dt} + R_a i_a \tag{78}$$

where $e_a(t)$ is the applied armature voltage, R_a is the electrical resistance of the armature circuit, i_a the armature current, and L_a is the armature circuit's electrical inductance. Substituting Eq. (77) into (78) and taking the derivative of armature current alone yields

$$\frac{di_a(t)}{dt} = -\frac{K_b}{L_a}\omega(t) - \frac{R_a}{L_a} i_a(t) + \frac{1}{L_a} e_a(t) \tag{79}$$

The rotor partition produces the mechanical movement of the motor. The algebraic sum of all torques, τ, equals the product of inertia torque J_m and angular acceleration α.

$$\sum \tau = J_m \propto \tag{80}$$

The total torque consists of electrical torque, friction torque (proportional to angular velocity and opposite to electrical torque), and load torque (opposite in direction). Thus, Eq. (80) is expressed again as,

$$\tau_m - \tau_L - B_m \omega(t) = J_m \propto \tag{81}$$

where τ_L is load torque, B_m is motor viscous friction constant. Substituting Eq. (75) into Eq. (81) and isolating the angular acceleration alone concludes as follows,

$$\propto (t) = -\frac{B_m}{J_m}\omega(t) + \frac{K_a}{J_m} i_a(t) - \frac{1}{J_m}\tau_L \tag{82}$$

There is a differential relationship between angular acceleration α, angular velocity ω, and angular position θ as follows,

$$\alpha(t) = \frac{d^2}{dt^2}\theta(t), \qquad \omega(t) = \frac{d}{dt}\theta(t) \tag{83}$$

The following equation is obtained by substituting Eq. (83) into Eq. (82).

$$\frac{d^2}{dt^2}\theta(t) = \frac{d}{dt}\omega(t) = -\frac{B_m}{J_m}\omega(t) + \frac{K_a}{J_m}i_a(t) - \frac{1}{J_m}\tau_L \tag{84}$$

The state space model can be created by combining Eq. (83), (84), and Eq. (79).

$$\frac{d}{dt}\begin{bmatrix}\theta(t)\\ \omega(t)\\ i_a(t)\end{bmatrix} = \begin{bmatrix}0 & 1 & 0\\ 0 & -\frac{B_m}{J_m} & \frac{K_a}{J_m}\\ 0 & -\frac{K_b}{L_a} & -\frac{R_a}{L_a}\end{bmatrix}\begin{bmatrix}\theta(t)\\ \omega(t)\\ i_a(t)\end{bmatrix} + \begin{bmatrix}0 & 0\\ -\frac{1}{J_m} & 0\\ 0 & \frac{1}{L_a}\end{bmatrix}\begin{bmatrix}\tau_L\\ e_a\end{bmatrix} \tag{85}$$

The output equation of the system,

$$\mathbf{y} = [1 \quad 0 \quad 0]\begin{bmatrix}\theta(t)\\ \omega(t)\\ i_a(t)\end{bmatrix} \tag{86}$$

The system matrices are as follows,

$$\mathbf{x} = \begin{bmatrix}\theta(t)\\ \omega(t)\\ i_a(t)\end{bmatrix}, \quad \mathbf{A} = \begin{bmatrix}0 & 1 & 0\\ 0 & -\frac{B_m}{J_m} & \frac{K_a}{J_m}\\ 0 & -\frac{K_b}{L_a} & -\frac{R_a}{L_a}\end{bmatrix}, \quad \mathbf{B} = \begin{bmatrix}0 & 0\\ -\frac{1}{J_m} & 0\\ 0 & \frac{1}{L_a}\end{bmatrix}, \mathbf{u} = \begin{bmatrix}\tau_L\\ e_a\end{bmatrix}, \quad \mathbf{C} = [1 \quad 0 \quad 0] \tag{87}$$

The load torque is not an ordinary input; it may be considered a disturbance. Thus, the matrix **B** and vector **u** change as follows.

$$\mathbf{B} = \begin{bmatrix}0\\ 0\\ \frac{1}{L_a}\end{bmatrix}, \mathbf{u} = e_a \tag{88}$$

4. COMPUTATIONAL FINDINGS

This section presents numerical results by applying the control strategies discussed in the previous subsections to the DC motor's mathematical model.

4.1. Motor Model and Parameter Rates

The DC motor parameter rates, which are used to examine the performance of the LQR-based algorithms in the section above, are as follows:

Voltage supply=240 V, Rated current=10 A, B_m=0.002953 N·m·s, J_m=0.02215 kg·m^2,
K_a=1.011 N·m/A, K_b=1.011 V/(rad/s), L_a=0.028 H, R_a=2.581 Ω

According to the parameter rates above, the DC motor system matrices are as follows,

$$\mathbf{A} = \begin{bmatrix}0 & 1 & 0\\ 0 & -0.1333 & 45.6433\\ 0 & -36.1071 & -92.1786\end{bmatrix}, \quad \mathbf{B} = \begin{bmatrix}0\\ 0\\ 35.7143\end{bmatrix}, \quad \mathbf{C} = [1 \quad 0 \quad 0] \tag{89}$$

4.2. LQR Controller Calculations

To obtain optimal state feedback gain matrix, using the matrices and vector in Eq. (89), the Eq. (6) and Eq. (14) are calculated respectively. The state and input weight matrices are chosen as **Q**=diag([1 1 1]) and **R**=1. The solutions of Eq. (6) and Eq. (14) are as Eq. (90) and (91), respectively.

$$\mathbf{P}_{\boldsymbol{lqr}} = \begin{bmatrix} 1.4723 & 0.0651 & 0.0280 \\ 0.0651 & 0.0375 & 0.0127 \\ 0.028 & 0.0127 & 0.0109 \end{bmatrix} \tag{90}$$

$$\mathbf{K}_{\boldsymbol{lqr}} = [1 \quad 0.4526 \quad 0.3886] \tag{91}$$

Eq. (91) is substituted into Figure 2, and the linear quadratic state feedback application works. However, the reference desired input vector $\mathbf{x}_d$ must be calculated by considering the derivative of state variables in Eq. (85) equals zero. In addition, the load torque is deemed a disturbance, so it is considered zero, too.

$$\mathbf{x}_d = \begin{bmatrix} \theta_d \\ 0 \\ 0 \end{bmatrix} \tag{92}$$

θ_d is the desired angular position.

4.3. LQR With Integral Control Calculations

The optimal linear quadratic gain matrix is obtained by making extended matrices in Eq. (23) and solving Eq. (26)-(27), respectively. The state and input weight matrices are decided upon as $\mathbf{Q}_{lqri}$=diag([1 1 1 1]) and $\mathbf{R}$=1. The extended matrices are as follows,

$$\mathbf{A}_{lqri} = \begin{bmatrix} 0 & 1 & 0 & 0 \\ 0 & -0.13 & 45.65 & 0 \\ 0 & -36.1071 & -92.1786 & 0 \\ -1 & 0 & 0 & 0 \end{bmatrix}, \qquad \mathbf{B}_{lqri} = \begin{bmatrix} 0 \\ 0 \\ 35.7143 \\ 0 \end{bmatrix} \tag{93}$$

The solutions of Eq. (26) and Eq. (27) are as follows.

$$\mathbf{P}_{lqri} = \begin{bmatrix} 2.9797 & 0.1309 & 0.0562 & -1.5164 \\ 0.1309 & 0.0404 & 0.0139 & -0.0655 \\ 0.0562 & 0.0139 & 0.0114 & -0.0280 \\ -1.5164 & -0.0655 & -0.0280 & 2.0082 \end{bmatrix} \tag{94}$$

$$\mathbf{K}_x = [2.0082 \quad 0.4967 \quad 0.4075], \qquad \mathbf{K}_{in} = -1 \tag{95}$$

$\mathbf{K}_{in}$ and $\mathbf{K}_x$ are substituted into Figure 3, and LQR with integral action can be realized.

4.4. Optimal PID Controller Calculations

The designing PID controller consists of calculating the controller parameters so that the system behaves as desired. The desired behavior may require an optimized control input or settling time optimization. This subsection proposes designing an optimal PID controller equivalent to an optimal state feedback controller. The optimal PID controller algorithm works based on the sequential calculation of equations Eq. (42)-(45). The state and input weight matrices are selected to serve as $\bar{\mathbf{Q}}$=diag([1 1 1 1]) and $\mathbf{R}$=1. The output of the algorithm allows the optimal PID controller to gain matrices. According to the system matrices (89), the algorithm's output gives the controller gains as $\mathbf{K}_p$=2.0082, $\mathbf{K}_i$=1, and $\mathbf{K}_d$=0.4967. This output is substituted into the block diagram in Figure 4, and the optimal PID algorithm works.

4.5 Optimal Sliding Mode

The whole solution algorithm is discussed in the final paragraph in section 0. The state and input weight matrices are utilized due to their purpose as $\mathbf{Q}_{ismc}$=diag([1 1 1 1 1 1]) and $\mathbf{R}$=1. According to the suggested solution, all calculations give the following results:

$$\mathbf{P}_{ismc} = \begin{bmatrix} 2 & 803 & 0 & 803 & -112 \\ 803 & -5277 & 0 & -5170 & -36650 \\ 0 & 0 & 0 & 0 & 0 \\ 803 & -517 & 0 & -5063 & -36665 \\ -112 & -3.665 & 0 & -3.6665 & 5106 \end{bmatrix} \cdot 10^4 \quad (96)$$

$$\mathbf{S} = [-1.0407 \quad 2.0217 \quad -1 \quad 0 \quad 0 \quad 0] \quad (97)$$

$$\boldsymbol{\sigma} = [-2.0217 \quad -1.0407 \quad -1 \quad -1 \quad 0 \quad 0] \quad (98)$$

Eq. (98) is substituted into Eq. (59), and the control signal is applied to the system. k and ρ constants should be selected large enough. They are selected as 50 and 5, respectively.

5. SIMULATION RESULTS

The illustrative results are related to the optimal control algorithms presented in previous sections.

Figure 6 demonstrates the step response of the DC motor for which the parameters are presented in Section 0. The armature voltage is chosen as 240 V as the step function input. The field windings are supplied with 300 V to provide magnetization. The field current is measured as 1.0665 A. Figure 6a shows the angular replacement of the DC motor shaft. It also seems it does not have a settling time of angular position. Figure 6b illustrates that the angular speed of the DC motor reaches the stable speed of 234.3 rad/s in 0.2 seconds.

The system appears unstable when the DC motor is considered a system with armature voltage as the input and angular position as the output. It is also insensitive to disturbances and load torque. Elimination of the lack of robustness, the controllers are required to be used.

Figure 7 demonstrates the simulation result of the whole DC motor control system. The reference angular speed is chosen as θ_d=π/2 radian and applied to the control system as a step function beginning at the end of the first second. Figure 7a shows that the optimal PID controller and ISMC respond with overshoot. However, the other controllers have responses without overshoot. All angular position responses settle in about five seconds. The load torque equals zero at the beginning. As seen in Figure 7e, the load torque is applied to the system as a disturbance input T_L=0.5 Nm at the 15th second—all optimal control algorithms respond to the load torque disturbance input except the LQR. The optimal control algorithms' robustness is caused by the integral term used in LQRI, PID, and ISMC. LQR seems to have no robustness against load disturbance, resulting in a collapsing position control response after 15 seconds. However, the other controllers have robust responses, so their responses settle in about six seconds with no steady-state error. Figure 7b depicts the angular velocity derivative of the angular position. It reaches zero speed within six seconds. Figure 7c shows the armature current, which has a settling time of less than three seconds. Figure 7d illustrates the system signal's control signal. It seems the most reactive behavior belongs to the ISMC. It has the chattering phenomena by its nature. Once the load torque is applied to the system, all algorithms exhibit nearly identical behaviors except the LQR.

The variations in the values of cost functions within the first 15 seconds are shown in Figure 8. The cost function associated with the PID controller exhibits a notably faster increase than the others. Over time, the cost function that increases at the slowest rate is attributed to the LQR controller.

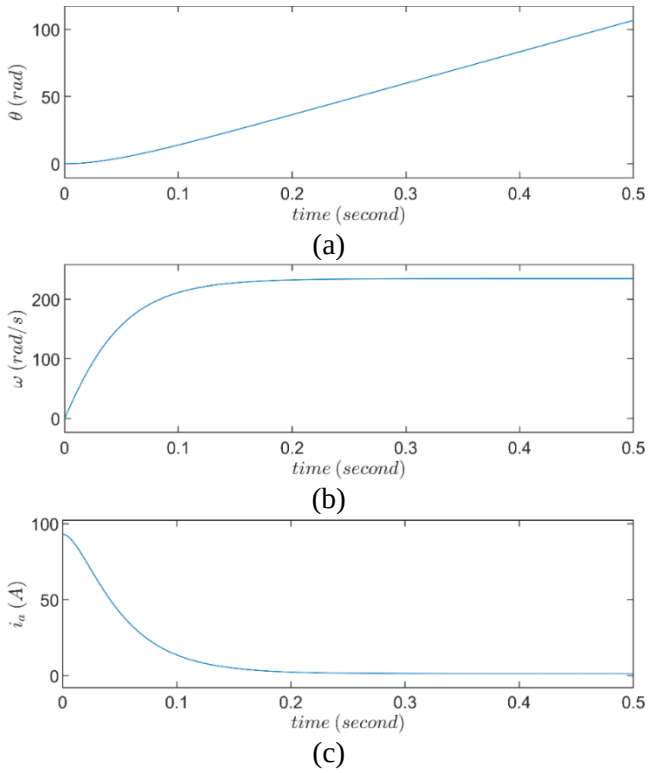

***Figure 6**. DC motor step response of the state variables when the e_a=240 V and e_f=300 V. **a)** angular position **b)** angular speed **c)** armature current*

6. CONCLUSIONS

The study explicates some optimal control techniques and depicts their performances by implementing the DC motor for position control. LQR-based control does not perform as robustly as other controllers. When the load torque is applied as a disturbance, the ISMC behaves robustly for angular position control. A single LQR-based controller does not seem as robust and sufficient as it can eliminate the disturbance-based error. However, LQR with an integral action controller eliminates the error. Besides, the other control algorithms seem to possess similar robustness.

This study's comparative analysis is crucial in selecting the robust and optimal controller. The LQR control includes the least number of terms, but it does not have enough robustness. LQRI action contains an extra state variable term compared to the single LQR. The optimal PID controller needs to have an extra one-state variable. The ISMC contains a state variable two times more than the original system, but the robustness seems acceptable.

The DC motor model, which has three state variables, is used for examining the algorithms. LQR and ISMC controllers need all system state variables to be measurable or observable. However, the optimal PID controller needs only output to be measurable. This situation necessitates obtaining all state variables through estimation when LQR and SMC-based algorithms are employed. This study considers all DC motor state variables measurable or observable. At the same time, LQR and SMC-based algorithms are employed.

The optimal algorithms are designed for a linear system. Employing the optimal algorithms with observers for nonlinear systems and time-delayed systems can be a future work. Luenberger filter or Kalman filter are well-known observers for obtaining the unmeasurable state variables of any system. Using optimal control algorithms with observers will provide more detailed information about their usability.

In applications requiring time optimization, the power applied to the system input does not need to be limited. Optimal control will be helpful, especially in systems requiring energy saving and power and mechanical energy applications.

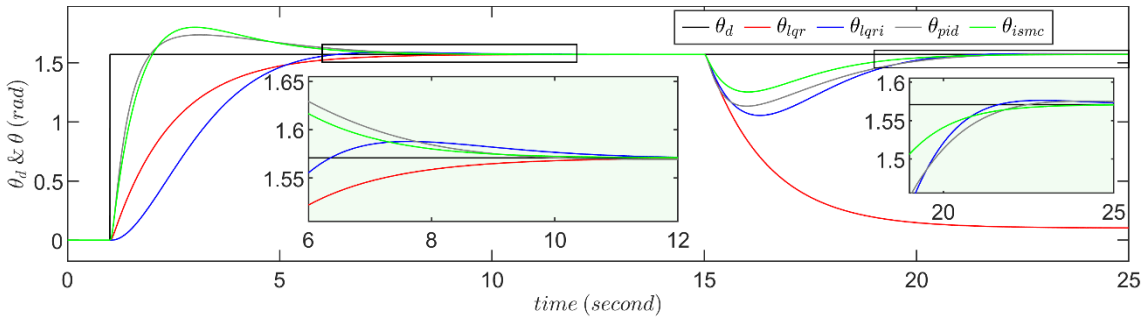

(a)

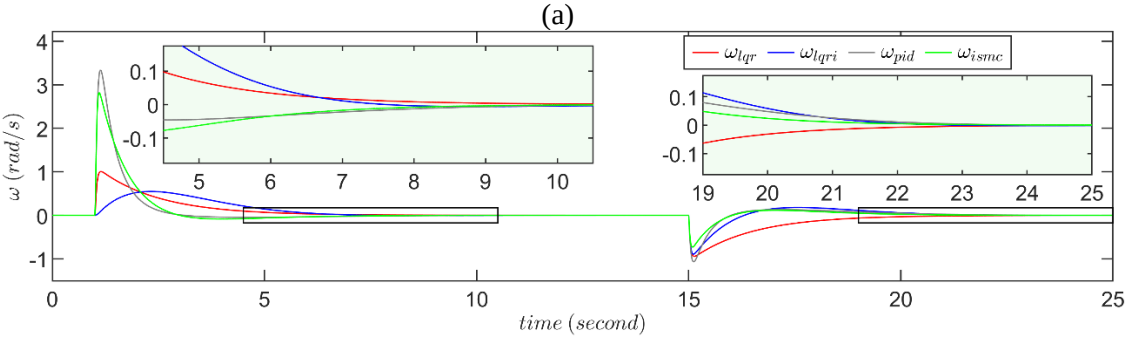

(b)

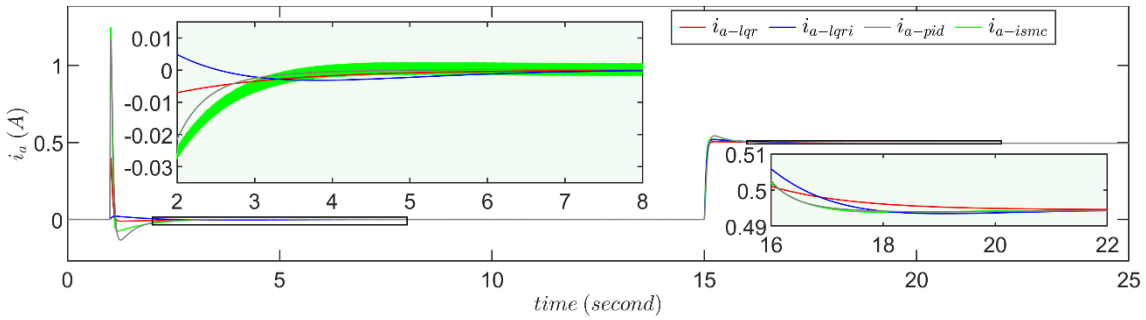

(c)

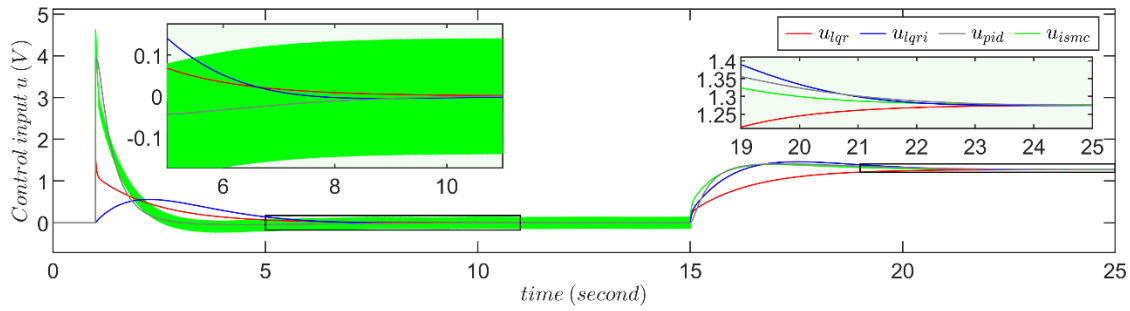

(d)

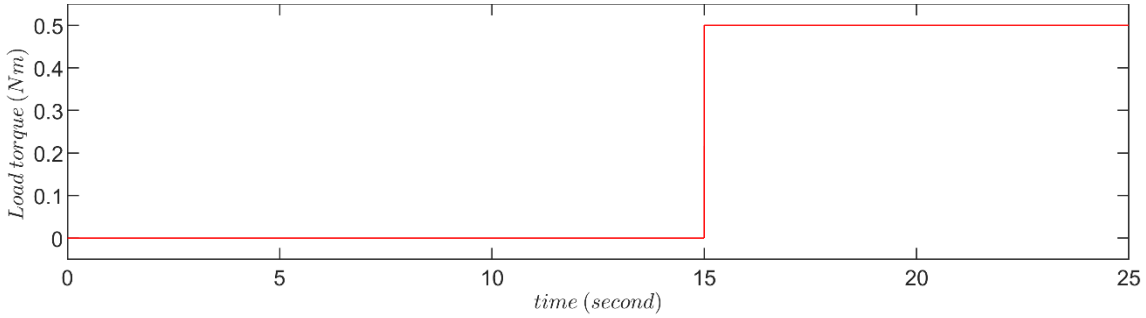

(e)

Figure 7*. The step response simulation results in DC motor control system* ***a)*** *angular position* ***b)*** *angular speed* ***c)*** *armature current* ***d)*** *control input signal* ***e)*** *load torque*

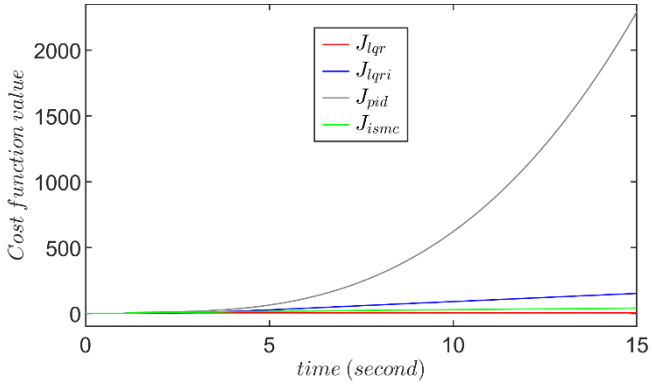

Figure 8*. The values of the cost functions according to time*

CONFLICT OF INTEREST

The author declares no conflict of interest.

REFERENCES

Anderson, B. D., & Moore, J. B. (2007). *Optimal Control Linear Quadratic Methods* (91.12 edition ed.). Dover Publications.

Aravind, M. A., Saikumar, N., & Dinesh, N. S. (2017, May 19-21). *Optimal position control of a DC motor using LQG with EKF*. In: Proceedings of the International Conference on Mechanical, System and Control Engineering (ICMSC), (pp. 149-154). St. Petersburg. https://www.doi.org/10.1109/ICMSC.2017.7959461

Burns, R. S. (2001). *Advanced Control Engineering*. Woburn, England: Butterworth-Heinemann.

Davis, J. H. (2002). Luenberger Observers. In: *Foundations of Deterministic and Stochastic Control* (pp. 245-254). Boston: Birkhäuser. https://www.doi.org/10.1007/978-1-4612-0071-0_8

Dorf, R. C., & Bishop, R. H. (2010). *Modern Control Systems* (12th ed.). (M. J. Horton, A. Gilfillan, A. Dworkin, S. Disanno, G. Dulles, & D. Sandin, Eds.) New Jersey, U.S.A.: Pearson.

Dreyfus, S. (1962). Variational problems with inequality constraints. *Journal of Mathematical Analysis and Applications*, *4*(2), 297-308. https://doi.org/10.1016/0022-247X(62)90056-2

Durdu, A., & Dursun, E. H. (2019). Sliding Mode Control for Position Tracking of Servo System with a Variable Loaded DC Motor. *Elektronika Ir Elekctrotechnika*, *25*(4), 8-16. https://www.doi.org/10.5755/j01.eie.25.4.23964

Edwards, C., & Spurgeon, S. K. (1998). *Sliding Mode Control Theory and Applications*. Boca Raton: CRC Press.

Eli, S. C., Idoniboyeobu, D. C., & Braide, S. L. (2023). Performance Evaluation of D.C. Motor Speed Using Sliding Mode Controller (SMC). *Journal of Emerging Trends in Electrical Engineering*, *5*(3), 1-6.

Feng, X., Liu, S., Yuan, Q., Xiao, J., & Zhao, D. (2023). Research on wheel-legged robot based on LQR and ADRC. *Scientific Reports*, *13*(15122). https://www.doi.org/10.1038/s41598-023-41462-1

Franklin, G. F., Powell, J. D., & Emami-Naeini, A. (2009). *Feedback Control of Dynamic Systems* (6th ed.). New Jersey, U.S.A.: Pearson Education.

Gao, W., & Hung, J. C. (1993). Variable Structure Control of Nonlinear Systems A New Approach. *IEEE Transactions On Industrial Electronics*, *40*(1), 45-55.

Golub, G. H., & Loan, C. F. (2013). *Matrix Computations*. Baltimore: The Johns Hopkins University Press.

Gorczyca, P., Hajduk, K., & Kołek, K. (2011). Optimal Control of A Laboratory DC Servo Motor. *Pomiary automatyka Robotyka*, *15*(12), 129-134.

He, S., Duan, X., Qu, X., & Xiao, J. (2023). Kinematic modeling and motion control of a parallel robotic antenna pedestal. *Robotica*, *41*(11), 3275-3295. https://www.doi.org/10.1017/S0263574723000917

Jouini, M., Dhahri, S., & Sellami, A. (2019). Combination of integral sliding mode control design with optimal feedback control for nonlinear uncertain systems. *Transactions of the Institute of Measurement and Control*, *41*(5), 1331-1339. https://www.doi.org/10.1177/0142331218777562

Khomenko, M., Voytenko, V., & Vagapov, Y. (2013). Neural Network based Optimal Control of Dc Motor Positioning System. *International Journal of Automation and Control*, *7*(1/2), 83-104. https://www.doi.org/10.1504/IJAAC.2013.055097

Kirk, D. E. (1998). *Optimal Control Theory: An Introduction*. New York, Mineola, USA: Dover Publications, Inc.

Krause, P. C., Wasynczuk, O., & Sudhoff, S. D. (2002). *Analysis of Electric Machinery and Drive Systems* (2nd ed.). U.S.A.: John Wiley & Sons.

Krishnan, R. (2001). *Electric Motor Drives Modeling Analysis and Control* (1st ed.). New Jersey: Prentice Hall.

Maghfiroh, H., Anwar, M., Anwar, M., & Ma'arif, A. (2022). Improved LQR Control Using PSO Optimization and Kalman Filter Estimator. *IEEE Access*, *10*, 18330-18337. https://www.doi.org/10.1109/ACCESS.2022.3149951

Mamta, & Singh, B. (2020). Optimal Control of DC motor using Equilibrium Optimization Algorithm. *International Journal of Engineering Research & Technology (IJERT)*, *9*(5), 1272-1275.

Mondal, R., & Dey, J. (2020). Performance Analysis and Implementation of Fractional Order 2-DOF Control on Cart-Inverted Pendulum System. *IEEE Transactions On Industry Applications*, *56*(6), 7055-7066.

Mukhopadhyay, S. (1978). P.I.D. Equivalent of Optimal Regulator. *Elektronics Letters*, *14*(25), 821-822.

Naidu, D. S. (2002). *Optimal Control Systems* (1st ed.). CRC Press.

Nise, N. S. (2011). *Control System Engineering* (6th ed.). Pomona, U.S.A.: John Wiley & Sons, Inc.

Ogata, K. (2010). *Modern Control Engineering* (5th ed.). Natick: Pearson.

Paraskevopoulos, P. N. (2002). *Modern Control Engineering*. CRC Press.

Pontryagin, L. S. (1986). *The Mathematical Theory of Optimal Processes* (Vol. Vol 4). Switzerland: Gordon and Breach Science Publishers.

Pratama, G. N., Setiawan, N., Saputra, S. A., Pambudi, L., Umam, A. D., & Hermansah, M. N. (2022). Optimal Quadratic Regulator PID for Motor DC. *Journal of Physics: Conference Series*, *2406*(012002), 1-7. https://www.doi.org/10.1088/1742-6596/2406/1/012002

Rasheed, L. T. (2020). Optimal Tuning of Linear Quadratic Regulator Controller Using Ant Colony Optimization Algorithm for Position Control of a Permanent Magnet Dc Motor. *Iraqi Journal of Computers, Communications, Control & Systems Engineering (IJCCCE)*, *20*(3), 29-41. https://www.doi.org/10.33103/uot.ijccce.20.3.3

Ruderman, M., Krettek, J., Hoffmann, F., & Bertram, T. (2008). Optimal State Space Control of DC Motor. *IFAC Proceedings Volumes*, *41*(2), 5796-5801. https://www.doi.org/10.3182/20080706-5-KR-1001.00977

Saputra, D. D., Ma'arif, A., Maghfiroh, H., Baballe, M. A., Tusset, A. M., Sharkawy, A.-N., & Majdoubi, R. (2023). Performance Evaluation of Sliding Mode Control (SMC) for DC Motor Speed Control. *Jurnal Ilmiah Teknik Elektro Komputer dan Informatika (JITEKI)*, *9*(2), 502-510.

Simon, D. (2006). *Optimal State Estimation*. Hoboken: John Wiley & Sons.

Tanveer, A., & Ahmad, S. M. (2023). Design and Testing Of a Compack Inexpensive Prototype Remotely Operated Underwater Vehicle for Shallow Water Operation. *Journal of Naval Architecture and Marine Engineering*, *20*(1), 1-10.

Utkin, V. I. (1977). Variable Structure Systems with Sliding Modes. *IEEE Transactions On Automatic Control*, *22*(2), 212-222. https://www.doi.org/10.1109/TAC.1977.1101446

Utkin, V. I. (1992). *Sliding mode In Control and Optimization*. New York, U.S.A.: Springer.

Utkin, V. I. (1993). Sliding Mode Control Design Principles and Applications to Electric Drives. *IEEE Transactions On Industrial Electronics*, *40*(1), 23-36. https://www.doi.org/10.1109/41.184818

Utkin, V. I., & Parnakh, A. (1978). *Sliding Modes and their Application in Variable Structure Systems* (Russian) (1st ed.). Mir.

Utkin, V. I., & Yang, K. D. (1978). Methods for construction of discontinuity planes in multidimensional variable structure systems. *Automat. i Telemekh.*, (10), 72-77.

Utkin, V. I., Guldner, J., & Shi, J. (2009). *Sliding Mode Control in Electromechanical Systems* (2nd ed.). CRC Press.

Wang, B., Liu, C., Chen, S., Dong, S., & Hu, J. (2019). Data-Driven Digital Direct Position Servo Control by Neural Network With Implicit Optimal Control Law Learned From Discrete Optimal Position Tracking Data. *IEEE Access*, *7*, 126962-126972. https://www.doi.org/10.1109/ACCESS.2019.2937993

Xiang, Z., & Wei, W. (2021). Design of DC motor position tracking system based on LQR. *Journal of Physics: Conference Series*, *1887*, 012052. https://www.doi.org/10.1088/1742-6596/1887/1/012052

Yousef, A. M. (2011). Experimental Set up Verification of Servo Dc Motor Position Control Based On Integral Sliding Mode Control Approach. *Journal of Engineering Sciences*, *39*(5), 1095-1110.

Yu, G.-R., Tseng, M.-H., & Lin, Y.-K. (2004, September 2-4). *Optimal Positioning Control of a DC Servo Motor Using Sliding Mode*. In: Proceedings of the 2004 IEEE International Conference on Control Applications. Taipei. https://www.doi.org/10.1109/CCA.2004.1387223

JOURNAL OF SCIENCE

PART A: ENGINEERING AND INNOVATION

| Correspondence Address |

Gazi University
Graduate School of Natural and Applied Sciences
Emniyet Neighborhood, Bandırma Avenue
No:6/20B, 06560, Yenimahalle - ANKARA
B Block, Auxiliary Building

| e-mail |
gujsa06@gmail.com

| web page |
https://dergipark.org.tr/tr/pub/gujsa

e-ISSN 2147-9542